

# Isotopic Proxies for Microbial and Environmental Change:

Insights from Hydrogen Isotopes and the  
Ediacaran Khufai Formation

Thesis by  
Magdalena Rose Osburn

In Partial Fulfillment of the Requirements for the  
degree of  
Doctor of Philosophy



CALIFORNIA INSTITUTE OF TECHNOLOGY

Pasadena, California

2013

(Defended May 28, 2013)



## ACKNOWLEDGEMENTS

This thesis would not have been possible without the generous help and support from many individuals and organizations. Specifically I would like to thank my advisors John Grotzinger and Alex Sessions, who have been pillars of support and guidance throughout this process. I would also like to acknowledge my current and former committee members Woody Fischer, Tim Lyons, Victoria Orphan, and Joe Kirschvink. In addition, I would like to thank the many other GPS professors that have contributed to my interests and background through classes and field trips including John Eiler, Jess Adkins, Jared Leadbetter, George Rossman, and Ken Farley. I am thankful for the editing prowess of Mitchell Barklage and Morgan Raven who were subjected to first drafts of parts of this thesis. Funding is a critical to modern science as well, which indebts me to the NSF GRFP, Petroleum Development Oman, the Gordon and Virginia Eaton Fellowship, and the Agouron Institute for their generous financial support.

Many people contributed directly and indirectly to the works presented here. I would like to acknowledge the additional coauthors on these manuscripts, John Spear, Chuck Pepe-Raney, Kristin Bergmann, Jeremy Owens, and Kat Dawson. I would particularly like to thank Kristin who has additionally served over the years as my field partner, cherished friend, and partner in crime. I have benefitted from the cooperative environments of the Sessions and Grotzinger lab groups over the years, in particular Lichun Zhang, Morgan Raven, Kat Dawson, Ying Wang, Guillaume Paris, Adam Subhas, and Sebastian Kopf for their direct and material assistance. A number of high school students and undergraduates assisted in rock and sample preparation including Haley Barnes, Sean Dembowski, Emma Dodd, and Angela Gerhardt. Lora Wingate, Ken Macleod, and Bob Criss were instrumental in generating carbon isotope data. Finally, I am thankful to Steve Bates who oversaw the preparation and analysis of sulfur isotopes.

The Caltech environment is one where anything is possible if you know whom to ask. The GPS administrative staff has been particularly helpful including Janice Grancich, Kathy Lima, Marcia Hudson, Liz Boyd, and Dian Buchness. I have also been lucky

enough to work closely with the Graduate Dean's office and would like to thank Felicia Hunt and Joe Shepard for enriching my life and allowing me to shake the boat. Various Caltech programs and organizations have contributed to my happiness during my time here including the Women Mentoring Women program, the Graduate Student Council, the Graduate Honor Council (Rob Craig in particular), and the Caltech community garden.

The strong support of family and friends was critical to my success. I would not be here without the encouragement of my parents Bob and JoAnne Osburn. I don't think they meant to turn me into a geologist, but with the multitude of early National Park focused road trips combined with canoeing, caving, and WashU geology field trips, I am not sure there was an alternative. My husband Mitchell Barklage was my rock during this process and I owe him a great deal of credit for helping maintain my sanity and enthusiasm. I still work hard every day to live up to the potential that he has seen in me from the very beginning. My friends both inside and outside of GPS have made my experience here really enjoyable.

I would be remiss if I did not include my early mentors and teachers in this list of gratitude. This begins with my sixth and seventh grade science teacher Wayne Baldwin who taught me the scientific method and encouraged my creativity with a very long leash. My string of excellent science teachers continued in high school with my chemistry teacher Dr. Bob Becker, who truly believed in hands-on science and whose thermite demonstration still might be the most impressive chemical reaction that I have ever seen. I must thank Dr. Everett Shock who took a chance on bringing a fourteen year old me to Yellowstone National Park as a field assistant. These experiences lead into my undergraduate work with D'Arcy Meyer-Dombard and Jan Amend where my interests began to take their current form. These scientists are not only great mentors, but also future collaborators and constant sources of inspiration.

## ABSTRACT

Microbes have profoundly influenced the Earth's environments through time. Records of these interactions come primarily from the development and implementation of proxies that relate known modern processes to chemical signatures in the sedimentary record. This thesis is presented in two parts, focusing first on novel proxy development in the modern and second on interpretation of past environments using well-established methods. Part 1, presented in two chapters, builds on previous observations that different microbial metabolisms produce vastly different lipid hydrogen isotopic compositions. Chapter 1 evaluates the potential environmental expression of metabolism-based fractionation differences by exploiting the natural microbial community gradients in hydrothermal springs. We find a very large range in isotopic composition that can be demonstrably linked to the microbial source(s) of the fatty acids at each sample site. In Chapter 2, anaerobic culturing techniques are used to evaluate the hydrogen isotopic fractionations produced by anaerobic microbial metabolisms. Although the observed fractionation patterns are similar to those reported for aerobic cultures for some organisms, others show large differences. Part 2 changes focus from the modern to the ancient and uses classical stratigraphic methods combined with isotope stratigraphy to interpret microbial and environmental changes during the latest Precambrian Era. Chapter 3 presents a detailed characterization of the facies, parasequence development, and stratigraphic architecture of the Ediacaran Khufai Formation. Chapter 4 presents measurements of carbon, oxygen, and sulfur isotopic ratios in stratigraphic context. Large oscillations in the isotopic composition of sulfate constrain the size of the marine sulfate reservoir and suggest incorporation of an enriched isotopic source. Because this data was measured in stratigraphic context, we can assert with confidence that these isotopic shifts are not related to stratigraphic surfaces or facies type but instead reflect the evolution of the ocean through time. This data integrates into the chemostratigraphic global record and contributes to the emerging picture of changing marine chemistry during the latest Precambrian Era.

## TABLE OF CONTENTS

Acknowledgements .....	iii
Abstract.....	v
Table of Contents .....	vi
List of Illustrations and/or Tables .....	viii
 Introduction .....	 1
 Part 1: Compound-Specific D/H of lipids as a proxy for microbial metabolism .....	 12
 Chapter I: Hydrogen-isotopic variability in fatty acids from Yellowstone National Park hot spring microbial communities .....	 13
Abstract .....	14
Introduction .....	15
Sample Locations and Descriptions .....	17
Methods.....	20
Results .....	26
Discussion .....	34
Conclusions.....	49
References .....	51
 Chapter II: Fractionation of hydrogen isotopes by anaerobic bacteria .....	 57
Abstract .....	58
Introduction .....	59
Materials and methods .....	61
Results .....	67
Discussion .....	77
Conclusions.....	99
References .....	101
 Part 2: Characterization of the Ediacaran Khufai Formation .....	 104
 Chapter III: Facies, Stratigraphy, and Evolution of a Middle Ediacaran carbonate ramp: Khufai Formation, Sultanate of Oman .....	 105
Abstract .....	106
Introduction .....	106
Geological Setting.....	108
Methods.....	117
Facies and facies tracts: Huqf Area .....	118
Facies and facies tracts: Oman Mountains .....	141

Sequence Stratigraphy .....	146
Discussion .....	153
Conclusions .....	163
References Cited .....	165
Chapter IV: Dynamic changes in the isotopic record of sulfate preceding the Shuram Excursion .....	172
Abstract .....	173
Introduction .....	174
Geological Setting .....	175
Background – S-isotopic and concentration proxies .....	178
Materials and Methods .....	179
Results: Formation-scale chemostratigraphy .....	183
Evaluation of trends .....	187
Discussion .....	197
Conclusions .....	215
References .....	217
Appendices .....	221
Appendix A: Supplementary tables from the electronic annex of Chapter 1 .....	222
A1: Sample locations and descriptions .....	222
A2: Identification of measured fatty acids .....	224
A3: Relative abundance of fatty acids (%) .....	225
A4: Measured $\delta D$ values for spring water and fatty acids .....	228
A5: Calculated fractionations (‰) between fatty acid and water .....	230
A6: Geochemical parameters of sampled spring water .....	232
Appendix B: Data from Chapter 2 .....	235
B1: Lipid composition and abundance .....	235
B2: Isotopic measurements .....	237
Appendix C: Chemostratigraphic data for the Khufai Formation .....	243
C1: Chemostratigraphic data for the Huqf .....	243
C1: Chemostratigraphic data for the Oman Mountains .....	272

## INTRODUCTION AND SUMMARY

Microbial life has been witness to dramatic physical and chemical changes to its environment over the course of Earth history. Many of the most fundamental questions in geobiology center on how and why the environment changed and the role of biology in mediating those changes. Ancient depositional environments can be investigated on the basis of clues preserved in the sedimentary record, many of which are extrapolated from studies of modern depositional environments and microbial processes. Geobiological research is often split between projects that develop tools to understand modern processes and those that adapt these techniques to interpreting the past. This thesis embraces both of these trajectories, incorporating modern environmental microbiology, modern and ancient geochemistry, and sedimentology and stratigraphy of ancient environments.

Isotopic proxies are a unifying toolset for interpreting the environmental conditions of both modern and ancient environments. The stable isotope ratios of chemically or biologically active elements reflect the history of processes that acted on them before preservation. The final isotopic composition of a certain species convolves isotopic fractionations from both equilibrium and kinetic isotope effects (Criss, 1999). Marine calcite is an example of a species where both equilibrium and kinetic fractionation generally contribute to the carbon isotopic ratios preserved in rocks. The fractionation between carbonate ion and the calcite mineral is an equilibrium process that is controlled primarily by temperature (Craig, 1953). However, a large kinetic isotope effect resulting from oxygenic photosynthesis contributes to the isotopic composition of precursor carbonate ion. During photosynthesis, the enzymatic conversion of CO<sub>2</sub> into

organic matter has a strong preference for  $^{12}\text{C}$ , which drives the residual marine carbonate pool isotopically more enriched (Hayes, 2001). Bulk measurements of carbonate carbon isotopes in rocks are commonly used to estimate the burial flux of organic carbon through time (Des Marais et al., 1992). In addition, isotopic measurements of organic matter itself can reveal aspects of both biological processes and environmental conditions.

This thesis is presented in two parts that are united by the use of isotopic proxies to interpret environments and distinguished by dramatically different timescales. The first part concerns the development and preliminary implementation of compound-specific hydrogen isotope ratios of organic matter to learn about microbial metabolism. The second part uses classical stratigraphic and isotope-ratio measurements to understand eustatic and chemical changes in the ocean during the latest Ediacaran period. Much like the field of geobiology itself, this work uses one set of proxies to probe the modern and another to interpret the ancient. Ultimately, it seeks to understand the interactions between the Earth system and its inhabitants.

## PART 1: COMPOUND-SPECIFIC D/H OF LIPIDS AS PROXY FOR MICROBIAL METABOLISM

Organisms produce many types of organic compounds that record information about their phylogeny, metabolic pathways, and biological activity. Compound classes of biomolecules commonly used by geobiologists include nucleic acids, proteins, and lipids. However, the potentially long preservation timescale of lipids make them particularly attractive for application to the geological record. Lipids include a functionally and structurally diverse array of hydrocarbons. Major compound classes include N-alkyl lipids, which form straight linear chains, and isoprenoid lipids, which form a variety of

branched chains and cyclic structures (Peters et al., 2005). Functional groups, including alcohols, ketones, aldehydes, thiols, and carboxylic acids, can be attached to these carbon and hydrogen skeletons. The fatty acids are alkyl lipids with carboxylic acid functional groups and form the majority of the lipid bilayer present in bacteria and eukaryotes (White, 2000). These lipids are abundant in the environment and were the primary analytes in Part 1 of this thesis.

The isotopic composition of C and H in lipids can record cellular and environmental processes. Atoms used to construct biological molecules are ultimately sourced from the environment and are assembled and transferred through the cell by a number of enzyme-mediated reactions. This is true for both carbon, which originates in the form of either CO<sub>2</sub> or an organic food source, and hydrogen, which can come from water or food. The carbon isotopic composition of organic matter has been successfully used to differentiate carbon fixation pathways in autotrophs, which impart strong and distinctive fractionations (Hayes, 2001). Carbon isotopic trends can be observed in both bulk organic matter and individual compounds, with bulk values representing a combination of sources. This is in contrast to organic hydrogen isotopes, where bulk measurements include an intractable mixture of bound and exchangeable hydrogen, necessitating the use of compound-specific techniques (Sessions et al., 1999).

Hydrogen is the most abundant element in the universe, permeating the Earth and its biomass. The largest reservoir of hydrogen in the surface Earth is the ocean, which is also the isotopic standard to which measurements are referenced. Fractionation of hydrogen isotopes across land (and to a lesser extent the surface ocean) occurs via evaporation and precipitation processes. Deuterium preferentially partitions into the

condensed phase, depleting the vapor phase as it progresses from the evaporative source (Friedman, 1953). This process creates isotopic gradients where increasing depletion is observed away from the equator and inland from ocean basins (Gat, 1996). Ocean water  $\delta D$ -values are near zero, but at high latitude inland locations,  $\delta D$ -values of  $< -200\text{‰}$  are common. On top of this hydrologic baseline, biological fractionations produce additional enrichments and depletions (Estep and Hoering, 1980), requiring normalization in order to compare processes. Hydrogen isotopic compositions are reported here as fractionations ( $\epsilon_{l-w}$ ) from local water.

The path of hydrogen prior to incorporation into lipids differs from that of carbon, and thus resultant isotopic values record a different set of processes. In addition to forming a primary constituent of biomass as water and biomolecules, hydrogen also performs biochemical functions in the cell, establishing proton gradients and serving as an electron donor (White, 2000). In general, lipid hydrogen reflects the isotopic composition of growth water offset by some fractionation ( $\epsilon_{l-w}$ ) (Sachse et al., 2012). Early culturing and environmental studies showed a roughly linear relationship between  $\delta D_{\text{water}}$  and  $\delta D_{\text{lipid}}$  (Sauer et al., 2001; Huang et al., 2002). Subsequently, small changes in fractionation were shown based on growth rate, salinity, and organism type (Z. Zhang and Sachs, 2007; Sachse and Sachs, 2008; Z. Zhang et al., 2009; Romero-Viana et al., 2013).

In 2009, a groundbreaking study was published that linked the hydrogen isotopic fractionation in lipids with variations in metabolism (X. Zhang et al., 2009). The observed trends had little relationship with the isotopic composition of metabolic substrates and instead varied by carbon source. In this study, C1 carbon compound

metabolism produced strong D-depletions, sugar metabolism produced intermediate D-depletions, and organic acid metabolism produced either small D-depletions or D-enrichments (Z. Zhang and Sachs, 2007). It was hypothesized that the variability in lipid  $\delta D$  reflects variability in the isotopic composition of NADPH, a hydrogen carrier that accepts hydrogen during metabolic reactions and donates that hydrogen during lipid biosynthesis (White, 2000). A number of questions remained after this initial study. How do these signals translate in natural samples? And, do anaerobic metabolisms produce similar signals?

In Part 1 of this thesis, I attempt to answer these questions using a combination of field and laboratory studies. My first contribution, described in Chapter 1, was to study the environmental hydrogen isotopic compositions of well-characterized natural microbial populations. Samples of hydrothermal microbial mats from Yellowstone National Park yielded a rich variety of hydrogen isotopic fractionations that varied with mat type and temperature regime. Comparisons between isotope data and phylogenetic diversity suggested that autotrophic bacteria produced D-depleted lipids and heterotrophs produced D-enriched lipids, in agreement with culturing studies. This study demonstrates that trends in hydrogen isotopic fractionation between microbes with different metabolisms can be produced and observed in environmental samples. Further application of the lipid hydrogen isotope proxy was precluded by a significant lack of data from anaerobic microorganisms. Chapter 2 includes a preliminary study aimed at addressing this knowledge gap by assessing the patterns of hydrogen isotopic fractionation produced by anaerobic bacteria. I cultured both strict and facultative anaerobic bacteria using a large variety of metabolic substrates to probe the fractionations

produced by each. Facultative anaerobes appear to produce similar D-depletions or D-enrichments under both aerobic and anaerobic conditions. However, strict anaerobes produce strong D-depletions regardless of metabolic substrate. These data complicate the interpretation of hydrogen isotopic measurements produced in strictly anaerobic environments and suggest previously unrecognized complexity in the processes that influence these measurements.

## PART 2: CHARACTERIZATION OF THE EDIACARAN KHUFUAI FORMATION

The Ediacaran Period, the last of the Neoproterozoic Era, records the chemical and biological transition from the Precambrian to the Phanerozoic. The Ediacaran is bracketed at ~635 Ma and 542 Ma by sediments that record the last global “Snowball Earth” glaciation and the Cambrian boundary, respectively (Knoll et al., 2006). Ediacaran sections preserve large perturbations to the carbon and sulfur isotopic systems, evidence for oxygenation of deep ocean basins, and the enigmatic Ediacaran fauna. While it is generally accepted that the surface ocean was oxygen replete throughout this interval, the chemical state of the deep ocean remains controversial (Canfield et al., 2008). Inconsistencies in chronology and correlation along with the lack of a unified sea level curve exacerbate questions of environment and chemistry and often preclude interpretation. My approach in Part 2 of this thesis is to combine stratigraphic and isotopic measurements to make a more complete record of this volatile time.

The chemical record of ancient oceans comes from measurements and interpretations of sedimentary composition through time, known as chemostratigraphy. Widely used archives of sedimentary information include the isotopic ratios of carbon, oxygen, sulfur, and trace elements as well as elemental ratios (Halverson et al., 2010). Ediacaran records show large swings in the isotopic compositions of both carbon and sulfur. The largest of these negative carbon isotopic

excursions is called the Shuram Excursion and was first observed in Shuram Formation of Oman (Burns and Matter, 1993). Here,  $\delta^{13}\text{C}$  values drop from strongly positive values of +6‰ to a minimum of -12‰, and strongly negative  $\delta^{13}\text{C}$  values persist for several million years (Le Guerroue, Allen, Cozzi, et al., 2006). The mechanism for the onset and maintenance of this excursion is controversial. Potential explanations include catastrophic methane release, oxidation of a large DOC reservoir, input of light  $\text{CO}_2$  through diagenesis of an inferred terrestrial biosphere, and others (Grotzinger et al., 2011). Like carbonate carbon, marine sulfate sulfur had highly variable isotopic compositions and concentrations during the Ediacaran. Models suggest that the large observed excursions in sulfate sulfur  $\delta^{34}\text{S}$  are consistent with an increase in marine sulfate concentration from extremely low levels to near modern values over the course of the period (Halverson and Hurtgen, 2007). The mechanism(s) and precise timing of these changes are poorly understood. The carbon and sulfur isotope records could both respond to similar processes, but their frequent decoupling limits the likelihood of a single driving mechanism.

A more traditional approach to understanding past depositional environments is to use the tools of sedimentology and stratigraphy. Sedimentary deposits record a wealth of information about environmental parameters at the time of their formation including wave energy, water depth, tidal strength, salinity, and microbial colonization. Carbonate sediments can often yield a detailed cementation history for the emplacement of different fabrics and textures (Fléugel and Munnecke, 2010). Because carbonate platforms are particularly sensitive to changes in relative sea level, studies of their sequence stratigraphic relationships and stacking patterns can reveal the history of relative accommodation (Sarg, 1998). A full understanding of the depositional and stratigraphic framework of a sedimentary unit is a vital prerequisite for chemostratigraphic techniques. To do otherwise could result in major misinterpretation. For instance, a chemostratigrapher without proper stratigraphic context might interpret a depositional hiatus during a gradual environmental change as an abrupt isotopic excursion.

The Khufai Formation is an Ediacaran carbonate ramp complex that records environmental conditions prior to and at the onset of the Shuram isotopic excursion. Previous work in the Khufai Formation includes broad sedimentological characterization as part of regional surveys (Wright et al., 1990; McCarron, 1999; Forbes et al., 2010) and coarse chemostratigraphic and organic geochemical characterization as part of large-scale studies on the Huqf Super Group (Fike et al., 2006; Love et al., 2009) or the Shuram Formation (Le Guerroue, Allen and Cozzi, 2006). While providing a useful framework, previous studies left a number of outstanding questions regarding the depositional history and chemical environment of the Khufai Formation. Proposed depositional frameworks failed to capture much of the actual variability, and detailed facies characterization was beyond the scope of the work. Importantly, reports regarding an unconformity with the overlying Shuram Formation were vague (Gorin et al., 1982; Wright et al., 1990; Fike et al., 2006), and the relationship between this surface and the onset of the Shuram Excursion was previously unknown. This last question is of great importance to the possible driving mechanism of the isotopic excursion, and its answer has global ramifications.

In Part 2 of this thesis, I present detailed sedimentological and stratigraphic frameworks for the Khufai Formation in parallel with high-resolution carbon and sulfur isotopic records. Chapter 3 is a characterization of facies, parasequence stacking patterns, and stratigraphic evolution of the Khufai Formation. Using the principles of sequence stratigraphy, I identify key stratigraphic surfaces and their relationship to changes in facies development. While I do identify a sequence boundary in the upper Khufai Formation, it does not show evidence for significant erosion or an extended depositional hiatus and occurs well below the onset of the Shuram Excursion. This surface cannot have a direct causal relationship with this isotopic event, which is instead associated with a strong transgressive surface. In Chapter 4, I present and evaluate a detailed chemostratigraphic record of carbon and sulfur isotopes in stratigraphic context. This analysis reveals rapid, statistically significant, sulfur isotopic excursions that occur both

independently and in concert with changes in carbon isotopic composition. Evaluation and modeling of these trends suggests extremely low marine sulfate concentrations and major changes to sulfur isotopic fractionation and pyrite burial. These chapters represent the most complete environmental record of the ocean preceding and during the onset of the Shuram Isotopic Excursion presented thus far.

## REFERENCES

- Burns S. J. and Matter A. (1993) Carbon isotopic record of the latest Proterozoic from Oman. *Eclogae geologicae Helvetiae* **86**, 595–607.
- Canfield D. E., Poulton S. W., Knoll A. H., Narbonne G. M., Ross G., Goldberg T. and Strauss H. (2008) Ferruginous Conditions Dominated Later Neoproterozoic Deep-Water Chemistry. *Science* **321**, 949–952.
- Craig H. (1953) The geochemistry of the stable carbon isotopes. *Geochimica et Cosmochimica Acta* **3**, 53–92.
- Criss R. E. (1999) *Principles of Stable Isotope Distribution*, Oxford University Press, USA.
- Estep M. F. and Hoering T. C. (1980) Biogeochemistry of the stable hydrogen isotopes. *Geochimica et Cosmochimica Acta* **44**, 1197–1206.
- Fike D. A., Grotzinger J. P., Pratt L. M. and Summons R. E. (2006) Oxidation of the Ediacaran Ocean. *Nature* **444**, 744–747.
- Flügel E. and Munnecke A. (2010) *Microfacies of Carbonate Rocks*, Springer.
- Forbes G., Jansen H. and Schreurs J. (2010) *Lexicon of Oman Subsurface Stratigraphy*, GeoArabia Special Publication, Manams, Bahrain.
- Friedman I. (1953) Deuterium content of natural waters and other substances. *Geochimica et Cosmochimica Acta* **4**, 89–103.
- Gat J. R. (1996) OXYGEN AND HYDROGEN ISOTOPES IN THE HYDROLOGIC CYCLE. *Annu. Rev. Earth Planet. Sci.* **24**, 225–262.
- Gorin G., Racz L. and Walter M. (1982) Late Precambrian-Cambrian sediments of the Huqf Supergroup, Sultanate of Oman. *Bulletin* **66**, 2209–2627.
- Grotzinger J. P., Fike D. A. and Fischer W. W. (2011) Enigmatic origin of the largest-known carbon isotope excursion in Earth's history. *Nat Geosci* **4**, 285–292.
- Halverson G. and Hurtgen M. T. (2007) Ediacaran growth of the marine sulfate reservoir. *Earth and Planetary Science Letters* **263**, 32–44.

- Halverson G. P., Wade B. P., Hurtgen M. T. and Barovich K. M. (2010) Neoproterozoic chemostratigraphy. *Precambrian Research* **182**, 337–350.
- Hayes J. M. (2001) Fractionation of Carbon and Hydrogen Isotopes in Biosynthetic Processes. *Reviews in Mineralogy and Geochemistry* **43**, 225–277.
- Huang Y., Shuman B., Wang Y. and Webb T. III (2002) Hydrogen isotope ratios of palmitic acid in lacustrine sediments record late Quaternary climate variations. *Geology* **30**, 1103–1106.
- Knoll A., Walter M., Narbonne G. and Christie-Blick N. (2006) The Ediacaran Period: a new addition to the geologic time scale. *Lethaia* **39**, 13–30.
- Le Guerroue E., Allen P. A. and Cozzi A. (2006) Chemostratigraphic and sedimentological framework of the largest negative carbon isotopic excursion in Earth history: The Neoproterozoic Shuram Formation (Nafun Group, Oman). *Precambrian Research* **146**, 68–92.
- Le Guerroue E., Allen P. A., Cozzi A., Etienne J. L. and Fanning M. (2006) 50 Myr recovery from the largest negative  $\delta^{13}\text{C}$  excursion in the Ediacaran ocean. *Terra Nova* **18**, 147–153.
- Love G. D., Grosjean E., Stalvies C., Fike D. A., Grotzinger J. P., Bradley A. S., Kelly A. E., Bhatia M., Meredith W., Snape C. E., Bowring S. A., Condon D. J. and Summons R. E. (2009) Fossil steroids record the appearance of Demospongiae during the Cryogenian period. *Nature* **457**, 718–721.
- Marais Des D. J. D., Strauss H. H., Summons R. E. R. and Hayes J. M. J. (1992) Carbon isotope evidence for the stepwise oxidation of the Proterozoic environment. *Nature* **359**, 605–609.
- McCarron G. M. (1999) Sedimentology and stratigraphy of the Nafun Group, Huqf Supergroup, Oman. Thesis.
- Peters K. E., Walters C. C. and Moldowan J. M. (2005) The Biomarker Guide. *The Biomarker Guide*.
- Romero-Viana L., Kienel U., Wilkes H. and Sachse D. (2013) Growth-dependent hydrogen isotopic fractionation of algal lipid biomarkers in hypersaline Isabel Lake (Mexico). *Geochimica et Cosmochimica Acta* **106**, 490–500.
- Sachse D. and Sachs J. (2008) Inverse relationship between D/H fractionation in cyanobacterial lipids and salinity in Christmas Island saline ponds. *Geochimica et Cosmochimica Acta* **72**, 793–806.
- Sachse D., Billault I., Bowen G. J., Chikaraishi Y., Dawson T. E., Feakins S. J., Freeman K. H., Magill C. R., McInerney F. A. and Van der Meer M. T. (2012) Molecular paleohydrology: interpreting the hydrogen-isotopic composition of lipid biomarkers from photosynthesizing organisms. *Annu. Rev. Earth Planet. Sci.* **40**, 221–249.
- Sarg J. F. (1998) Carbonate Sequence Stratigraphy. In *Sea-Level Changes -- An integrated Approach* SEPM Special Publications. pp. 155–181.
- Sauer P. E., Eglinton T. I., Hayes J. M., Schimmelmann A. and Sessions A. L. (2001)

- Compound-specific D/H ratios of lipid biomarkers from sediments as a proxy for environmental and climatic conditions. *Geochimica et Cosmochimica Acta* **65**, 213–222.
- Sessions A. L., Burgoyne T. W., Schimmelmann A. and Hayes J. M. (1999) Fractionation of hydrogen isotopes in lipid biosynthesis. *Organic Geochemistry* **30**, 1193–1200.
- White D. (2000) *The physiology and biochemistry of prokaryotes*, Oxford University Press, USA.
- Wright V., Ries A. and Munn S. (1990) Intraplatformal basin-fill deposits from the Infracambrian Huqf Group, east Central Oman. In *The geology and tectonics of the Oman region* (eds. A. Robertson, M. Searle, and A. Ries). Geological Society. pp. 1–16.
- Zhang X., Gillespie A. and Sessions A. L. (2009) Large D/H variations in bacterial lipids reflect central metabolic pathways. *PNAS* **106**, 1–7.
- Zhang Z. and Sachs J. P. (2007) Hydrogen isotope fractionation in freshwater algae: I. Variations among lipids and species. *Organic Geochemistry* **38**, 582–608.
- Zhang Z., Sachs J. P. and Marchetti A. (2009) Hydrogen isotope fractionation in freshwater and marine algae: II. Temperature and nitrogen limited growth rate effects. *Organic Geochemistry* **40**, 428–439.

*Part 1:*

Compound-Specific D/H of lipids as a proxy for microbial metabolism

## *Chapter 1*

Originally published in *Geochimica et Cosmochimica Acta* 75 (2011) 4830-4845

### **Hydrogen-isotopic variability in fatty acids from Yellowstone National Park hot spring microbial communities**

Magdalena R. Osburn<sup>1</sup>, Alex L. Sessions<sup>1</sup>, Charles Pepe-Ranney<sup>2</sup>, John R. Spear<sup>2</sup>

Author affiliations:

1. Division of Geological and Planetary Sciences, California Institute of Technology, Pasadena,  
CA 91125, USA.
2. Division of Environmental Science and Engineering, Colorado School of Mines, Golden, CO  
80401, USA.

Keywords: hydrogen isotopes, D/H, Yellowstone, hydrothermal spring, lipids, metabolism

Running head: D/H variability in hot spring microbial communities

## Abstract

We report the abundances and hydrogen-isotopic compositions (D/H ratios) of fatty acids extracted from hot-spring microbial mats in Yellowstone National Park. The terrestrial hydrothermal environment provides a useful system for studying D/H fractionations because the numerous microbial communities in and around the springs are visually distinct, separable, and less complex than those in many other aquatic environments. D/H fractionations between lipids and water ranged from -374‰ to +41‰ and showed systematic variations between different types of microbial communities. Lipids produced by chemoautotrophic hyperthermophilic bacteria, such as icosenoic acid (20:1), generally exhibited the largest and most variable fractionations from water (-374‰ to -165‰). This was in contrast to lipids characteristic of heterotrophs, such as branched, odd chain-length fatty acids, which had the smallest fractionations (-163‰ to +41‰). Mats dominated by photoautotrophs exhibited intermediate fractionations similar in magnitude to those expressed by higher plants. These data support the hypothesis that variations in lipid D/H are strongly influenced by central metabolic pathways. Shifts in the isotopic compositions of individual fatty acids across known ecological boundaries show that the isotopic signature of specific metabolisms can be recognized in modern environmental samples, and potentially recorded in ancient ones. Considering all sampled springs, the total range in D/H ratios is similar to that observed in marine sediments, suggesting that the trends observed here are not exclusive to the hydrothermal environment.

## 1. INTRODUCTION

Recent studies of compound-specific D/H ratios in lipids from marine sediments and particulate organic matter (POM) have documented significant variability, even among molecules with similar biochemical sources of contemporaneous marine origin (JONES et al., 2008; LI et al., 2009; SACHSE and SACHS, 2008). Given that the isotopic composition of seawater is nearly invariant, these data suggest the existence of controlling factors independent of water isotopic composition. This is contrary to the prevalent assumption of a nearly constant biological fractionation between lipids and environmental water. Nevertheless, further interpretation of the marine data was hampered by the difficulty of relating individual lipids to specific organisms in complex environmental samples (LI et al., 2009).

Zhang et al. (2009) described culture experiments in which lipid/water fractionations in bacteria appeared to depend on the central metabolic pathway(s) employed by the organism. Moreover, growth on substrates that activate different catabolic pathways lead to dramatically disparate lipid D/H ratios, even in the same organism. Zhang et al. (2009) therefore hypothesized that various enzymes used in central metabolism to reduce  $\text{NADP}^+$  have very different isotope effects, and so produce NADPH (and ultimately lipids) with distinct isotopic compositions. This hypothesis remains to be confirmed in environmental samples.

The cultured organisms employed by Zhang et al (2009) such as *Escherichia coli* and *Cupriavidus oxalaticus* are unlikely to be prevalent in most environmental samples. More importantly, the bacteria were grown as axenic cultures in minimal media on single substrates, conditions that bear little resemblance to the complex nutrient and trophic structures present in natural environments. There is thus some uncertainty whether the patterns described by Zhang et al. (2009) will be applicable to microbes in their native habitat. To address that question, we studied the fractionation of hydrogen isotopes in bacterial fatty acids from microbial mats

growing in hydrothermal environments of Yellowstone National Park (YNP). We report here the  $\delta D$  values of spring waters and fatty acids in 41 samples collected from 16 springs across YNP.

The terrestrial hydrothermal environment provides a useful system in which to study D/H fractionations in lipids both because of its simplicity and accessibility, and because many of the organisms living there have been intensively studied by others (FOUKE, 2003; HUGENHOLTZ et al., 1998; JACKSON, 2001; Spear et al., 2005; Walker et al., 2005; SHOCK et al., 2010; WARD et al., 1998). The numerous microbial communities in and around the springs have limited diversity compared to most soil and/or marine ecosystems, easing the burden of connecting particular lipids to specific parent organisms. This task is further aided by the fact that many representatives of microbial communities featured herein have been isolated in culture (BROCK et al., 1972; BROCK and FREEZE, 1969; HUBER et al., 1998; PIERSON and CASTENHOLZ, 1974) and their lipids have been previously characterized. YNP has the additional benefit of extensive previous phylogenetic and isotopic studies that provide significant context for our studies (JAHNKE et al., 2001; JAHNKE et al., 2004; MEYER-DOMBARD et al., 2011; MEYER-DOMBARD et al., 2005; ZHANG et al., 2004).

Whereas simplicity is a virtue for identifying the sources of lipids, comparisons across a wide range of physical, chemical, and biological parameters are desirable for surveying the breadth of microbial metabolism. Here again hydrothermal systems provide substantial advantages. Even within a single spring, communities vary systematically with temperature and are frequently visually distinct from one another, allowing for targeted sampling and comparison between different mat types. For example, a classic ecological succession follows temperature and has been studied extensively in outflow channels of Lower Geyer Basin (LGB) type springs such as Octopus Spring (BROCK, 1978). The sequence begins with chemolithoautotrophic communities dubbed “pink streamers” living at the highest temperatures (JAHNKE et al., 2001), followed by photosynthetic mats ranging from thin yellow biofilms to thick orange and brown mats depending

on temperature and water velocity (CASTENHOLZ, 1969). Apart from the LGB type springs, extremely variable chemical compositions and energetic potentials exist in the many different geyser basins around the park, giving rise to remarkable microbial diversity (SHOCK et al., 2010; SPEAR et al., 2005) and the potential for broad comparisons of isotopic fractionations.

## 2. SAMPLE LOCATIONS AND DESCRIPTIONS

Samples were taken from sixteen springs in seven hydrothermal areas over the course of two sampling expeditions in June of 2008 and 2009 (Fig. 1), and were chosen to cover a range of microbial mat and spring types. The primary focus was to sample classic mat types from LGB runoff channels along with samples of specific mat types from different kinds of springs (Table 1). LGB-type springs included Octopus Spring, 'Bison Pool', Ojo Caliente, Imperial Geyser, and four smaller features in the White Creek area. Where possible, we took samples of all three main mat types from these springs including high temperature pink or white streamers, yellow biofilms, and orange photosynthetic mats (BROCK, 1978; BROCK and FREEZE, 1969; CASTENHOLZ, 1969). During the 2009 visit, layered mat samples were further dissected into three distinct layers. Samples of the common orange photosynthetic mats were quite variable in morphology and could be broadly divided into two groups, with higher temperature mats being generally thicker with planar stratification and occasionally a green upper surface, whereas lower temperature mats displayed more irregular to coniform laminations. We collected both types of orange mat at Octopus Spring in 2009.

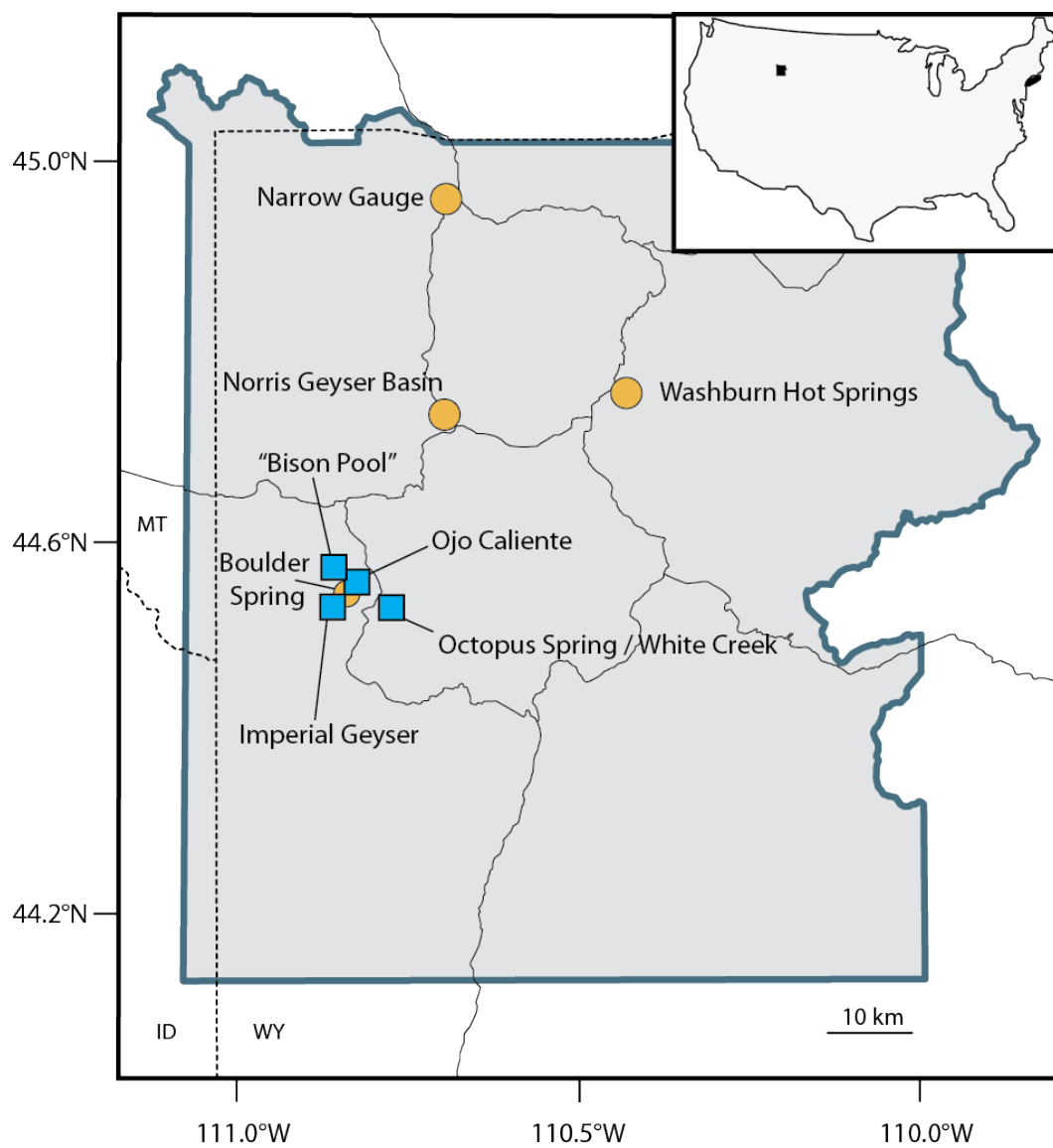


**Figure 1:** Location of sampling sites. YNP is shown in grey, state boundaries are dashed lines, and roads are thin gray lines. Sample locations are indicated by squares for LGB type springs and by circles for all others.

In addition to the LGB sample suite, we also collected mats from springs with more varied chemistry. *Zygonium* mat and green biofilms from Norris Geyser basin, and black sediments from Washburn Hot Spring Group, represent sulfur-rich acidic systems. Boulder Spring in the

Sentinel Meadow area was neutral to alkaline although high in sulfide and contains unusual black sediments. Mats from Narrow Gauge spring in the Mammoth area are carbonate- rather than silica-depositing springs. Further details and samples names are provided in Table 1 and EA-1.

**Table 1:** Description of samples.

Spring Name <sup>a</sup>	Park Reference	Latitude (°N)	Longitude (°W)	Sample number <sup>b</sup>	Type <sup>c</sup>	temp	pH
<i>Lower Geyser Basin</i>							
Octopus Spring	LWCGG138	44.53405	110.79784	OS08-1	PS	--	7.9
				OS08-2	YB	--	
				OS08-3	OM-LT	--	
				OS09-1	PS	86.1	
				OS09-2	YB	74.1	
				OS09-3	OM-HT	63.1	
				OS09-4abc	OM-LT	37.9	
‘Brain pool’	LWCG149	44.53225	110.79654	BP09-1	PS	85±2	8.9
				BP09-2	PS	82.5	
‘Spent Kleenex’	--	44.53247	110.79757	SK09-1	PS	86.9	9.0
				SK08-1	PS	--	--
‘Fallen Log’	LWCGNNO51			FL08-1	OM-HT	--	--
‘Log Jam’	--			LJ08-1	YB	--	--
‘White Creek’	--			WC08-1	OM-HT	--	--
<i>Sentinel Meadows</i>							
Bison Pool	LSMG013	44.56953	110.86511	B09-1	PS	81.5	8.4
				B09-2	PS	76.6	
				B09-3	YB	64.5	
				B09-4abc	OM-LT	--	
Ojo Caliente	LR001			OC09-1	PS	80.2	--
Boulder Spring	--	44.55873	110.84383	BS09-1	SR	81.8	9.2
	--			BS09-2	SR	78.6	6.9
Imperial Geyser	--	44.53167	110.87643	IG09-1	YB	69	9.0-9.1
				IG09-2abc	OM-HT	64.2	
				IG09-3	OM-HT	62.5	
<i>Norris Geyser Basin</i>							
‘Zygonium mat’	--	44.72885	110.71178	NR08-1	SR	--	2.3
	--			NR09-1	SR	25.2	
	--			NR09-2	SR	25.2	
	--	44.72747	110.71162	NR09-3	SR	36.6	3.2
<i>Washburn Hot Spring Group</i>							
‘Boomerang’	WHSNN014	44.75573	110.43007	WB09-1	SR	76.1	3.3

'DEDS'		44.75573	110.43007	WB09-2	SR	73.5	5.0
<i>Mammoth Hot Springs</i>							
Narrow Gauge	MA042	44.96933	110.71044	NG09-1	Carb	46.5	7.9
				NG09-2	Carb	46.5	
				NG09-3	Carb	46.5	
Old Narrow Gauge	MA041	44.96983	110.7103	NG09-4	PS	58.6	6.3
				NG09-5	Carb	34.6	

(a) Spring names are official park names unless indicated with quotation marks

(b) Samples are named as XX YY-Za, where XX is an abbreviation of the spring name, YY is sampling year, Z is sample number from that location, and a is the mat layer (present only for samples that were dissected). For example OS09-4a refers to Octopus Spring, 2009, location 4, layer a (top).

(c) Mat types are abbreviated as follows: PS - pink streamer, YB - yellow biofilm, OM-LT - orange mat low temperature, OM- HT - orange mat high temperature, SR - Sulfur Rich, Carb - carbonate hosted orange mat.

### 3. METHODS

#### 3.1 Lipid Extraction

Samples for lipid analysis were collected using solvent-washed tongs, spoons, or spatulas, and placed directly into pre-combusted glass jars with Teflon cap liners. During the 2009 field season, thick layered photosynthetic mat samples were dissected with a sterile scalpel and dissecting needle using pre-combusted aluminum foil as a work surface. All samples were stored on ice until their arrival at Caltech (<4 days), then were frozen, lyophilized, and stored at -20°C until lipid extraction. Samples NR09-3 and OS09-2 were thin biofilms on pieces of sinter,

and were collected by submerging coated rocks in spring water in sample jars. In the lab, the samples were treated in an ultrasonic bath for 30 min to disaggregate the biofilms. Biomass laden water was then lyophilized to yield concentrated microbial biomass. Temperature and pH of the springs were measured at the time of sampling (Table 1).

Dry biomass samples were first ground to a powder in a solvent-washed mortar and pestle. Samples collected in 2008 were extracted using a modified Bligh-Dyer procedure (BLIGH and DYER, 1959). Samples were first shaken vigorously in a single-phase mixture of dichloromethane (DCM):methanol (MeOH):water (1:2:0.8 v/v). Addition of DCM and H<sub>2</sub>O caused the mixture to separate into organic and aqueous phases, from which the organic fraction was collected. Samples collected in 2009 were extracted using a Microwave Accelerated Reaction System (MARS Xpress, CEM corp) with 20 ml DCM/MeOH (9:1) at 100°C for 15 minutes, with stirring. Direct comparison of these two methods on several 2009 samples indicated that both yield similar fatty acid distributions, but with a 4-5 times greater yield from the MARS system.

Total lipid extracts were filtered, dried under a stream of N<sub>2</sub>, and saponified in 10 mL of aqueous 0.5M NaOH at 70°C for 4 hours. Saponified samples were then extracted three times with methyl tert-butyl ether (MTBE). Elemental sulfur was removed by eluting through acid-washed copper powder (-40 to +100 mesh). After resuspension in hexane, samples were separated into 4 fractions by solid phase extraction (SPE) on an aminopropyl stationary phase following the method of SESSIONS (2006). Only data from the fatty acid fraction (F4, eluted in 8 mL of 2% formic acid in DCM) are reported here. Fatty acids were derivatized by heating with 100µl BF<sub>3</sub>/MeOH at 70°C for 10 min to form fatty acid methyl esters (FAMES), and a known amount of palmitic acid isobutyl ester (PAIBE) was added to each sample as an internal standard. Some samples contained significant amounts of hydroxy-fatty acids that complicated the GC chromatograms. These compounds were separated by column chromatography on 5% deactivated

silica gel, eluting the FAMES in 3 bed-volumes of hexane, and the hydroxy-FAMES in 3 bed-volumes of acetone.

### 3.2. Geochemical Analyses

Water samples for D/H analysis were collected in pre-combusted glass 2 mL vials with Teflon coated screw caps. Turbid or sediment-laden samples were filtered through 4  $\mu\text{m}$  and 0.2  $\mu\text{m}$  syringe filters. Samples were stored on ice in the field and at 4°C until analysis at Caltech using a Los Gatos DLT-100 Liquid Water Isotope Analyzer. Samples were measured in six-fold replicate against two working standards ( $\delta\text{D} = -154.1$  and  $-117.0\text{‰}$ ). Measured isotope ratios were converted to  $\delta\text{D}$  values by comparison with the two standards, and normalized to the SMOW-SLAP scale. Typical precision for these analyses was 1-2‰. All data reduction was performed using Visual Basic code written by us.

Fifteen milliliters of water from each sampling site was collected by syringe, sterile filtered and acidified ( $\text{pH} < 2$ ) for measurement of metals and major cations by inductively coupled plasma atomic emission (ICP-AE) spectroscopy. A second 15 mL aliquot of water was collected and sterile-filtered for analysis of major anions by ion chromatography (IC). Both analyses were performed at the Colorado School of Mines.

Samples for measurement of dissolved  $\text{H}_2$  concentrations were collected via a bubble-stripping method modified from Spear et al. (2005). Water was pumped at approximately 200 mL/min for 20 min through gas-impermeable, Tygon FEP-lined tubing into and through a 1 L gas sampling bulb. Thirty mL of air was injected into the gas sampling bulb. Gas samples were collected by syringe and transferred to nitrogen-charged, hydrogen-impermeable glass septum

vials and shipped to Microseeps (Pittsburg, PA) for analysis of H<sub>2</sub> content on an RGA3 reduction gas analyzer (Trace Analytical, Newark, DE).

### 3.3. Lipid analyses

Lipids were identified and quantified by gas chromatography-mass spectrometry (GC-MS). One microliter of each organic extract was injected into a ThermoFinnigan Trace GC with the effluent split ~9:1 between a DSQ mass spectrometer and a flame ionization detector (FID). The sample was injected into a programmable temperature vaporization (PTV) injector operated in splitless mode and heated to 330°C in 24 sec. The GC was equipped with a ZB-5ms GC column (30 m long, 0.25 mm I.D., 0.25µm film thickness) and was operated with a He carrier gas flow rate of 0.8 ml/min. The oven temperature was held for 1 min at 100°C, ramped at 20°C/min to 140°C, ramped at 3.0°C/min to 250°C and held for 1 min, then ramped at 20°C/min to 310°C and held for 10 minutes. Compounds were identified by comparison of mass spectra to the NIST 2004 library and/or by retention time to authentic standards. Concentrations were calculated by comparing integrated FID signals for each peak to the PAIBE internal standard assuming identical response factors for all FAMEs. FAMEs are reported using the nomenclature “X:Y” where X is carbon number and Y is number of double bonds. The position and stereochemistry of double bonds was not determined. We follow the convention of naming compounds with iso- or anteiso- methyl branches, or cyclopropyl rings, as the total carbon number preceded by *i*-, *a*-, or *cy*- respectively. Thus ‘i-17’ is 15-methylhexadecanoic acid.

D/H ratios of FAMEs were measured using a ThermoFinnigan Trace GC coupled to a Delta+XP isotope ratio mass spectrometer (IRMS) via a pyrolysis interface (GC/TC) operated at 1430°C. External FAME standards were analyzed after every fifth sample. Eight microliters of each sample was injected using a PTV injector operated in splitless mode with solvent venting. A

thick-film ZB-5ms column (30 m long, 0.25mm I.D., 1.00  $\mu\text{m}$  film) was used for isotope analysis with He carrier gas flow rate at 1.4 ml/min. The GC oven temperature was held at 100°C for 1 min, ramped at 20°C/min to 205°C, ramped at 0.8°C/min to 220°C, ramped at 8°C/min to 320°C and held for 10 min. Peaks were identified by comparison of retention order and relative height to GC-MS chromatograms. Isotope ratios were calculated using ISODAT NT 2.5 software by comparison to methane reference gas peaks as described previously (WANG and SESSIONS, 2008) and are reported in the standard  $\delta\text{D}$  notation ( $\equiv R_{\text{sample}}/R_{\text{std}} - 1$ ) as permil (‰) variations relative to the VSMOW standard. The root-mean-squared (RMS) error for external FAME standards run both before and between sample runs was 5.47‰ ( $n = 48$ ) for 2008 samples and 5.85‰ ( $n = 156$ ) for 2009 samples. The standard deviation for replicate analyses of unknown analytes averaged 7.5‰ ( $n = 247$ ). Samples were analyzed in triplicate where possible, however low sample abundance prevented this in some samples. The  $\text{H}_3$  factor averaged 3.90 ppm/mV (range 3.838 - 4.021) during analyses of the 2008 samples, and averaged 7.09 (range 6.56 - 7.46) during analyses of the 2009 samples. Fractionations between lipids and environmental water were calculated as  $\epsilon_{\text{l-w}} = ((\delta\text{D}_\text{l}+1)/(\delta\text{D}_\text{w}+1) - 1)$  and are reported as permil (‰) variations.

### 3.4. DNA Extraction, PCR and DNA Sequencing

DNA was extracted from samples using the Powersoil extraction kit (MoBio). The manufacturer's protocol was followed with the 10 min lysis/vortexing step replaced by 1 min bead-beating. qPCR was conducted on a Lightcycler 480 II (Roche) to monitor the plateau point of amplification. A PCR-touchdown annealing temperature strategy (DON, 2010) was employed for 10 cycles to minimize primer dimer formation and the final 15-20 cycles combined the annealing and elongation steps. PCR was stopped for each sample when it appeared the amplification was beginning to plateau. qPCR volumes were 30  $\mu\text{L}$  total, 9.6  $\mu\text{L}$  of which was

DNA template. Reagents and final concentrations were: 1X Phusion DNA Polymerase MasterMix with HF Buffer (New England Biolabs), 0.5  $\mu$ M forward and reverse primer, 8% v/v DMSO, 0.4X Sybr Green I (Invitrogen). Primers incorporated the adapter sequences for pyrosequencing on the GSFLX platform of the Roche 454 Pyrosequencing technology. Additionally, each forward primer had an 8 nt barcode corresponding to an environmental sample that allowed amplicon pools to be sequenced in parallel and binned by sample *in silico* post-sequencing. The small sub-unit (SSU) rRNA gene primers were attached to adapters only (reverse primer) or adapters and barcodes (forward primer) by a 2 nt linker. The sequence for the linker was the two least abundant bases at the adjacent positions to the primer in the Silva SSURef102\_NR alignment and database (PRUESSE, 2007) for which the *E.coli* sequence did not have a gap. SSU rRNA gene primers were adapted from 515F (LANE, 1991) and 927R (JURGENS et al., 1997) to account for observed mis-pairings of the primers with archaeal and bacterial sequences from the Silva SSURef102\_NR database. Evaluation of primers was done using custom Python scripts that employed bioinformatics modules from PyCogent (KNIGHT, 2007). The specific SSU rRNA gene primers used were 515f-modified, 5'-GTGYCAGCMGCCGCGGTAA-3', and 927r-modified, 5'-CCGYCAATTCMTTTRAGTTT-3'. Individual sample amplicon volumes were pooled and gel purified (Montage DNA Gel Extraction Kit. Millipore) prior to sequencing. Although, GSFLX adapters were used during PCR amplification, sequencing was done on the later generation Roche 454 Titanium platform.

Sequences shorter than 150 nt and longer than 500 nt were discarded. Additionally, sequences with average quality scores less than 25, errors in the barcode or primer, homopolymer runs greater than 6 nt, and ambiguous base-calls were removed from analyses to improve the quality of the final data as described (HUSE, 2007). Initial quality control steps were completed with QIIME (CAPORASO, 2010). The flow grams for the remaining sequences were sent through a noise

removal algorithm to clean up characteristic pyrosequencing errors (REEDER and KNIGHT, 2010). Following noise removal, the sequences were clustered at 97% identity using UClust (EDGAR, 2010) and the most abundant sequence from each cluster was chosen as the cluster representative. Chimeric representative sequence OTUs were identified with ChimeraSlayer and removed from further analyses (HAAS et al., 2011). Cluster representatives were classified by recruiting reads to taxonomically annotated near full-length SSU rRNA gene sequences in Silva SSURef102\_NR using BLAST (ALTSCHUL, 1990). Prior to classification, sequences in the Silva SSURef102\_NR database with values for the seq\_qual\_slv and align\_qual\_slv metadata fields less than or equal to 50 and the pintail\_slv field less than or equal to 40 were discarded. UClust, BLAST, noise removal and cluster representative picking were done using Python scripts and wrappers available in the QIIME software package. DNA Sequencing data from this study has been deposited in the Sequence Read Archive (Acc#: SRA029100).

## 4. RESULTS

### 4.1. Hot Spring Geochemistry

Hot spring geochemical parameters illustrate the great variability between different types of springs sampled in this study (Table 1 and EA-1). Temperature and pH of source pools varied with location. LGB and Sentinel Meadow springs were near boiling (<95 °C at these elevations) at their sources with neutral to alkaline pH (mean of 8.4), whereas springs in Norris Geyser Basin were characteristically very acidic and cooler than the LGB type springs. The Washburn hot spring group had diverse fluid compositions, but the springs we sampled were sub-boiling (73.5-76.1 °C) and acidic (3.26-4.98). Carbonate springs at Mammoth Hot Springs were more uniform and slightly cooler than the LGB springs and of neutral pH.

Trends in major anion and cation abundance were similar within individual thermal areas. LGB samples were generally characterized by high F, Cl, and Na, and low SO<sub>4</sub> and Fe. Sample BP09-2 had generally lower concentrations of these species as it was taken from the confluence of the hot spring and a creek with presumably mixed meteoric and hydrothermal composition. Norris and Washburn groups were generally similar to each other and were characterized by low F and high SO<sub>4</sub>, B, Ca, Fe, and Mg. Significant differences between the two springs are seen in Cl, K, and Na with Norris being higher than average for the total data set and Washburn lower. Samples from the carbonate hosted Narrow gauge system were not correlated with any of the other areas, showing very high Ca, Mg, and K, low F, Br, Fe, and moderate values for Cl and Na. Sulfate showed the most striking variability of any measured species ranging between 15.28 and 2501.9 mg/L, and was qualitatively correlated to the type of microbial mats present in a spring. Br and NO<sub>3</sub> were universally low throughout the sampled springs. The complete geochemical dataset is presented in the electronic annex (EA-1).

#### **4.2. Patterns of Microbial Phyla and Lipid Abundance**

We identified 43 distinct fatty acid structures present in 41 samples. Of these only two (16:0 and 18:0) were found in all samples. The great diversity and patchy distribution of these compounds makes a simultaneous comparison of all samples difficult. In general though, the distribution of fatty acids in a sample varied predictably by mat type, and so for simplicity we discuss the samples in groups based on mat types. The six main groups are denoted as: PS, chemoautotrophic streamers (includes pink, white, and yellow types); YB, yellow biofilms (includes IG09-1 that was a yellow mat); OM-HT, high temperature orange mats; OM-LT, low temperature orange mats; Carb, carbonate hosted orange mats; and SR, sulfur rich samples (includes acidic mats, biofilms, and sediments). While these distinctions are qualitative, they

effectively separate lipid-based compositional groups and correspond qualitatively to phylum-level genetic diversity based on 16S rRNA gene sequencing results.

The average phylum-level phylogenetic compositions for each mat-type group are presented in Figure 2 and are broadly consistent with the results of previous phylogenetic studies (Meyer-Dombard et al., 2005; Meyer-Dombard et al., 2011; Spear et al., 2005; Ward et al., 1998). Individual samples within the groups were similar enough to justify averaging except in the case of the SR group, where it was more appropriate to present the hydrothermal areas separately. The most striking compositional distinction is the dominance of the Aquificae in PS samples. They are also present, but at much lower levels, in both YB and OM-HT mats. The phototrophic mats (YB, OM-HT, OM-LT, and Carb) show an expected high proportion of photosynthesizing organisms, each comprising greater than half the population. There is a relative lack of Chloroflexi in YB mats compared to the large populations present in the other mat types, perhaps representing an upper temperature bound for the Chloroflexi as YB mats are the hottest photosynthetic mat samples. While the phototrophic populations of OM-HT and OM-LT mats are quite similar at the phylum level, the other (non-phototrophic) halves of these communities are quite different from one another. The heterotrophic population in OM-HT mats is extremely diverse with the largest components being Thermus, Thermotoga, Acidobacteria, and Candidate division OP10. This contrasts with OM-LT type mats that instead have significant contributions from Bacteroidetes, Acidobacteria, and Proteobacteria. This is similar to bacterial clone libraries in Meyer-Dombard et al., 2011 which show significant variability in the non-photosynthetic portion of biofilms between various downstream LGB samples. The Carb mats have low numbers of heterotrophs relative to phototrophs and relative to the other mat types.

SR type samples were extremely diverse, precluding their representation as a single diversity wheel. Boulder spring samples contain significant contributions of Aquificae, Thermodesulfobacteria, Proteobacteria, and various heterotrophs. Washburn samples were

dominantly split between Aquificae and Crenarchaeota with minor contributions from Firmicutes and Proteobacteria. The Norris diversity wheel includes only NR09-2 and NR09-3 because NR09-1 (Zygonium mat) failed to amplify. These samples were both dominated by Proteobacteria but NR09-3 shows a significant (42.9%) proportion of chloroplast sequences that we attribute to diatoms based on microscopic inspection. Previous studies have shown that Zygonium mats contain significant proportions of eukaryotic algae from the genera *Zygonium* and *Cyanidium* (Rothschild, 2001; Walker et al., 2005).

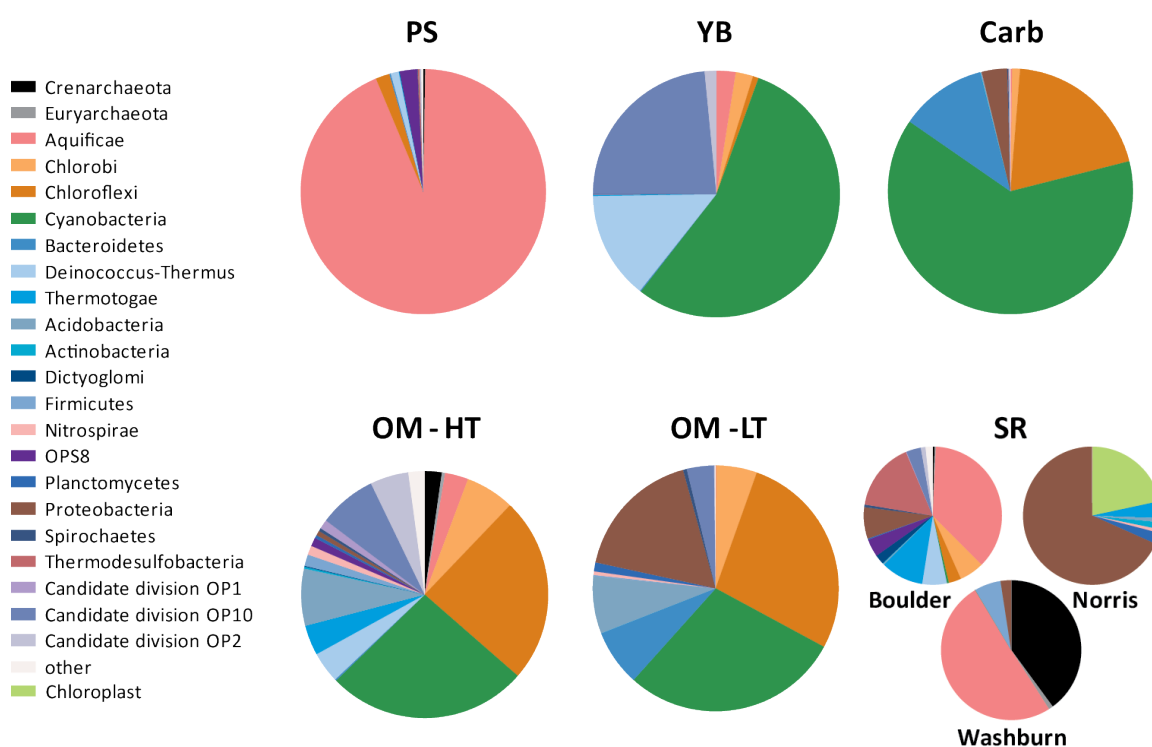


**Figure 2:** Phylum-level genetic diversity of mat types based on SSU rRNA gene sequence. Large circles represent average compositions for particular mat types, whereas small circles represent average compositions for individual hydrothermal areas.

The relative abundances of fatty acids (FA) in each sample are summarized in Figures 3 and 4, illustrating the similarity between individual samples in a mat type and clear compositional distinctions between the different mat types. The streamer (PS) communities were the most variable, but are also distinct from all other groups. They were characterized by a large proportion of 20:1 and cy-21 FA, along with significant amounts of branched compounds. Samples BP09-2 and NG09-4 showed visual evidence of pigmented microbes encrusting streamers and were distinguished by lower relative abundances of 20:1 and cy-21 and much larger amounts of cy-19. YB mats contained >70% straight-chain FA (both even and odd chain lengths) and cy-19, with minor abundances of branched and unsaturated compounds in some samples. OM-HT samples were similar to YB samples but with higher proportions of odd-chain FA and variable contributions of unsaturated and branched compounds. OM-LT, Carb, and SR mats were very different from those above but quite similar to each other. These groups were comprised primarily of equal proportions of even-chain and unsaturated FA. The OM-LT mats were differentiated from the others by a slightly larger contribution of odd-chain and branched FA, whereas the SR samples showed a unique contribution of long-chain FA (C<sub>22</sub>-C<sub>28</sub>).

Specific locations that were sampled in both 2008 and 2009 showed significant variability over time. This is particularly true in the higher temperature pairs OS08-1/OS09-1, SK08-1/SK09-1, and OS08-2/OS09-2. For these three pairs, the relative proportion of odd-chain FA decreased from 2008 to 2009, but there was no systematic trend in corresponding increases. Samples of low temperature orange mat from Octopus Spring were roughly consistent between years (OS08-3/OS09-4abc). Subsections (abc) of dissected mat samples had similar lipid profiles despite appearing visually distinct.

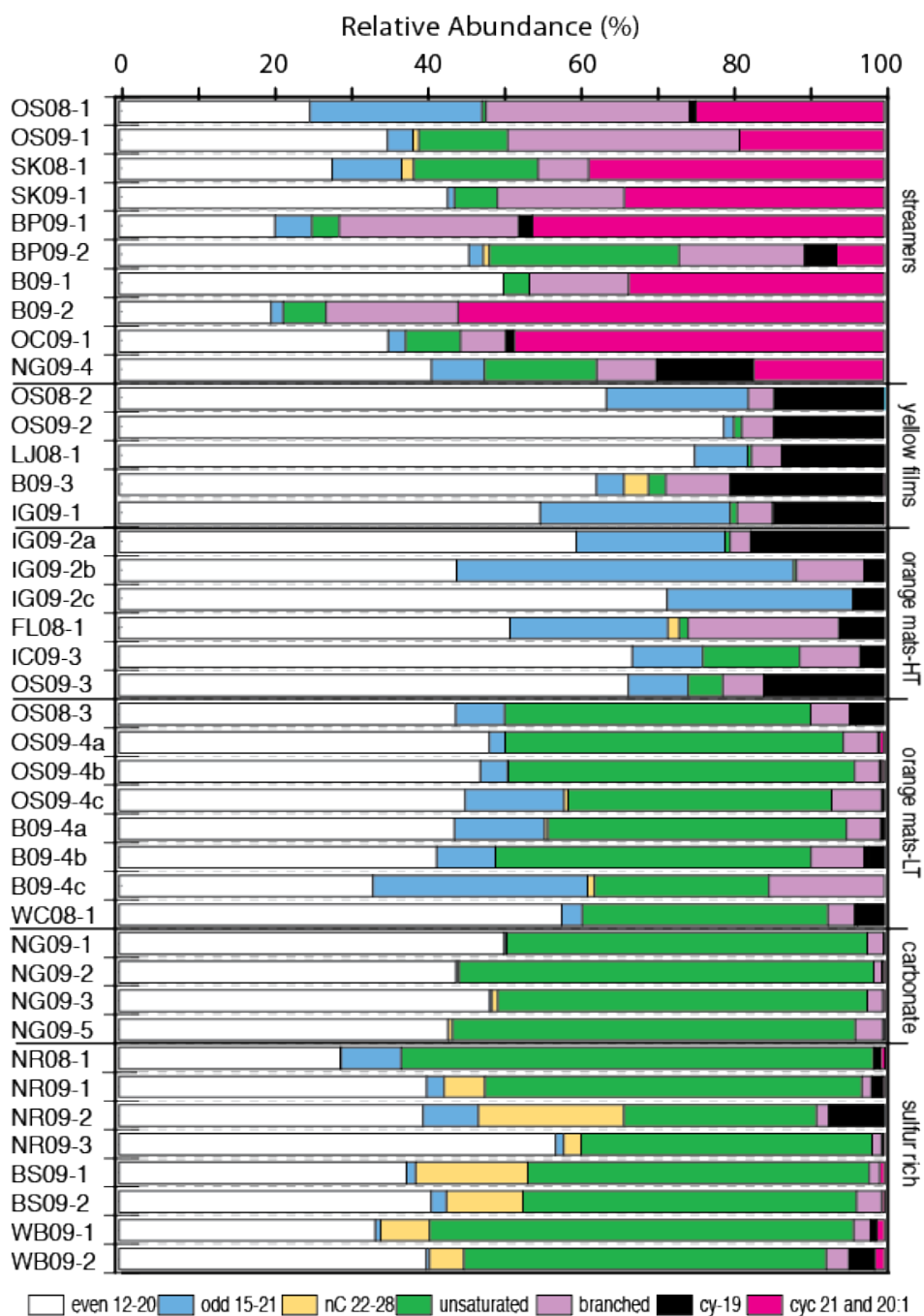


**Figure 3:** Fatty acid distributions for each sample. Fatty acids with related structures and/or origins are binned together. Samples are ordered into characteristic groups based on mat type as described in the text, and as indicated on the right side of the graph.

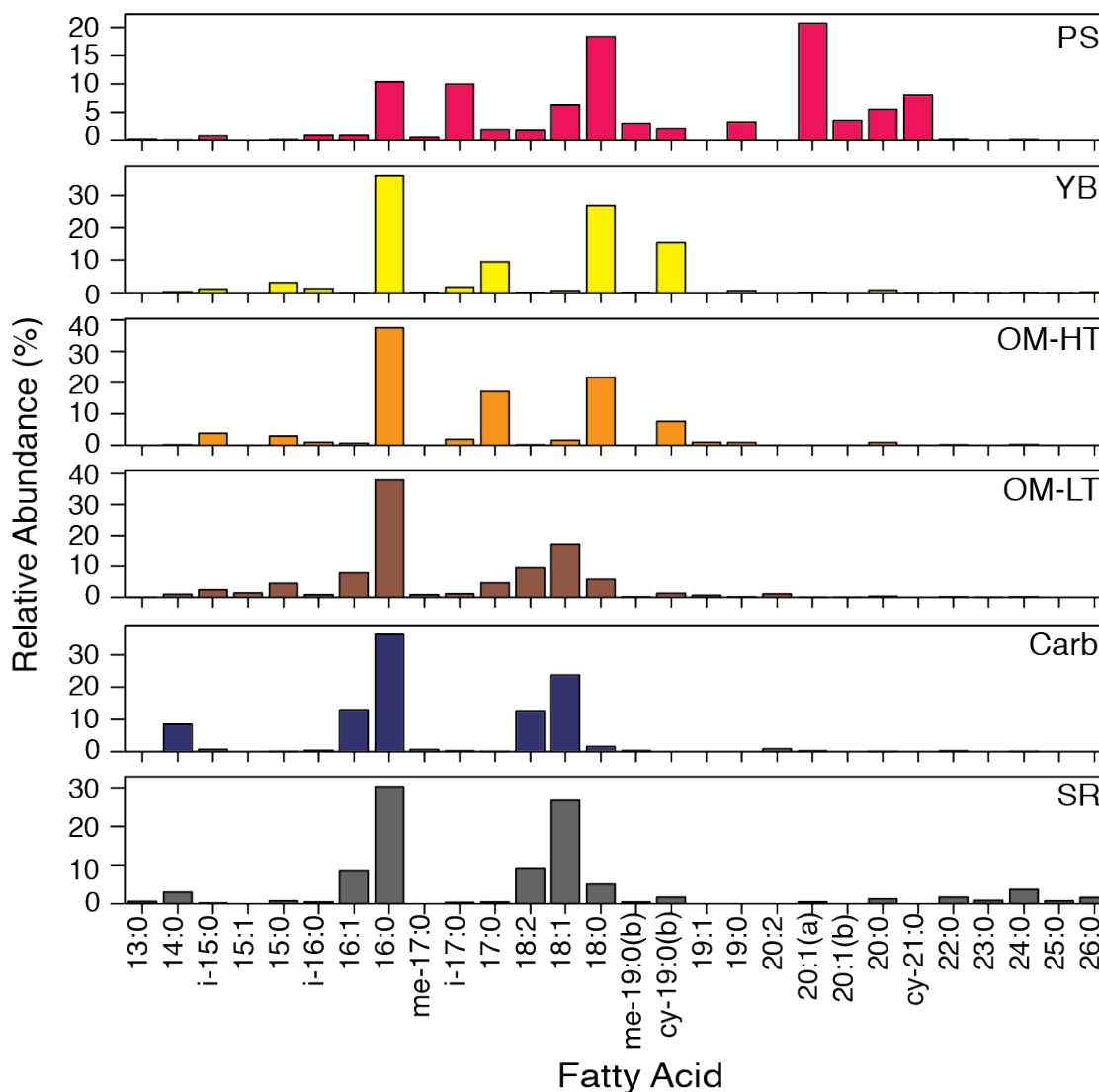


**Figure 4:** Average relative abundances of individual FA in each mat type. Compounds with very low relative abundance (<0.6%) are not shown.

#### 4.3. Isotopic Compositions of Lipids and Water.

Values of  $\delta D$  for the different spring waters were fairly consistent and averaged  $-132 \pm 5\text{‰}$  for the 2008 samples and  $-138 \pm 8.5\text{‰}$  for 2009 samples (EA-1). Most of the 2009 samples were

near -140‰, but samples WB09-1 and WB09-2 were more D-enriched at -117‰. These values are consistent with measured cold-water and snow from the YNP area which ranged from -115 to -153‰ and -88 to -178‰, respectively (Kharaka et al., 2002). In comparison, lipid  $\delta D$  values spanned a >400‰ range, providing a vivid demonstration of the highly variable biotic fractionations that occur.

D/H fractionations between fatty acids and source spring waters (quantified as  $e_{L/w}$ ) observed in this study ranged from -374‰ to +41‰ (Fig 5). In addition, these fractionations varied systematically by mat type, with streamer samples exhibiting larger and more variable fractionations ( $-191 \pm 100$ ‰) than the other types, and extending to extremely negative values (i.e., strong D-depletions of lipids). Fractionations in other mat types were more consistent, and decreased in the order YB ( $-151 \pm 71$ ‰), OM-HT ( $-147 \pm 65$ ‰), Carb ( $-137 \pm 69$ ‰), SR ( $-116 \pm 44$ ‰), and OM-LT ( $-97 \pm 53$ ‰). Lipids from OM-LT mats were the least D-depleted on average, and in some cases the fractionations were positive, indicating that lipids were D-enriched relative to water. Interestingly, orange mats from the carbonate system had  $\delta D$  values more similar to those from OM-HT mats in siliceous springs, even though lipid abundance and 16S diversity suggest they were more similar to OM-LT type mats. Duplicates samples from the same spring in multiple years show variable consistency. PS mat pairs from Octopus Spring shifted significantly toward smaller fractionations in 2009 compared to 2008, whereas YB and OM-LT samples were relatively consistent.

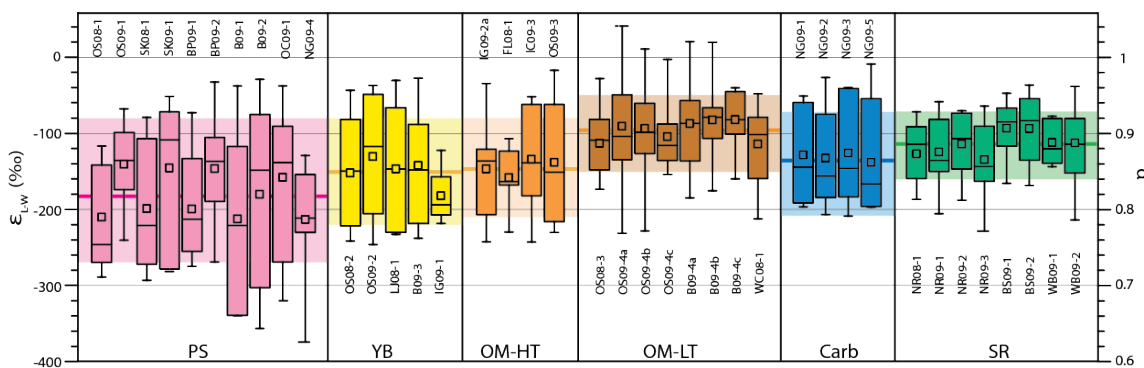


**Figure 5:** The range of isotopic fractionations in each sample (individual bars) and for mat types (separate colors). For each sample the boxes contain 50% of the data with the upper and lower quartile shown by the whiskers. The mean and median of the data points are indicated by the square and line, respectively. The mean values ( $\pm 2\sigma$ ) for each group are shown in the background lines and shading.

## 5. DISCUSSION

The striking covariance between mat type, FA abundance, microbial community composition, and lipid D/H fractionations highlights the influence of individual species on isotopic fractionation. We first examine the characteristic fractionations of specific microbes as deduced from biomarker FAs. We then relate these trends to the larger dataset to examine which organisms control the isotopic variability that is apparent in these systems.

### 5.1. Streamer Communities

Bacteria in the order *Aquificales* produce a unique distribution of fatty acids that can help differentiate the contributions of these organisms to environmental samples. *Aquificales* isolates

from Octopus Spring make abundant 20:1, cy-21, and 18:0 FA with minor amounts of 16:1, 16:0, 18:1, cy-19, 20:0 and 22:1 (Fig 5a; JAHNKE et al., 2001). The 20:1 and cy-21 FA are unusual and have not been reported in high abundance in organisms beyond these chemoautotrophic bacteria. These same lipids also dominate pink streamer samples from Octopus Spring (Fig 6c-d), though they were not the only lipids present.

Another important member of the highest-temperature ecosystems of YNP are filamentous bacteria from the genus *Thermus*. The best known is *Thermus aquaticus*, first isolated from springs in the White Creek, Boulder Spring, and Sentinel Meadow areas (BROCK and FREEZE, 1969). Lipids of *Thermus* species are also unusual for Gram-negative bacteria and consist primarily of iso- and anteiso- branched FA (Figure 5). When grown at its optimum growth temperature, *T. aquaticus* lipids are dominated by *i*-15, *i*-16, 16:0, and *i*-17 with smaller amounts of *a*-15, 16:1, and *a*-17 (NORDSTROM and LAAKSO, 1992). The relative proportions of these lipids are variable both with strain color and with growth temperature (NORDSTROM, 1993). The presence of abundant *i*-19 – which has not been previously reported in *Thermus* – in our samples might be attributed either to a broader spectrum of lipids produced by *Thermus*, or to an alternative microbial source such as the uncultured OPS8 found in our sequencing libraries. The genus *Thermotoga* has also been reported as a major constituent of the Bison Pool streamer communities (MEYER-DOMBARD et al., 2005). Although there is no published lipid information for *Thermotoga*, a similar lipid profile seems reasonable based on its phylogenetic and physiological similarity to *Thermus* (HUBER et al., 1998).

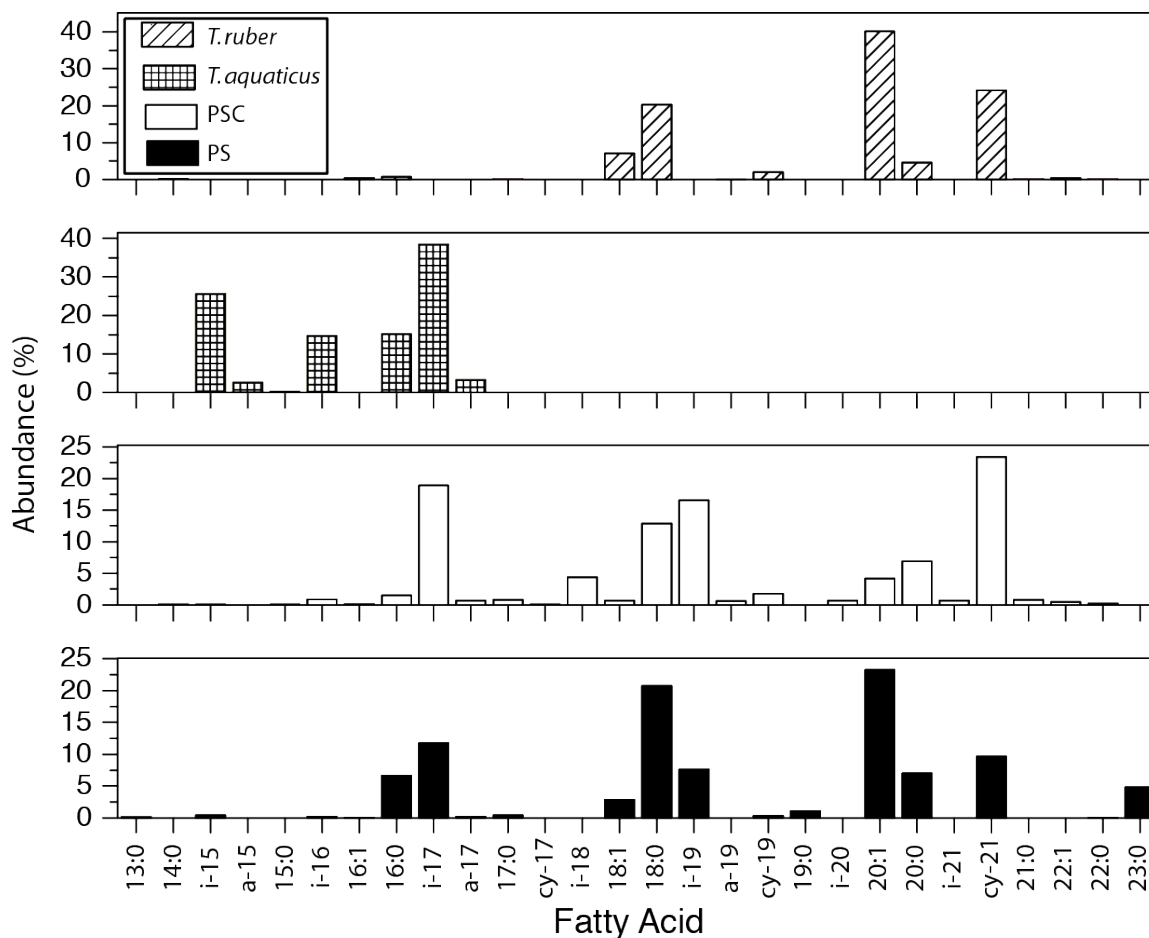


**Figure 6:** Relative abundances of FA produced by *Thermocrinus ruber* (panel A)(JAHNKE et al., 2001), *Thermus aquaticus* grown at 70°C (B)(NORDSTROM, 1993), and pink streamer communities examined by Janhke et al., 2001 (C) and this study (D). The distribution of fatty acids in the environmental samples can largely be explained as a combination of the upper two diagrams.

Based on these published lipid profiles, the fatty acids in PS type mats can be explained as resulting mainly from a combination of *Aquificales* and *Thermus*-like organisms (Fig 6). The abundance of 20:1 FA is strongly correlated with the abundance of *Aquificae* 16S sequences across all spring types ( $r=0.76$ ), further supporting that attribution. Of course, contributions from

other uncharacterized organisms cannot be entirely ruled out. Some streamer samples contained small amounts of odd-chain and cy-19 FA, tentatively attributed to *Chloroflexus*- and *Chlorobium*-like organisms (see below). This is supported by the small amount of Chloroflexi DNA in the streamer samples (Figure 2). These lipid contributions are thus in accord with previous phylogenetic studies on the composition of pink streamer communities (MEYER-DOMBARD et al., 2005), and with our own sequencing data.

The average D/H fractionations between fatty acids and source water for PS type mats are shown in Figure 7a, together with their likely source organisms. Data for *i*-19 FA was not available because it partially co-eluted with the internal standard. Fractionations span a very large range and exhibit an apparently systematic increase with chain length. Lipids that are diagnostic of the chemoautotrophic *Aquificales* (20:0, 20:1, cy-21) exhibit very strong D-depletions, whereas those attributable to heterotrophic *Thermus* (*i*-15, *i*-16, *i*-17) are D-enriched. Fatty acids of intermediate chain length, particularly 18:0, 18:X, and cy-19, have isotopic compositions between the two end members. It is unclear whether they derive solely from Aquificales, from other (possibly photosynthetic) bacteria, or perhaps have mixed sources. The latter is quite likely for the common 18:0 and 18:X fatty acids. It is thus possible that the trend of decreasing  $\delta D$  value with FA chain length does not represent a biosynthetic feature per se, but rather reflects the varying contributions of different organisms. On the other hand, this trend is one of the most persistent features of our dataset, and so could conceivably be related to lipid biosynthesis. It is in the opposite direction of the correlation observed by Chikaraishi et al. (2004) for FA in marine macroalgae.

These trends in fatty acid  $\delta D$  values are broadly consistent with the conclusions of Zhang et al. (2009) about the influence of metabolism on D/H fractionations. At the extreme temperatures where the PS communities thrive, the base of the food chain is supported by the chemoautotrophic *Aquificales*. While these organisms have been previously shown to grow on

H<sub>2</sub>, elemental S, or formate, their actual growth substrate in this environment has not been determined. Regardless, any of these substrates would be predicted to yield large D-depletions in lipids (VALENTINE et al., 2004; ZHANG et al., 2009), consistent with our data. Similarly, the relative D-enrichment observed in biomarker lipids from heterotrophic *Thermus* in these samples is also in accord with the work on cultured isolates, where aerobic heterotrophy consistently produced the most D-enriched fatty acids (Zhang et al., 2009).

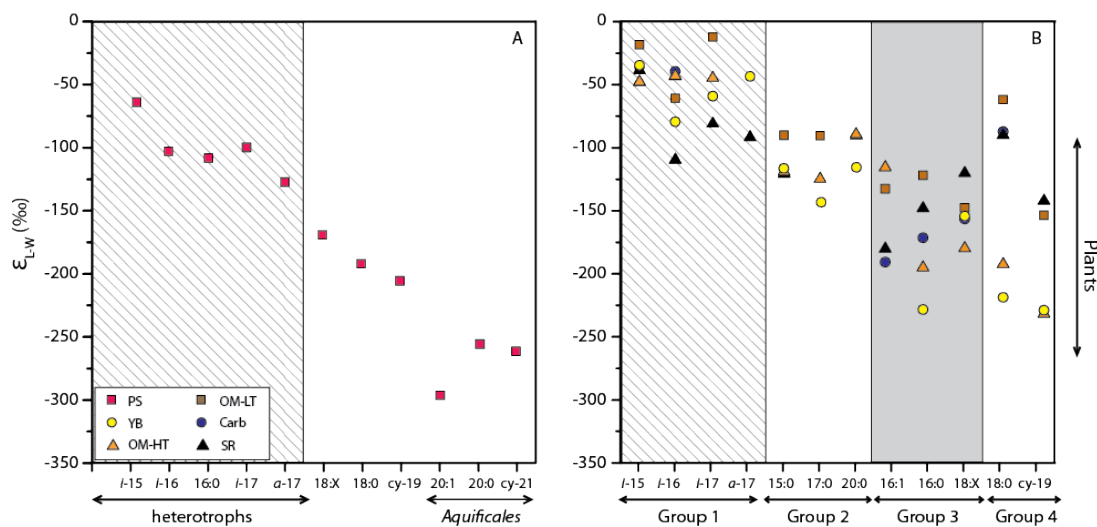


**Figure 7:** Average D/H fractionations between fatty acids and spring waters in PS (Panel A) and YB, OM-HT, OM-LT, Carb, and SR (Panel B) type mats. The typical range of fractionations in higher plants is shown to the right for reference. Compounds are ordered along the x-axis to group FAs from apparently similar sources, and the specific groups (1-4) are discussed in the text.

## 5.2. Photosynthetic Mats

Photosynthetic mat communities are significantly more diverse than the chemolithoautotrophic PS type mats making precise identification of lipid sources more difficult. In general, the phototrophic mats of LGB type runoff channels are composed of cyanobacteria,

anoxygenic phototrophs (*Chloroflexus* and Chlorobi), and various heterotrophs. Our 16S rRNA gene sequence data support these distinctions with 21-82% of sequences belonging to cyanobacteria, 20-27% (except YB which is low) belonging to Chloroflexi, and much of the remainder attributable to heterotrophic bacteria. For clarity we separate the discussion of the lipids from these samples into 4 groups. Group 1 consists of D-enriched, methyl-branched FA characteristic of heterotrophic bacteria. Group 2 comprises 15:0, 17:0, and 20:0 FA with fractionations clustering tightly around -100 to -125‰, suggesting a common origin. Group 3 includes 16:0, 16:1, 18:X and shows a significantly larger range in isotopic composition, with  $\epsilon$  values ranging from -125 to -225‰. The fourth group comprises only cy-19 and 18:0 but is remarkable because these compounds appear to have two very different sources in various mat types.

Long-chain ( $C_{22}$ - $C_{28}$ ) FAs were also present in relative abundance in SR type springs, though were rare in other samples. Possible sources for these compounds include windblown leaf waxes, fungi, and unusual bacterial products. We regard an *in situ* source as more plausible given the lack of mechanism for concentrating windblown contributions in these samples relative to all others. The abundances of these compounds show strong covariation with *Thermodesulfobacteria* and proteobacterial 16S rRNA gene sequence abundance, and so might originate in those groups. However, due to uncertainty about their origins, we do not consider these compounds further.

### 5.2.1. Group 1: Heterotrophs

The methyl-branched FA in our dataset form a coherent group based on  $\delta D$  values (Fig. 7B) as well as relative abundance between mat types (Fig. 3). These compounds are D-enriched compared both to other FA in the same samples, and to the same FA in PS type samples (Fig. 7A). The average  $\delta D$  values for these FA are similar between the different mat-type groups, although there is a slight apparent enrichment of OM-LT samples over YB and SR samples.

Among photosynthetic mats, these lipids are most abundant in the OM-HT and OM-LT mat types although they are still present at low abundance in Carb and SR mats.

As discussed above, thermophilic aerobic heterotrophs such as *Thermus* are known to produce large abundances of branched fatty acids, and so are the presumed main sources of these lipids. However, both the isotopic variability of the branched FA and the greater phylogenetic diversity of the OM-HT and OM-LT samples suggest additional heterotrophic sources in these samples. Based on the phylogenetic data, one possible source of these lipids are the Acidobacteria. *Acidobacterium capsulatum* was shown to produce large amounts (>50% of total fatty acid) of *i*-15:0 (KISHIMOTO et al., 1991). This is supported by the observation that in PS samples, *i*-17:0 is more abundant than *i*-15:0, whereas in samples from photosynthetic mats *i*-15:0 is more abundant. The cultured strains of *Thermus* produce both FA but with more *i*-17:0 than *i*-15:0. On the other hand, most of the Acidobacterial 16S rRNA gene sequences from OM-HT and OM-LT are most closely related to the photoheterotrophic *Candidatus Chloracidobacteria thermophilum* (Bryant et al., 2007). With no published fatty acid production profiles for this newly isolated organism, we are unable to determine if it is responsible for the *i*-15:0 FA. Our 16S data also reveal large numbers of *Deinococcus-Thermus* in YB and to a lesser extent OM-HT mats. Carb samples did not contain large amounts of either phyla and instead the heterotrophic communities are largely Thermotogae and Proteobacteria.

The relative D enrichments and significant isotopic variability of the branched FAs are consistent with their derivation from a mixed community of heterotrophs (Zhang et al., 2009). The D enrichment is particularly strong in OM-HT and OM-LT type mats where typical fractionations are around -50‰, whereas YB and SR type mats are typically somewhat less D-enriched (except for *i*-15:0 FA).

### 5.2.2. Group 2: *Chloroflexus*

The second group of lipids includes 15:0, 17:0, and 20:0 FA and exhibits relatively little isotopic variance with mean  $\delta D$  values near -100‰. Three lines of evidence suggest that *Chloroflexus*-like organisms are the primary source for 15:0 and 17:0 FA. First, cultured representatives of the genus *Chloroflexus* are known to produce both 17:0 and 19:0 (along with other fatty acids described below; (KENYON and GRAY, 1974), whereas odd-chain FA are not commonly found in cyanobacteria. The production of 15:0 FA by Chloroflexi has not been previously described, but seems likely based on the presence of 17:0 and 19:0 FA. Second, odd-chain FA are most abundant in the OM-HT and OM-LT mats, where organisms from the phylum Chloroflexi account for roughly one-quarter of the 16S rRNA gene sequences (Fig 2), making them one of the two most abundant organisms in this mat type. Moreover, the abundances of 15:0 and 17:0 FA are well correlated with each other ( $r=0.63$ ) and with the abundances of Chloroflexi 16S rRNA gene sequences ( $r= 0.74$  and  $0.50$ , respectively) in our samples. Third, the  $\delta D$  values of the Group 2 lipids are similar to each other but different from those of other lipids (such as 16:1 and 18:X) that can likely be attributed at least in part to cyanobacteria (see below), the other abundant group of organisms in these mats.

Based on this evidence, we suggest that 15:0 and 17:0 FA are dominantly produced by green non-sulfur bacteria from the phylum Chloroflexi. The origin(s) of 20:0 FA are less clear. *Chloroflexus* is known to produce 20:0 as a minor fatty acid (KENYON and GRAY, 1974), but the abundances of 20:0 FA and Chloroflexi 16S rRNA gene sequences are *inversely* correlated ( $r=-0.40$ ), suggesting that some other source is probable. Nevertheless, the isotopic compositions of 20:0 are virtually identical to those of 15:0 and 17:0.

One of the more interesting aspects of these lipids is that – for a given mat type – the putative Chloroflexi lipids appear to be D-enriched by 25-50‰ relative to those produced wholly or partially by cyanobacteria (see group 3 below). This trend is also supported by the systematic enrichment of OM-LT lipids over those in Carb and YB, given that OM-LT mats are rich in

*Chloroflexus* compared to the other two. Zhang et al. (2009) observed a relative D-enrichment of the lipids of *R. palustris* during photoheterotrophic versus photoautotrophic growth. This is potentially significant given that culture-based studies reveal *Chloroflexus* commonly employs photoheterotrophic metabolism under anaerobic conditions (PIERSON and CASTENHOLZ, 1974), as well as previous C-isotopic work suggesting a photoheterotrophic metabolism for *Chloroflexus* in these mat communities (VAN DER MEER et al., 2007). However, the signal may be complicated by increased inputs of heterotroph lipids to OM-LT that may also serve to enrich the average isotopic composition.

### 5.2.3. Group 3: Mixed phototrophs

Unsaturated C<sub>16</sub> and C<sub>18</sub> FA make up approximately half of the fatty acids from OM-LT, Carb, and SR mat types, but <5% of the fatty acids in OM-HT mats. This is the dominant compositional difference between OM-LT and OM-HT mat types (Fig. 3, 4). These lipids are grouped with 16:0 FA based on isotopic composition, though their patterns of abundance are only slightly correlated ( $r=0.42$  for 16:0 vs 16:1 FA,  $0.17$  vs 18:1 FA, and  $0.34$  vs 18:2 FA). This group likely represents contributions from a number of sources, with the Chloroflexi and cyanobacteria being the most abundant. Cultured *Chloroflexus* species are known to produce significant quantities of 16:0, 18:0, and 18:1 FA, with minor quantities of other fatty acids including 16:1, 18:2, and 20:1 (KENYON and GRAY, 1974). Cultured thermophilic *Synechococcus* strains have been shown to produce mostly 16:0, 16:1, and 18:1 fatty acids (KENYON, 1972). This distribution is also consistent with the sole report of fatty acid distributions for the filamentous cyanobacterium *Phormidium* (JAHNKE et al., 2004). This genus has been implicated in forming the coniform orange mat morphologies in low temperature mats similar to samples OS08-3 and OS09-4 (JAHNKE et al., 2004). Although the C<sub>16</sub> and C<sub>18</sub> fatty acids potentially have very diverse sources, comparison between lipid abundance and sequence data shows cyanobacterial abundance to be well correlated ( $r=0.67$ ) with 16:0 FA abundance, moderately correlated with 16:1 and 18:2

FA ( $r=0.38$  and  $0.35$ , respectively), and uncorrelated ( $r=0.01$ ) with 18:1 FA. Thus, cyanobacteria are likely a prominent – but not sole – source for these lipids.

The relatively low abundance of unsaturated fatty acids in YB and OM-HT samples is hard to reconcile with the large numbers of cyanobacterial sequences in these mats. While homeoviscous adaptation to growth at high temperature is one possible explanation for these composition trends, it is not supported by the isotopic data. However, cyanobacterial diversity at the genus level indicates distinctly different populations in YB and OM-HT mats compared to all other photosynthetic mat types (Fig 8). We suggest that this diversity is contributing to the differences in production of unsaturated FA by cyanobacteria in different mat types.

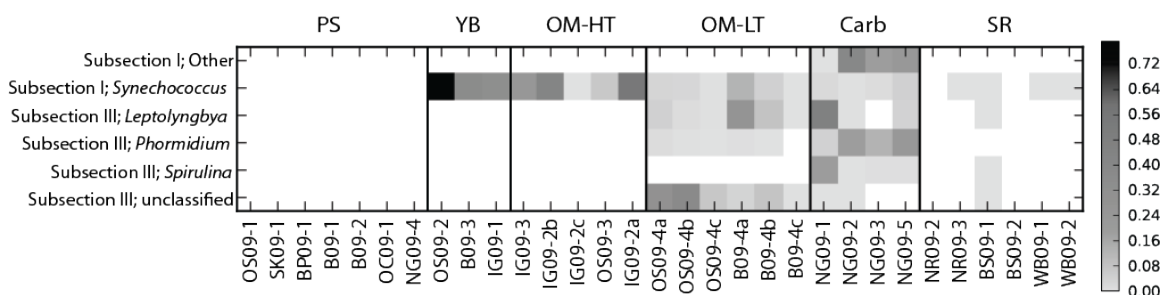


**Figure 8:** Distribution of 16S rRNA gene sequences for selected phyla and subdivisions of the cyanobacteria in different mat types. Plotted values are the fractional abundance of sequences in that group relative to all sequences in the sample.

The isotopic compositions of group 3 lipids exhibit two main characteristics. First, they are highly variable, typically spanning a  $\sim 100\%$  range of  $\delta D$  values. We attribute this primarily to the fact that they represent mixtures of products from multiple and different, although probably still photosynthetic, sources in each spring, and that these multiple sources apparently express somewhat different fractionations. Second, the isotopic compositions of these fatty acids are completely overlapping with the range commonly observed in plants and algae (Fig 7). The mean

value for this group in our study (-151‰) is very similar to the mean for C<sub>16</sub> and C<sub>18</sub> fatty acids in Santa Barbara Basin sediments (Li et al., 2009) where they are believed to derive from marine algae. Thus we infer that the fractionations exhibited by photoautotrophic thermophiles are not inherently different from those in higher plants and algae despite their relatively extreme environmental setting.

#### 5.2.4. Group 4: 18:0 and cy-19

Lipid group 4 is comprised of 18:0 and cy-19 FA. These compounds are united by their unusual, bimodal distribution of D/H fractionations where the generally low-temperature Carb, OM-LT, and SR samples yield relatively small fractionations (more D-enriched lipids) compared to the high-temperature PS, OM-HT, and YB samples that exhibit larger fractionations (more D-depleted lipids).

While 18:0 FA is present in relatively high abundance throughout most samples, and has many possible sources, cy-19 FA is abundant only in YB and OM-HT samples where it contributes between 3 and 20% of total FA abundance. Despite its correlation with the high-temperature mat samples, cy-19 is not yet known in the published literature to be produced by *Synechococcus* or *Chloroflexus*. While many bacteria are capable of producing FA containing cyclopropyl rings (GROGAN and CRONAN, 1997), most are not found in the hydrothermal environment. An exception is the thermophilic green-sulfur bacterium *Chlorobium tepidum* (WARD et al., 1998). Our sequencing libraries confirm the presence of Chlorobi in many of the samples that contain cy-19, however correlation between the abundance of Chlorobi sequences and cy-19 FA is low ( $r=0.11$ ). *Thermocrinus ruber* (an *Aquificales*) is also known to produce small amounts of cy-19 FA, and is also uncorrelated with cy-19 abundance ( $r=-0.19$ ). Surprisingly, the abundance of Candidate division OP10 was well correlated to cy-19 ( $r=0.56$ ), and could account for the high concentrations found in the YB and OM-HT. Additional potential

sources of these lipids are the alphaproteobacterial genera *Acidiphilium* and *Acidomonas* that have been shown to produce cy-19 up to 20% of total fatty acid abundance (KISHIMOTO et al., 1991).

The magnitude of D/H fractionations exhibited in both 18:0 and cy-19 FA are near -200‰ in high temperature mats (PS, YB and OM-HT), marking them as likely photoautotroph or perhaps even chemoautotroph products (i.e., compare to Group 3 and *Aquificales* in Fig. 7). This is interesting given that neither OP10 nor the mentioned alphaproteobacteria are known to be photo- or chemo-autotrophs. However, in the case of OP10 only a single isolate has so far been described, and is a thermophilic aerobic heterotroph (STOTT, 2008). These observations lead to three competing hypotheses regarding the origins of 18:0 and cy-19 in high-temperature mats: 1) They are produced exclusively by *Aquificales* in all high-temperature mat types, but their  $\delta D$  values are inexplicably different from the other FA attributed to this group. This explanation is not consistent with the higher abundance of cy-19 in YB and OM-HT mat types. 2) They are produced by previously undescribed species of OP10 or alphaproteobacteria with photoautotrophic or chemoautotrophic metabolism and hence large D/H fractionations. A potential problem with this explanation is that the putative source organisms are not readily apparent in 16S rRNA gene sequences from PS type mats. 3) They represent a mixture of sources, including *Aquificales*, *Chlorobi*, OP10, and alphaproteobacteria, and their average isotopic compositions coincidentally arrive at roughly the same values in all mat types. The latter hypothesis is most likely for 18:0 FA, given that  $e_{L/W}$  values for individual samples span a fairly wide range (-116 to -247‰). However, for cy-19 the range of fractionations is much smaller (-195 to -242‰ for the PS, YB, and OM-HT mat types), and a single source (or less diverse consortium) in all three mat types seems more likely. Our current data do not allow us to resolve this question. Nevertheless, our ability to predict that organisms in Candidate phylum OP10

might be capable of photo- or chemoautotrophy highlights the potential utility of hydrogen-isotopic data.

In OM-LT, Carb, and SR type mats, the 18:0 and cy-19 FA both have significantly more D-enriched compositions. For 18:0 the fractionations reach -50‰, suggesting that this lipid must derive almost entirely from heterotrophs in those mat types. This is somewhat surprising given that phototrophs still make up >50% sequence abundance in Carb and OM-LT samples. For cy-19, the fractionations are closer to -150‰, suggesting either a phototrophic source (similar to 16:0 and 18:X FA) or a mixture of both D-depleted (similar to those in YB and OM-HT mats) and D-enriched (presumably heterotroph) lipids.

#### **5.4. Applications of Lipid D/H Ratios**

The preceding discussion focuses on the metabolic basis for large differences in D/H fractionations between different microbes. But regardless of mechanism, the patterns of lipid  $\delta D$  observed in YNP springs are robust and – in many cases – diagnostic of particular mat types. They may thus serve as useful ‘fingerprints’ for assessing the composition and function of ancient hydrothermal systems via organic biomarkers.

To facilitate such an analysis, we compared the abundances and hydrogen isotopic compositions of several common fatty acids as a function of mat type (Figure 9). Fatty acids with double bonds or cyclopropyl rings were excluded because of their relatively poor preservation potential. Fig 9 indicates several characteristics that could be usefully employed in an ancient system. For example, streamer communities are characterized by great abundance and strong D-depletion of long-chain (especially C<sub>20</sub>) fatty acids. Yellow biofilm-type mats are distinguished by abundant, strongly D-depleted 16:0 and 18:0 FA, whereas orange LGB-type mats are typified

by abundant, D-enriched short-chain branched and odd-numbered FA (e.g., *i*-15:0). High- versus low-temperature orange mats seem to be differentiated by the  $\delta D$  value of 16:0, with lower-temperature mats having a more D-enriched composition. We tentatively interpret this signal as reflecting a more dominant heterotrophic source for 16:0 in the lower-temperature mats.

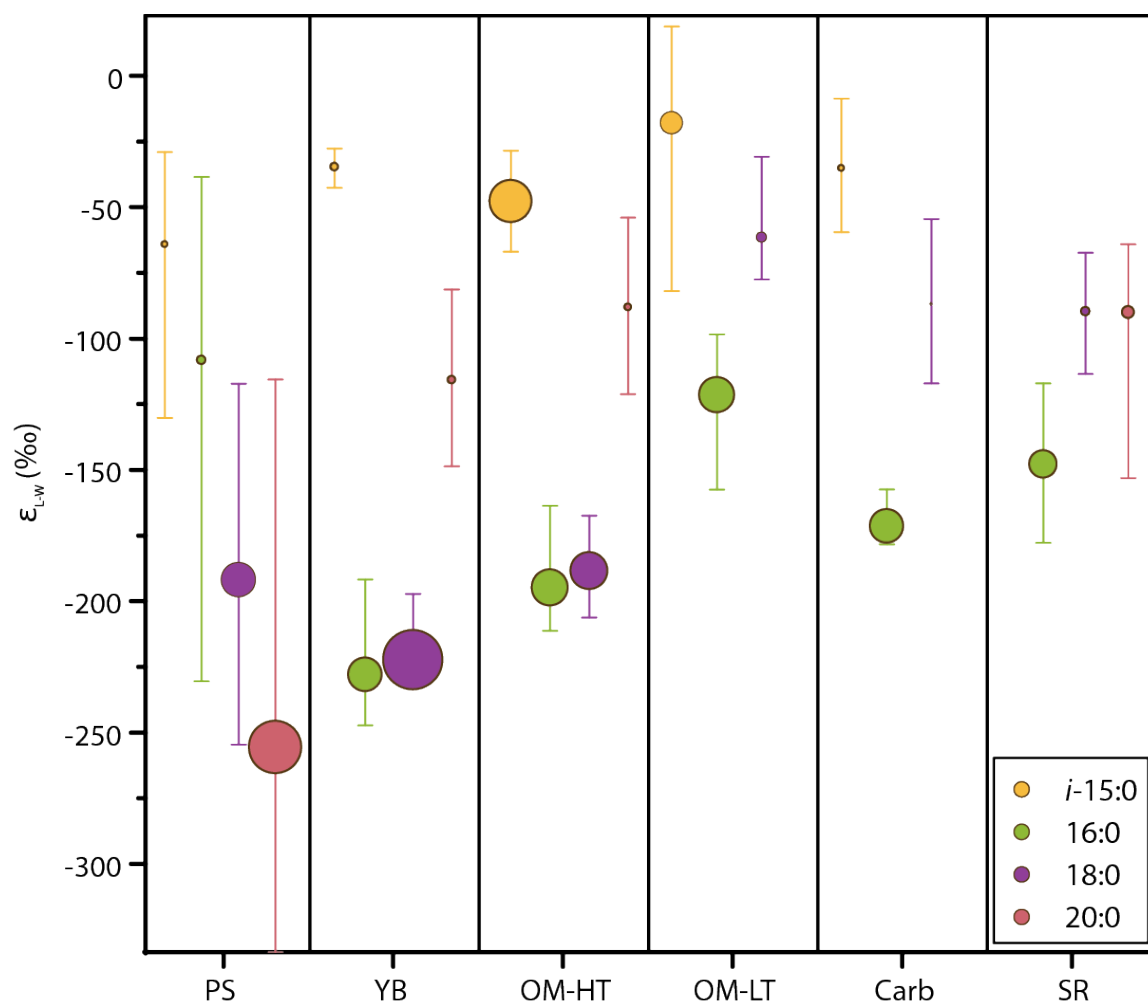


**Figure 9:** Mean isotopic compositions for *i*-15:0, 16:0, 18:0, and 20:0 FAMES in each mat type. The size of each symbol is proportionate to lipid abundance, but each compound is scaled independently. Bars represent the total range of  $\delta D$  values.

The utility of these kinds of ‘fingerprints’ will, of course, depend on whether the signals observed in YNP are ubiquitous or more regional in character. They do at least seem to be consistent across the greater Yellowstone region and in a recent report of fatty acid  $\delta D$  from Naruko Hot spring in northeastern Japan (NARAOKA et al., 2010). The fidelity of H-isotopic compositions in quite warm environments over long times will also have to be investigated, as hydrogen exchange may be fairly rapid at the ambient temperatures of these systems. Nevertheless, given the large and (apparently) systematic variations in lipid D/H across YNP, there is significant potential for the use of these data as fingerprints for ancient hydrothermal environments.

A second potential use for lipid  $\delta D$  values in these hydrothermal systems is the attribution of lipids with unknown origins to particular microbes. For example, the cy-19 FA can be tentatively attributed to OP10 in YB and OM-HT type mats based on strong D-depletions, but must have other origins in Carb and OM-LT mats. Because of the large variance, lipid D/H ratios can also be quite useful for quantitative apportionment of multiple sources. For example, palmitic acid (16:0) is extremely common and can have a wide range of bacterial (and eukaryotic) sources. Based on comparisons of  $\delta D$  values in PS and OM-LT type mats, the palmitic acid appears to derive mainly from heterotrophs (e.g., *Thermus*), whereas in YB and OM-HT type mats it is almost exclusively an autotrophic product (cyanobacteria and/or *Chloroflexus*).

### **5.5. Relevance to Other Environments**

While this study focuses on a terrestrial hydrothermal environment, the trends observed here are likely applicable to more moderate environments as well. Previous studies of both marine and lacustrine samples have observed very large ranges in lipid  $\delta D$  values. These included a range of -32 to -348‰ for n-alkyl lipids in marine sediments (LI et al., 2009), -73 to -237‰ for

fatty acids extracted from marine particulate organic matter (JONES et al., 2008), and -166 to -255‰ for fatty acids from lacustrine sediments (CHIKARAISHI and NARAOKA, 2005). The bulk of the fractionations observed in the current study fall within these ranges, although the total range is somewhat larger at +41 to -374‰. Additionally, a trend of D-enriched heterotroph lipids relative to those of photosynthetic algae has been observed in the marine environment (JONES et al., 2008; LI et al., 2009). Similar to our findings, Jones et al. (2008) observed an inexplicable D enrichment in *i*-15:0 and 15:0 fatty acids compared to all others. Based on the results presented here, we suggest that these lipids might be produced by marine heterotrophs where the less D-enriched lipids might come from phototrophs or another metabolism with characteristically moderate isotopic signatures. While the extreme values observed in this study are exceptional, we suggest that the hydrothermal environment may not be unusual in the production of extreme isotopic values, but rather in our ability to separate communities so that these values can be observed.

We have demonstrated that differences in the sources of common lipids can have a significant effect on their H-isotopic composition. While many of the organisms discussed in this study are specific to the hydrothermal realm, the metabolisms they practice are much more cosmopolitan. Here, subtle shifts in microbial communities were significant enough to influence the bulk signal. We suggest that over sufficient timescales, hydrogen isotopic variability of lipids from marine and lacustrine sediments may be influenced both by the water  $\delta D$  and by variations in microbial community.

## 6. CONCLUSIONS

Fatty acids from a diverse suite of microbial communities living in terrestrial hydrothermal environments show systematic variations in H-isotopic composition that appear linked to the presence of specific types of bacteria. Lipids derived from chemoautotrophic

bacteria (mainly *Aquificales*) showed strong D-depletions, down to -374‰ relative to growth water. In comparison, lipids derived from heterotrophic bacteria were relatively D-enriched, with fractionations relative to growth water typically only -50 to -100‰. Fatty acids from photosynthetic bacteria exhibited intermediate fractionations similar to those found in higher plants. Lipids from Chloroflexi were slightly D-enriched relative to those of cyanobacteria, perhaps reflecting photoheterotrophic metabolism in the former organism. These data, based on well-characterized environmental samples, both confirm and extend the observations of Zhang et al (2009) that the utilization of different central metabolic pathways by bacteria is recorded in the H-isotopic composition of lipids.

*Acknowledgements:* This work was conducted under YNP scientific research and collecting permit YELL-2008-SCI-5664 for 2008 and 2009 with thanks to the Yellowstone Center for Resources. Funding was provided by NSF award EAR-0645502 to ALS, NSF GRFP to MRO and Grant R-8196-G1 from US Air Force Office of Scientific Research to JRS. We would like to thank the Agouron Institute supported International GeoBiology Summer Course for facilitating our 2008 field season, Lichun Zhang for technical assistance, and Roger Summons and Everett Shock for helpful discussions.

## References

- Altschul S. F. (1990) Basic local alignment search tool. *J. Mol. Biol.* **215**, 403-410.
- Bligh E. G. and Dyer W. J. (1959) A rapid method of total lipid extraction and purification. *Can. J. Biochem. Phys.* **37**, 911-917.
- Brock T. D. (1978) *Thermophilic microorganisms and life at high temperatures*. Springer-Verlag, New York.
- Brock T. D., Brock K. M., Belly R. T., and Weiss R. L. (1972) *Sulfolobus*: A new genus of sulfur-oxidizing bacteria living at low pH and high temperature. *Arch. Microbio.* **84**, 54-68.
- Brock T. D. and Freeze H. (1969) *Thermus aquaticus* gen. nov. and sp. nov., a nonsporulating extreme thermophile. *J. Bacteriol.* **98**, 289-297.
- Bryant D. A., Costas A. M. G., Maresca J. A., Chew A. G. M., Klatt C. G., Bateson M. M., Tallon L. J., Hostetler J., Nelson W. C., Heidelberg J. F., and Ward D. M. (2007) *Candidatus Chloracidobacterium thermophilum*: An Aerobic Phototrophic Acidobacterium. *Science* **317**, 523-526.
- Caporaso G. (2010) QIME allows analysis of high-throughput community sequencing data. *Nature Methods* **7**, 335-336.
- Castenholz R. W. (1969) Thermophilic blue-green algae and the thermal environment. *Bacteriol.Rev.* **33**, 476-504.
- Chikaraishi Y. and Naraoka H. (2005)  $\delta^{13}\text{C}$  and  $\delta\text{D}$  identification of sources of lipid biomarkers in sediments of Lake Haruna (Japan). *Geochim. Cosmochim. Acta* **69**, 3285-3297.
- Don R. (2010) Touchdown PCR to circumvent spurious priming during gene amplification. *Nucleic Acids Res.* **19**, 4008.
- Edgar R. C. (2010) Search and clustering orders of magnitude faster than BLAST. *Bioinformatics* **26** 2460.

- Fouke B. W. (2003) Partitioning of bacterial communities between travertine depositional facies at Mammoth Hot Springs, Yellowstone National Park, USA. *Can. J. of Earth Sci.* **40**, 1531.
- Grogan D. and Cronan J. Jr (1997) Cyclopropane ring formation in membrane lipids of bacteria. *Microbiol. Mol. Biol. Rev.* **61**, 429-441.
- Haas B. J., Gevers D., Earl A., Feldgarden M., Ward D. V., Giannokous G., Ciulla D., Tabbaa D., Highlander S. K., Sodergren E., Methe B., Desantis T. Z., Petrosino J. F., Knight R., and Birren B. W. (2011) Chimeric 16S rRNA sequence formation and detection in Sanger and 454-pyrosequenced PCR amplicons. *Genome Res.* **21**, 494.
- Huber R., Eder W., Heldwein S., Wanner G., Huber H., Rachel R., and Stetter K. O. (1998) *Thermocrinis ruber* gen. nov., sp. nov., a pink-filament-forming hyperthermophilic bacterium isolated from Yellowstone National Park. *Appl. Environ. Microbio.* **64**, 3576-3583.
- Hugenholtz P., Pitulle C., Hershberger K. L., and Pace N. R. (1998) Novel division level bacterial diversity in a Yellowstone hot spring. *J. Bacteriol.* **180**, 366-376.
- Huse S. (2007) Accuracy and quality of massively parallel DNA pyrosequencing. *Genome Biol.* **8**, R143.
- Jackson C. R. (2001) Molecular analysis of microbial community structure in an arsenite-oxidizing acidic thermal spring. *Environ. Microbio.* **3**, 532.
- Jahnke L. L., Eder W., Huber R., Hope J. M., Hinrichs K.-U., Hayes J. M., Des Marais D. J., Cady S. L., and Summons R. E. (2001) Signature lipids and stable carbon isotope analyses of Octopus Spring hyperthermophilic communities compared with those of *Aquificales* representatives. *Appl. Environ. Microbio.* **67**, 5179-5189.
- Jahnke L. L., Embaye T., Hope J. M., Turk K. A., van Zuilen M., des Marais D. J., Farmer J. D., and Summons R. E. (2004) Lipid biomarker and carbon isotopic signatures for

- stromatolite-forming, microbial mat communities and Phormidium cultures from Yellowstone National Park. *Geobiology* **2**, 31-47.
- Jones A. A., Sessions A. L., Campbell B. J., Li C., and Valentine D. L. (2008) D/H ratios of fatty acids from marine particular organic matter in the California Borderland Basins. *Org. Geochem.* **39**, 485-500.
- Jurgens G., Lindstrom K., and Sanano A. (1997) Novel group within the kingdom Crenarchaeota from boreal forest soil. *Appl. Environ. Microbio.* **63**, 803-805.
- Kenyon C. N. (1972) Fatty Acid Composition of Unicellular Strains of Blue-Green Algae. *J. Bacteriol.* **109**, 827-834.
- Kenyon C. N. and Gray A. M. (1974) Preliminary Analysis of Lipids and Fatty Acids of Green Bacteria and Chloroflexus aurantiacus. *J. Bacteriol.* **120**, 131-138.
- Kharaka Y. K., Thordsen J. J., and White L. D. (2002) Isotope and chemical Compositions of Meteoric and Thermal Waters and Snow from the Greater Yellowstone National Park Region. USGS Open-file Report 02-194.
- Kishimoto N., Kosako Y., and Tano T. (1991) *Acidobacterium capsulatum* gen. nov., sp. nov.: An Acidophilic Chemoorganotrophic Bacterium Containing Menaquinone from Acidic Mineral Environment. *Current Microbio.* **22**, 1-7.
- Knight R. (2007) PyCogent: a toolkit for making sense from sequence. *Genome Biol.* **8**, R171.
- Lane D. (1991) 16S/23S rRNA sequencing. In: Stackebrandt, E. and Goodfellow, W. D. Eds. *Nucleic Acid Techniques in Bacterial Systematics*. Wiley and Sons, Chichester, UK.
- Li C., Sessions A. L., Kinnaman F. S., and Valentine D. L. (2009) Hydrogen-isotopic variability in lipids from Santa Barabara Basin sediments. *Geochim. Cosmochim. Acta* **73**, 4803-4823.
- Meyer-Dombard D. R., Shock E. L., and Amend J. P. (2005) Archaeal and bacterial communities in geochemically diverse hot springs of Yellowstone National Park, USA. *Geobiology* **3**, 211-227.

- Meyer-Dombard D. R., Swingley W., Raymond J., Havig J., Shock E. L., and Summons R. E. (2011) Hydrothermal ecotones and streamer biofilm communities in the Lower Geyser Basin, Yellowstone National Park. *Environ. Microbio.* **13**.
- Naraoka H., Uehara T., Hanada S., and Kakegawa T. (2010)  $\delta^{13}\text{C}$ - $\delta\text{D}$  distribution in lipid biomarkers in a bacterial mat from a hot spring in Miyagi Prefecture, NE Japan. *Org. Geochem.* **41**, 398-403.
- Nordstrom K. M. (1993) Effect of Temperature on Fatty Acid Composition of a White Thermus Strain. *Appl. Environ. Microbiol.* **59**, 1975-1976.
- Nordstrom K. M. and Laakso S. V. (1992) Effect of Growth Temperature on Fatty Acid Composition of Ten Thermus Strains. *Appl. Environ. Microbiol.* **58**, 1656-1660.
- Pierson B. K. and Castenholz R. W. (1974) A phototrophic gliding filamentous bacterium of hot springs, *Chloroflexus aurantiacus*, gen. and sp. nov. *Arch. Microbio.* **100**, 5-24.
- Pruesse E. (2007) SILVA: a comprehensive online resource for quality checked and aligned ribosomal RNA sequence data compatible with ARB. *Nucleic Acids Res.* **35**, 7188-7196.
- Reeder J. and Knight R. (2010) Rapidly denoising pyrosequencing amplicon reads by exploiting rank-abundance distributions. *Nature Methods* **7**, 668-669.
- Rothschild L. J. (2001) Algal Physiology at High Temperature, Low pH, and Variable pCO<sub>2</sub> Implications for Evolution and Ecology. In: Reysenbach, A., Voytek, M., and Mancinelli, R. L. Eds., *Thermophiles: Biodiversity, ecology, and evolution*. Kluwer Academic/Plenum Publishers, New York.
- Sachse D. and Sachs J. P. (2008) Inverse relationship between D/H fractionation in cyanobacterial lipids and salinity in Christmas Island saline ponds. *Geochim. Cosmochim. Acta* **72**, 793-806.
- Sessions A. L. (2006) Seasonal changes in lipid D/H fractionation by *Spartina alterniflora*. *Geochim. Cosmochim. Acta* **70**, 2153-2162.

- Shock E. L., Holland M., Meyer-Dombard D. A., Amend J. P., Osburn G. R., and Fischer T. P. (2010) Quantifying inorganic sources of geochemical energy in hydrothermal ecosystems, Yellowstone National Park, USA. *Geochim. Cosmochim. Acta* **74**, 4005-4043.
- Spear J. R., Walker J. J., McCollom T. M., and Pace N. R. (2005) Hydrogen and bioenergetics in the Yellowstone geothermal ecosystem. *PNAS* **102**, 2555-2560.
- Stott M. B. (2008) Isolation of novel bacteria, including a candidate division, from geothermal soils in New Zealand. *Environ. Microbio.* **10**, 2030.
- Valentine D. L., Sessions A. L., Tyler S. C., and Chidthaisong A. (2004) Hydrogen isotope fractionation during H<sub>2</sub>/CO<sub>2</sub> acetogenesis: hydrogen utilization efficiency and the origin of lipid-bound hydrogen. *Geobiology* **2**, 179-188.
- van der Meer M. T. J., Schouten S., Sinninghe Damste J. S., and Ward D. M. (2007) Impact of carbon metabolism on <sup>13</sup>C signatures of cyanobacteria and green non-sulfur-like bacteria inhabiting a microbial mat from an alkaline siliceous hot spring in Yellowstone National Park (USA). *Environ. Microbio.* **9**, 482-491.
- Walker J. J., Spear J. R., and Pace N. R. (2005) Geobiology of a microbial endolithic community in the Yellowstone geothermal environment. *Nature* **434**, 1011-1014.
- Wang Y. and Sessions A. L. (2008) Memory Effects in Compound-Specific D/H Analysis by Gas Chromatography/Pyrolysis/Isotope-Ratio Mass Spectrometry. *Anal. Chem.* **80**, 9162-9170.
- Ward D. M., Ferris M. J., Nold S. C., and Bateson M. M. (1998) A Natural View of Microbial Biodiversity within Hot Spring Cyanobacterial Mat Communities. *Microbiol. Mol. Biol. Rev.* **62**, 1353-1370.
- Zhang C. L., Fouke B. W., Bonheyo G. T., Peacock A. D., White D. C., Huang Y., and Romanek C. S. (2004) Lipid biomarkers and carbon-isotopes of modern travertine deposits

(Yellowstone National Park, USA): Implications for biogeochemical dynamics in hot-spring systems. *Geochim. Cosmochim. Acta* **68**, 3157-3169.

Zhang X., Gillespie A. L., and Sessions A. L. (2009) Large D/H variations in bacterial lipids reflect central metabolic pathways. *PNAS* **106**, 12580-12586.

## *Chapter 2*

In preparation for publication in *Organic Geochemistry*

### **Fractionation of hydrogen isotopes by anaerobic bacteria**

Magdalena R. Osburn<sup>1\*</sup>, Alex L. Sessions<sup>1</sup>, and Katherine S. Dawson<sup>1,2</sup>

Author affiliations:

1. Division of Geological and Planetary Sciences, California Institute of Technology,

Pasadena, CA 91125, USA.

2. Geosciences Department, Pennsylvania State University, University Park,

Pennsylvania 16801

## ABSTRACT

Recently, large variations in the hydrogen isotopic composition of lipids were observed for heterotrophic bacteria utilizing carbon sources fixed via different central metabolic pathways. This work provided a basis for a metabolism-based environmental lipid isotope proxy, but was limited to aerobic bacteria. Here we report on the hydrogen isotopic fractionation of lipids from cultured strict and facultative anaerobic bacteria. We find significant differences both between the behavior of the two groups and between aerobic vs. anaerobic growth conditions. The sulfate reducers studied here produced D-depleted lipids during both autotrophic and heterotrophic growth conditions that are similar across a range of electron donors. Facultative anaerobes broadly followed the metabolism-based trends shown previously, but large differences were observed between aerobic and anaerobic growth conditions. We speculate on the possible role of the electron acceptor in modulating the isotopic composition of cellular hydrogen pools. Comparison of isotopic data shows no significant trends relating to growth rate, free energy yield, or patterns of electron transport, although they do differentiate facultative anaerobes from sulfate reducers. These results suggest that the D/H fractionations observed in lipids are the product of both the specific metabolic pathway and the electron acceptor used for growth, as well as potentially other factors. While our results are not inconsistent with previous studies, the emerging picture is more complex than the simple correspondence between  $\delta D$  and metabolic pathway previously understood from aerobic bacteria. Despite the complexity, the large signals and rich variability of observed lipid  $\delta D$  values suggest much potential as an environmental recorder of metabolism.

## 1. Introduction

Hydrogen isotopic compositions of organic molecules are used as recorders of biosynthetic processes (Chikaraishi and Naraoka, 2001; Chikaraishi et al., 2009), patterns of organic matter cycling (Chikaraishi and Naraoka, 2005; Jones et al., 2008), and the isotopic composition of water and salinity in paleoenvironmental reconstructions (Sauer et al., 2001; Huang et al., 2002; Sachse et al., 2012). To first order, the hydrogen isotopic composition of organic material reflects the  $\delta D$  value of growth water, offset by fractionations associated with biosynthesis (Hayes, 2001). However, very large ranges of  $\delta D$  values are observed in natural samples, even those occurring in a single growth water or environment, suggesting that other processes are at play (Jones et al., 2008; Li et al., 2009; Osburn et al., 2011). Variability can be caused by processes that change the isotopic composition of intracellular water such as salinity in planktonic environments or humidity and transpiration in plants (Sachse and Sachs, 2008; Pu and Weiguo, 2011; Romero-Viana et al., 2013), or processes that affect biosynthetic fractionation such as biosynthetic pathway (Sessions et al., 1999). Recently it has been shown that the central metabolic pathway utilized by microorganisms has a profound effect on lipid D/H (Zhang, Gillespie, et al., 2009). This metabolic effect spans a 500 ‰ range in a single fatty acid, far exceeding most other forms of variability.

Beyond just producing variability, the metabolism-based trends observed in Zhang et al. (2009) show clear signals of heterotrophy, photoautotrophy, and chemoautotrophy. In that study, heterotrophic lipids were D-enriched and the level of enrichment was dependent on the central metabolic pathway used during a given growth condition. The tricarboxylic acid cycle (TCA cycle) was inferred to produce the most

extreme D-enrichments (Zhang, Gillespie, et al., 2009). In contrast, organisms using C1-based metabolism (interpreted as chemoautotrophy) produced extreme D-depletions and photoautotrophic lipids fell intermediate. The proposed mechanism to explain metabolic control of variability in D/H centers on the role of the electron donor NADPH. During central metabolism NADP<sup>+</sup> is reduced via hydride transfer to NADPH + H<sup>+</sup> that can be subsequently used in biosynthetic reactions (White, 2000). Differences in the enzyme responsible for this reduction provide a physical distinction to introduce isotopic variability on biosynthetic products (Zhang, Gillespie, et al., 2009).

Metabolism-specific hydrogen isotopic fractionation is of great interest as an environmental indicator and would extend compound-specific hydrogen isotopic composition from simply recording environmental water, to recording the metabolic diversity of a paleoenvironment. The first step to making this connection is to evaluate the expression of metabolism-specific isotopic fractionation trends in modern environmental samples. Osburn et al. (2011) studied a range of microbial mats in Yellowstone National Park and found evidence for both heterotrophic D-enrichment and autotrophic D-depletion of lipids (Osburn et al., 2011). Studies of marine biomass show D-enrichment of lipids of probable heterotrophic origin such as branched fatty acids (Jones et al., 2008). These initial studies are promising, but further extension of laboratory trends requires that we empirically understand the signatures produced from a reasonable breadth of environmental metabolisms. Zhang et al. (2009) cultured only aerobic heterotrophs, which while environmentally relevant, do not account for extensive anaerobic microbial activity occurring in sediments, microbial mats, and oxygen minimum zones.

Here we report on the hydrogen isotopic fractionations of lipids produced by nitrate and sulfate reducing bacteria. We studied facultative anaerobes to provide a direct comparison between aerobic and anaerobic behavior. Obligate anaerobic sulfate reducers are common constituents of marine sediment, and thus understanding their role in fractionation is critical to extension of compound-specific D/H as a paleoenvironmental marker. We were able to study sulfate reducing bacteria (SRB) under both autotrophic and heterotrophic conditions, whereas a previous study of SRBs only included autotrophic metabolisms (Campbell et al., 2009). Our results suggest that significant differences exist between fractionation of D/H under aerobic and anaerobic conditions, complicating the potential of lipid D/H as a metabolic proxy. This study is the first to evaluate the behavior of anaerobic microbes in the context of this metabolic proxy.

## **2. Materials and methods**

### ***2.1 Culturing: strains and methods***

Strains for growth trials were selected based on their metabolic capability, preliminary biochemical characterization, and accessibility. Two sulfate reducers, *Desulfobacterium autotrophicum* (DSM 3382) and *Desulfobacter hydrogenophilus* (DSM-3380), were purchased from the DSMZ culture collection. *Escherichia coli* K-12 MG1655 was present in the Sessions lab culture collection. *Paracoccus denitrificans* (B-3785) was supplied by the ARS culture collection. *P. denitrificans* and *E. coli* were grown in a low salt base medium (LWB) for all experiments. LWB contained per liter of water: 0.1 g NaCl, 0.5 g MgSO<sub>4</sub>\*7H<sub>2</sub>O, 0.1 g CaCl<sub>2</sub>\*2H<sub>2</sub>O, 0.05 g KCl, 0.03 g NH<sub>4</sub>Cl, 0.11 g KH<sub>2</sub>PO<sub>4</sub>\*H<sub>2</sub>O, 1 ml vitamin solution, and 1 ml trace element solution. Vitamin and trace element solution were modeled after (Breznak and Leadbetter, 2006). The

sulfate reducers were grown in a modified Medium 383 (DSMZ) with the trace element solution substituted from the LWB medium. Growth medium base was autoclaved for 20 min at 120°C before cooling and filter sterilized addition of 1 g/l NaHCO<sub>3</sub> as a buffer, carbon source to 10 mM, and trace element and vitamin solutions. Flasks, Balch tubes, and serum bottles for growth experiments were stripped of organic contamination in a muffle furnace prior to use. For anaerobic media, the cooling and final media preparation took place in an anaerobic chamber.

The sulfate reducers chosen for this study are closely related deltaproteobacteria that differ significantly in both metabolic function and known biochemical pathways (Muyzer and Stams, 2008). They are both able to oxidize organic carbon substrates completely to CO<sub>2</sub> and have been studied previously for carbon isotopic fractionation (Londry and Marais, 2003). *D. autotrophicum* is able to use a relatively broad range of substrates, successfully oxidizing H<sub>2</sub>, acetate, succinate, pyruvate, glucose, lactate, and formate (Strittmatter et al., 2009). In contrast, *D. hydrogenophilus* can operate only autotrophically or using acetate (Schauder et al., 1986; 1987; Widdel, 1987). The central metabolic pathways that are used for carbon oxidation also differ with *D. autotrophicum* using the Acetyl-CoA pathway in both directions and *D. hydrogenophilus* using a modified TCA cycle (Brandis-Heep et al., 1983; Londry and Marais, 2003; Strittmatter et al., 2009). Given that the current proposal for the mechanism of D/H fractionation in lipids depends on central metabolic pathway, this distinction was considered particularly important.

Facultative anaerobes chosen for study are there soil bacterium *P. denitrificans* and the enteric bacterium *E. coli*. Both are able to utilize either O<sub>2</sub> or NO<sub>3</sub> as terminal

electron acceptor. A key difference is that *P. denitrificans* is a denitrifying bacteria and thus reduces  $\text{NO}_3$  to the level of  $\text{N}_2$ . *E. coli* in contrast is unable to denitrify and instead reduces  $\text{NO}_3$  to  $\text{NO}_2$  and then to ammonia (Shapleigh, 2006). Also, *P. denitrificans* has additional metabolic flexibility allowing for autotrophic growth and growth using either  $\text{H}_2$  or thiosulfate as an electron donor (Friedrich and Mitrenga, 1981; Friedrich and Schwartz, 1993). The metabolic flexibility of these two organisms allows for direct comparison between aerobic and anaerobic growth in a single organism, as well as autotrophic vs. heterotrophic growth.

The growth experiments in this study were designed to sample the breath of metabolic flexibility for each of the cultured strains. Table 1 includes a list of growth conditions applied to each microbe. All sulfate reducers were grown in an atmosphere of either 80:20  $\text{N}_2$ : $\text{CO}_2$  or  $\text{H}_2$ : $\text{CO}_2$  (hydrogen experiments). Anaerobic media was prepared and sealed in an anaerobic chamber and subsequently purged with the final headspace gas composition. Facultative anaerobes were grown either open to the atmosphere for aerobic growth or under  $\text{N}_2$ : $\text{CO}_2$  or  $\text{H}_2$ : $\text{CO}_2$  as above for anaerobic growth. For *P. denitrificans* cultures requiring  $\text{H}_2$  and  $\text{O}_2$ , media was degased under  $\text{H}_2$ : $\text{CO}_2$  as before and lab air was introduced by filter sterilization.  $\text{D}_2\text{O}$  enriched media up to 1410 ‰ was prepared by volumetric addition of a sterile 5%  $\text{D}_2\text{O}$  spike solution to final media preparations. Cultures for lipid collection (generally 100 ml) were inoculated with 0.5-1 ml of actively growing culture before incubation at 25°C. Inoculum accounts for <1% of final harvested biomass. Growth was monitored spectrophotometrically at 600 nm. Cultures were harvested in late exponential or early stationary phase.

Table 1: Experiment list

Name	e- donor	e- acceptor	doubling time (hrs)	$\delta D_w$
<i>Desulfobacterium autotrophicum</i>				
DA_A	Acetate	SO <sub>4</sub>	43.1	-70, -70
DA_S	Succinate	SO <sub>4</sub>	43.5	-66, -67
DA_F	Formate	SO <sub>4</sub>	55.0	-71, -70
DA_P	Pyruvate	SO <sub>4</sub>	34.3	-71, -70
DA_G	Glucose	SO <sub>4</sub>	72.8	-68, -68
DA_H	H <sub>2</sub>	SO <sub>4</sub>	34.0	-70, -64
<i>Desulfobacter hydrogenophilus</i>				
DH_A	Acetate	SO <sub>4</sub>	16*	-67
DH_H	H <sub>2</sub>	SO <sub>4</sub>	16*	-60
<i>Escherichia coli</i>				
EC_A	Acetate	O <sub>2</sub>	7.2	-82
EC_An	Acetate	NO <sub>3</sub>	3.2	-80, -13
EC_S	Succinate	O <sub>2</sub>	3.75	-83
EC_Sn	Succinate	NO <sub>3</sub>	4.7	-79
EC_P	Pyruvate	O <sub>2</sub>	3.97	-82
EC_Pn	Pyruvate	NO <sub>3</sub>	9.3	-2.6
EC_L	Lactate	O <sub>2</sub>	3.84	-87
EC_Ln	Lactate	NO <sub>3</sub>	15.2	-83
EC_G	Glucose	O <sub>2</sub>	1.6	-82
EC_Gn	Glucose	NO <sub>3</sub>	4.3	-79, 43, 170
EC_Gf	Glucose	--	4.6	-79
<i>Paracoccus denitrificans</i>				
PD_A	Acetate	O <sub>2</sub>	2.3	-69, -57, 292, 430
PD_An	Acetate	NO <sub>3</sub>	NM	-49
PD_S	Succinate	O <sub>2</sub>	2.05	-69, -69, 265, 394, -85, 177, 421, 635, 910, 1180
PD_Sn	Succinate	NO <sub>3</sub>	NM	-71, 263, 394, 194, 437, 691, 976, 1181, 1409
PD_P	Pyruvate	O <sub>2</sub>	2.88	-68
PD_L	Lactate	O <sub>2</sub>	2.43	-73, -82
PD_Ln	Lactate	NO <sub>3</sub>	NM	-82
PD_G	Glucose	O <sub>2</sub>	2.1	-69, 288, 433
PD_Gn	Glucose	NO <sub>3</sub>	NM	-60
PD_T	Thiosulfate	O <sub>2</sub>	10.8	-82, -29.5, 11, 51, 91
PD_Tn	Thiosulfate	NO <sub>3</sub>	NM	-83
PD_M	MeOH	O <sub>2</sub>	1.1	-38
PD_H	H <sub>2</sub>	O <sub>2</sub>	4.0	-82, 3, 209
PD_Hn	H <sub>2</sub>	NO <sub>3</sub>	NM	-64, -41, 289, 427

\* from Schauder et al. (1987)

NM = not measured

## ***2.2 Lipid extraction and analysis***

Pelleted samples of microbial biomass were frozen, lyophilized, and stored at -20°C until lipid extraction. Fatty acid methyl esters (FAMES) were produced from cellular material in a 1-step combined extraction and derivatization procedure (Rodríguez-Ruiz et al., 1998). For each sample, 1 to 100 milligrams of dry biomass was sealed into a 7.5 ml vial with 1 ml of hexane and 2 ml of 20:1 anhydrous methanol: acetyl chloride and reacted at 100°C for 10 mins. After cooling, 2 ml of water was added to the mixture followed by 3-fold extraction with ~3 ml hexane. Separation of saturated from unsaturated FAMES was achieved using Discovery® Ag-Ion solid phase extraction columns (Supelco). Extracted samples were dried to 1 ml and applied to preconditioned columns followed by elution of saturated, monounsaturated, and diunsaturated FAMES in 96:4 hexane: acetone, 90:10 hexane: acetone, and acetone respectively. Fractions were evaporated to dryness and suspended in 1.5 ml hexane for analysis.

Fatty acids in each fraction were identified and quantified by gas chromatography- mass spectrometry (GC-MS) of the FAME derivatives. One microliter of each organic extract was injected into a ThermoFinnigan Trace GC with the effluent split ~9:1 between a DSQ mass spectrometer and a flame ionization detector (FID). The sample was injected into a programmable temperature vaporization (PTV) injector operated in splitless mode and heated to 330°C in 24 sec. The GC was equipped with a ZB-5ms GC column (30 m long, 0.25 mm I.D., 0.25µm film thickness) and was operated with a He carrier gas flow rate of 0.8 ml/min. The oven temperature was held for 1 min at 100°C, ramped at 20°C/min to 140°C, ramped at 3.0°C/min to 250°C and held for 1 min, then ramped at 20°C/min to 310°C and held for 10 minutes. Compounds were identified

by comparison of mass spectra to the NIST 2004 library and/or by retention time to authentic standards. Samples were quantified by GC-FID relative to a known amount of either palmitic acid isobutyl ester (PAIBE) or a C<sub>23</sub> *n*-alkane standard. The position and stereochemistry of double bonds was inferred based on comparison to previously published reports from each strain. FAMES are reported using the nomenclature “X:Y” where X is carbon number and Y is number of double bonds. We follow the convention of naming compounds with iso- or anteiso- methyl branches, or cyclopropyl rings, as the total carbon number preceded by *i*-, *a*-, or *cy*- respectively. Thus ‘i-17’ is 15-methylhexadecanoic acid.

### ***2.3 Isotopic analyses***

Samples of culture medium for water hydrogen isotopic analysis were collected by filtering through a 0.2 μm syringe filter or by collecting centrifuge supernatant after cell pelleting. Waters were analyzed using a Los Gatos DLT-100 Liquid Water Isotope Analyzer. Samples were measured in eight-fold replicate against appropriate working standards ( $\delta D = -117.0\text{‰}$ ,  $-10.6$ ,  $+287.3$ , and  $+457.6$ ). Measured isotope ratios were converted to  $\delta D$  values by comparison with the two standards, and normalized to the SMOW-SLAP scale. Typical precision for these analyses was 1-2‰. All data reduction was performed using Visual Basic code written by us.

D/H ratios of FAMES were measured using a ThermoFinnigan Trace GC coupled to a Delta+XP isotope ratio mass spectrometer (IRMS) via a pyrolysis interface (GC/TC) operated at 1430 °C. External FAME standards were analyzed after every four samples. Eight to 24 μL of each sample was injected into a PTV injector operated in splitless mode

with solvent venting. A thick-film ZB-5ms column (30 m long, 0.25mm I.D., 1.00  $\mu\text{m}$  film) was used for isotope analysis with He carrier gas flow rate at 1.4 ml/min. The GC oven temperature was held at 100°C for 1 min, ramped at 20°C/min to 205°C, ramped at 0.8°C/min to 220°C, ramped at 8°C/min to 320°C and held for 10 min. Peaks were identified by comparison of retention order and relative height to GC-MS chromatograms. Isotope ratios were calculated using ISODAT NT 2.5 software by comparison to methane reference gas peaks as described previously (Wang and Sessions, 2008) and are reported in the standard  $\delta\text{D}$  notation ( $\equiv R_{\text{sample}}/R_{\text{std}} - 1$ ) as permil (‰) variations relative to the VSMOW standard. The root-mean-squared (RMS) error for external FAME standards run both before and between sample runs was  $3.28 \pm 0.8$  ‰ ( $n = 190$ ). Data was corrected for the calculated offset of bracketing external FAME standards. The standard deviation for replicate analyses of unknown analytes averaged 6.8‰ ( $n = 450$ ). Samples were analyzed in triplicate. The  $H_3$  factor averaged  $3.48 \pm 0.16$  ppm/mV and was measured daily. Fractionations between lipids and environmental water were calculated as  $\epsilon_{l-w} = ((\delta\text{D}_l + 1)/(\delta\text{D}_w + 1) - 1)$  and are reported as permil (‰) variations.

### 3. Results

#### 3.1 Microbial growth and lipid production

All strains used in these experiments grew to turbidity under the specified growth conditions. *D. autotrophicum* grew the most slowly of all strains with doubling times (dt) on the order 1.5 of 3 days. The most rapid growth and highest final densities for *D. autotrophicum* were observed for pyruvate and autotrophic cultures, whereas glucose was apparently the least desirable substrate. *D. hydrogenophilus* grew rapidly on both acetate

and H<sub>2</sub> reaching turbidity in 2-3 days (dt 72.8 hr). *E. coli* grew most rapidly on glucose (1.6 hr doubling time), similarly between lactate, succinate, and pyruvate (dt ~4 hr), and more slowly on acetate (dt ~7 hr). Doubling times were slightly slower but rapid during anaerobic growth (3.2 to 15 hrs). *P. denitrificans* grew at almost identical rates on all heterotrophic substrates (dt 1.1 to 2.9) with slightly slower growth autotrophically on H<sub>2</sub> (dt 4 hr) and thiosulfate (10.8 hr). Very high final densities were observed under all conditions except methanol oxidation, which produced rapid doubling times, but only for a brief period thus limiting the final observed density.

Each strain produced a characteristic suite of fatty acids that generally varied little between growth conditions, including substrate. Both sulfate reducers produced a complex mixture of fatty acids whereas facultative anaerobes produced a more restricted set, consistent with previous reports (Taylor and Parkes, 1983; Dowling et al., 1986). *D. autotrophicum* was dominated by 16:0 and 16:1 FAMES but produced a large amount of i-17, cy-17, 18:1, and the odd chain fatty acids 15:0 and 17:0 (Figure 1). The only apparent metabolism specific effect was the production of 20:0, 22:0, and 24:0 FAMES by formate cultures and a lower prevalence of odd chain FAMES during growth on glucose. The lipids produced by *D. hydrogenophilus* under both conditions were similar to *D. autotrophicum* including primarily 14:0, 16:1, 16:0, 17:0, and cy-17 FAMES. *E. coli* produced primarily 16:1, 16:0, cy-17, and 18:1 FAMES with lesser quantities of 14:0, 15:0, 17:0 and cy-19 (Figure 1). Relative proportions of FAMES varied slightly with substrate with an increase in cy-17 at the expense of 16:1 in glucose and pyruvate cultures. Fatty acids from *P. denitrificans* were completely dominated by two isomers of 18:1 FAME with only minor amounts of 16:0 and 18:0. Trace levels of cy-12, a-15:0,

17:0, me-19, and cy-19 were observed in some cultures with abundant cy-19 only occurring in the methanol cultures. Clean up and separation techniques generally allowed for isotopic measurement of all but the trace peaks in each chromatogram. The separation of saturated from unsaturated FAMES was particularly necessary for *P. denitrificans* where the tail of the abundant 18:1 would otherwise obscure the 18:0 peak in GC-IRMS chromatograms.

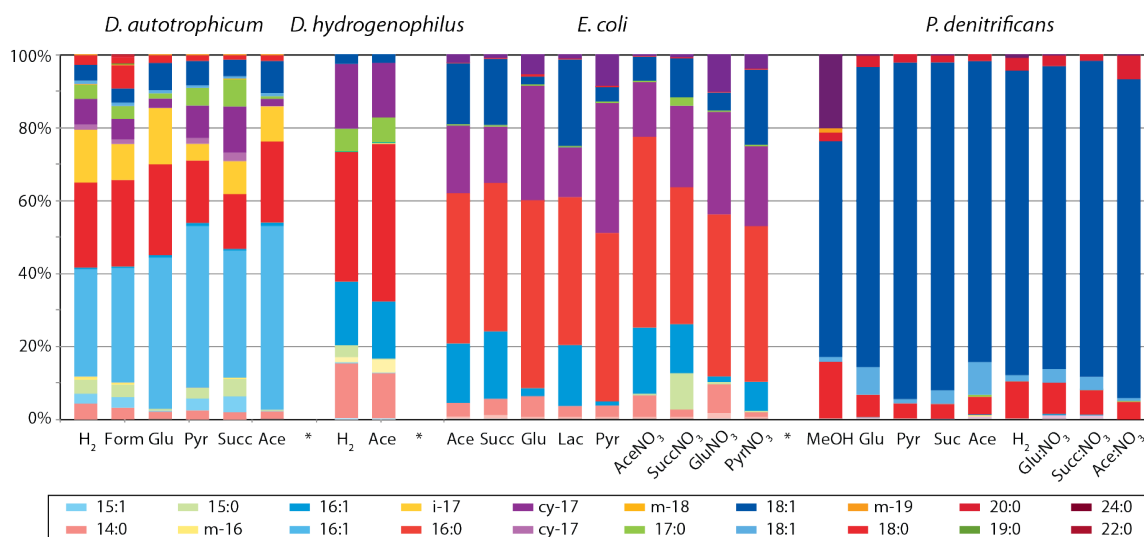


**Figure 1:** Fatty acid compositions of microbial strains on various metabolic substrates

### 3.2 Isotopic compositions

A large range of hydrogen isotopic compositions was observed for the microorganisms in this study, consistent with both previous culturing studies and the ranges observed in natural samples (Li et al., 2009; Zhang, Gillespie, et al., 2009; Osburn et al., 2011). The total range in fractionation from water ( $\epsilon_{1-w}$ ) for non-labeled experiments ranged from -284.3 to 67.8 ‰ and varied systematically by strain and by metabolism (Table A2). To eliminate variability caused by changes in fatty acid composition, an abundance-weighted mean fractionation was calculated for each culture.

These mean values showed similar trends to those from individual acids and ranged from -270 to + 30 ‰. Fractionation values are dependent on the isotopic composition of growth water (see discussion) and for this reason only experiments using non-spiked water were included in this composition (-60 to -80 ‰). The data in Figure 2 fall into two groups that separate the sulfate reducing bacteria from the facultative anaerobes.

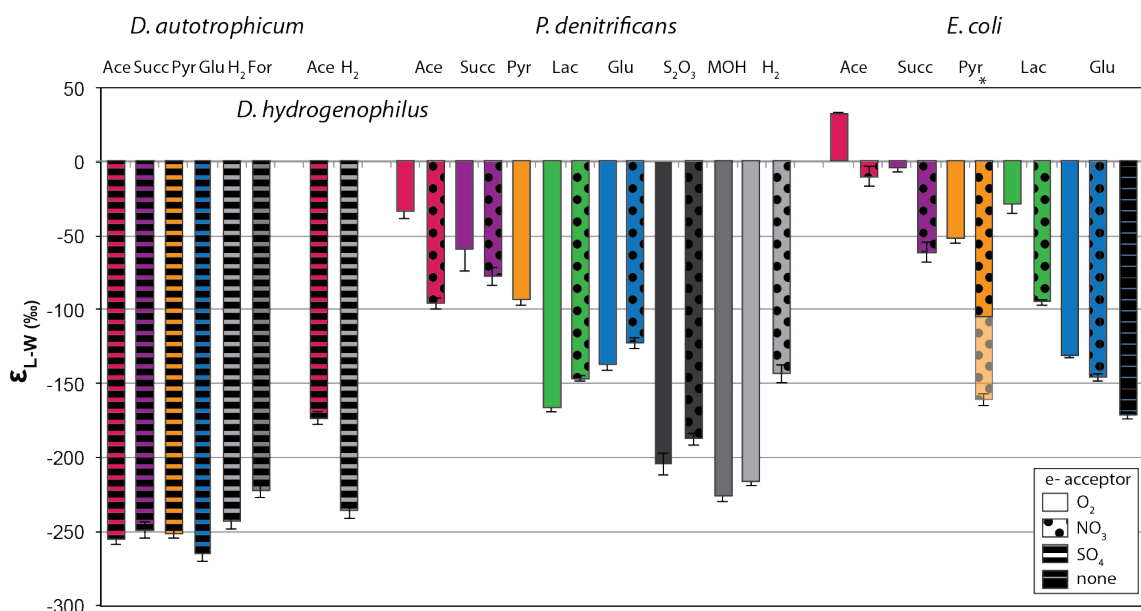


**Figure 2:** Summary of fractionations between lipid and water for each metabolism grouped by organism. Colors only highlight trends given by the labels. The anaerobic pyruvate *E. coli* culture was grown in D-enriched water, artificially lowering the fractionation (shaded bar). An estimated value is shown that was calculated using the relationship between water and lipid  $\delta D$  for an anaerobic glucose culture.

Sulfate reducing strains produced consistently D-depleted lipids with fractionations for all lipids in the range of -284.3 to -86.5 ‰. Interestingly, this D-depletion occurs regardless of heterotrophic substrate. This trend is most visible in *D. autotrophicum* where no significant differences are observed between acetate, succinate, pyruvate, glucose, or formate cultures. The autotrophic cultures from the two sulfate reducers produced a similar fractionation with water (~-225‰). Our results are consistent with those of Campbell (2009), who observe fractionations from -189 to -295

‰ for *D. autotrophicum* under autotrophic conditions. The lipids from the acetate culture of *D. hydrogenophilus* are significantly D-enriched relative to those of *D. autotrophicum*, but still well below the range observed for lipids from *P. denitrificans* or *E. coli* grown on acetate

Fractionation data from facultative anaerobes for all lipids spanned a very large range (-267.2 to 67.8 ‰) and appear to vary both with electron acceptor and electron donor. In general, heterotrophic cultures are enriched relative to autotrophic ones, with the magnitude of isotopic fractionation reflecting the specific carbon source. While fractionations from the two microbes trend similarly with growth on similar substrates, *E. coli* produces more enriched lipids on the whole (-202.6 to 67.8 ‰ compared to -267.2 to 7.2 ‰). In addition, growth on lactate produces more D-depleted lipids in *P. denitrificans* compared to *E. coli*. Another unusual feature is the relatively D-enriched signature of denitrification with H<sub>2</sub> as an electron donor in *Paracoccus*. There is an apparent isotopic offset between aerobic and nitrate reducing cultures for facultative anaerobes (Figure 2, dotted vs. solid bars). This offset varies by substrate and by microbe and is discussed in more detail in the following section.

### ***3.3 Aerobic vs. nitrate reducing metabolisms***

A key contribution of this study is to document the isotopic differences between cultures grown aerobically vs. anaerobically. To compare these trends directly, Figure 3 plots the offset between lipid-water fractionations exhibited by aerobic and anaerobic cultures of *P. denitrificans* and *E. coli* for the same electron donors. Comparisons in this space show the difference between the isotopic composition (relative to water) of a

particular lipid (shown in symbols) between growth on  $O_2$  vs.  $NO_3$  for otherwise identical culturing conditions. If aerobic and nitrate reducing cultures produced similar fractionations the data would cluster around zero when plotted in this space. As the data range from 75 to -75 ‰ it is clear that electron acceptor can alone affect isotopic fractionation, and that the difference can be in opposite directions for different substrates.

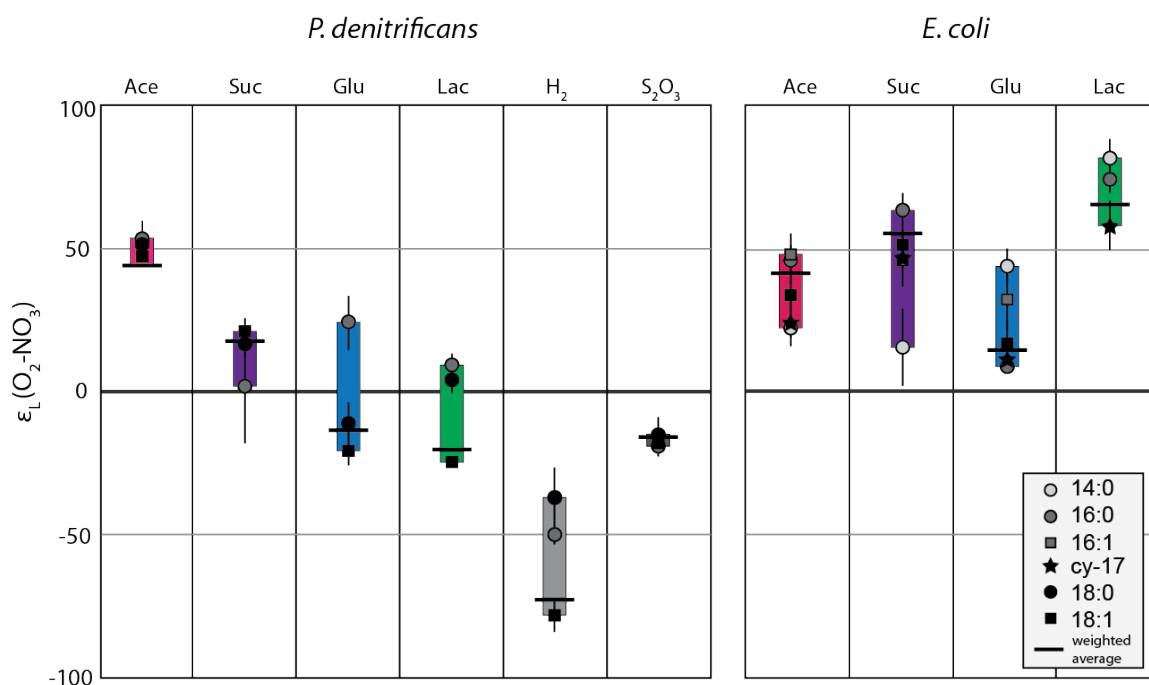


**Figure 3:** The difference in fractionation between aerobic and anaerobic cultures on various substrates. The differences between the weighted average for all lipids from each culture are indicated by the solid horizontal bar. Error bars reflect propagated instrumental error on isotope measurements. Colors are for emphasis.

The behavior of *P. denitrificans* and *E. coli* differ in this space, as do the trends observed for heterotrophic vs. autotrophic metabolisms. For *P. denitrificans*, acetate and succinate cultures grown on nitrate are D-depleted relative to aerobic cultures, glucose and lactate are intermediate, and hydrogen is strongly enriched. In contrast, all anaerobic

cultures of *E. coli* produce lipids that are depleted relative to aerobic cultures. Previous observations and models of fractionation of hydrogen isotopes in microbial lipids do not predict the differences observed here. Neither O<sub>2</sub> nor NO<sub>3</sub> contain hydrogen, so clearly cannot directly contribute hydrogen to the cell.

### ***3.4 Autotrophic vs. heterotrophic metabolisms***

A major contribution of previous studies was to differentiate between autotrophic and heterotrophic cultures based on  $\delta D$  alone (Valentine, 2009). This distinction is in the form of strong D-enrichment of heterotrophic cultures relative to autotrophic cultures and has been demonstrably shown to exist in some environmental samples (Osburn, 2011). In Zhang et al. (2009), heterotrophic strains were metabolically flexible; each possessing complete biochemical pathways to fix different organic substrates. In contrast, many environmentally relevant microbes such as sulfate reducers possess significantly less versatile biochemical networks. It is not known if the previously observed D-enrichment of heterotrophic lipids is present for growth under anaerobic conditions.

#### ***3.4.1 Sulfate reducers***

In order to visualize the offset between autotrophic and heterotrophic cultures, the difference in fractionation for heterotrophic substrates vs. H<sub>2</sub> utilizing cultures of the sulfate reducers are shown in Figure 4. This analysis was done for specific fatty acids in addition to the weighted averages of all lipids for each culture. *D. hydrogenophilus* only has one bar for acetate because it is unable to utilize other organic compounds. Cultures with fractionations similar to the H<sub>2</sub> culture will plot around zero in this space, with D-enrichment and D-depletion in positive and negative epsilon values, respectively.

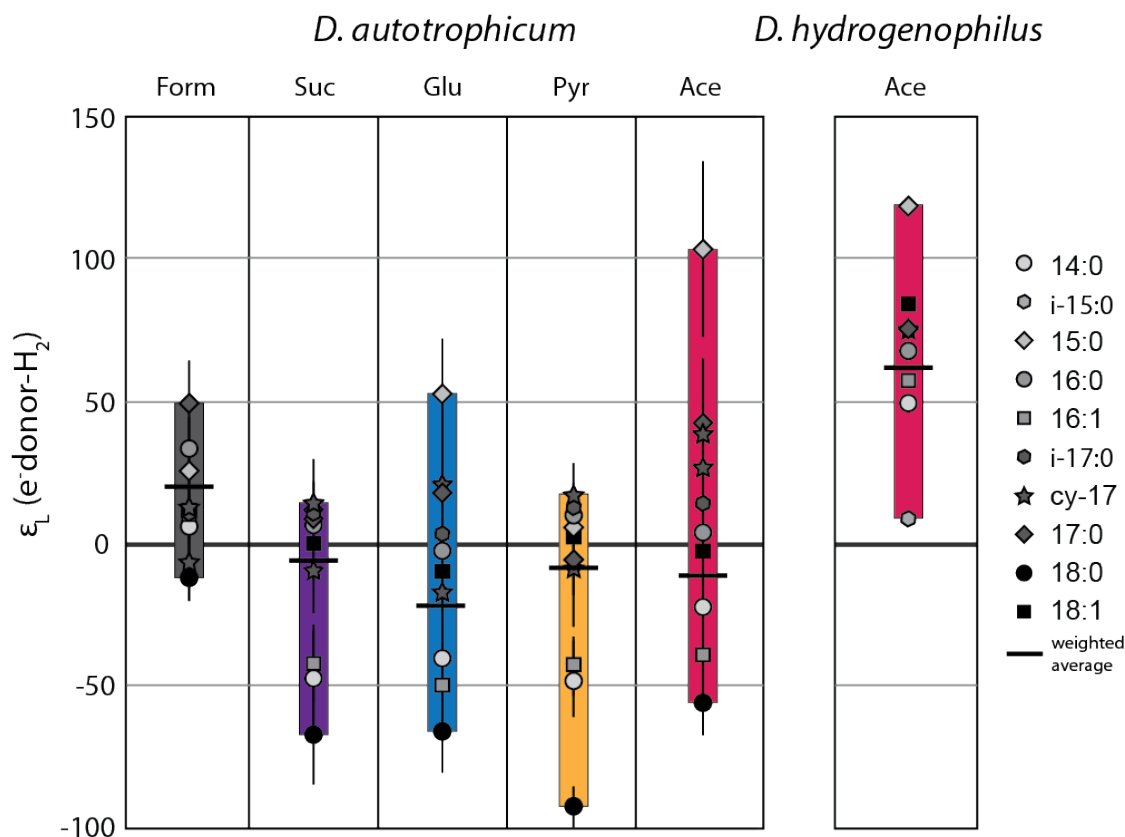


**Figure 4:** The difference in fractionation between heterotrophic and autotrophic cultures of sulfate reducing bacteria. The differences between the weighted average for all lipids from each culture are indicated by the solid horizontal bar. Error bars reflect propagated instrumental error on isotope measurements. Colors are for emphasis.

For *D. autotrophicum*, data for formate, succinate, glucose, pyruvate, and acetate cultures are compared to data from the hydrogen culture. As formate is oxidized to  $CO_2$  before autotrophic growth, this culture is expected to resemble the cultures grown on  $H_2$ , where the others will illustrate heterotrophic metabolism in this organism. The difference in fractionation for formate cultures ranges from -10 to 50 ‰ for individual acids with a weighted mean of +20 ‰. In contrast, the heterotrophic cultures produced larger ranges for all fatty acids and weighted average between -10 and -25 ‰. The behavior of *D. hydrogenophilus* on acetate differs from that of *D. autotrophicum*, and ranges from 10 to 125 ‰ with an average of 65 ‰. The isotopic offset between the two acetate cultures

and the difference in their metabolic capability suggest a change in process. Regardless of mechanism, this data is not consistent with the general D-enrichment of heterotrophic cultures over autotrophic ones.

Significant isotopic variability is also observed between the different types of fatty acids measured in each culture. In most cases, the most positive fractionations and the largest difference with autotrophic cultures are observed for odd chain fatty acids (diamonds). In contrast, even-chain fatty acids are generally more depleted (Figure 4, circles), with unsaturated (squares) and cyclopropyl (stars) fatty acids being intermediate. Each type of fatty acid has a slightly different biosynthetic process. We may be able to use these differences to inform the mechanism of fractionation.

#### 3.4.2 *P. denitrificans*

This analysis was repeated for cultures of *P. denitrificans* to illustrate differences between autotrophy and heterotrophy in an organism with flexible metabolic constraints. Comparisons were made between autotrophic and heterotrophic cultures under both aerobic and anaerobic conditions (Figure 5). Cultures using methanol and thiosulfate are also autotrophic, and thus, might be expected to fall close to 0 ‰ in this space, consistent with the data. In contrast, very large differences in fractionation are observed between acetate and succinate cultures compared to autotrophic cultures especially under aerobic conditions. This effect appears to be lower, although in the same direction, in the anaerobic comparisons. Differences in fractionation for glucose and lactate cultures plot intermediate between those for acetate and succinate. In both aerobic and anaerobic cases, the autotrophic end members fall either enriched or very similar to the hydrogen

cultures. As *P. denitrificans* only produces a limited range of FAs, the trends for individual acids are minimal as is the spread in data.

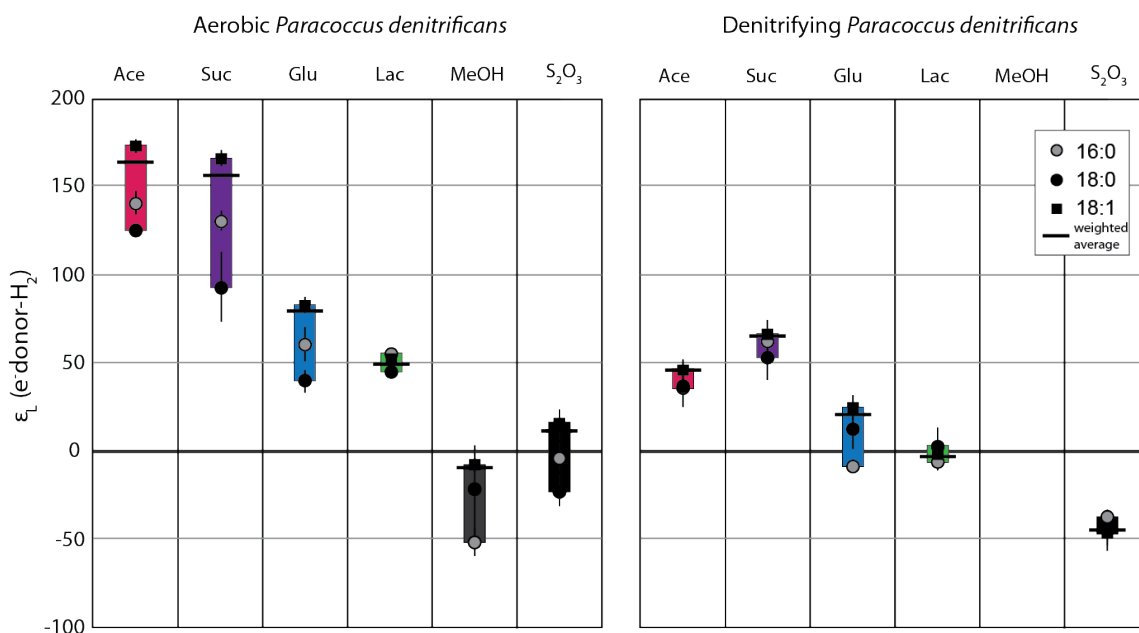


**Figure 5:** The difference in fractionation between heterotrophic and autotrophic cultures of facultative anaerobic bacteria. The differences between the weighted average for all lipids from each culture are indicated by the solid horizontal bar. Error bars reflect propagated instrumental error on isotope measurements. Colors are for emphasis.

Overall, data from *P. denitrificans* support the previously observed D-enrichment of lipids produced by heterotrophs over those from autotrophs. Autotrophic cultures exhibited similar patterns of fractionation to one another, whereas large differences are observed between acetate and succinate cultures compared to those using sugars. While the trend is present in data from anaerobic cultures, the magnitude is muted and there is less agreement between autotrophic cultures. These features, once again, illustrate the influence that changing electron acceptor can have on lipid D/H.

#### 4. Discussion

We infer from this data that the D/H ratios of lipids are sensitive to both the electron donor and electron acceptor. Dependence of fractionation on electron acceptor is not anticipated by the Zhang model, which indicates that there may be previously unexpected mechanisms at play. Electron acceptor appears to only produce small effects on fractionation in our facultative strains, overprinting on the first order trend that is presumably still produced during central metabolism. In contrast, the fractionations produced by sulfate reducing bacteria appear to not vary with changing metabolism at all. Understanding how specifically the electron donor influences pools of cellular hydrogen is not straight forward, and requires consideration of dynamic links between very different biochemical pathways.

Fatty acid biosynthesis is conserved throughout the bacterial domain and is therefore not expected to be a major source of variability in this study. During biosynthesis, chain elongation occurs by progressive addition of acetyl-CoA molecules to the primer molecule. A number of hydrogen additions occur during hydration of double bonds with either water or NADPH serving as the donor (White et al., 2005). It follows, then, that sources of hydrogen on the final fatty acid are acetyl-CoA, water, and NADPH. The stoichiometry of these reactants depends slightly on FA chain length and structure (unsaturated, saturated, methyl branched, etc), but approximately half of nonexchangeable hydrogen on fatty acids comes from NADPH. The other half is split equally between water and the precursor acetyl-CoA. If we assume that fractionations occurring during fatty acid biosynthesis are similar in a single organism growing on

different substrates, then the isotopic composition of either water or the biosynthetic precursors acetyl-CoA or NADPH must change.

#### ***4.1 Relationship between $\delta D_{lipid}$ and $\delta D_{water}$***

We performed growth experiments using D-enriched water to evaluate the role of water on the variable fractionations observed in our data. As shown and discussed previously (Sessions and Hayes, 2005), the isotopic composition of a lipid ( $R_l$ ) can be expressed as a function of the isotopic composition of water ( $R_w$ ), substrate ( $R_s$ ), mole fraction of lipid H derived from water ( $X_w$ ), and the fractionation factors between lipid and these pools ( $\alpha_{l/w}$ ,  $\alpha_{l/s}$ ) following equation 1 (Sessions and Hayes, 2005):

$$(1) \quad R_l = X_w \alpha_{l/w} R_w + (1 - X_w) \alpha_{l/s} R_s$$

This equation defines a linear relationship with respect to  $R_l$  and  $R_w$ , where the slope of the line is  $X_w \alpha_{l/w}$  and the intercept is  $(1 - X_w) \alpha_{l/s} R_s$ . Experimentally, in cultures either  $R_s$  or  $R_w$  could be manipulated to create data on which to make this regression. In this case  $R_w$  was varied between -80 and (up to) 1400 ‰ for otherwise identical cultures growing on the same substrate ( $R_s$ ).

Data for experiments on *P. denitrificans* grown aerobically and anaerobically on succinate, aerobically on acetate and glucose, and both aerobically and anaerobically on  $H_2$  are compared (Figure 6). All experiments produce well-supported linear relationships, even to up to extremely D-enriched isotopic compositions (1400 ‰). Similar trends were observed for different fatty acids in the same sample compared to the mean. The slopes of linear regressions vary between 0.51 and 0.68. In cases where aerobic and anaerobic cultures were compared, slopes varied considerably between the two states; however, no

coherent directional trend was apparent between aerobic vs. anaerobic cultures as a whole.

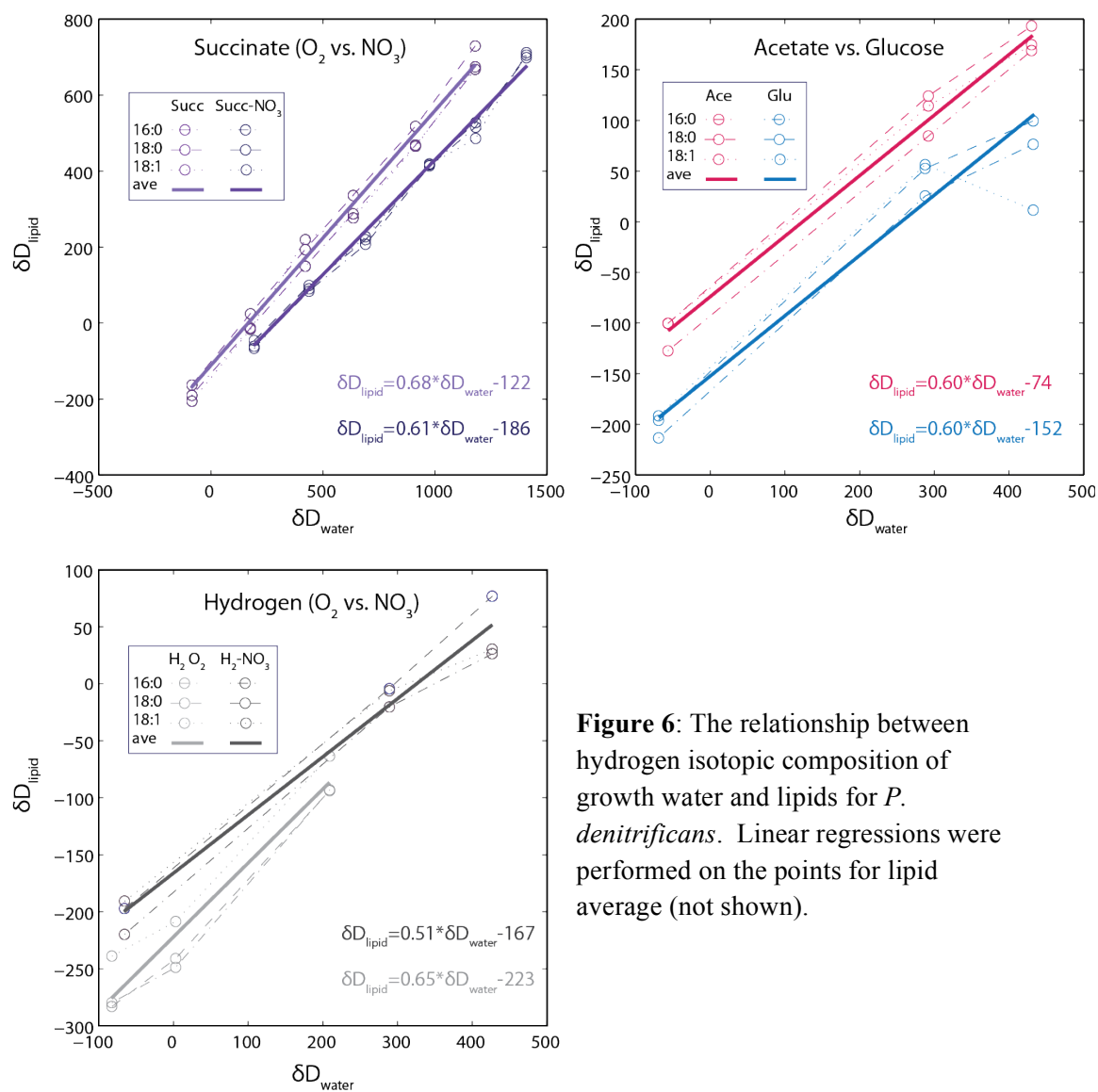


**Figure 6:** The relationship between hydrogen isotopic composition of growth water and lipids for *P. denitrificans*. Linear regressions were performed on the points for lipid average (not shown).

While it is not possible to independently solve for both fractionation factors in heterotrophic cultures, the slope and intercept of regression lines produced above can be used to calculate curves of possible solutions for known values of  $X_w$ . Zhang et al. (2009) used this analysis to assess incorporation of substrate and water hydrogen into lipids.

Comparing the trajectory of these curves for different experimental conditions can suggest the mechanism for changing fractionation. Fractionation curves for *P. denitrificans* are shown in Figure 7. The black circle indicates the solution for  $X_w = 0.5$  on each curve to create a reference point for comparison.

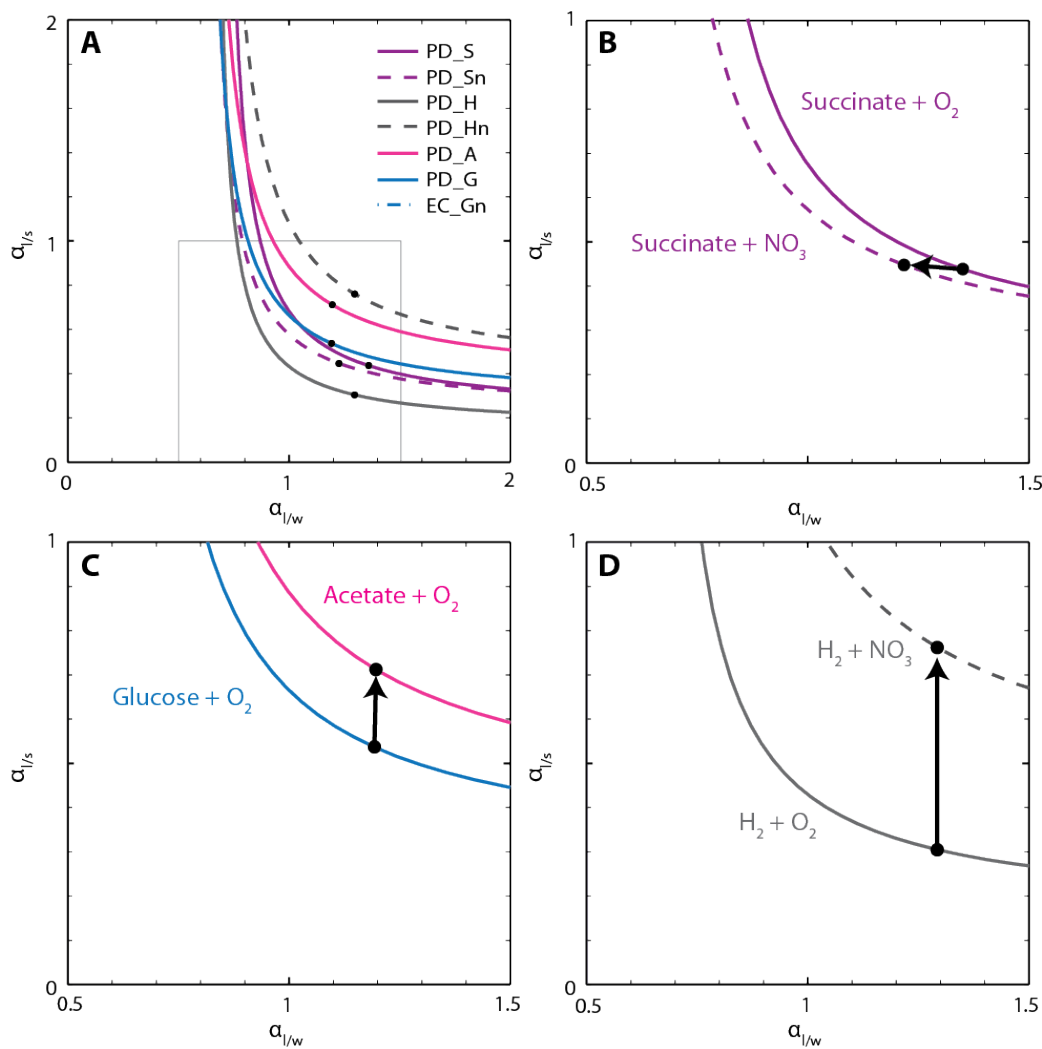


**Figure 7:** Solutions for the fractionation factor between lipid and water and lipid and substrate for a range of  $X_w$  values. Subplots show blow up of grey box in upper left panel for specific metabolisms. Arrows show the vectors connecting  $X_w = 0.5$  on pairs of curves.

Panel A plots all the curves on a single plot for comparison and does not reveal any particular grouping between similar metabolisms. Panel B compares growth on

succinate under aerobic (solid) vs. denitrifying conditions (dashed). For a given  $X_w$ , the fractionation between lipid and substrate does not change between the two curves, and instead a shift to lower lipid water fractionation is observed. If we assume constant incorporation of water under both conditions, the trend suggests that the change in fractionation between these two growth conditions does not result from a fundamental change in how the substrate is incorporated in central metabolism. In contrast, panel C shows the difference between glucose and acetate cultures. In this case, the fractionation between lipid and water is constant between the two experiments, but the lipid substrate fractionation changes significantly. Given that the substrate itself changed, as well as the central metabolic pathway by which the substrate is oxidized, this is the expected result. Panel D illustrates curves for autotrophic growth on  $H_2$  under both anaerobic and aerobic conditions. While hydrogen from  $H_2$  may have been incorporated into lipids in each case, it is not clear why the fractionation associated with its incorporation should change under aerobic vs. anaerobic conditions. For  $X = 0.5$ , the switch to  $NO_3$  is exhibited through a change in  $\alpha_{l/s}$  with constant  $\alpha_{l/w}$ . For  $X_w$  approaching 1,  $\alpha_{l/w}$  approaches 0.654 for both cultures.

#### ***4.2 The role of central metabolism in D/H fractionation***

Central metabolism has been suggested to play a critical role in producing hydrogen isotopic variability of lipids (Zhang, Gillespie, et al., 2009). The link between metabolism and lipid biosynthesis is the hydrogen carrier NADPH, which is reduced primarily as organic substrates are processed through the TCA cycle or pentose phosphate pathways and donates roughly half of lipid hydrogen during biosynthesis. The primary mechanism invoked by Zhang et al. (2009) to explain isotopic differentiation of

NADPH is differences in isotope effects expressed by critical enzymes that transfer H- in each pathway. Depending on the organic substrate being oxidized, different starting points and routes through the metabolic network are used, subject to the biochemical capabilities of each microbe.

#### *4.2.1 Central Metabolism in selected strains*

A schematic diagram of the metabolic pathways used by the organisms in this study is shown in Figure 8a. Electron donors are labeled and outlined by bold boxes to illustrate their entry point in the metabolic network. Major pathways shown are the glycolytic pathway, pentose phosphate pathway, Enter-Doudoroff pathway, TCA cycle, the acetyl-CoA pathway, the Calvin cycle, and pathways for methanol and hydrogen oxidation. Stars and diamonds indicate reduction points for NADPH and NADH respectively. Figure 8b and 8c tailor the summary to each organism, including only the pathways present and utilized in each. This diagram is by not meant to capture the breath of metabolic reactions that could occur in each organism, but rather to summarize the route that each substrate used here takes on its way to CO<sub>2</sub> as a means to understanding the balance of hydrogen carriers in each case.

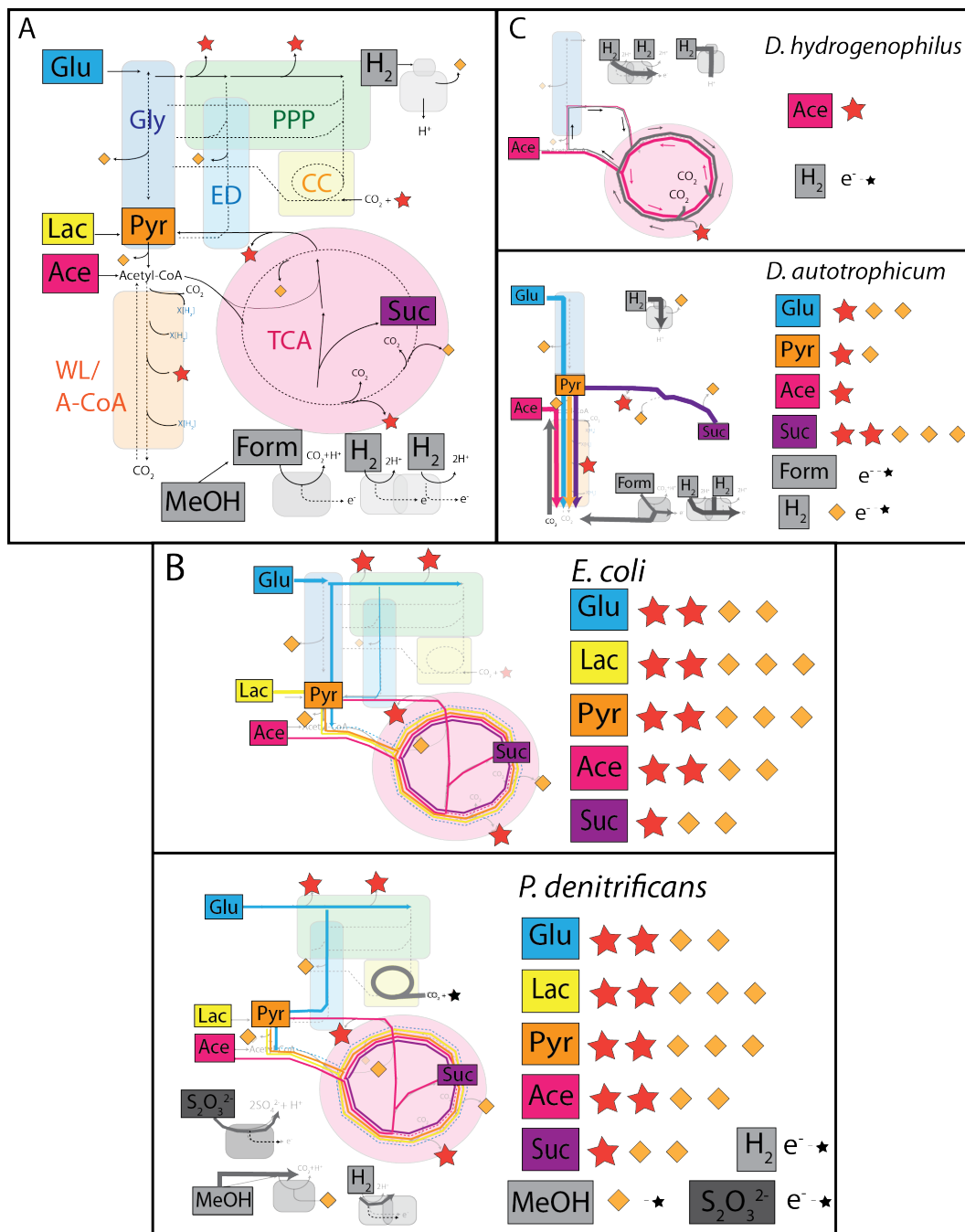


**Figure 8:** Schematic describing central metabolic pathways and substrate utilization routes for each substrate and organism. **A.** Metabolic pathway key including all pathways and enzymes from all organisms. Substrates are showing in colored boxes. Abbreviations are as follows: Gly, glycolytic pathway; PPP, pentose phosphate pathway; ED, Entner Douforoff Pathway; CC, Calvin Cycle; TCA, Tricarboxylic acid cycle; WL/A-CoA, Wood Ljungdahl/ Acetyl-CoA pathway. Stars and diamonds indicate points where NADPH and NADH are produced respectively. **B.** Metabolic pathways of *E. coli* and *P. denitrificans*. The tally of produced reducing equivalents is shown to the right of pathway schematic. **C.** Metabolic pathways of sulfate reducers.

As illustrated in Figure 8b, the metabolic networks *P. denitrificans* and *E. coli* are complex and include various production points for NAD(P)H. Growth on glucose by *E. coli* illustrates the metabolic branching that the cell modulates to balance production of biosynthetic precursors and intermediates. Glucose is routed primarily through the glycolytic pathway, but branches through the pentose phosphate and Entner Doudoroff pathways as well. In contrast, pyruvate, lactate, succinate and acetate are processed via the TCA cycle. To preserve carbon for biosynthesis, acetate routed through the glyoxylate shunt in the TCA cycle rather than being oxidized to CO<sub>2</sub>. *P. denitrificans* has generally similar metabolic structure to *E. coli* with the exception that it lacks a complete glycolytic pathway, and instead uses the Entner Doudoroff pathway as the primary mechanism of glucose consumption. Methanol is oxidized by a cytoplasmic enzyme complex to CO<sub>2</sub> then fixed autotrophically via the Calvin cycle.

Our results for *E. coli* under aerobic conditions agree with those of Zhang et al. (2009) and thus a similar mechanism may explain the data. In general, growth with acetate, succinate, and pyruvate produce lipids that are D-enriched relative to those from autotrophic growth or growth on sugars. The same trends are present in experiments with *P. denitrificans* although the absolute D-enrichments of the acetate and succinate cultures are less extreme than in *E. coli*. The isotopic fractionations observed for lactate cultures differ between organisms without a clear biochemical reason. In *E. coli*, aerobic growth on lactate produces similar D-enrichments to other TCA-cycle intermediates. As lactate is directly converted to pyruvate, this behavior was expected. However, in *P. denitrificans*, significant D-depletions are observed for growth on lactate, exceeding even the glucose cultures. This behavior is not expected by the current model and suggests

that either the lactate dehydrogenase in *P. denitrificans* introduces a larger isotope effect, or lactate is processed through a more complicated path than our scheme predicts. In addition, the fractionations produced during aerobic growth on glucose are practically identical between *P. denitrificans* and *E. coli* despite utilization of different primary oxidation pathways. Central metabolic pathway does not appear to account for the relative D-enrichment or D-depletion of lipids from aerobic relative to anaerobic cultures. Overall, the mechanism present in Zhang et al. (2009) can explain some but not all of the results from aerobic cultures, and do not explain the variability produced during anaerobic growth.

In contrast to the facultative anaerobes, the sulfate reducers studied here have simple metabolic networks consisting of one major pathway each with anaplerotic reactions to produce necessary metabolic intermediates (Schauder et al., 1987). *D. autotrophicum* uses the Acetyl-CoA pathway for both oxidation and fixation of carbon (Strittmatter et al., 2009). Membrane-bound complexes oxidize formate and hydrogen, either donating electrons directly down the electron transport chain or to NADH. Glucose is incorporated via the glycolytic pathway, whereas succinate is converted to malate and then pyruvate before entering the main pathway. Genomic sequencing has provided a clear picture of carbon metabolism for *D. autotrophicum* (Strittmatter et al., 2009). *D. hydrogenophilus* is less well studied, but early enzymatic studies reveal the existence of a modified TCA cycle and suggest that this cycle operates in both directions for autotrophic and heterotrophic growth (Schauder et al., 1987). Notably, the TCA cycle present in *D. hydrogenophilus* does not use  $\text{NAD}^+$  as an electron acceptor, and thus does

not produce NADH as in the normal TCA cycle. This difference may be significant in budgeting of cellular hydrogen.

Central metabolic pathway appears to have a limited effect in the lipid D/H composition of *D. autotrophicum*. Glucose, succinate, pyruvate, and acetate all follow different enzymatic steps before conversion to acetyl-CoA and subsequent oxidation, but the lipids, and therefore the resultant NADPH, are isotopically similar. Growth on hydrogen and formate both require CO<sub>2</sub> fixation, and thus running the pathway in reverse. The similarity in isotopic fractionation produced by hydrogen and formate cultures, and the divergence from the fractionations produced in heterotrophic cultures are predicted by this biochemistry. It is not specifically clear why these changes would result in a D-enrichment of lipids from autotrophic cultures. While not enough data exists to compare autotrophic and heterotrophic pathways of *D. hydrogenophilus*, the hydrogen based autotrophic culture has very similar fractionations to that of *D. autotrophicum* despite a different pathway. These results suggest that the role of metabolic pathway in setting isotopic fractionation is limited in these sulfate reducers.

#### 4.2.2 *The role of transhydrogenases and NADH*

In addition to NADPH, NADH is also produced during metabolic reactions, but is not used as a reductant for lipid biosynthesis. NADH functions similarly to NADPH, but generally serves as the donor to the electron transport chain during energy production rather than during anabolic reactions (White, 2000). The hydrogen on NADH can be transferred to NADP<sup>+</sup> via an energy-dependent, membrane-bound transhydrogenase (Griffiths and Robertson, 1966). The opposite reaction is mediated by a soluble

transhydrogenase and is generally not energy dependent (Sauer et al., 2003). Significant isotope effects of 800 to 3500 ‰ are associated with the protonation of NADP<sup>+</sup> (Zhang, Gillespie, et al., 2009) by membrane bound transhydrogenases, and thus this process could also greatly influence the isotopic composition of pools of cellular reduction equivalents.

Transhydrogenases modulate the balance between NADH and NADPH necessary to perform cellular functions. While it is difficult to constrain the specific requirements at a given moment in growth, isotopic labeling can reveal how much NADPH is directed through the transhydrogenase. This analysis was performed for *E. coli* growing on glucose and found that 35-45 % of NADPH is produced by the transhydrogenase under these conditions (Sauer et al., 2003). Imbalances in the production of either NADH or NADPH will require the conversion of one to the other. Based on the metabolic paths and produced reducing equivalents presented in Figure 8 we can predict growth conditions that would require the action of transhydrogenases. For instance, during growth on pyruvate, *E. coli* produces 3 NADH to 1 NADPH and growth on glucose produces 2 NADH to 2 NADPH. Sauer et al. (2003) showed that growth on glucose required secondary production of NADPH even for this 2:2 ratio; therefore, we might expect proportionally more transhydrogenase-based NADPH production in the pyruvate culture.

The NADH/NADPH production budget is a means for damping or amplifying isotope effects but cannot independently explain specific trends in our data. If that were the case, we would expect metabolisms producing similar NADH: NADPH ratios to produce similar fractions, which is not observed. For instance *E. coli* growing on

succinate and *D. autotrophicum* growing on glucose each produce 2 NADH per 1 NADPH, yet have very different fractionations (see Figure 8). The specific isotopic values of hydrogen from NADPH and NADH that enters into the transhydrogenase will have been set by upstream enzymatic fractionations. In our previous example of glucose vs. pyruvate in *E. coli*, the transhydrogenase activity will differ, but the original molecules are produced in the glycolytic and pentose phosphate cycles for glucose compared to the TCA cycle for pyruvate. If the individual fractionations associated with metabolic pathways and the NADPH demand could be constrained for each organism, then the fractionation associated with transhydrogenase activity could be constrained. At this point though, it appears to not overwhelm the effects of metabolic pathway in *E. coli*.

#### ***4.3 Differences between aerobic and anaerobic growth***

Our data indicate that the electron acceptor chosen for growth can make a significant difference in the isotopic fractionation of lipids, producing D-enrichments of up to 82 ‰ and D-depletions of -78 ‰ for pairwise cultures. However, it is not clear how the electron acceptor can exert influence over pools fed by central metabolism and intracellular water. Fatty acid abundance is comparable between aerobic and anaerobic cultures using the carbon source, and thus the observed trends cannot be attributed to shifts in relative abundance. A number of factors change between aerobic and anaerobic growth; the question here is which of those are relevant to hydrogen isotopic fractionation. Biological factors such as growth rate, phase, and nutrient stress have been previously shown to affect hydrogen isotopic fractionations. Changes in these parameters are evaluated in light of the recent data. Other factors that are known to change with terminal electron acceptor are free energy yield and electron transport pathway. While the

connections between these concepts and lipids are less direct, both have the potential to affect pools of reducing equivalents within the cell and will be evaluated in this context.

#### 4.3.1 Growth parameters

Changes in growth rate and stage have been shown previously to affect the isotopic composition of lipids in culturing studies (Kreuzer-Martin et al., 2006; Schouten et al., 2006; Zhang, Sachs, et al., 2009). These effects are on the order of ~30 ‰ which is significantly smaller than those for changing metabolic substrate, but are similar to the offsets seen between aerobic and anaerobic cultures. All cultures in this study were harvested at a similar growth stage (late exponential to early stationary phase) and thus this effect is not considered in the following discussion. One control sample was harvested well into stationary phase (PD\_LSP) and found to have similar hydrogen isotopic composition to the paired culture harvested with the rest of the samples. All cultures were grown under optimized conditions (temp, pH, nutrient replete) for the given substrate. These conditions did not change between aerobic vs. anaerobic cultures, and thus cannot be responsible for changes in fractionation. Growth rate, however, does vary significantly between the different microbes and conditions in this study, and the possible effect that this has on lipid isotopic composition is discussed below.

The slowest growing organism in this study was *D. autotrophicum*, with doubling times between 34 and 73 hours. *D. hydrogenophilus* grew comparatively rapidly with 16 hours doubling times under both autotrophic and heterotrophic conditions, far closer to rates observed for the facultative anaerobes. Despite the large range of doubling times, similar isotopic compositions are observed for all conditions. The two fastest doubling conditions (pyruvate and H<sub>2</sub>) are as different isotopically as the fastest from the slowest

(H<sub>2</sub> vs. glucose). The hydrogen cultures of the two sulfate reducers are virtually identical isotopically, despite a two-fold difference in growth rate. These observations and regression between the two data sets ( $R^2=0.54$ ) do not support a strong relationship between lipid isotopic composition and growth rate. Growth rate data from the facultative anaerobes are remarkably uncorrelated with lipid D/H fractionation ( $R^2 = 0.00213$ ). Both *E. coli* and *P. denitrificans* grew rapidly under most conditions, yet produce a large range in fractionation (See table 1). Growth rate cannot explain substrate level trends in facultative anaerobes as *E. coli* grew very rapidly with both lactate and glucose, but produced fractionations that differed by 100 %. Overall, growth rate accounts for little of the observed changes in fractionation.

#### 4.3.2 Free energy of reaction

The terminal electron acceptor contributes to the energetic yield of metabolic reactions. This effect is responsible for the classical trend in electron acceptor utilization with depth in marine sediment, and the reason that facultative anaerobes will use oxygen over nitrate when it is available. We might expect differences in energetic yield to influence the fluxes of metabolites through the cell, thereby contributing to hydrogen isotopic fractionation. Using basic principles of thermodynamics, we can calculate the free energy yield of metabolic reactions (Amend and Shock, 2001) following equation 2:

$$(2) \quad \Delta G^0 = \sum \Delta G_f^0 (\text{products}) - \sum \Delta G_f^0 (\text{reactants})$$

This exercise was performed at standard conditions pH 7, 25°C that are realistic for the cultures in this experiment. Table 2 presents calculations of free energy for balanced reactions of sulfate reducing, aerobic, denitrifying, and ammonifying

metabolisms used in this study. Each electron acceptor produces a distinct range of free energy per mole (electron acceptor) with sulfate ranging from -72 to -326 kJ/mole, oxygen ranging from -409 -479 kJ/mole, and nitrate ranging from -479 to -609 kJ/mole. When  $\Delta G^{0'}$  is normalized per mole of electrons and plotted against average fractionation, there is a weak negative correlation ( $R^2 = 0.49$ ) (Figure 9). Sulfate-reducing reactions are the least energetic and the lipids are the most D-depleted. Similarly, oxygen-reducing reactions are the most energetic and produce the most D-enriched lipids. However, chemoautotrophic metabolisms from *P. denitrificans* (open symbols) produce D-depleted lipids relative to heterotrophic cultures, despite similar energy yield, and lipids from ammonifying heterotrophic cultures of *E. coli* are similarly enriched to those from aerobic cultures, falling well off of the regression line. The different electron donors create the spread in fractionation for each group. Overall, there is little dependence of fractionation on free energy yield for a given electron acceptor.

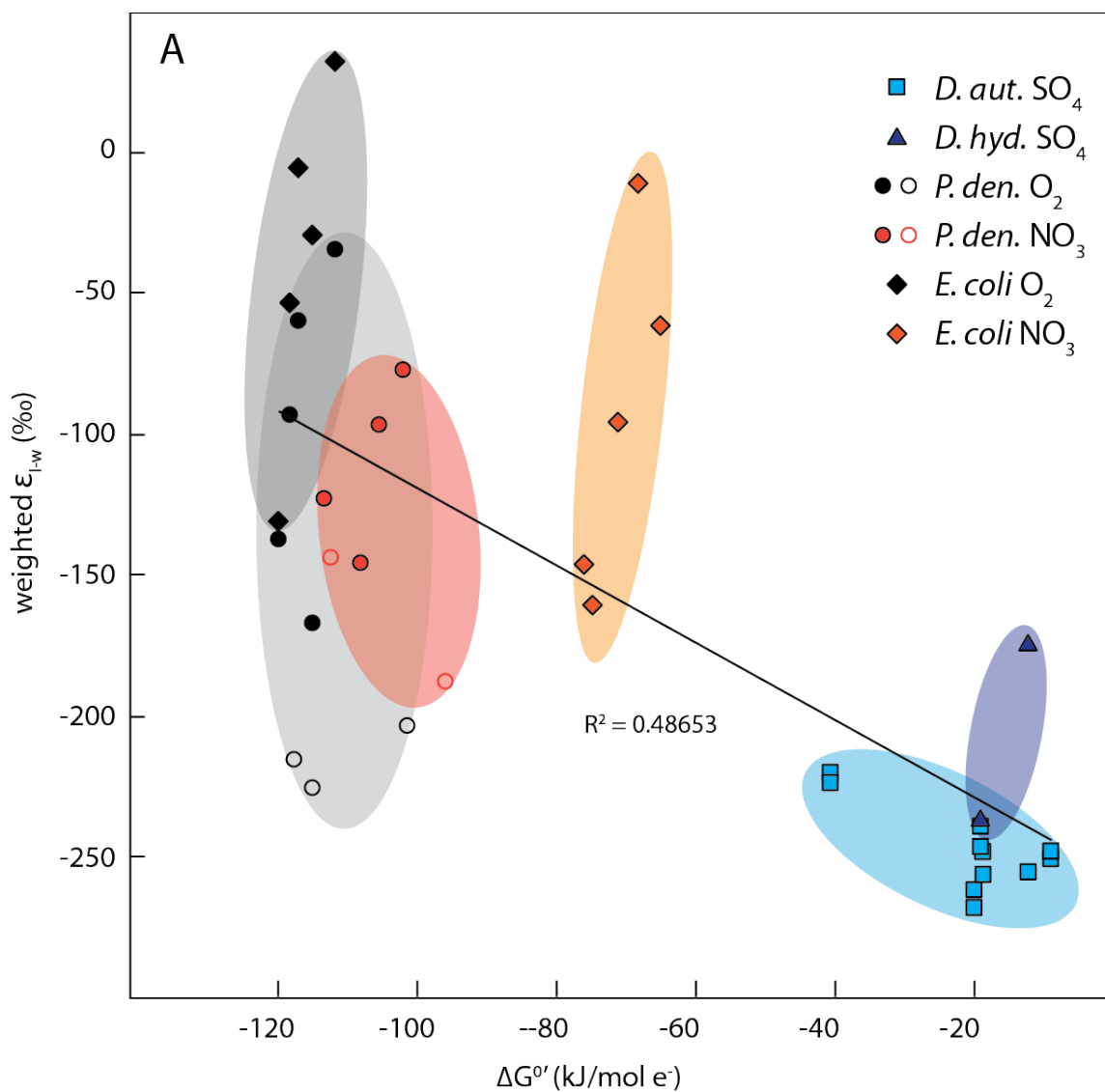


**Figure 9:** Comparison between free energy of reaction and net lipid fractionation. Calculations are shown per mole of electrons. Symbol shape corresponds to organism: *D. autotrophicum* (squares), *D. hydrogenophilus* (triangles), *E. coli* (diamonds), and *P. denitrificans* (circles). Shaded ellipses highlight data from a single electron acceptor and organism. In *P. denitrificans*, filled symbols indicate heterotrophic metabolisms where open symbols indicate autotrophic metabolisms. Colors indicate electron acceptor where blue, red/orange, and black tones correspond to sulfate, nitrate, and oxygen respectively.

### 4.3.3 *Electron transport*

Another biochemical system that varies by electron acceptor and organism is electron transport. Electron transport describes the route that electrons take from the electron donor to the terminal electron acceptor (TEA). While bacteria can utilize many organic substrates, few directly contribute to electron transfer, and instead NADH acts as the primary donor. Electrons are transferred from the donor to a variety of quinones and cytochrome complexes before serving to reduce the TEA (White, 2000). Coupling between electron transfer and proton pumping serves to produce the proton motive force that ultimately generates ATP. The specific molecules involved in electron transport depend on the TEA, and the number of protons per  $2e^-$  (or per O) for different transport systems varies significantly. We propose that this process could indirectly affect lipid isotopic composition in two ways. First, NADH serves as the donor, drawing down the pool of reducing equivalents and competing with transhydrogenases enzymes. Second, variation in pathway, number of electrons required to oxidize the donor, and charge produced per electron combine to influence the balance of NADPH-producing and NADPH-consuming reactions. This balance could affect lipid isotope composition through isotope effects associated with each reaction.

Electron transport has been studied extensively in *P. denitrificans* because of its similarity to the mitochondria, and will be used to illustrate the role of changing electron acceptor can play (Stouthamer, 1980; Ferguson, 1982; White, 2000; van Spanning et al., 2005). Under aerobic conditions, NADH, succinate, methanol, or methylamine can serve as electron donors each of which are directed to individual dehydrogenase enzymes. Succinate and NADH donate electrons to a ubiquinone and then into either a cytochrome

bc<sub>1</sub> complex followed by cyt. cbb<sub>3</sub>, or directly to cyt. bb<sub>3</sub>. In *P. denitrificans*, proton pumping (charge separation, q<sup>+</sup>/2e<sup>-</sup>) occurs at the cytochrome complexes and at the NADH dehydrogenase (van Spanning et al., 2005). The result of the scheme is that for NADH a total of 10 protons per 2e<sup>-</sup> are pumped whereas for succinate only, the maximum is 6 protons. Methanol induces the production of cytochrome aa<sub>3</sub> and, as a result, also can pump 10 protons per 2e<sup>-</sup> (van Spanning et al., 2005). Under anaerobic conditions, only NADH and succinate are possible donors to electron transport. While the transport chains proceed in the same path as aerobic growth up to the ubiquinone, subsequent flows branch to the nitrate reductase and the cyt. bc<sub>1</sub> complex. The only proton translocation sites in this network are the nitrate reductase (2), cyt. bc<sub>1</sub> (2), and NADH dehydrogenase (4). The resultant stoichiometry is 8q<sup>+</sup>/2e<sup>-</sup> for NADH and only 4q<sup>+</sup>/2e<sup>-</sup> for succinate. In short, more protons are pumped across the membrane for a given molecule during aerobic growth than during anaerobic growth. If the same level of ATP is required for similar growth rates, more electron donor will be required during anaerobic growth, potentially altering the flux of reducing equivalents to biosynthesis.

This type of analysis was repeated for the organisms and metabolism studied here and the q<sup>+</sup>/2e<sup>-</sup> ratio for each are reported in Table 2. *E. coli* also alters its electron transport chain in response to electron acceptor and overall differs from *P. denitrificans* in both aerobic and anaerobic electron stoichiometry (Unden and Bongaerts, 1997). This type of data is less well developed for the sulfate reducers and likely involves electron bifurcation (Strittmatter et al., 2009). At the very least, periplasmic hydrogenases would pump 8 protons, but this does not produce sufficient ATP to overcome energetic costs associate with sulfate reduction. Proton (or sodium) pumping is likely amended by

ferredoxin driven pumps or heterodisulfide reductases (Strittmatter et al., 2009). By combining the effects of electron donor, energetic potential ( $e^-$  required to oxidize fully), and the proton gradient created by a particular electron transport complex, one can calculate the moles of ATP produced by oxidizing a donor. While this metric is quite variable for the studied metabolisms (2.6 to 40), and certainly separates the data by metabolism, no significant relationship is observed with lipid fractionation (Figure 10). In conclusion, the energetic parameters evaluated here do not clearly explain the differences that we see in isotopes, but they do provide insight into how TEA choice might affect the flow of H through the cell.

Table 2: Free energy of specified metabolic reactions

Donor pair	Acceptor pair	Reaction	$\Delta G^{0'}/\text{mol}$ e-donor	$\Delta G^{0'}/\text{mol}$ e-accept.	e- donor	Mole s	$q^+ / 2e^-$ acc.
Ace/ CO <sub>2</sub>	SO <sub>4</sub> / H <sub>2</sub> S	CH <sub>3</sub> COOH + SO <sub>4</sub> <sup>2-</sup> + 2H <sup>+</sup> → 2CO <sub>2</sub> + H <sub>2</sub> S + 2H <sub>2</sub> O	-97.48	-97.48	8	1	8
Succ/ CO <sub>2</sub>	SO <sub>4</sub> / H <sub>2</sub> S	4C <sub>4</sub> H <sub>6</sub> O <sub>4</sub> + 7SO <sub>4</sub> <sup>2-</sup> + 22H <sup>+</sup> → 16CO <sub>2</sub> + 7H <sub>2</sub> S + 12H <sub>2</sub> O	-125.78	-71.88	14	1.75	8
Form/ CO <sub>2</sub>	SO <sub>4</sub> / H <sub>2</sub> S	4CHOOH + SO <sub>4</sub> <sup>2-</sup> + 2H <sup>+</sup> → 4CO <sub>2</sub> + H <sub>2</sub> S + 4H <sub>2</sub> O	-81.47	-325.87	2	0.25	8
Pyr/CO <sub>2</sub>	SO <sub>4</sub> / H <sub>2</sub> S	4CH <sub>3</sub> COCOOH + 5SO <sub>4</sub> <sup>2-</sup> + 10H <sup>+</sup> → 12CO <sub>2</sub> + 5H <sub>2</sub> S + 8H <sub>2</sub> O	-187.6	-150.1	10	1.25	8
Glu/ CO <sub>2</sub>	SO <sub>4</sub> / H <sub>2</sub> S	C <sub>6</sub> H <sub>12</sub> O <sub>6</sub> + 3SO <sub>4</sub> <sup>2-</sup> + 6H <sup>+</sup> → 6CO <sub>2</sub> + 3H <sub>2</sub> S + 6H <sub>2</sub> O	-483.45	-161.15	24	3	8
H <sub>2</sub> / H <sub>2</sub> O	SO <sub>4</sub> / H <sub>2</sub> S	4H <sub>2</sub> + SO <sub>4</sub> <sup>2-</sup> + 2H <sup>+</sup> → H <sub>2</sub> S + 4H <sub>2</sub> O	-38.11	-152.43	2	0.25	8
Ace/ CO <sub>2</sub>	O <sub>2</sub> /H <sub>2</sub> O	CH <sub>3</sub> COOH + 2O <sub>2</sub> → 2CO <sub>2</sub> + 2H <sub>2</sub> O	-894	-447	8	2	10 (8)
Succ/ CO <sub>2</sub>	O <sub>2</sub> /H <sub>2</sub> O	2C <sub>4</sub> H <sub>6</sub> O <sub>4</sub> + 7O <sub>2</sub> + 4H <sup>+</sup> → 8CO <sub>2</sub> + 7H <sub>2</sub> O	-1638	-468	14	3.5	6-10 (8)
Pyr/CO <sub>2</sub>	O <sub>2</sub> /H <sub>2</sub> O	2CH <sub>3</sub> COCOOH + 5O <sub>2</sub> → 6CO <sub>2</sub> + 4H <sub>2</sub> O	-1183	-473	10	2.5	10 (8)
Lac/ CO <sub>2</sub>	O <sub>2</sub> /H <sub>2</sub> O	C <sub>3</sub> H <sub>5</sub> O <sub>3</sub> H + 3O <sub>2</sub> → 3CO <sub>2</sub> + 3H <sub>2</sub> O	-1377	-459	12	3	10 (8)
Glu/ CO <sub>2</sub>	O <sub>2</sub> /H <sub>2</sub> O	C <sub>6</sub> H <sub>12</sub> O <sub>6</sub> + 6O <sub>2</sub> → 6CO <sub>2</sub> + 6H <sub>2</sub> O	-2872	-479	24	6	10 (8)
S <sub>2</sub> O <sub>3</sub> / SO <sub>4</sub>	O <sub>2</sub> /H <sub>2</sub> O	S <sub>2</sub> O <sub>3</sub> <sup>2-</sup> + 2O <sub>2</sub> + H <sub>2</sub> O → 2SO <sub>4</sub> <sup>2-</sup> + 2H <sup>+</sup>	-818	-409	8	2	2.5
MeOH/ CO <sub>2</sub>	O <sub>2</sub> /H <sub>2</sub> O	2CH <sub>3</sub> OH + 3O <sub>2</sub> → 2CO <sub>2</sub> + 4H <sub>2</sub> O	-693	-462	6	1.5	10
H <sub>2</sub> / H <sub>2</sub> O	O <sub>2</sub> /H <sub>2</sub> O	2H <sub>2</sub> + O <sub>2</sub> → 2H <sub>2</sub> O	-237	-474	2	0.5	10
Ace/ CO <sub>2</sub>	NO <sub>3</sub> /N <sub>2</sub>	5CH <sub>3</sub> COOH + 8NO <sub>3</sub> <sup>-</sup> + 8H <sup>+</sup> → 10CO <sub>2</sub> + 4N <sub>2</sub> + 14H <sub>2</sub> O	-842	-526	8	1.6	8

Succ/ CO <sub>2</sub>	NO <sub>3</sub> /N <sub>2</sub>	$5C_4H_6O_4 + 14NO_3^- + 24H^+ \rightarrow 20CO_2 + 7N_2 + 22H_2O$	-1428	-510	14	2.8	4-8
Lac/ CO <sub>2</sub>	NO <sub>3</sub> /N <sub>2</sub>	$5C_3H_5O_3H + 12NO_3^- + 12H^+ \rightarrow 15CO_2 + 6N_2 + 21H_2O$	-1299	-541	12	2.4	8
Glu/ CO <sub>2</sub>	NO <sub>3</sub> /N <sub>2</sub>	$5C_6H_{12}O_6 + 24NO_3^- + 24H^+ \rightarrow 30CO_2 + 12N_2 + 42H_2O$	-2716	-566	24	4.8	8
S <sub>2</sub> O <sub>3</sub> / SO <sub>4</sub>	NO <sub>3</sub> /N <sub>2</sub>	$5S_2O_3^{2-} + 8NO_3^- + H_2O \rightarrow 10SO_4^{2-} + 4N_2 + 2H^+$	-766	-479	8	1.6	2.5
H <sub>2</sub> / H <sub>2</sub> O	NO <sub>3</sub> /N <sub>2</sub>	$5H_2 + 2NO_3^- + 2H^+ \rightarrow N_2 + 6H_2O$	-224	-560	2	0.4	8
Ace/ CO <sub>2</sub>	NO <sub>3</sub> / NH <sub>4</sub>	$NO_3^- + CH_3COOH + 2H^+ \rightarrow NH_4^+ + 2CO_2 + H_2O$	-545	-545	8	1	6
Succ/ CO <sub>2</sub>	NO <sub>3</sub> / NH <sub>4</sub>	$4C_4H_6O_4 + 7NO_3^- + 22H^+ \rightarrow 7NH_4^+ + 16CO_2 + 5H_2O$	-909	-519	14	1.75	6
Pyru/CO <sub>2</sub>	NO <sub>3</sub> / NH <sub>4</sub>	$4CH_3COCOOH + 5NO_3^- + 10H^+ \rightarrow 5NH_4^+ + 12CO_2 + 3H_2O$	-747	-598	10	1.25	6
Lac/ CO <sub>2</sub>	NO <sub>3</sub> / NH <sub>4</sub>	$2C_3H_5O_3H + 3NO_3^- + 6H^+ \rightarrow 6CO_2 + 3NH_4^+ + 3H_2O$	-854	-569	12	1.5	6
Gluc/ CO <sub>2</sub>	NO <sub>3</sub> / NH <sub>4</sub>	$C_6H_{12}O_6 + 3NO_3^- + 6H^+ \rightarrow 6CO_2 + 3NH_4^+ + 3H_2O$	-1826	-609	24	3	6

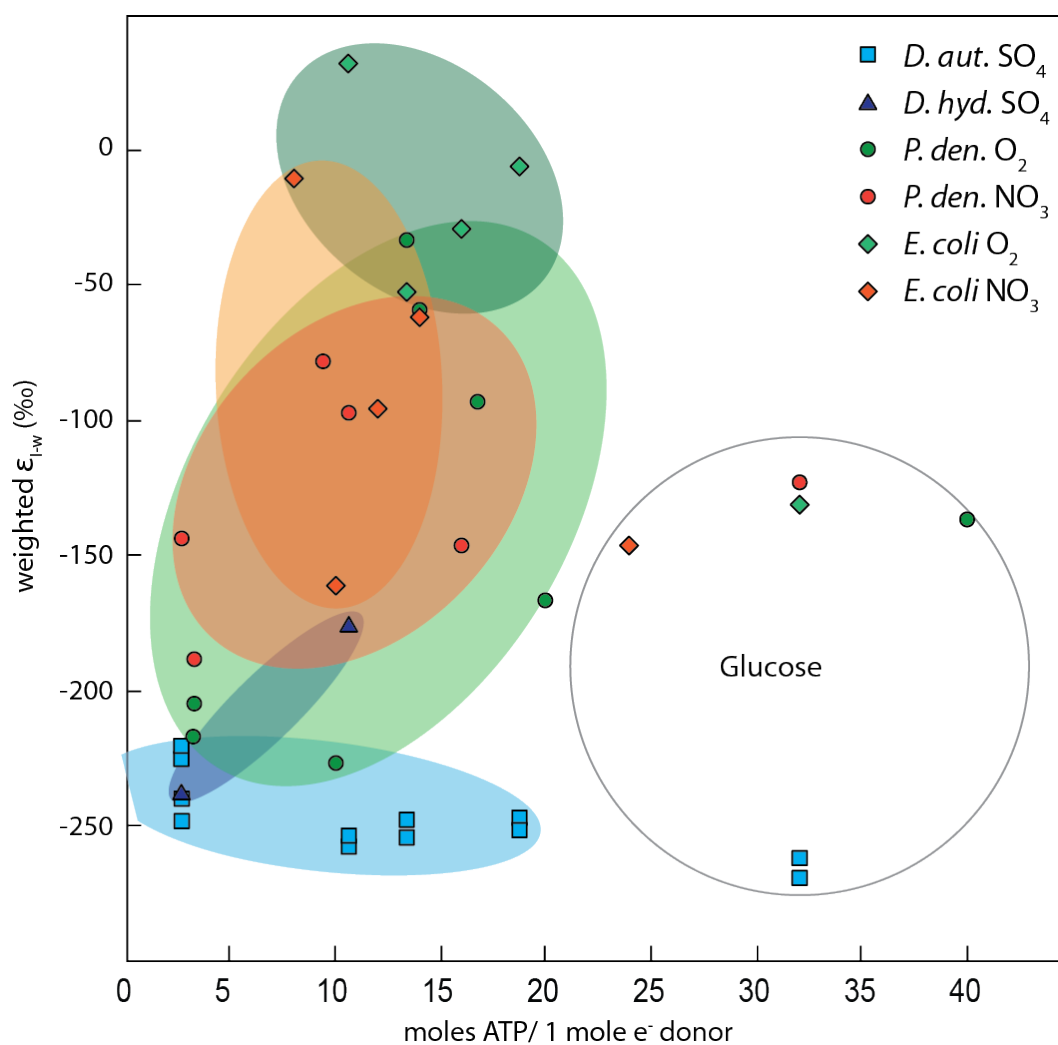


**Figure 10:** Comparison of energetic yield for electron donor (plotted as possible ATP/ mole electron donor) and weighted lipid water fractionation for all cultures. Transparent ellipses encompass data from each organism with colors indicating electron acceptors.

#### ***4.4 The current picture of D/H fractionation by metabolism***

Zhang et al. (2009) present a framework of metabolism-based effects on lipid D/H that distinguishes autotrophs and heterotrophs, and subdivides heterotrophs based on specific central metabolic pathway. A goal of the current research is to evaluate how these trends change for anaerobic metabolisms. This step is critical for understanding the fractionations present in the environment and constraining the interpretation of isotopic data.

Hydrogen isotopic data from the two sulfate reducers in this study do not exhibit a clear distinction between autotrophic and heterotrophic metabolisms. Lipids from autotrophic cultures are consistent between the two bacteria and overlap isotopically with the ranges previously presented for photoautotrophs and the upper end (of the range of data) of chemoautotrophs (Figure 11). New isotopic data from experiments with heterotrophic sulfate reducing bacteria span the entire range of fractionation produced in experiments with autotrophs. *D. autotrophicum* and *D. hydrogenophilus* have fundamentally different carbon metabolic pathways (Acetyl-CoA vs. TCA cycle), which perhaps makes it surprising how similar they are isotopically. For these organisms and culture conditions, the carbon-fixation pathway apparently does not influence H-isotope fractionations. These strains do share a number of physiological features including slow growth rates, low free-energy yield, and unusual electron transport mechanisms. It is not yet clear which, if any, of these parameters affect the final hydrogen isotopic composition.

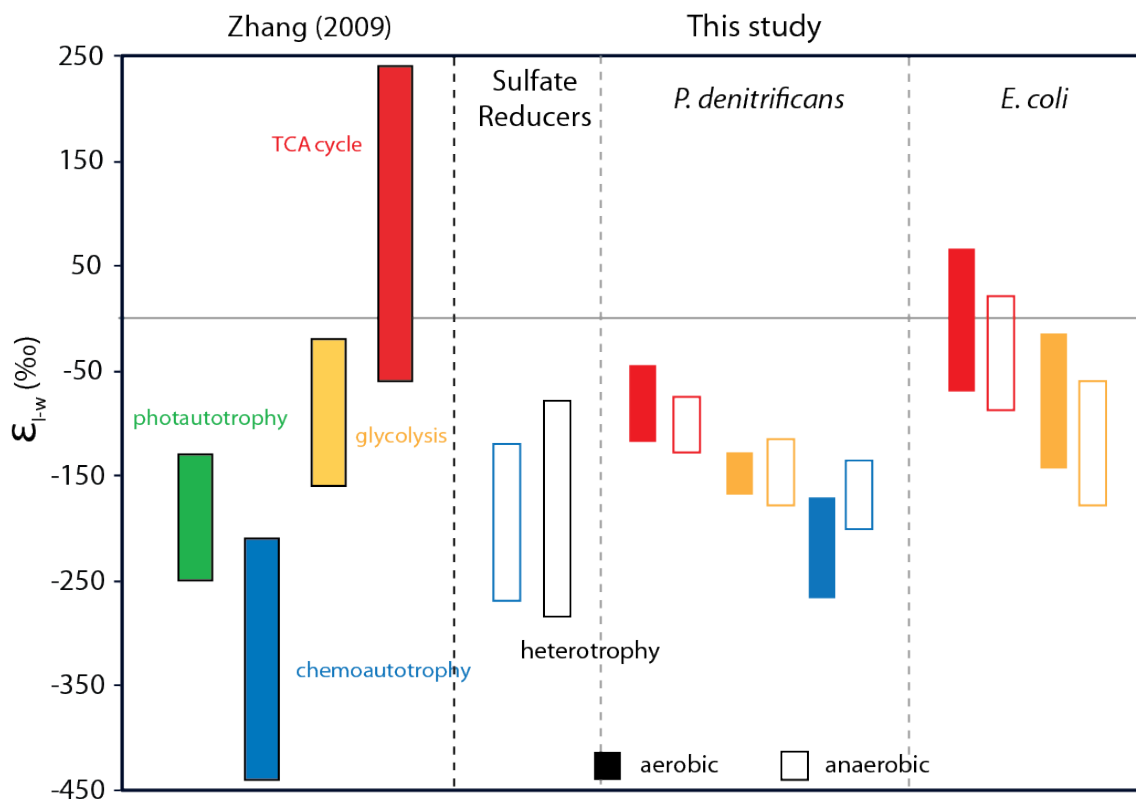


**Figure 11:** Summary of fractionation ranges produced by different metabolisms found Zhang et al. (2009) and this study.

Facultative anaerobes appear to produce fractionations that are similar to those observed previously. Ranges of isotopic fractionation for both aerobic and anaerobic growth of *P. denitrificans* and *E. coli* are summarized in Figure 11. For both strains, fractionations produced by aerobic and anaerobic cultures using the same major pathway scale with one another. However, data from anaerobic cultures are often offset from those of aerobes. Strains using the glycolytic pathway (or Entner Doudoroff in the case of *P. denitrificans*) produce lipids whose isotopic compositions are very similar to the previously reported range (Figure 11). Cultures using TCA cycle intermediates produce similar fractionations as in previous studies, but are overall slightly more depleted and

overlap significantly with the glycolytic range. Lipids produced during chemoautotrophic growth of *P. denitrificans* are depleted relative to heterotrophic experiments, but not to same extreme as would have been predicted previously. Anaerobic chemoautotrophic experiments produced D-enriched lipids relative to aerobic experiments, further weakening the depleted signal and overlapping significantly with the range in fractionation previously reported for glycolysis. Overall, the trends are similar to those previously reported, but boundaries between groups are less defined and previous extremes are not achieved in anaerobic cultures.

## 5. Conclusions

This study reveals (at least) two distinct trends in hydrogen isotopic fractionation divided between sulfate reducers and facultative anaerobes. The sulfate reducers produce very D-depleted lipids, regardless of growth substrate. The distinction between autotrophic and heterotrophic growth observed by Zhang et al. (2009), appears to have been a coincidence of the metabolic pathways utilized by the microbes in the original study. From our data, it is clear that utilization of heterotrophic substrates can produce lipids that match or exceed D-depletions observed from autotrophic growth. It is not clear, at this point, if the divergence from previously reported trends shown for these sulfate reducers is the an exception or the rule for strict anaerobes, and further work will be required to understand the mechanism of these changes.

For facultative anaerobes, data are consistent with the hypothesis that central metabolic pathway is the dominant controlling factor on lipid  $\delta D$  values. Second order trends overprint these values producing variation away from primary trends. For most

heterotrophic experiments, anaerobic cultures were D-depleted relative to aerobic ones, whereas in autotrophic experiments the trend was reversed. Changes in water incorporation, free energy yield, and electron transport chain are associated with anaerobic growth, but none can sufficiently account for the observed trends. For the moment, the mechanism of this variability remains elusive.

### **Acknowledgements**

We would like to thank Jared Leadbetter, Jake Waldbauer, and Victoria Orphan for initial guidance and use of laboratory facilities, the ARS culture collection for strain access, and Sebastian Kopf for helpful discussions. Funding for the project was supplied to MRO as an NSF GRFP.

### **See Appendix for B for Supplementary data**

Table B1: Lipid composition

Table B2: Isotopes

## References

- Amend, J., Shock, E., 2001. Energetics of overall metabolic reactions of thermophilic and hyperthermophilic Archaea and Bacteria. *FEMS Microbiology Reviews* 25, 175–243.
- Brandis-Heep, A., Gebhardt, N.A., Thauer, R.K., Widdel, F., Pfennig, N., 1983. Anaerobic acetate oxidation to CO<sub>2</sub> by *Desulfobacter postgatei*. *Archives of Microbiology* 136, 222–229.
- Breznak, J.A., Leadbetter, J.R., 2006. Termite Gut Spirochetes. In: Dworkin, M., Falkow, S., Rosenberg, E., Schleifer, K.-H., Stackebrandt, E. (Eds.), *The Prokaryotes*. Springer New York, pp. 318–329.
- Chikaraishi, Y., Naraoka, H., 2001. Organic hydrogen-carbon isotope signatures of terrestrial higher plants during biosynthesis for distinctive photosynthetic pathways. *Geochemical Journal* 451–458.
- Chikaraishi, Y., Naraoka, H., 2005.  $\delta^{13}\text{C}$  and  $\delta\text{D}$  identification of sources of lipid biomarkers in sediments of Lake Haruna (Japan). *Geochimica et Cosmochimica Acta* 69, 3285–3297.
- Chikaraishi, Y., Tanaka, R., Tanaka, A., Ohkouchi, N., 2009. Fractionation of hydrogen isotopes during phytol biosynthesis. *Organic Geochemistry* 40, 569–573.
- Dowling, N.J., Widdel, F., White, D., 1986. Phospholipid Ester-linked Fatty Acid Biomarkers of Acetate-oxidizing Sulphate-reducers and Other Sulphide-forming Bacteria. *Journal of General Microbiology* 132, 1815–1825.
- Ferguson, S., 1982. Aspects of the control and organization of bacterial electron transport. *Biochemical Society Transactions* 10, 198–200.
- Friedrich, B., Schwartz, E., 1993. Molecular biology of hydrogen utilization in aerobic chemolithotrophs. *Annual Review of Microbiology* 47, 351–383.
- Friedrich, C., Mitrenga, G., 1981. Oxidation of thiosulfate by *Paracoccus denitrificans* and other hydrogen bacteria. *FEMS Microbiology Letters* 10, 209–212.
- Griffiths, D.E.D., Roberton, A.M.A., 1966. Energy-linked reactions in mitochondria: studies on the mechanism of the energy-linked transhydrogenase reaction. *Biochimica et Biophysica Acta (BBA) - Bioenergetics* 118, 453–464.
- Hayes, J.M., 2001. Fractionation of Carbon and Hydrogen Isotopes in Biosynthetic Processes. *Reviews in Mineralogy and Geochemistry* 43, 225–277.
- Huang, Y., Shuman, B., Wang, Y., Webb, T., III, 2002. Hydrogen isotope ratios of palmitic acid in lacustrine sediments record late Quaternary climate variations. *Geology* 30, 1103–1106.
- Jones, A.A., Sessions, A.L., Campbell, B.J., Li, C., Valentine, D.L., 2008. D/H ratios of fatty acids from marine particulate organic matter in the California Borderland Basins. *Organic Geochemistry* 39, 485–500.
- Kreuzer-Martin, H.W., Lott, M.J., Ehleringer, J.R., Hegg, E.L., 2006. Metabolic Processes Account for the Majority of the Intracellular Water in Log-Phase *Escherichia coli* Cells As Revealed by Hydrogen Isotopes. *Biochemistry* 45, 13622–13630.
- Li, C., Sessions, A.L., Kinnaman, F., Valentine, D.L., 2009. Hydrogen-isotopic variability in lipids from Santa Barbara Basin sediments. *Geochimica et Cosmochimica Acta* 73, 4803–4823.
- Londry, K.L., Marais, Des, D.J., 2003. Stable Carbon Isotope Fractionation by Sulfate-Reducing Bacteria. *Applied and Environmental Microbiology* 69, 2942–2949.

- Muyzer, G., Stams, A.J.M., 2008. The ecology and biotechnology of sulphate-reducing bacteria. *Nature Reviews Microbiology*.
- Osburn, M., 2011. *Thermogladius shockii* gen. nov., sp. nov., a hyperthermophilic crenarchaeote from Yellowstone National Park, USA. *Archives of Microbiology*.
- Osburn, Sessions, Spear, 2011. Hydrogen-isotopic variability in fatty acids from Yellowstone National Park hot spring microbial communities. *Geochimica et Cosmochimica Acta* 75, 4830–4845.
- Pu, Z., Weiguo, L., 2011. Effect of plant life form on relationship between  $\delta D$  values of leaf wax n-alkanes and altitude along Mount Taibai, China. *Organic Geochemistry* 42, 100–107.
- Rodríguez-Ruiz, J., Belarbi, E.-H., Sánchez, J.L.G., Alonso, D.L., 1998. Rapid simultaneous lipid extraction and transesterification for fatty acid analyses. *Biotechnology techniques* 12, 689–691.
- Romero-Viana, L., Kienel, U., Wilkes, H., Sachse, D., 2013. Growth-dependent hydrogen isotopic fractionation of algal lipid biomarkers in hypersaline Isabel Lake (Mexico). *Geochimica et Cosmochimica Acta* 106, 490–500.
- Sachse, D., Billault, I., Bowen, G.J., Chikaraishi, Y., Dawson, T.E., Feakins, S.J., Freeman, K.H., Magill, C.R., McInerney, F.A., Van der Meer, M.T., 2012. Molecular paleohydrology: interpreting the hydrogen-isotopic composition of lipid biomarkers from photosynthesizing organisms. *Annual Review of Earth and Planetary Sciences* 40, 221–249.
- Sachse, D., Sachs, J., 2008. Inverse relationship between D/H fractionation in cyanobacterial lipids and salinity in Christmas Island saline ponds. *Geochimica et Cosmochimica Acta* 72, 793–806.
- Sauer, P.E., Eglinton, T.I., Hayes, J.M., Schimmelmann, A., Sessions, A.L., 2001. Compound-specific D/H ratios of lipid biomarkers from sediments as a proxy for environmental and climatic conditions. *Geochimica et Cosmochimica Acta* 65, 213–222.
- Sauer, U., Canonaco, F., Heri, S., Perrenoud, A., Fischer, E., 2003. The Soluble and Membrane-bound Transhydrogenases UdhA and PntAB Have Divergent Functions in NADPH Metabolism of *Escherichia coli*. *Journal of Biological Chemistry* 279, 6613–6619.
- Schauder, R., Eikmanns, B., Thauer, R.K., Widdel, F., Fuchs, G., 1986. Acetate oxidation to  $CO_2$  in anaerobic bacteria via a novel pathway not involving reactions of the citric acid cycle. *Archives of Microbiology* 145, 162–172.
- Schauder, R., Widdel, F., Fuchs, G., 1987. Carbon assimilation pathways in sulfate-reducing bacteria II. Enzymes of a reductive citric acid cycle in the autotrophic *Desulfobacter hydrogenophilus*. *Archives of Microbiology* 148, 218–225.
- Schouten, S., Ossebaar, J., Schreiber, K., Kienhuis, M., Langer, G., Benthien, A., Bijma, J., 2006. The effect of temperature, salinity and growth rate on the stable hydrogen isotopic composition of long chain alkenones produced by *Emiliana huxleyi* and *Gephyrocapsa oceanica*. *Biogeosciences* 3, 113–119.
- Sessions, A., Hayes, J., 2005. Calculation of hydrogen isotopic fractionations in biogeochemical systems. *Geochimica et Cosmochimica Acta* 69, 593–597.
- Sessions, A.L., Burgoyne, T.W., Schimmelmann, A., Hayes, J.M., 1999. Fractionation of hydrogen isotopes in lipid biosynthesis. *Organic Geochemistry* 30, 1193–1200.

- Shapleigh, J.P., 2006. The Prokaryotes. Springer New York.
- Stouthamer, A., 1980. Bioenergetic studies on *Paracoccus denitrificans*. Trends in biochemical sciences 5, 164–166.
- Strittmatter, A.W., Liesegang, H., Rabus, R., Decker, I., Amann, J., Andres, S., Henne, A., Fricke, W.F., Martinez-Arias, R., Bartels, D., Goesmann, A., Krause, L., Pühler, A., KLENK, H.-P., Richter, M., Schüler, M., Glöckner, F.O., Meyerdierks, A., Gottschalk, G., Amann, R., 2009. Genome sequence of *Desulfobacterium autotrophicum* HRM2, a marine sulfate reducer oxidizing organic carbon completely to carbon dioxide. Environmental Microbiology 11, 1038–1055.
- Taylor, J., Parkes, R.J., 1983. The Cellular Fatty Acids of the Sulphate-reducing Bacteria, *Desulfobacter* sp., *Desulfobulbus* sp. and *Desulfovibrio desulfuricans*. Microbiology 129, 3303–3309.
- Uden, G., Bongaerts, J., 1997. Alternative respiratory pathways of *Escherichia coli*: energetics and transcriptional regulation in response to electron acceptors. Biochimica et Biophysica Acta 1320, 217–234.
- Valentine, D.L., 2009. Isotopic remembrance of metabolisms past. PNAS 106, 12565–12566.
- van Spanning, R.J.M., de Boer, A., Reijnders, W.N.M., De Gier, J.L., DeLorme, C.O., Stouthamer, A., Hans V Westerhoff, Harms, N., van der Oost, J., 2005. Regulation of oxidative phosphorylation: The flexible respiratory network of *Paracoccus denitrificans*. Journal of Bioenergetics and Biomembranes 27, 499–511.
- White, D., 2000. The physiology and biochemistry of prokaryotes, Oxford University Press.
- White, S.W., Zheng, J., Zhang, Y.-M., Rock, C.O., 2005. The Structural Biology of Type II Fatty Acid Biosynthesis. Annual Review of Biochemistry 74, 791–831.
- Widdel, F., 1987. New types of acetate oxidizing, sulfate-reducing *Desulfobacter* species, *D. hydrogenophilus* sp. nov., *D. latus* sp. nov., and *D. curvatus* sp. nov. Archives of Microbiology 148, 286–291.
- Zhang, X., Gillespie, A., Sessions, A.L., 2009. Large D/H variations in bacterial lipids reflect central metabolic pathways. PNAS 106, 1–7.
- Zhang, Z., Sachs, J.P., Marchetti, A., 2009. Hydrogen isotope fractionation in freshwater and marine algae: II. Temperature and nitrogen limited growth rate effects. Organic Geochemistry 40, 428–439.

*Part 2:*

Characterization of the Ediacaran Khufai Formation

### *Chapter 3*

Accepted for publication in *AAPG bulletin*, 2013

**Facies, Stratigraphy, and Evolution of a Middle Ediacaran carbonate ramp: Khufai  
Formation, Sultanate of Oman**

Magdalena Osburn<sup>1\*</sup>, John Grotzinger<sup>1</sup>, Kristin Bergmann<sup>1</sup>

<sup>1</sup> California Institute of Technology, 1200 E. California Blvd, Pasadena CA 91125

*\*corresponding author; [maggie@gps.caltech.edu](mailto:maggie@gps.caltech.edu)*

## **Abstract**

The Khufai Formation is the oldest carbonate platform of the Cryogenian to earliest Cambrian Huqf Supergroup. A stratigraphic characterization of this unit includes detailed facies descriptions, a sequence stratigraphic model, and evaluation of lateral heterogeneity and overall ramp evolution. The Khufai Formation comprises one and a half depositional sequences with a maximum flooding interval near the base of the formation and a sequence boundary within the upper peritidal facies. The majority of deposition occurred during highstand progradation of a carbonate ramp. Facies tracts include outer-ramp and mid-ramp mudstones and wackestones, ramp crest grainstone shoals, and extensive inner-ramp, microbially-dominated peritidal deposits. Outcrops in the Oman Mountains are deep-water deposits including turbiditic grainstone and wackestone interbedded with siliciclastic-rich siltstone and crinkly laminite. Facies patterns and parasequence composition are variable both laterally across the outcrop area and vertically through time due to a combination of ramp morphology, siliciclastic supply, and possible syndepositional faulting. The lithostratigraphic boundary between the Khufai Formation and the overlying Shuram Formation is gradational and represents significant flooding of the carbonate platform. The stratigraphic characterization presented here along with identification of key facies and diagenetic features will help further future exploration and production of hydrocarbons from the Khufai Formation.

## **Introduction**

Neoproterozoic strata of Oman provide an exceptionally complete and well-preserved sedimentary record of a highly variable period in Earth history. Recorded in these

sediments are two of the proposed “Snowball Earth” glaciations, the largest carbon isotopic excursion in Earth history, the origination of Ediacaran calcified metazoans, and the Precambrian/Cambrian boundary (Burns and Matter, 1993; Wood et al., 2002; Allen, 2007; Bowring et al., 2007). In addition, the Huqf Supergroup hosts the oldest commercially viable hydrocarbon system with producing reservoirs in the latest Ediacaran/earliest Cambrian rocks (Al-Siyabi, 2005).

Regional stratigraphic surveys of the Huqf Supergroup provide a basic understanding of the depositional setting, and chemostratigraphic studies document concurrent changes in marine chemistry and enhance regional stratigraphic correlation (Wright et al., 1990; Burns and Matter, 1993; McCarron, 1999; Halverson, 2005; Fike et al., 2006; Le Guerroue et al., 2006a; Fike and Grotzinger, 2008). Considerable attention was devoted to understanding the older siliciclastic Masirah Bay Formation shelf sequence (Allen and Leather, 2006), the overlying Shuram Formation (Le Guerroue et al., 2006a), and the younger Buah Formation carbonate ramp (Cozzi and Grotzinger, 2004; Cozzi et al., 2004). Conversely relatively little is known about Khufai Formation development, beyond its inclusion in regional surveys (Gorin et al., 1982; Wright et al., 1990; McCarron, 1999).

A firm understanding of sedimentological and stratigraphic context is necessary for evaluation of both geochemical measurements and the potential for hydrocarbon exploration. We have undertaken this study to better understand the processes, environment, and timescale of Khufai Formation deposition. This paper presents an analysis of the facies distributions from both platform and distal sections along with a detailed sequence stratigraphic interpretation of the Khufai Formation. We will evaluate

the stratigraphic position and extent of depositional hiatuses in the terminal Khufai Formation to better interpret chemostratigraphic records. In addition, the presentation of key facies and facies relationships in stratigraphic context will provide a valuable framework for future hydrocarbon exploration and development.

### **Geological Setting**

The Huqf Supergroup is a sequence of Cryogenian to early Cambrian sedimentary rocks, deposited on Archean to Neoproterozoic crystalline basement (Allen, 2007; Bowring et al., 2007). Huqf strata outcrop in four main areas including the Huqf-Haushi uplift and Mirbat areas of central and southern Oman, and near Jebel Akhdar and Saih Hatat in the Oman mountains (Figure 1). The Huqf Supergroup comprises, in ascending order, the Abu Mahara, Nafun, and Ara Groups representing glaciomarine sediments, marine siliciclastics and carbonates, and carbonates cyclically interstratified with sulfate and halite evaporites, respectively. The Nafun Group was further subdivided (Figure 2) into the successive Hadash, Masirah Bay, Khufai, Shuram, and Buah formations (Gorin et al., 1982; Wright et al., 1990; Forbes et al., 2010). The Hadash Formation is a thin dolostone capping the Ghadir Manquil (Marinoan) glacial sediments, but is included in the Nafun Group. The overlying four units comprise two large siliciclastic-to-carbonate cycles; where the Masirah Bay and Shuram formations contain primarily siltstone and sandstone with minor carbonate, and the Khufai and Buah formations contain primarily carbonate facies with subordinate siliciclastic components (Forbes et al., 2010). The Nafun Group is well exposed on the Huqf-Haushi uplift (Huqf area) and in the Wadis of Jebel Akhdar.

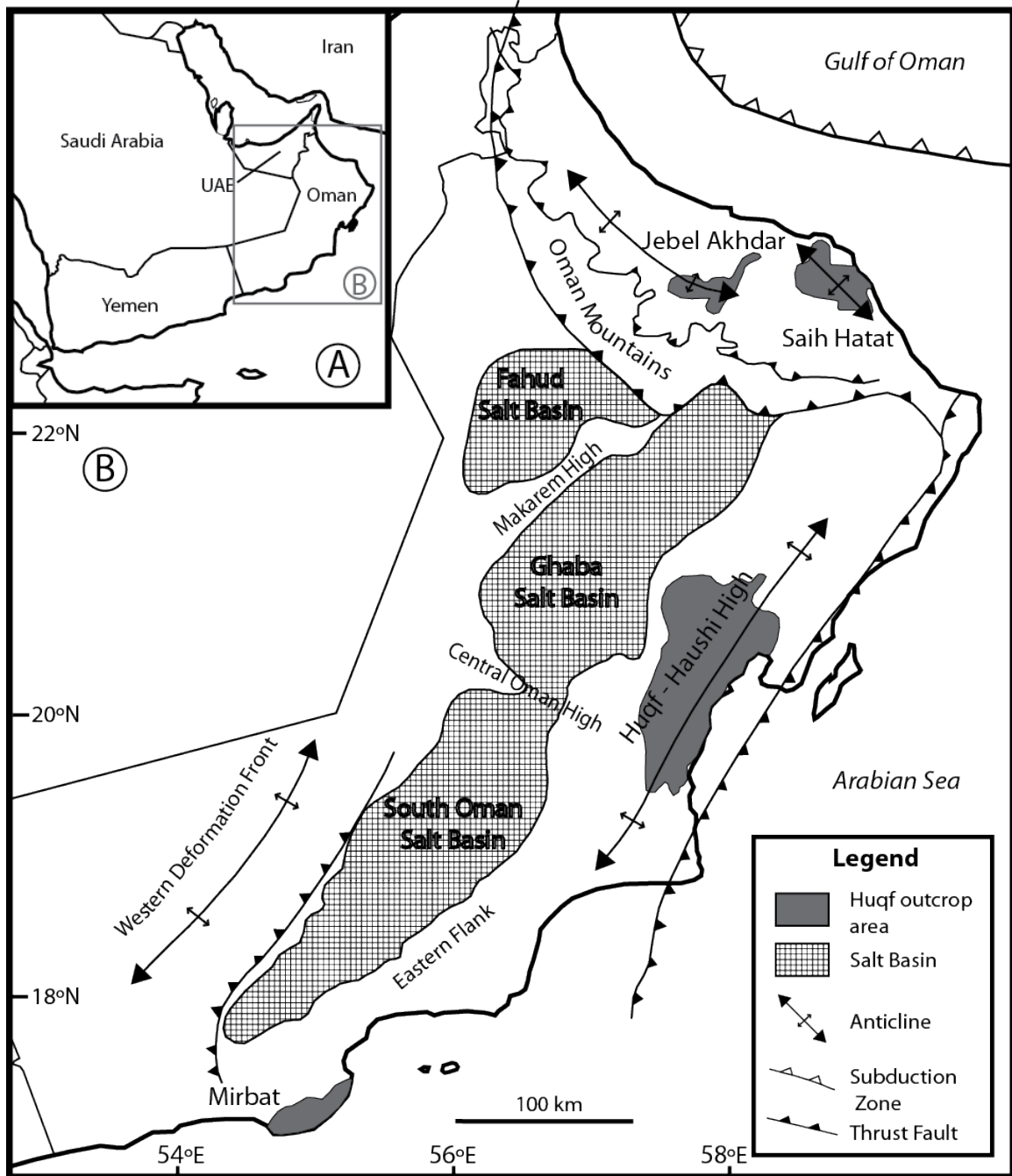


**Figure 1:** Regional map of Oman illustrating the outcrop localities for the Huqf Supergroup, regional tectonic features, and salt basins. Adapted from Bowring et al. (2007).

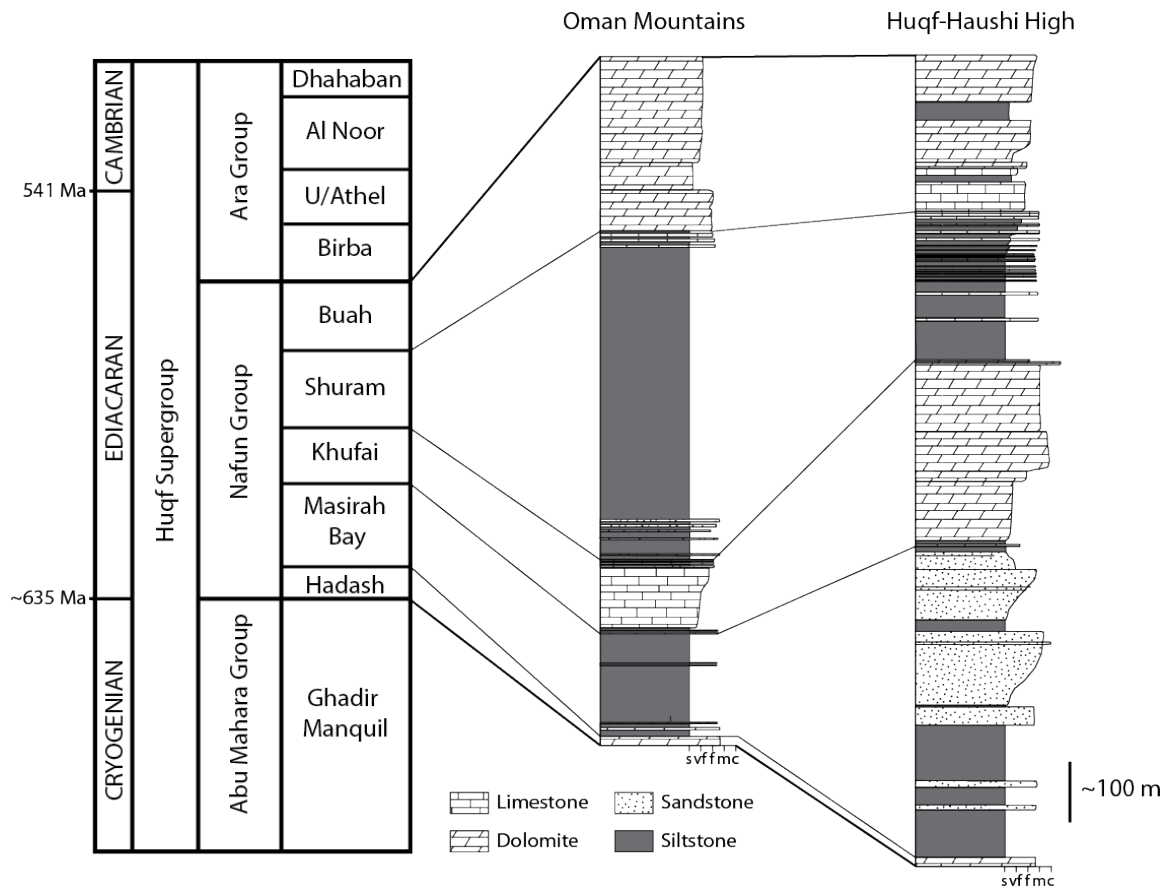


**Figure 2:** Stratigraphic nomenclature for the Huqf Supergroup. Basic lithostratigraphic logs of the Nafun group in the Huqf-Haushi High and Oman Mountain areas. Adapted from Forbes (2010), Bowring (2007), McCarron (1999), and Allen and Leather (2006).

### *Age control and tectonic setting*

The absolute ages of the Abu Mahara and Ara groups are relatively well constrained by U-Pb dating, but there are few chronostratigraphic constraints in the intervening Nafun Group. The Abu Mahara Group is deposited on approx. 824 Ma granodioritic basement (Bowring et al., 2007). A tuffaceous sandstone within the Ghubrah Member of the lower Abu Mahara Group was deposited ~713 Ma (Bowring et al., 2007), revising upward a previous date of 723 +16/-10 Ma (Brasier et al., 2000). A

population of zircons from well Lahan-1 gives a maximum age constraint of 645 Ma for the latest glacial deposits. Furthermore, global correlation with glacial events suggest a correlative date of the Hadash cap carbonate of ~635 Ma (Bowring et al., 2007). The Ara Group has a number of ash beds ranging in age from  $546 \pm 0.21$  Ma in the A0 interval, to  $541.00 \pm 0.13$  Ma in the A4C (Bowring et al., 2007). While there are no known ash beds in the Nafun Group, interpolation of sedimentation rates from well-dated sections of the upper Buah and Ara formations were extrapolated to give an approximate age of the basal Shuram Formation of 554 to 562 Ma. This analysis assumed a significant depositional hiatus at the Khufai-Shuram Boundary, and thus does not constrain the age of the Khufai Formation.

The tectonic setting of the Nafun Group is also not well constrained. A suture zone in Yemen and arc related volcanic basement of the Huqf suggests accretion of the Oman terrain onto the Arabian-Nubian plate prior to the deposition of Nafun strata. The Abu Mahara sediments and volcanics accumulated in extensional basins whereas subsequent sedimentary deposition was regionally extensive and suggestive of relative tectonic quiescence (Allen, 2007). Accommodation for the Nafun Group was created primarily through thermal-contraction of the crust in a passive margin sequence (Allen, 2007). Others have argued that this mechanism is insufficient to accommodate the whole of the Nafun Group and suggest dynamic lithospheric depression related to subduction (Grotzinger and Amthor, 2002; Grotzinger et al., 2002). Significant transtensional tectonic and volcanic activity resumed during Ara time, creating the South Oman, Ghaba, and Fahud evaporite basins (Grotzinger and Amthor, 2002; Allen, 2007; Bowring et al., 2007).

### *The Nafun Group*

Previous work has focused on the deposition and sedimentary features of the Nafun Group as a whole (Gorin et al., 1982; McCarron, 1999; Forbes et al., 2010) with additional studies focusing on aspects of the Masirah Bay (Allen and Leather, 2006), Shuram (Le Guerroue et al., 2006a, 2006b), Buah (Cozzi and Grotzinger, 2004) formations, and Ara Group (Mattes and Conway Morris, 1990). The Khufai Formation was initially interpreted as a uniformly shallow platform carbonate with abundant evaporitic collapse features (Gorin et al., 1982). Subsequent interpretations have favored a prograding ramp model with the basal strata representing sub-wave base deposition (Wright et al., 1990; McCarron, 1999). The lower contact between the Masirah Bay Formation and the Khufai Formation is gradational, displaying interfingering of siltstones and carbonates over several meters of the contact (Allen and Leather, 2006).

There is little agreement on the nature of the lithostratigraphic contact between the Khufai and Shuram formations. Citing unpublished seismic data from PDO and a potential localized karstic surface, some favor a significant depositional hiatus and major sequence boundary (McCarron, 1999; Bowring et al., 2007; Forbes et al., 2010). Others have noted minor hardground features in an oolite marking the uppermost Khufai Formation, but do not assign significant time to the boundary (Wright et al., 1990).

The Khufai Formation represents a key interval in Earth history, capturing the onset of a global excursion in the isotopic composition of carbonate carbon (Grotzinger et al., 2011), but has lacked complete characterization regarding its facies, stratigraphy, and ramp evolution. This excursion was first observed in Oman (Burns and Matter, 1993) and

is initially recorded by the upper Khufai Formation, reaching a minimum in the overlying Shuram Formation, and recovering well into the Buah Formation (Fike et al., 2006; Le Guerroue et al., 2006c). Multiple explanations for this excursion were proposed, including some that have significant implications for the oxidation state of the global ocean and the evolution of the Ediacaran fauna (Grotzinger et al., 2011).

### ***Distribution of Khufai Formation***

The Khufai Formation is best exposed in the Huqf area and in Jebel Akhdar. Continuous sections of the Khufai Formation exist in the Huqf area outcrop within three large anticlines: Mukhaibah, Khufai, and Buah domes (Figure 3A). These locations feature generally good textural preservation and minimal structural deformation beyond the simple, open folds that define the domes. Primary carbonate sediments were pervasively dolomitized which obscures fine detail in strongly affected intervals. This contrasts with exposures in the core of the Jebel Akhdar uplift in the Oman Mountains (Figure 3B) where the Khufai Formation shows extensive ductile folding with associated penetrative cleavage, severe neomorphic recrystallization, and extensive faulting.

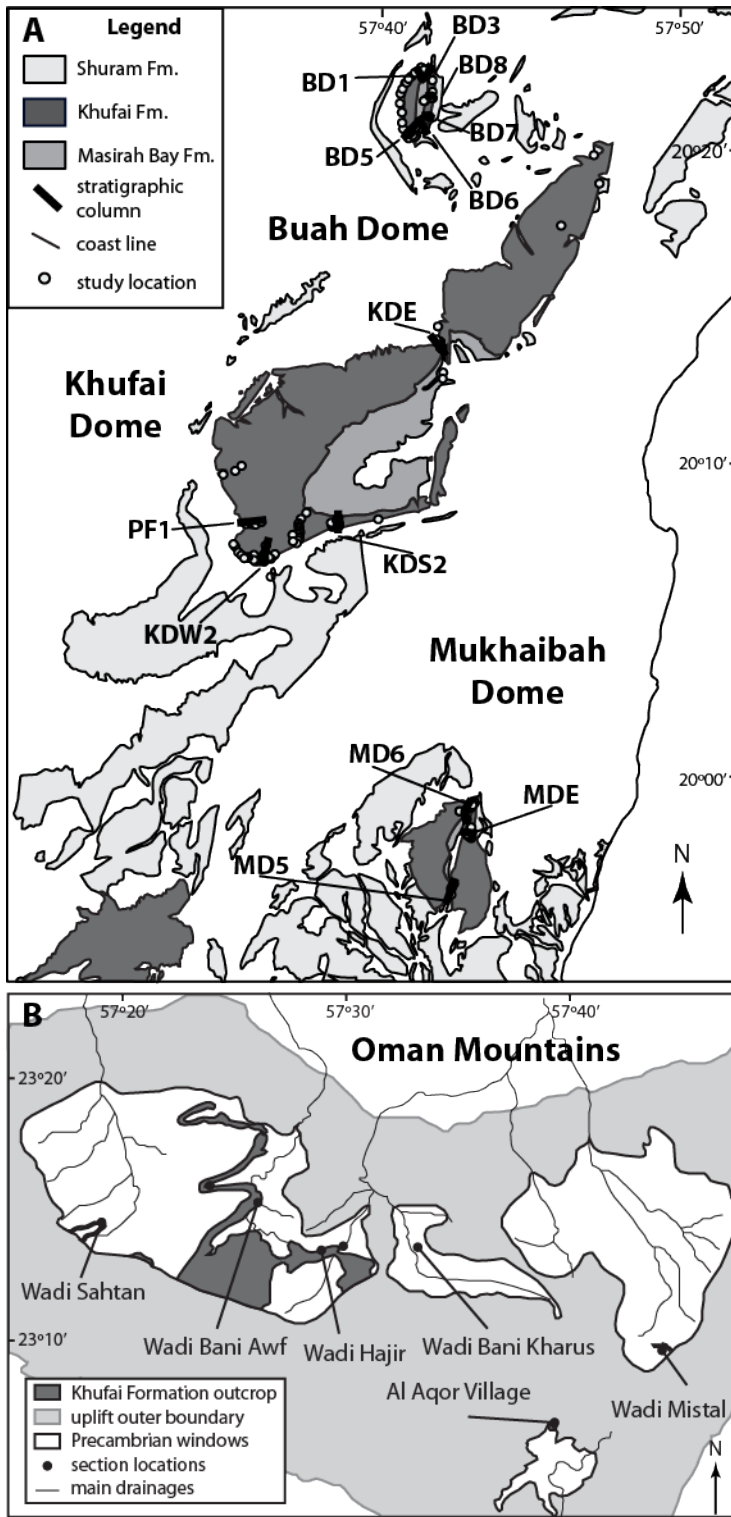


**Figure 3:** Geological map showing study locations and stratigraphic sections. **A.** Geological map of Huqf area showing the distribution of the Masirah Bay, Khufai, and Shuram formations and domes discussed in the text. **B.** Sketch map of the Oman Mountains defined by the outer boundary of sedimentary uplift (grey). Erosional windows into the Precambrian are shown in white and Khufai Formation outcrop is in dark grey. Names and paths of major wadis are shown for reference.

The Khufai Formation in the Huqf area is approximately 300 to 320 m thick and forms a modern topographic high (Figure 4a). Both upper and lower contacts appear to be gradational, although the upper contact is rarely preserved. A regionally extensive, Tertiary-aged erosional event truncated the Khufai Formation preserved in the anticlines and left erosional peneplanation surfaces mantled in thick siliceous breccias. Differential erosion of the Khufai Formation compared to the Masirah Bay and Shuram formations often obscures the contacts and creates a steep gradient between the peneplanation surface and the valley floor 100 m below (Figure 4a). The Khufai Formation in the Oman Mountains is a fetid black limestone with gradational upper and lower contacts (Figure 4b). The lower and upper contacts are preserved within mixed siliciclastic-carbonate transitional members that are consistently ~30 m thick. In contrast, the main phase of carbonate deposition shows significant thickness variability, ranging from 20 to 122 m (Figure 5). While penetrative strain adds error to thickness determinations, the stratigraphic variability appears to mimic primary bed thickness and grain size variations.

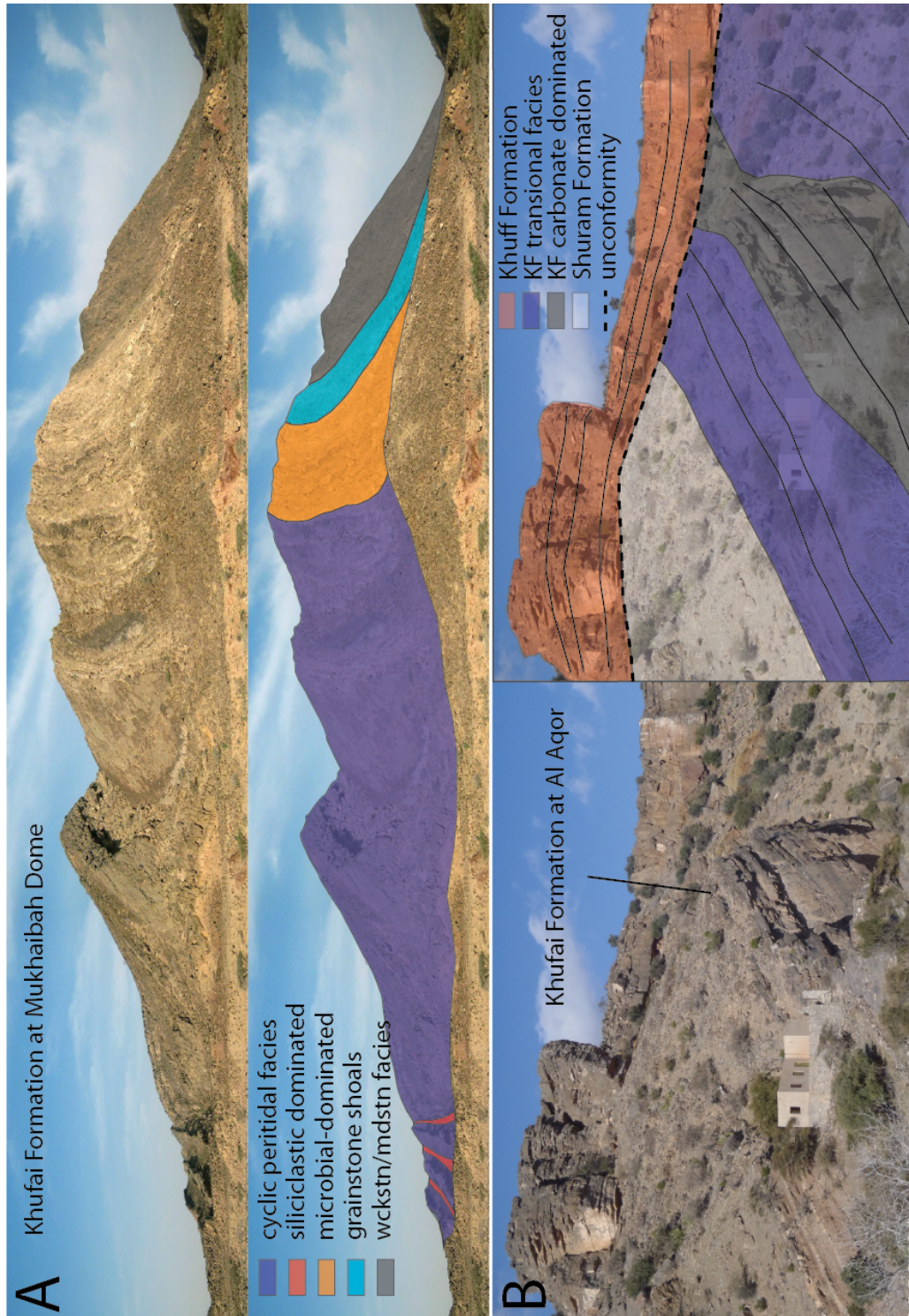


**Figure 4:** Interpreted outcrop photos from (A) Mukhaibah dome and (B) Al Aqor Village in the Oman mountains illustrating major facies groups.

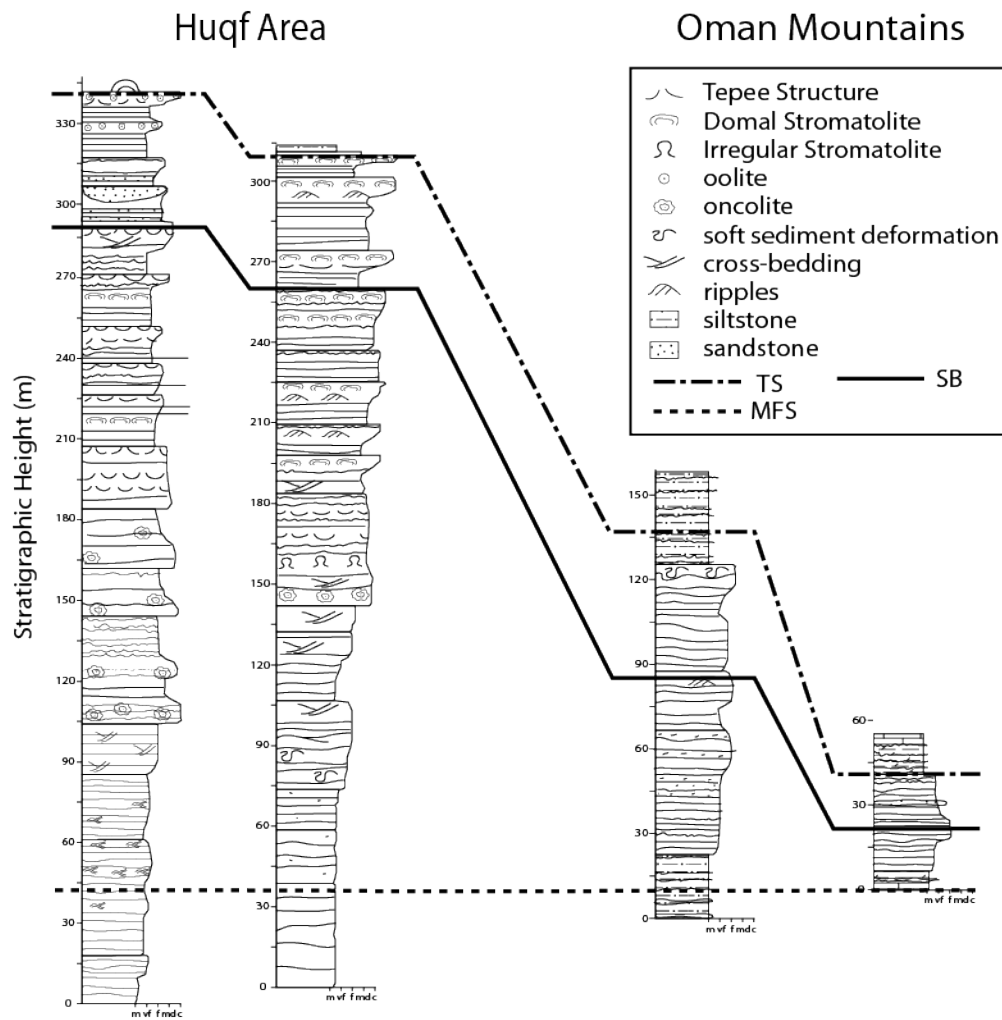


**Figure 5:** Generalized stratigraphic columns from Huqf and Oman Mountains illustrating low resolution facies variability and the position of major stratigraphic surfaces: MFS (Dashed line), SB (solid line), subordinated PS2-scale SB (lighter solid line), TS (Dot and Dashed line)

## Methods

During the course of this study, a total of eight stratigraphic sections covering the full Khufai Formation stratigraphy and 7 shorter sections were logged in the Huqf Area, covering a modern plan view distance of ~85 km (Figure 3A). Five complete sections and

one partial section were logged in the Oman Mountains, covering 55 km (Figure 3B). Stratigraphic sections document facies patterns, diagenetic overprints, and parasequence stacking with approximately 10 cm resolution. Samples were collected for slab scale textural analysis and petrographic analysis.

The stratigraphic architecture of the Khufai Formation was analyzed in hierarchical order beginning with parasequences, followed by parasequence sets, and ramp architecture as a whole. Meter-scale parasequences are easily recognizable in outcrop and combine to form a maximum of four orders of cycles including: parasequence, parasequence set (PS1), compound parasequence set (PS2), and sequence. Parasequences are the smallest observable scale of variability described from observations of accommodation minima and maxima within sets of depositional facies. The facies compositions of parasequences change systematically indicating net increasing and decreasing accommodation, allowing for grouping of parasequences into parasequences sets (PS1). These PS1 sets can often also be grouped into a higher order of compound parasequence set (PS2) based on the same criteria. The sequence is the largest scale of viability observed and corresponds to the formation scale. Ramp geometry was determined from facies and facies stacking patterns within the parasequences.

### **Facies and Facies tracts: Huqf Area**

Depositional facies of the Khufai Formation in the Huqf area and the Oman Mountains differ significantly, and are discussed separately. The Huqf Area defines a broadly shallowing-upward ramp sequence. The lower Khufai Formation is characterized

by outer-ramp facies with little evidence for storm wave reworking, whereas the upper Khufai Formation is characterized by peritidal and supratidal deposits. Following the nomenclature of Burchette and Wright (1992) we define outer-, middle-, and inner-ramp facies and group them into facies tracts following the model of Tinker (1998). In this usage facies tracts contain genetically linked facies and facies successions that record a discrete energy, water depth, and sediment supply setting (Tinker, 1998). The most distal facies form the *outer-* and *middle-ramp* facies tracts, whereas the inner-ramp is more complex and is sub-divided by energy and water depth into *subtidal*, *variable-energy subtidal to intertidal*, *high-energy subtidal to intertidal*, and *intertidal to supratidal facies tracts*. Finally, where the Khufai Formation includes abundant siliciclastic material it is appropriate to erect a final facies tract: *siliciclastic-influenced facies*. The composition of these facies tracts and descriptions of individual facies are summarized in Table 1 and detailed in the text below.

### ***Outer-ramp facies tract***

The outer-ramp facies tract consists of *peloidal intraclast wackestone/packstone*, *thick-laminated mudstone*, rare *intraclast breccia*, and *siliciclastic siltstone* facies. These facies intercalate with those of the middle-ramp facies tract to form a 90 to 130 meter thick, laterally continuous blanket that records the transgressive system tract (TST) and MFI of the lower Khufai Formation. A continuous mineralogic gradation from underlying siliciclastic siltstones of the Masirah Bay is recorded by the transitional contact and intercalation of siltstone into overlying carbonate facies for the first ~10 m of the formation (Figure 6a). The carbonate sediments reflect alternations between fallout of

suspended fine carbonate mud and storm remobilized density currents containing inner ramp derived intraclasts.

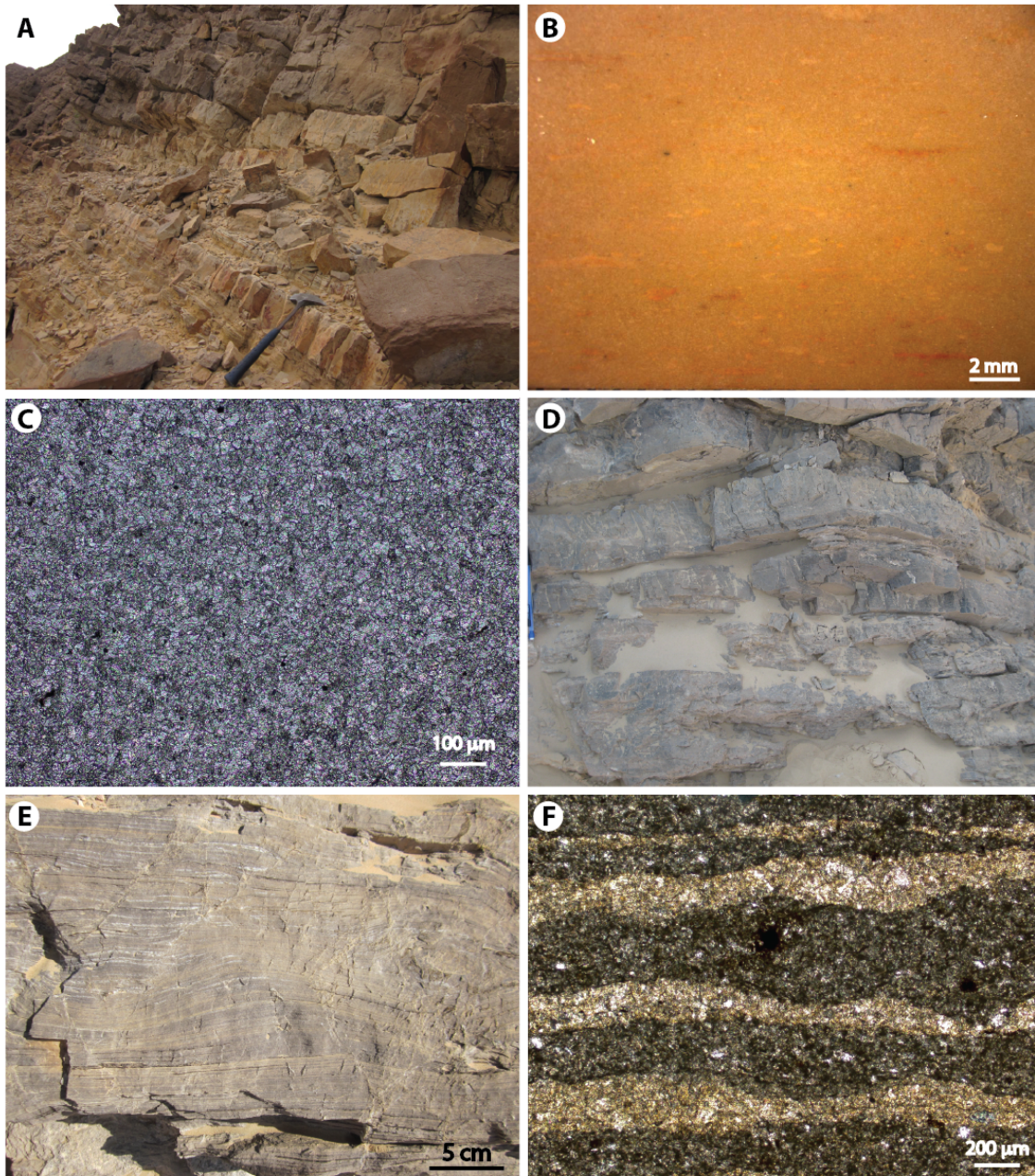


**Figure 6:** *Outer and Middle Ramp Facies Tracts* **A.** Contact between Masirah Bay and Khufai formations in at KDS2, hammer is 32cm tall; **B.** KDS2 0.7 intraclast wackestone slab from the section base. (scale in mm); **C.** Photomicrograph of MD5 0.1 very fine recrystallized dolomite; **D.** Hummocky cross stratification from KDE section (pencil is 15cm); **E.** Planar laminated mudstone facies are MDE; **F.** Photomicrograph of BD1 244.5 Black and tan laminite showing dark silt-rich laminae interbedded with more coarsely crystalline, cleaner calcite.

*Peloidal intraclast wackestone/packstone:* Peloidal intraclast

wackestone/packstone comprise the bulk of the outer-ramp facies tract. Beds are meter-scale and wavy, with scoured bases and cream-colored mudstone intraclasts mms to cms long concentrated at bed bases. The matrix is dark grey dolomite mudstone or grey, peloidal, very fine-grained packstone, and was pervasively dolomitized to a very fine interlocking crystalline fabric (Figure 6c). At Buah Dome the intraclasts can be much larger (cm-scale) and more abundant than in Khufai and Mukhaibah domes grading into a matrix-supported pebble conglomerate. This facies records down-ramp export of sediment by storm-generated currents consistent with a distal setting (Tucker and Wright, 1990; Betzler et al., 1999). In this below-wavebase setting density currents produced by storms would be sufficient to transport peloids and intraclasts from the inner-ramp to the outer-ramp environment (Schlager et al., 1994). Remobilization of pelagic mud accumulations creates the observed matrix components. Intraclasts show facies composition and early lithification more characteristic of inner-ramp shallower water facies and were thus likely eroded and incorporated into deeper water deposits (e.g., Fairchild and Herrington, 1989).

*Thick-laminated mudstone:* The thick-laminated mudstone forms meter-scale beds in the lower Khufai Formation outwardly resembling the wackestones described above. Laminae are cm-scale and discontinuous forming an irregular fabric that is highlighted by silicification and dedolomitization. There is no evidence for wave reworking. We interpret this facies to record a low energy depositional environment below storm wave base (McCarron, 1999). Thin silty to micritic laminae separating thin packages were previously interpreted as benthic microbial colonization (McCarron, 1999), however it is

alternatively suggested here that this fabric represents pelagic fallout and accumulation of suspended organics.

*Intraclast breccia:* Intraclast breccias are rare and consist of very coarse, matrix-supported breccia with laminated micrite clasts (1 to 20 cm in length), occurring in 1-5 m thick laterally discontinuous lenses. The matrix is muddy, however recrystallization generally obscures primary clast and matrix components. The intraclast breccia facies was interpreted as evaporite collapse breccias (Gorin et al., 1982) and as slope collapse breccias (McCarron, 1999). Given their lateral equivalence with sub-wave base intraclast wackestone/packstone facies we suggest that they record debris flows of slope materials on the distal ramp. These deposits are very rare in all sections and do not create the laterally continuous facies belt characteristic of steep-sided platform margins (Read, 1985).

*Siliciclastic Siltstone:* Siltstones interbedded with dolomite at the Khufai-Masirah Bay transition correspond to the siltstone component of facies E2 described in Allen and Leather (2006) (Figure 6a). Beds are 5-20 cm thick, separating larger packages of fine-grained carbonate. Siltstone is interpreted to have deposited below wave-base by pelagic fallout of suspended sediment.

### ***Middle-ramp Facies Tract***

The middle-ramp facies tract consists of *hummocky-cross stratified (HCS) peloidal packstone* and *silty planar-laminated mudstone* and records the slow progradation of the early highstand system tract after the MFI. It is distinguished from the

outer-ramp facies tract by containing storm generated sedimentary structures including increased evidence of wave reworking.

*HCS peloidal packstone:* HCS peloidal packstone is composed of fine peloids with hummocky cross-strata, slump structures, and convolute bedding amalgamated in meter-scale packages (Figure 6d). It alternates with peloidal intraclast packstone and caps depositional cycles. Dolomitization obscures primary grain boundaries. The onset of storm reworking, gradual increase in grain size, and stratigraphic position suggest the HCS cross-bedded packstone/grainstones represent progradation of the ramp sequence. The amalgamated packages of HCS are interpreted as the product of storm wave activity.

*Silty planar-laminated micrite:* Strikingly planar-laminated silty micrite (Figure 6e) contains mm to cm scale very even laminations, with occasional small-scale scours, slumps, and self-sourced imbricated intraclast conglomerate. This unit overlies the HCS sections and directly precedes the transition to the inner ramp facies in all domes. This facies is similar to the rhythmically interbedded limestone-argillite facies described from the Mississippian (Erick and Read, 1991), albeit without evidence for burrowing. The lack of evidence for desiccation or frequent wave action, combined with evidence for quiet water suspension fallout with occasional storm reworking is consistent with the middle-ramp environment. The production of rigid clasts from these laminae suggests a degree of early cementation not observed in the deeper-water facies.

*Black and tan laminite subtype (Buah Dome only):* At Buah Dome, the silty planar-laminated micrite facies is a distinctive dark gray and tan, strongly petroliferous, planar-laminite (Figure 6f). Beds are 1-3 m thick and extended the entire length of the

outcrop area (5 km) and exhibit both plastic and brittle small-scale deformation. The depositional environment of these laminites is interpreted to be physically similar to that of the silty laminites described above. However, the relative plasticity and cohesion of laminae clasts indicate less extensive early cementation and strong organic and pyrite components visible in thin section suggest a low-oxygen environment.

***Inner ramp facies tract: subtidal***

The inner ramp subtidal facies tract consists of *peloidal to coated grainstone* and *intraclastic dolosiltite*. These two facies appear in distinct parts of the depositional sequence: first as the facies shallow during the HST and second, as the ramp is flooded during transgression into the basal Shuram Formation. They are grouped here because they represent a similar sediment supply, wave energy, and water depth, consistent with the concept of a facies tract (Kerans and Fitchen, 1995).

*Peloidal to coated-grain grainstone:* The peloidal to coated-grain grainstone facies is the first unambiguous appearance of extensively cross-bedded grainstone within the facies succession (Figure 7a). This light grey to white peloidal dolomite occurs in decimeter-scale discontinuous beds. Grains are fine micritic peloids with or without a coating of micritic cement, with larger grains congregating in ripple troughs. The appearance of peloidal grainstone is abrupt across the Huqf area, indicating shoaling of the platform to fair weather wave base and forming a 15 to 25 m thick stratigraphic band that is laterally continuous with minor interfingering of facies from stratigraphically above and below. This transition is frequently coeval with a formation-scale visual character change from dark grey and fetid facies below to buff colored above (Figure 4a).

This facies is often poorly exposed, coinciding with the level of the Tertiary-age peneplanation surface and associated silcrete breccias.

*Intraclast dolosiltite:* Intraclast dolosiltite occurs as a two-meter thick package at the Khufai-Shuram boundary at Mukhaibah Dome. It consists of thin swaley-bedded cream to pink dolosiltite that includes increasing amounts of red siliciclastic silt upward in the package (Figure 7b). Ripped up pebble-sized clasts of this facies are preserved as thin intraclast conglomerate beds. The dolomicrite beds onlap stromatolitic bioherms on the underlying bedding surface (see below). This facies is interpreted to record an abrupt deepening of the platform during the large-scale transgression into the Shuram Formation, recording high wave energy events in a subtidal setting. Increasing silt content with stratigraphic height marks the transition into the lower Shuram Formation.

***Inner ramp: variable-energy subtidal to intertidal***

The variable-energy subtidal to intertidal facies tract is a diverse group and includes *oncolite grainstone/boundstone*, *peritidal microbialite (tufted and irregular)*, *flaser-bedded peloidal packstone*, and *lagoonal mudstone and dolosiltite* deposits. These facies are distributed within the peritidal portion of the Khufai Formation, beginning above the first grainstone shoals.

*Oncolite grainstone/boundstone:* Oncolite grainstone consists of thick cross-bedded, channelized packages of oncoids and coated grains. Large oncoids (up to 5 mm) occur in channel and bed bases and are elliptical with crinkly micritic rims commonly showing multiple concentric although irregular rings (Figure 7c). Microbial laminae bind

oncoids within some beds, forming boundstone facies. These facies are often heavily silicified with near complete replacement of carbonate.

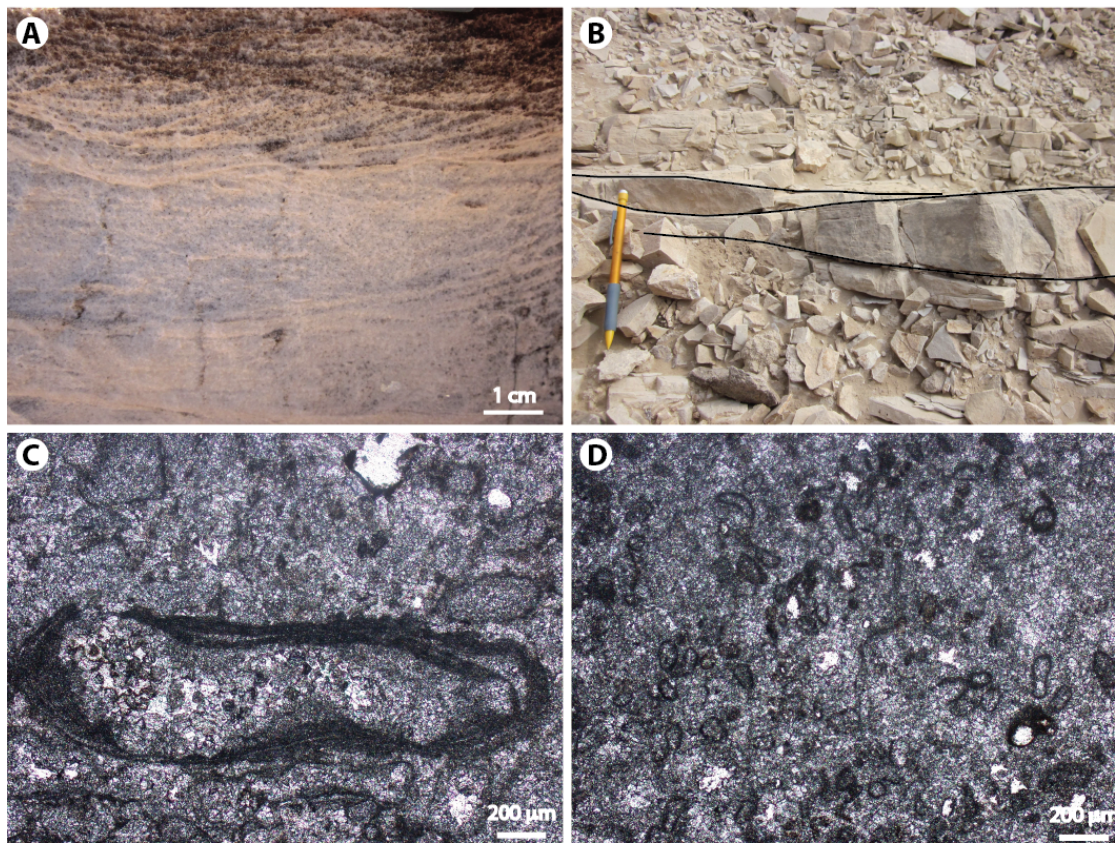


**Figure 7:** *Inner ramp subtidal and intertidal grainstone facies* **A.** KDS 114.4, Festoon cross bedding in peloidal to coated grainstone facies; **B.** MDE, intraclast dolosiltite facies in outcrop showing hummocky cross stratification and blocky bedding. Contact with Shuram Formation is in rubble at top of photograph. Pencil is 15cm; **C.** MD5 152.0 Photomicrograph, Large oncolite grain in finer peloidal matrix from oncolite grainstone/ boundstone facies; **D.** MD5 131.5 Photomicrograph, Fine coated grains and peloids.

While oncoids are described from a variety of depositional environments (Tucker and Wright, 1990) a shallow, wave-agitated origin for this facies is suggested by the context presented here. Sedimentary structures indicate wave (or tidal) reworking, however, binding by microbial laminae suggests periods of quiescence. The oncolite

grains themselves suggest a similar genesis as the irregular coatings are indicative of colonization by microbial mats, but roundness of grains suggests at least periodic rolling (see discussion in Tucker and Wright (1990)). This facies is similar to the ooid and oncolite shallow ramp carbonate of the Upper Cambrian Nolichucky Formation described by Markello and Read (1981). In that setting, the carbonate sands formed a barrier between cyclic peritidal deposits of the shallow inner-ramp and deeper subtidal deposits (Markello and Read, 1981).

*Peritidal Microbialite:* Peritidal microbialite forms a subgroup of the variable-energy subtidal to intertidal facies tract and consists of tufted laminites, irregular laminites, and stromatolites. These microbial textures are intimately associated with one another and frequently grade laterally and vertically within the same bed. The term stromatolite is applied in cases where the synoptic relief formed by laminae is more than a few centimeters. Irregular laminite is defined by irregular micritic laminae with no systematic higher order structure, occurring both as thick-bedded units (Figure 8a) and as thin layers within oncolite or peritidal grainstones (see below). Laminae are irregular to convolute and trap pockets of coated grains (Figure 8b). Tufted laminite is similar, but the laminae form small tufts that show a high degree of inheritance, extending upward through beds at decimeter scale, although the synoptic relief at any given time was probably less than 1 cm (Figure 8c). Tufts are dampened where carbonate grains accumulate in troughs and are coated by the subsequent laminae (Figure 8d). Tufts can form the nuclei of small (3-10 cm) conical stromatolites. Both laminite types tend to be heavily silicified and often show evidence for intermittent subaerial exposure including blisters, mudcracks, tepees, and *in situ* breccias.

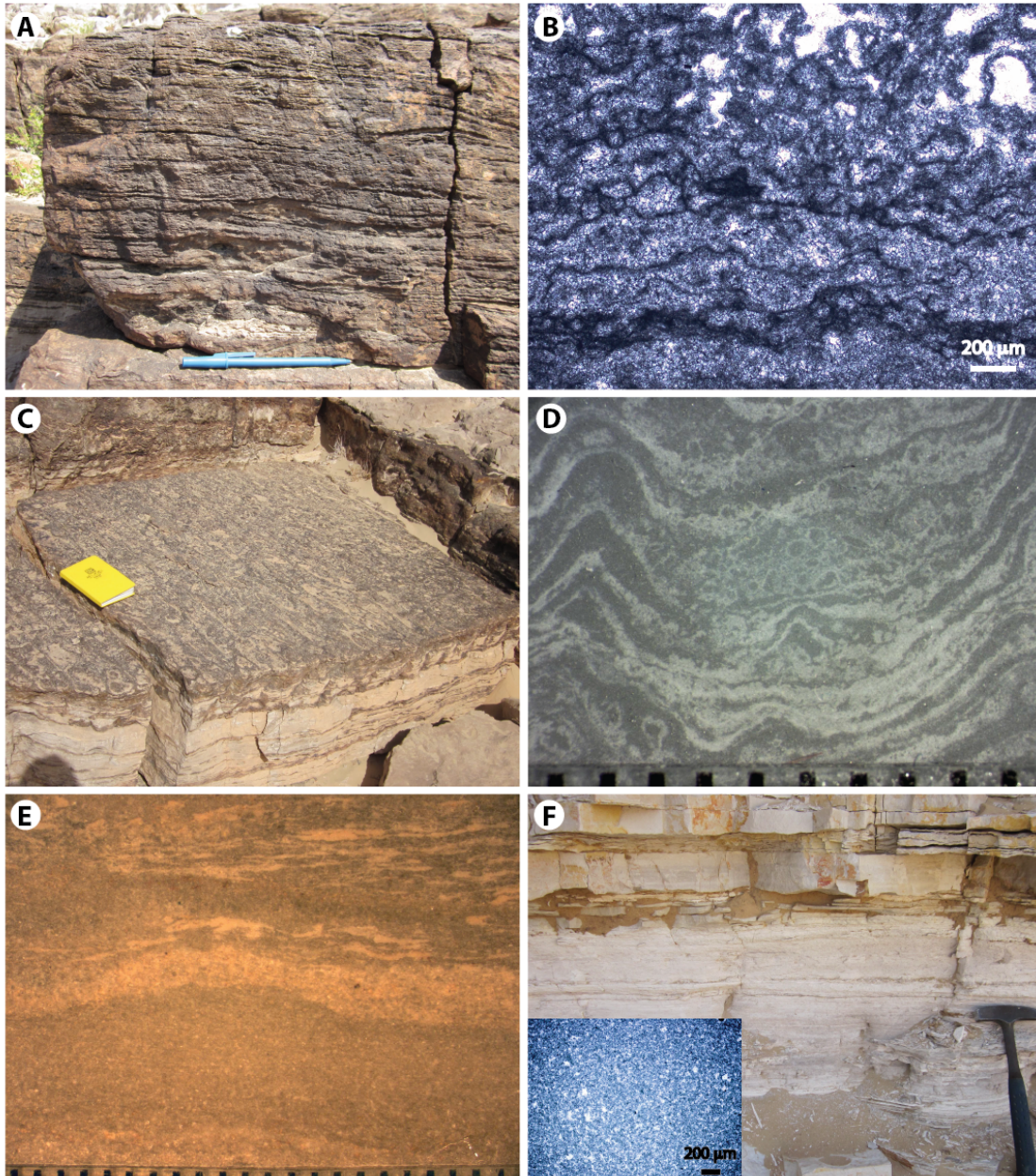


**Figure 8:** *Peritidal Microbialite and Inner Ramp: Subtidal Facies* **A.** Thick bed of irregular laminite. Pen is 16cm; **B.** KDW2 21.9 photomicrograph of irregular micritic laminae in both thick laminae and coating and binding grains; **C.** Plan and side view of tufted laminite bed showing parallel tuft crests. Notebook is 19cm tall; **D.** MDE 122 photomicrograph, tufted laminite with coated grains damping tuft topography. Scale in mm; **E.** BD5 Flaser bedded packstone facies in slab. Scale in mm; **F.** Laminated dolosiltite in outcrop. Hammer is 32cm long. Inset is photomicrograph of a similar material from Khufai Dome.

We interpret the peritidal microbialite facies group as forming by the preservation of microbial mats in the shallow intertidal zone. The carbonate accumulation likely occurred through a combination of trapping and binding (where there are grains visible) and direct precipitation of carbonate (Fairchild, 1991). Microbial laminite often caps facies of the subtidal and intertidal parasequences and parasequence sets. Distribution of desiccation structures confirms these shallowing upward trends. Primary porosity was occluded by early silicification.

*Flaser-bedded packstone:* Flaser-bedded packstone occurs at Buah Dome at the equivalent stratigraphic interval of microbially influenced sedimentation elsewhere. Here, laminae to thin beds of rippled fine carbonate sand (grains primarily include peloids and resedimented carbonate mud) alternate and are draped by carbonate and siliciclastic mud (Figure 8e) with no evidence for desiccation. Significant recrystallization forms coarse calcite spar that obscures primary fabrics within this facies. Flaser-bedded packstone beds commonly are associated with black and tan laminites; in one location a parasequence composed of these facies is capped by irregular laminite. This sequence defines a shallowing upward package suggesting that the flaser-bedded packstone formed in an intertidal depositional environment. Similar flaser-bedded ribbon rocks were described from South China and interpreted as tidal flat deposits (Lehrmann et al., 2001). However, the lack of desiccation features here suggests a deeper water setting with variable energy more similar to the ribbon rock carbonates described from the Middle Cambrian of Virginia (Koerschner and Read, 1989).

*Lagoonal Fines:* The lagoonal fines facies includes mudstone and laminated dolosiltite and represents low energy, deeper water portions of peritidal cycles in the

Khufai Formation. Mudstone is buff or white colored occurring in thinly bedded packages with no visible grain character or evidence for wave reworking. Very even planar lamination and thin irregular laminae occur in some beds. Laminated dolosiltite occurs regularly as parasequence bases and is defined by bright white packages of even thinly bedded to laminated dolosiltite with intercalated beds of carbonate-cemented silt (Figure 8f). Silicified beds contain evaporite molds, but no evidence of exposure is observed. Very low domal structures interpreted as stromatolites formed in a few intervals.

The origin of Precambrian mud is debated with possible explanations ranging from direct precipitation from the water column, precipitation as stromatolite laminae and subsequent disaggregation, or disintegration of algal skeletons similar to today (J.P. Grotzinger, 1989; Knoll and Swett, 1990; Tucker and Wright, 1990; Fairchild, 1991; Sumner and Corcoran, 2001; Dibenedetto and Grotzinger, 2005). Large accumulations of mudstone occur in Proterozoic carbonate platforms in a variety of depositional environments (J. P. Grotzinger, 1986; J. P. Grotzinger, 1989; Knoll and Swett, 1990; Sami and James, 1994, 1996). The sedimentary features described here are consistent with fallout of suspended or precipitated fines in a protected, low energy environment such as a back shoal lagoon. The lack of sedimentary structures, planar lamination, and stratigraphic context of dolosiltite facies also suggests a restricted lagoonal environment. This is similar to the thick-laminated dolosiltite described by Grotzinger (1986) in the Rocknest Formation of Northwest Canada. Sedimentary structures are more limited in the Khufai Formation example, but this could be attributed either to a more protected

environment or a deeper lagoon. Evaporite laths suggest a hypersaline pore water composition at least periodically during deposition.

***Inner ramp: High energy subtidal to intertidal facies tract***

The high energy subtidal to intertidal facies tract consists of mixed grain packstone and grainstone, smooth laminated stromatolite, oolitic intraclast grainstone, and stromatolite bioherm facies. The former two facies comprise a large proportion of peritidal deposits, where the latter two are characteristic of the transgressive surface of the upper most Khufai Formation.

*Mixed grain grainstone/packstone (peritidal grainstone):* The mixed grain grainstone/packstone facies is composed of fine wave-reworked heterolithic grainstone and packstone and can contain interbeds of many different facies including irregular laminite, intraclast conglomerate, and occasional micrite (Figure 9a). Ooids occur rarely and primarily from Mukhaibah Dome. Sedimentary structures include current ripples, climbing wave ripples (Figure 9b), small dunes, and mudcracks. Granular composition and sedimentary structures in the mixed grain grainstone/packstone indicate a high-energy intertidal environment (Tucker and Wright, 1990). Carbonate sands were deposited where wave and tidal energy was high and were then colonized by microbial communities and/or draped by mud during periods of quiescence. The oversized beds of similar composition may represent local tidal bars or sand waves.

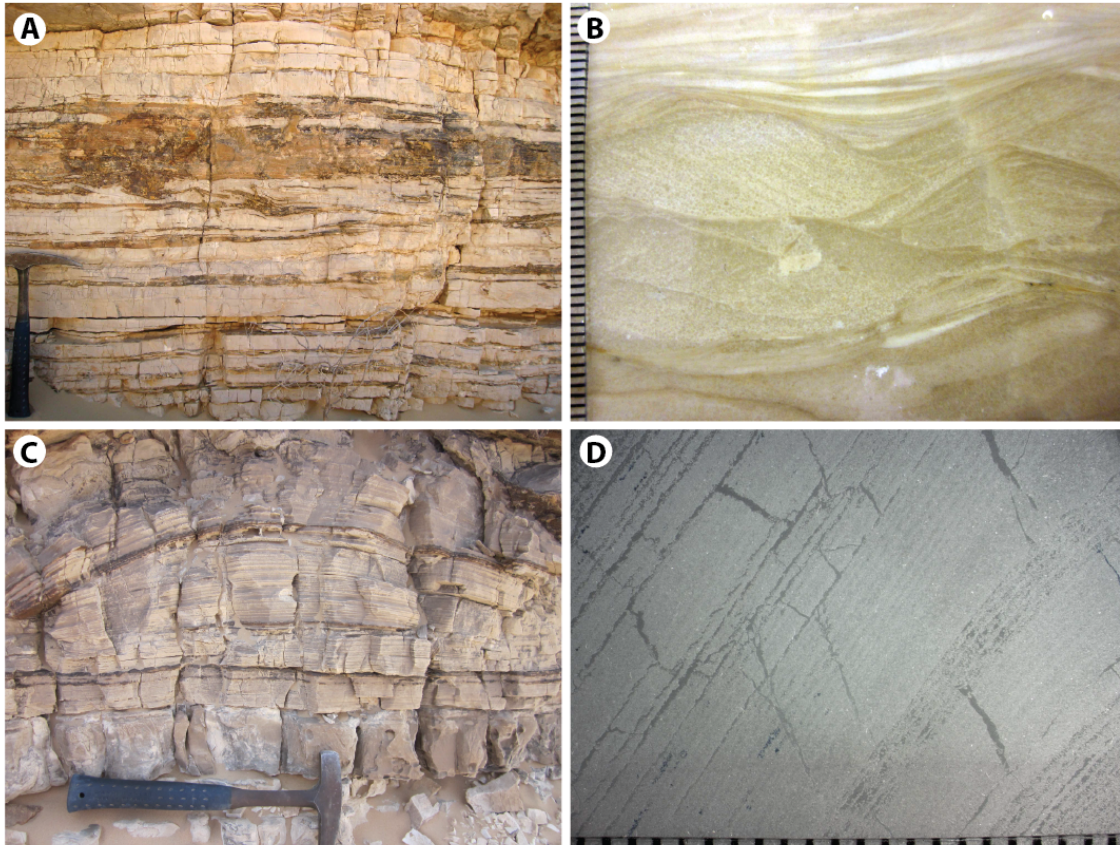


**Figure 9:** *Inner Ramp: High energy facies* **A.** Peritidal grainstone facies in outcrop at KDW, hammer is 32cm tall; **B.** NA1 1.4 slab, ripple cross-laminated coated grain to ooid grainstone. Scale in mm; **C.** KDS 264 outcrop, Low domal stromatolite. Hammer is 32cm tall; **D.** MD6 174 thin section, smooth laminated stromatolite. Scale in mm.

*Smooth-laminated stromatolite:* The smooth-laminated stromatolite facies includes a variety of morphologies with a common fine and even lamination style (Figure 9c,d). Stromatolitic beds form continuous sheets and are nucleated on rippled peritidal grainstone beds. Elliptical laterally linked domes are the most common morphology and range in size from 20 cm to several meters across (Figure 9c). Other morphologies include columns, cones, and domes. Morphologies grade laterally and vertically into one

another. This gradation is interpreted to represent local variability in wave energy and sediment supply as is noted in the modern examples at Shark Bay (Tucker and Wright, 1990; Grotzinger and Knoll, 1999). The smooth laminated texture suggests formation via precipitation onto the surface of microbial mats rather than by trapping and binding of carbonate clasts by mats. Water depth is likely related to the synoptic relief of any given stromatolite probably in these cases ranging from shallow intertidal to subtidal for the largest examples (e.g. J. P. Grotzinger, 1986; Fairchild, 1991; Riding, 2000).

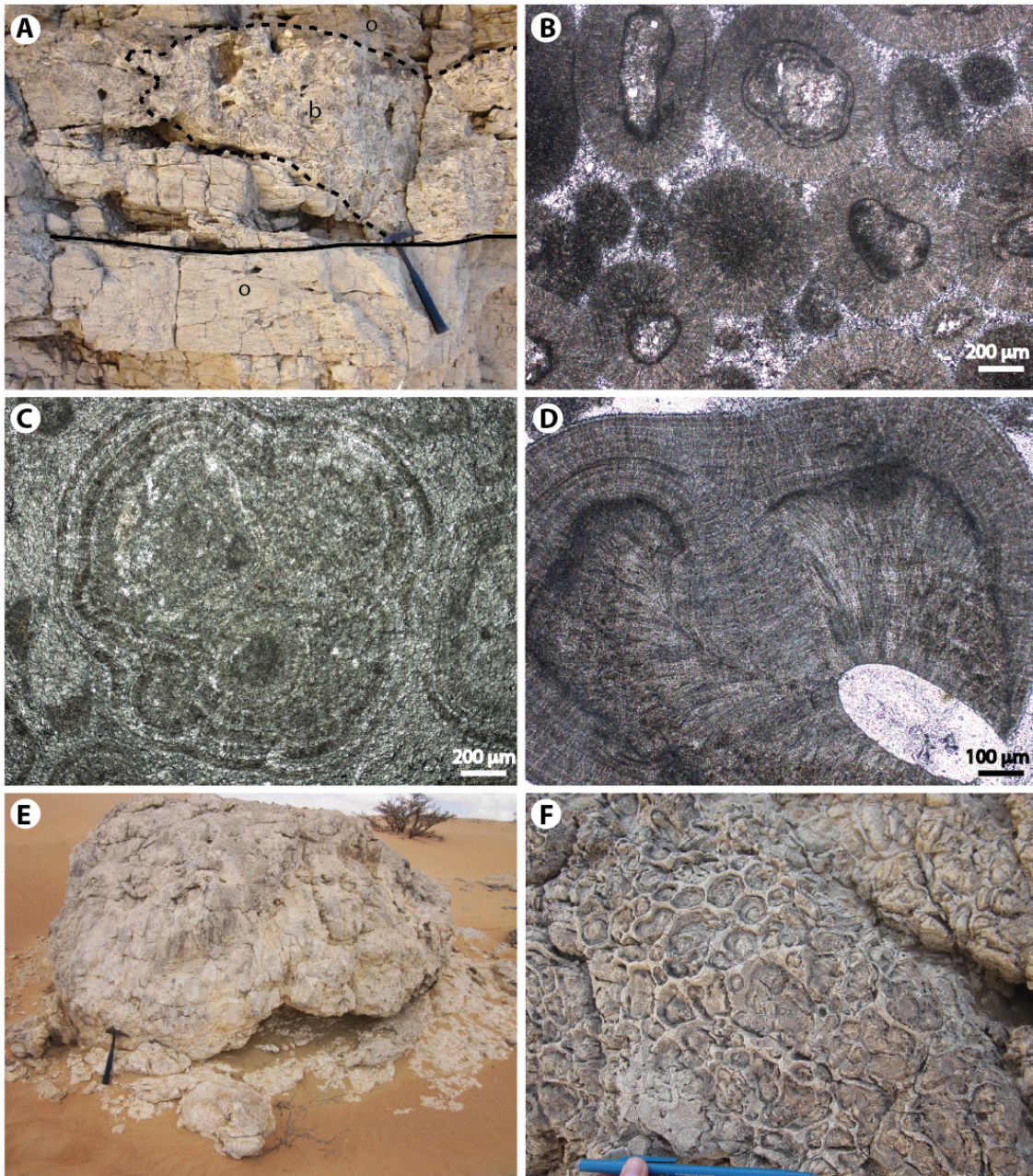
*Ooid-intraclast grainstone:* While ooid grainstone is rare through the majority of the Khufai Formation, the uppermost transgressive system tract is oolite-rich. In particular, a distinctive bed of coarse intraclast ooid grainstone occurs everywhere the contact with the Shuram Formation is preserved in the Huqf (Figure 10a). Additionally, oolites are common in the upper 35 meters of Buah Dome sections.

Ooid grainstone beds are cross-bedded ranging from large-scale bar forms, tabular cross beds, and ripples and contain spherical ooids, coated elongate clasts, and composite coated grains. In contrast to the oncoliths and coated grains that occur stratigraphically lower, these ooids show radially concentric crystal orientation along with distinctive plumose cement in ooid interiors (Figure 10b,d). Intraclasts are concentrated as lags and contain stromatolite laminae, mudstone, or cemented oolite clasts. A hardground is preserved within the oolite bed at Mukhaibah Dome (Figure 10a). We interpret the ooid-intraclast grainstone facies to have formed in a high-energy shoreface to shoal environment. The large cross-bedding in northern Khufai Dome was previously interpreted as tidal bars (Le Guerroue et al., 2006a) and other sedimentology is consistent

with modern and ancient ooid shoal deposits (Wilson, 1975). Intraclasts appear to derive primarily from coeval stromatolites and cemented oolite.

*Muddy stromatolite:* The muddy stromatolite facies describes an unusual stromatolite morphotype that differs from previous examples both in lamination style and gross morphology and are syndepositional with the ooid-intraclast facies described above. Laminae are thick microcrystalline micrite, with ooids incorporated between muddy laminae. The stromatolites form large isolated bioherms with up to 2 m of synoptic relief (Figure 10e). The stromatolitic subunits alternate between irregular clusters of small columns (Figure 10f) and thick continuous laminae. The stromatolites nucleate along a hardground within the upper oolite bed, and are overlapped by the intraclast dolomicrite facies and lowermost Shuram Formation.

**Figure 10:** *Inner Ramp: High-energy (transgressive) facies* **A.** Oolite bed in outcrop at MDE. Hardground outlined in solid line, stromatolite bioherms outlined in dashed line (b), and oolite indicated by (o). Hammer is 32cm tall; **B.** MD5 309.5 photomicrograph, Ooid grainstone showing radial fabric; **C.** KDW2 131.5 photomicrograph, Composite grain composed of small ooids with multiple exterior concentric coats; **D.** MD6 258.7, ooid detail showing plumose interior recrystallization and radial exterior fabric; **E.** KDW2 UPK10, Large micrite stromatolite bioherms in outcrop at Khufai-Shuram boundary. Hammer is 32cm tall; **F.** Detail of stromatolite bioherms at MDE showing small silicified stromatolites and surrounding matrix, pen is 16cm long.



***Inner-ramp: intertidal to supratidal***

The intertidal to supratidal facies tract consists of *fenestral mudstone/packstone/wackestone*, *tepee breccias*, and *rip-up intraclast conglomerate* and is characterized by evidence for periodic to prolonged subaerial exposure.

*Fenestral mudstone/packstone/wackestone:* The fenestral mudstone/packstone/wackestone facies is a mixed group that is united by close sedimentary proximity and evidence of exposure and/or very shallow water depositional conditions. Sediment types are interbedded in thin-bedded packages that often are deformed by tepee structures. Millimeter-scale sub-spherical to lozenge-shaped fenestrae and tabular crystal molds resembling gypsum laths are very common (Figure 11a). Primary evaporite minerals forming lath structures were replaced with silica, as noted previously by Gorin et al. (1982) and Wright et al. (1990). Grains are similar to those in the previous facies tract and sedimentary structures include mudcracks, low amplitude wave ripples, and tepee structures. In concurrence with previous interpretations (Wright et al., 1990; McCarron, 1999), this facies is interpreted to have formed on a shallow intertidal to supratidal flat. In contrast to the observations of Wright et al. (1990) who note a paucity of mud, we observe significant accumulations of muddy matrix within these deposits, consistent with the sedimentology of modern tidal flats (Shinn et al., 1969).

*Tepee breccia:* Tepee structures are ubiquitous in the upper hundred meters of the Khufai Formation at Khufai Dome and occur uncommonly at Mukhaibah and Buah Domes. Tepees grade from mild upwarping (Figure 11b) to extensive breccias (Figure 10c; Kendall and Warren, 1987) and form meter-scale polygonal fractures across exposed bedding planes. Tepees primarily deform fenestral mudstone facies; however, peritidal microbialite and grainstone facies also are affected. Cementation is extensive and includes calcite rim cements and coatings on breccia clasts, calcite spar in vugs, and silica replacement. Vadose pendant cements and large pisoids commonly associated with tepee

structures in other locations are not observed in the Khufai Formation (Assereto and Kendall, 1977; Kendall and Warren, 1987). Thin beds of red siltstone are occasionally preserved on the upper surface of tepee breccia deposits.

The tepee breccia facies is interpreted to have formed in a very restricted sabkha environment and indicates periodic subaerial exposure. Where tepee peaks are eroded or the breccias are most well developed, significant depositional hiatuses very likely occurred. At Khufai Dome, multiple parasequences of meter-scale tepees are superposed forming an amalgamated, highly restricted parasequence set (e.g. Grotzinger, 1986). The concentration of these features at Khufai Dome suggests these outcrops are the most proximal exposed for the Khufai Formation.

*Rip-up intraclast conglomerate:* Rip-up intraclast conglomerates are formed of coarse imbricated tabular intraclasts scoured from underlying beds in a coated grain to coarse oncoid grain-dominated matrix (Figure 11d). At Khufai Dome beds are laterally extensive and in some cases can be correlated for 10 km or more. The regionally extensive character and clast imbrication above scoured surfaces suggest these beds were deposited when storm-generated currents eroded the inner-ramp. The matrix derives from adjacent grainstone facies tracts, where large intraclasts were scoured and deposited locally. This facies is equivalent in origin to the regionally extensive intraclast packstone facies (e.g. Grotzinger, 1986).

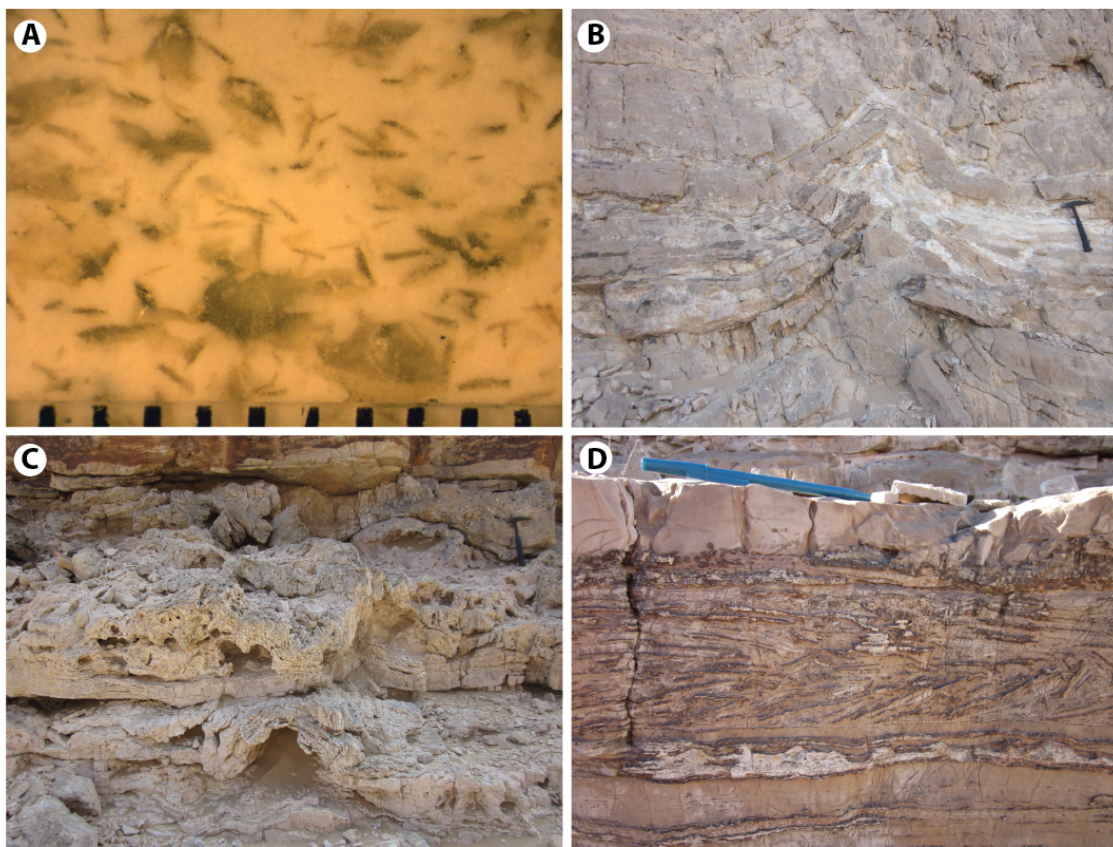


**Figure 11:** *Inner Ramp: Intertidal to Supratidal Facies* **A.** MDE, Fenestral mudstone slab with evaporite lathes of multiple morphologies. Scale in mm; **B.** Khufai Dome (DG) outcrop, large immature tepee. Hammer is 32cm tall; **C.** KDW2 32 outcrop, multiple sets of heavily deformed tepees in fenestral mudstone. Hammer is 32cm tall; **D.** Khufai Dome (PF1) outcrop, Silicified imbricated intraclast conglomerate. Pen is 16cm long.

***Inner ramp facies tract: siliclastic-influenced***

The siliclastic-influenced facies tract consists of *mixed calc- to quartz arenites* and *quartz sandstone* facies. Siliclastic sediments occur only locally at Khufai and Mukhaibah domes, whereas all sections at Buah Dome feature mixed carbonate-

siliciclastic sediments beginning ~90 m from the basal contact. This change in sediment type warrants a new facies tract.

*Calc- to quartz- arenites:* The calc- to quartz arenite facies contains medium to thick-bedded carbonate-cemented sandstone with a variable proportion of carbonate grains. Extensive scouring and cross bedding is present in most packages (Figure 12a). Carbonate-rich and sand-rich beds are intimately associated with each other and alternate at a fine scale with sand grains even serving as the nucleus for carbonate coatings (Figure 12b). Carbonate mud is the matrix in both quartz- and carbonate-dominated beds.

During deposition quartz sand grains were transported into a zone of carbonate production. A modern analog for this area is the mixed carbonate-siliciclastic deposition occurring in estuaries of the Great Barrier Reef, Australia. Here relatively coarse quartz sands are incorporated into variably muddy to grainy shallow marine sediments with sediment distribution controlled by local coastline and reef geometries (Orpin et al., 2004). The river system supplying siliciclastics into the underlying Masirah Bay Formation was hypothesized to be located to the north of Huqf exposures (Allen and Leather, 2006), consistent with the northern location of Buah Dome.

*Quartz sandstone:* Up to four packages of carbonate cemented quartz sandstone occur in upper Khufai and Mukhaibah domes. These packages are 1-3 meters thick and extensively cross-bedded (Figure 12d). Large (cm- to dm-scale) clasts of underlying carbonate beds are present as basal lags. Grains are fine to medium size well-sorted quartz sand. We differentiate this facies based on the high quartz content, cross bedding, and lack of lateral continuity. Bi-directional cross bedding suggests a tidal influence on

these sediments, and the scouring relationships and bed geometries suggest migrating channels. This facies was interpreted as southward extensions of tidal channels sourced from the Buah Dome area (McCarron, 1999). We concur with the tidal channel interpretation, however note that this facies occurs stratigraphically above the main sand bodies at Buah Dome.

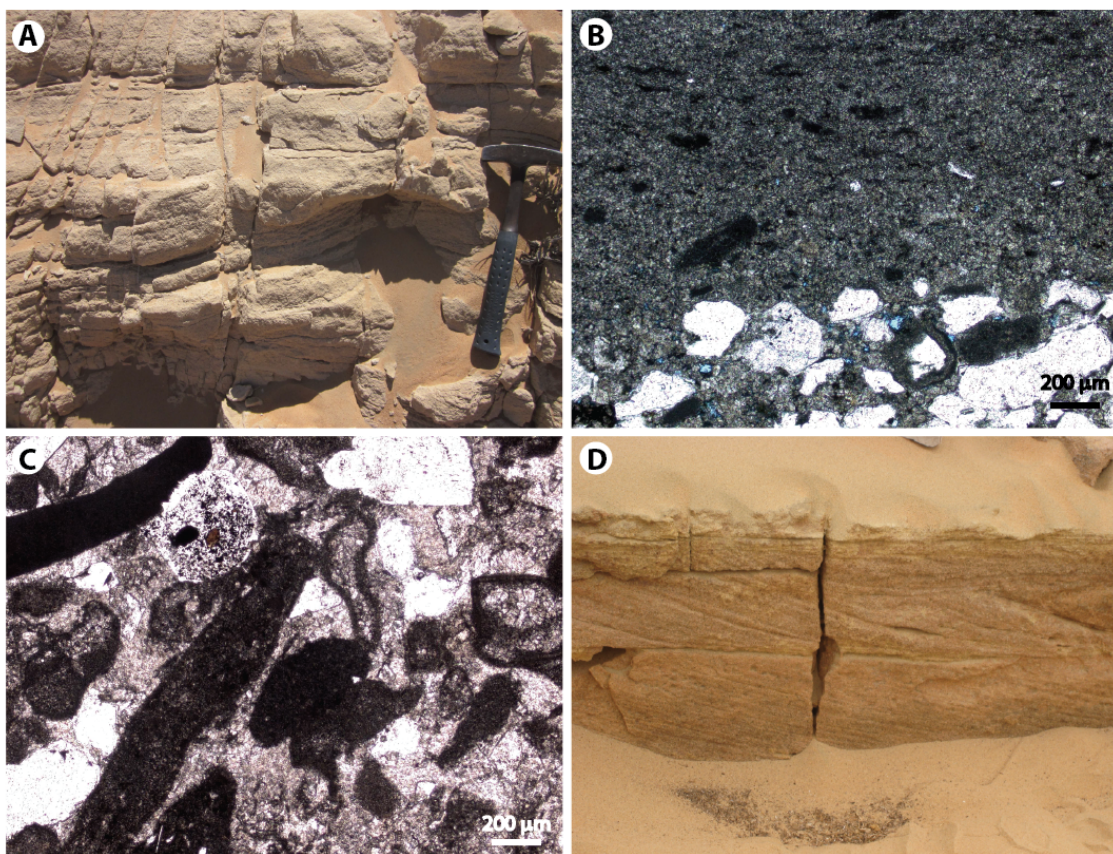


**Figure 12:** *Sand-containing facies* **A.** BD6 45 cross-bedded quartz sand in outcrop at Buah Dome. Hammer is 32cm long; **B.** BD1 106.3 photomicrograph, Intraclast wackestone interbedded with carbonate rich quartz sandstone **C.** BD1 164.5 photomicrograph, Primarily carbonate grainstone with micrite and coated grains with inclusion rich quartz sand, calcite cement; **D.** KDW2 upper sandstone in outcrop showing tabular planar cross bedding in quartz sand. Bed is approx. 20cm thick.

### **Facies and Facies tracts: Oman Mountains**

The Khufai Formation exposed in the Oman Mountains comprises two main facies tracts: transitional and carbonate-dominated (Table 2). The former is siliciclastic-dominated and occurs at the Masirah Bay-Khufai and Khufai-Shuram formation boundaries. Because the transitional facies are genetically related to the rest of the Khufai Formation they are included in our discussion. The carbonate-dominated facies tract varies considerably in thickness ranging from 20.1 m at Al Aqor section to 122.5 at Wadi Hajir. Thickness variation corresponds to bed thickness, suggesting a relationship with the supply of carbonate material. Significant post-depositional folding and faulting prevents quantitative analysis of the depositional distance between these sections.

#### ***Transitional facies tract***

The transitional facies tract consists of siliciclastic siltstone, crinkly laminite, and intraclast wackestone. The lower transition begins at the first major carbonate bed within the upper Masirah Bay Formation siltstone. Carbonate facies alternate with siltstone over a thickness of 10 to 30 meters before an abrupt transition to carbonate-dominated facies. The upper transition begins at the termination of the main body of carbonate deposition, and is marked by a meter thick bed of red siltstone after which marl and crinkly laminite alternate with siltstone. Quartz sand beds also punctuate the upper transition in some sections.

*Siliciclastic Siltstone:* Siltstone is volumetrically the largest component of the transitional facies tract, and is tan, white, or pink in outcrop, with thin crinkly laminations (Figure 13a). This facies was interpreted to record settling of fines from suspension in deep water (Allen and Leather, 2006).

*Thick-bedded Intraclast Wackestone:* The thick-bedded intraclast wackestone facies occurs in discontinuous beds 0.5 to 2 meters thick. The matrix is composed of grey, silty lime-mudstone with small siltstone intraclasts concentrated at bed bases. Bed thickness, intraclast entrainment, and composition suggest that these beds represent periodic transport of carbonate from higher on the ramp into the basin by sediment gravity flows. As the flows moved across silt beds they were reworked to provide intraclasts.

*Crinkly Laminite:* The crinkly laminite facies is dark grey to black and occurs both as coherent beds (10cm-50cm) or capping thick intraclast wackestone beds (Figure 13a). Small-scale plastic deformation of the crinkly laminite is common and includes small folds and roll-up structures. Crinkly laminites are unusually well preserved. The fabric consists of very fine, crinkly, silty, carbonate mud laminae separating pockets of calcite sediment (Figure 13b). The irregular texture and plastic deformation of the crinkly laminite facies suggest binding cohesion of microbial mats. The lack of physical abrasion, lack of evidence for phototaxis, and the facies association within which crinkly laminite facies occur suggests deep water environmental of deposition.

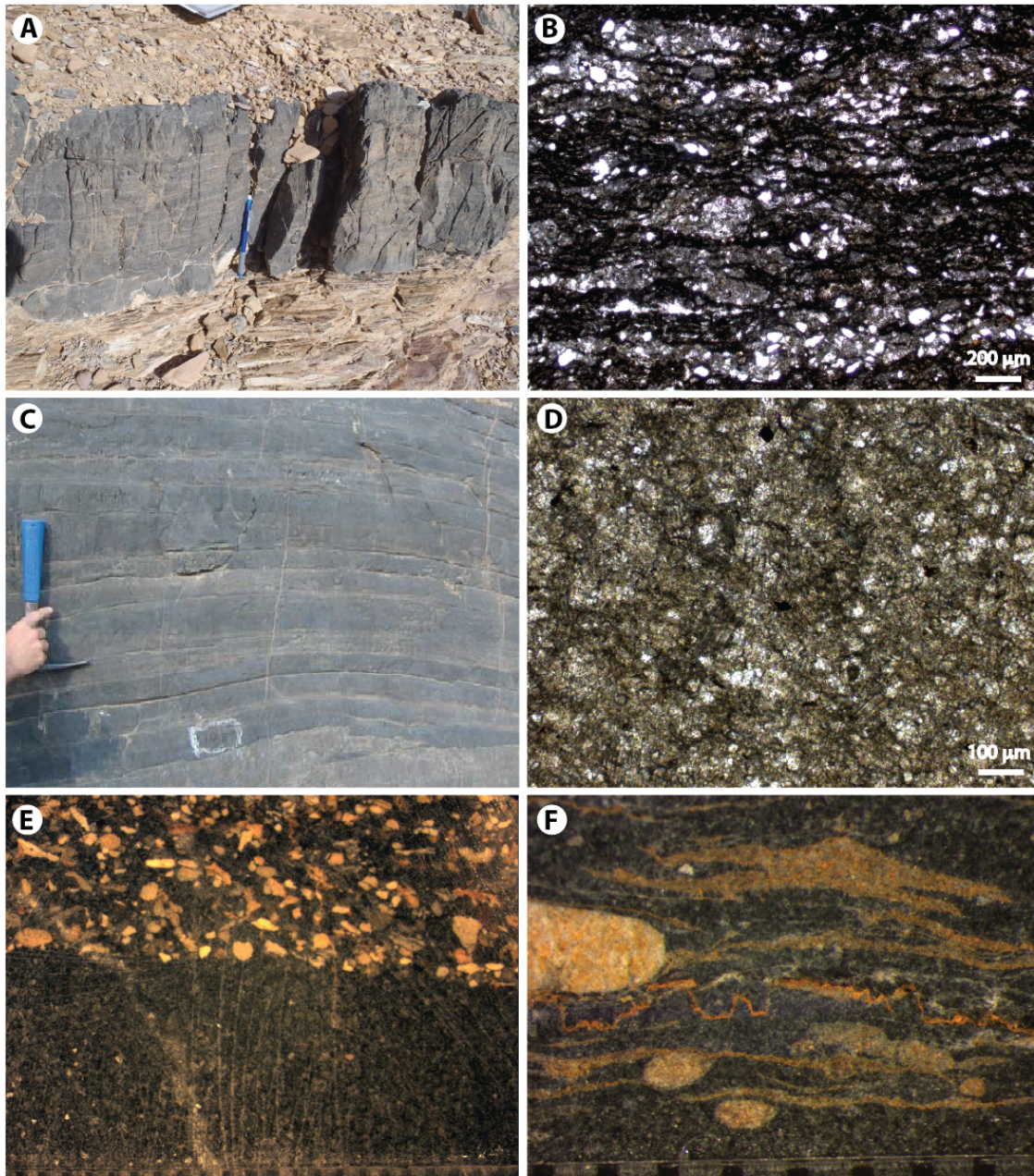


**Figure 13:** *Transitional facies and Carbonate Dominated, Oman Mountains.* **A.** Lensoidal bed of crinkly laminite in outcrop surrounded by pink and yellow Masirah Bay siltstone, Wadi Sahtan, pencil is 15cm long; **B.** WM1 16A photomicrograph, crinkly laminite facies showing dark irregular micritic laminations binding quartz silt and very fine-grained calcite sediment. **C.** Graded intraclast grainstone beds from Wadi Hajir (hammer is 30cm tall); **D.** Photomicrograph of recrystallized peloidal wackestone/packstone; **E.** WH1 Intraclast grainstone slab in reflected light showing a bed boundary with recrystallized calcite matrix and micritic dolomite clasts of a graded bed scouring a finer grainstone below, scale in mm; **F.** WM1 pebble conglomerate showing well rounded dolomite pebbles draped with irregular laminae. Stylolite cross cuts image. Scale in mm.

### **Carbonate-dominated facies tract**

The main body of the Khufai Formation in the Oman Mountains is a thin-bedded black limestone consisting primarily of graded intraclast wackestone/packstone, with minor accumulations of pebble grainstone/conglomerate, lime mudstone, graded grainstone, and slumped quartz sandstone. While the prevailing grain size varies between these facies, common sedimentary structures across beds of different mean grain size indicate similar depositional processes.

*Graded intraclast wackestone/packstone:* Graded intraclast wackestone/packstone is the predominate facies of the carbonate-dominated facies tract. Bedding is thin and beds are grouped into meter-scale units of similar grain size, character, and thickness (Figure 13c). Pervasive neomorphic recrystallization of calcite precludes accurate determination of grain sizes except where coarse grains appear (Figure 13d). Angular dolomudstone clasts are normally graded with matrix material (Figure 13e). Scouring is common at bed bases and soft sediment deformation such as ball and pillow and flame structures often accompany the coarsest beds. This facies is interpreted to represent deep-water turbidity currents originating along the steeper parts of the ramp at times of significant carbonate productivity (Schlager et al., 1994). Variability in bed thickness and grain size may correspond both to proximity to the main channelized flow path in a submarine fan complex, in addition to retrogradation/progradation patterns associated with highstand versus lowstand deposition (Betzler et al., 1999).

*Graded peloid/oid grainstone/Intraclast conglomerate:* The coarsest beds in this system are graded peloid/oid grainstone and conglomerate. These grainstones are

similar in bedding character to the wackestone/packstone facies but lack mud matrix and are composed of well-rounded dolomudstone clasts and degraded ooids. Coarser beds contain larger rounded intraclasts and often have draping irregular muddy laminations (Figure 13f). Coarse beds increase in abundance approaching the sequence boundary, at higher order cycle tops, and approaching the maximum flooding interval. Ghost rims of ooids are sometimes visible. Crosscutting diagenetic fabrics include an “orbicular” fabric and thick calcite spar veins. Increased grain size and character of clasts in this facies suggests transport from shallower on the ramp compared to the wackestone facies (Betzler et al., 1999). Lack of significant mud and development of irregular laminations suggests sediment bypass.

*Lime Mudstone:* Massive mudstone beds occur rarely and only as a significant component at Wadi Mistal. These mudstones are light grey and homogeneous, occurring above wackestone beds and deformed by subsequent wackestone deposition. The deformation either creates fluid escape structures and contorted bedding or nodular bedding. The occurrence of mudstone in one of the thinnest, presumably more distal sections suggests formation through settling of suspended fines away from the main turbidite fan network.

*Slumped Quartz Sandstone:* The uppermost beds of graded ooid/intraclast grainstone progressively incorporate quartz sand. Beds of pure quartz sandstone with carbonate intraclasts occur in some sections and particularly Wadi Bani Awf. Zones of extensive soft sediment deformation and recumbent folding are associated with the stratigraphically lowest, thick sandstone beds. Wave generated sedimentary structures are absent. Sandstone beds are interpreted to be chronostratigraphically equivalent with those

in upper Khufai and Mukhaibah domes, but are indicative of a deeper depositional environment. As this transition to siliciclastic facies occurs at the Khufai-Shuram boundary, we interpret these facies as a switch from transported carbonate sediments to reactivation of a source of siliciclastic sediment during flooding after the platform-wide lowstand.

### **Sequence Stratigraphy**

A sequence stratigraphic model of the Khufai Formation was constructed based on correlation of parasequences and parasequence sets, and mapping of key stratigraphic surfaces. There are 133-207 parasequences in each complete Khufai section in the Huqf outcrop area that combine into 34-45 PS1, 16 PS2, and 1.5 depositional sequences. Three formation-scale sequence stratigraphic surfaces are observed including: a maximum flooding interval (MFI) low in the formation, a type-2 sequence boundary (SB) in peritidal to supratidal deposits of the upper formation, and a transgressive surface (TS) representing the onset of Shuram Formation siltstone deposition. The MFI is very subtle in outcrop as the facies of this interval are thick-bedded and largely homogeneous. The SB is mostly visible in Khufai and Buah domes where amalgamated tepee breccias indicate extremely low accommodation. Parasequence stacking shows an increase in parasequence thickness approaching the maximum flooding interval and a systematic decrease approaching the sequence boundary. The upper transgressive boundary coincides with the lithostratigraphic formation boundary and is easily identified where exposed.

### *Parasequences*

Representative stratigraphic logs from Mukhaibah, Khufai, and Buah domes at three different stratigraphic intervals through the HST are shown in Figure 14a. These sections illustrate representative trends in parasequence composition during ramp progradation and may include either one parasequence or a small-scale parasequence set. The composition of each parasequence will be discussed in ascending stratigraphic order.

The early HST shows the most homogeneous facies distributions and parasequences are defined by subtle alteration in the influence of wave reworking on sedimentation patterns. The three domes show very similar facies distributions at this stratigraphic level, marked by interbedded intraclast wackestone/packstone and HCS packstone facies (Figure 14a). At Buah Dome the intraclast wackestones have larger clasts and the cross bedding is tabular rather than hummocky.

In the middle HST parasequence development is more prominent and involves a larger range of facies than lower in the formation. The largest difference compared to the early HST is the appearance of coated grainstone and microbially dominated facies such as irregular laminite and oncolite grainstone. Mukhaibah and Khufai domes show similar parasequence composition of oncolite grainstone-microbialite cycles. Each cycle base is defined by deposition of an oncolite or peloidal grainstone bed, followed by thin beds of alternating fine peloidal grainstone and irregular laminite, capped by a thick sequence of irregular or tufted laminite and/or stromatolite (Figure 14a). Grainstone-microbialite cycles frequently have an erosional base and desiccation features in the upper part of the cycle. This pattern is suggestive of a shallowing-upward package culminating in very

shallow water depths with intermittent exposure. Silicification of microbial facies enhances the appearance of cyclicity in this section. The middle HST facies patterns at Buah Dome instead show interbedded coarsely graded intraclast packstone beds capped with black and tan laminite. The black and tan laminite facies is interpreted to have formed in the middle-ramp with storm-wave activity; the intraclast packstone represents an even deeper, outer-ramp setting. These cycles record shallowing, although at relatively greater water depths compared to Khufai and Mukhaibah domes.

Parasequences of the late HST are diverse and vary considerably in both facies and thicknesses between outcrop areas (Figure 14a). At Mukhaibah Dome deposition of coated grainstone-microbialite cycles also incorporate lagoonal muds and silts at the parasequence base in addition to more complex stromatolite morphologies. Relatively high-energy conditions are recorded at parasequence tops by an abundance of cross bedding, especially climbing wave ripples. The late HST of Khufai Dome is dominated by tepee-capped cycles. Lagoonal fines and fenestral mudstone are overlain by coated grainstone and/or microbialite as at Mukhaibah Dome; however, instead of stromatolite buildups, these cycles are capped by large tepee structures and associated breccias. The upper surfaces of tepees often are truncated, indicating further subaerial exposure after tepee formation. Where relief was preserved, lenses of sediment fill tepee polygons. Tepee-capped parasequences are thinner than those in Mukhaibah dome (Figure 14a), likely because of sustained non-deposition and exposure events. Late HST cycles at Buah Dome again differ from the southern Huqf and feature cyclic alternations of calc- to quartz arenites with interbedded black and tan laminite or siltstone facies (Figure 14a). Parasequences begin with relatively pure, thickly bedded, quartz sandstone with

carbonate intraclasts and grade upward to more thinly bedded, carbonate-rich grainstone-sandstone mixtures. They are capped with silty carbonate beds and/or black and tan laminite. The presence of carbonate intraclasts in the basal sandstones is consistent with erosion of underlying carbonates during deposition and demarcates the cycle base.

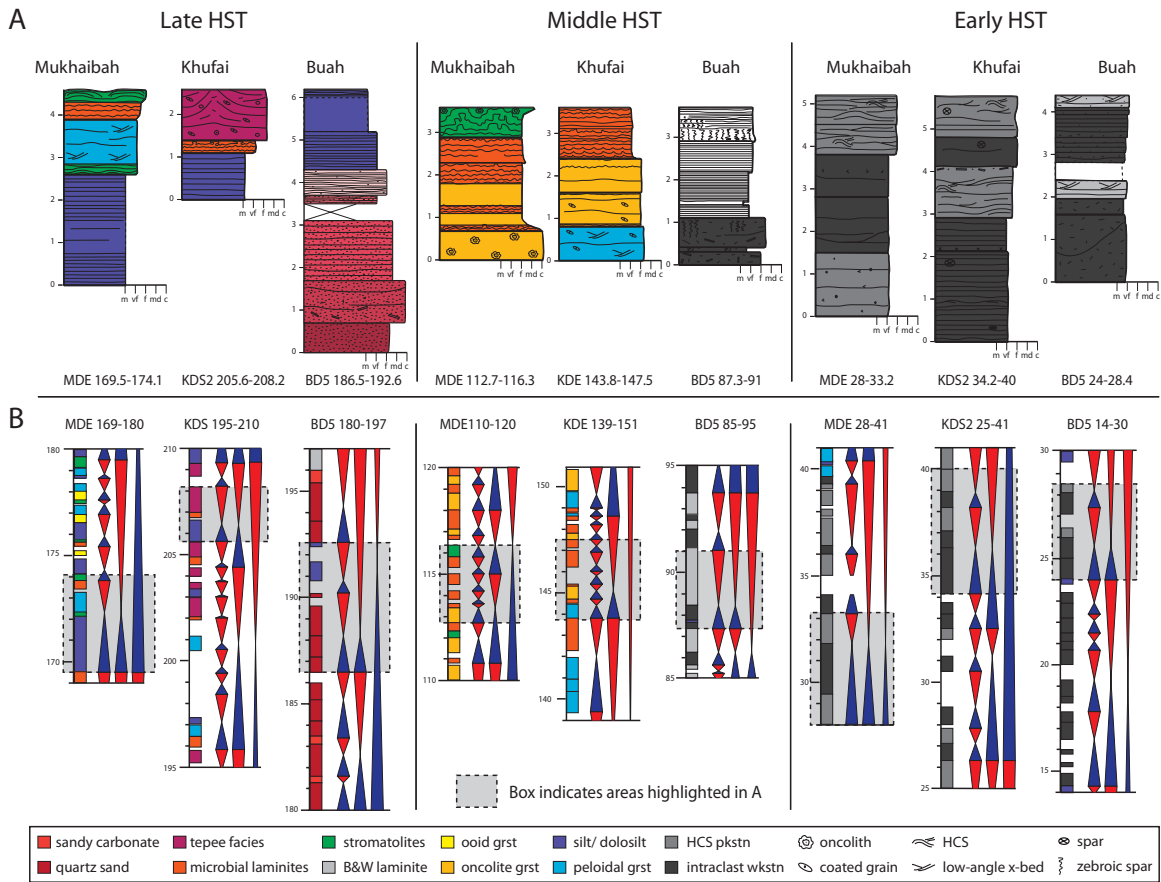


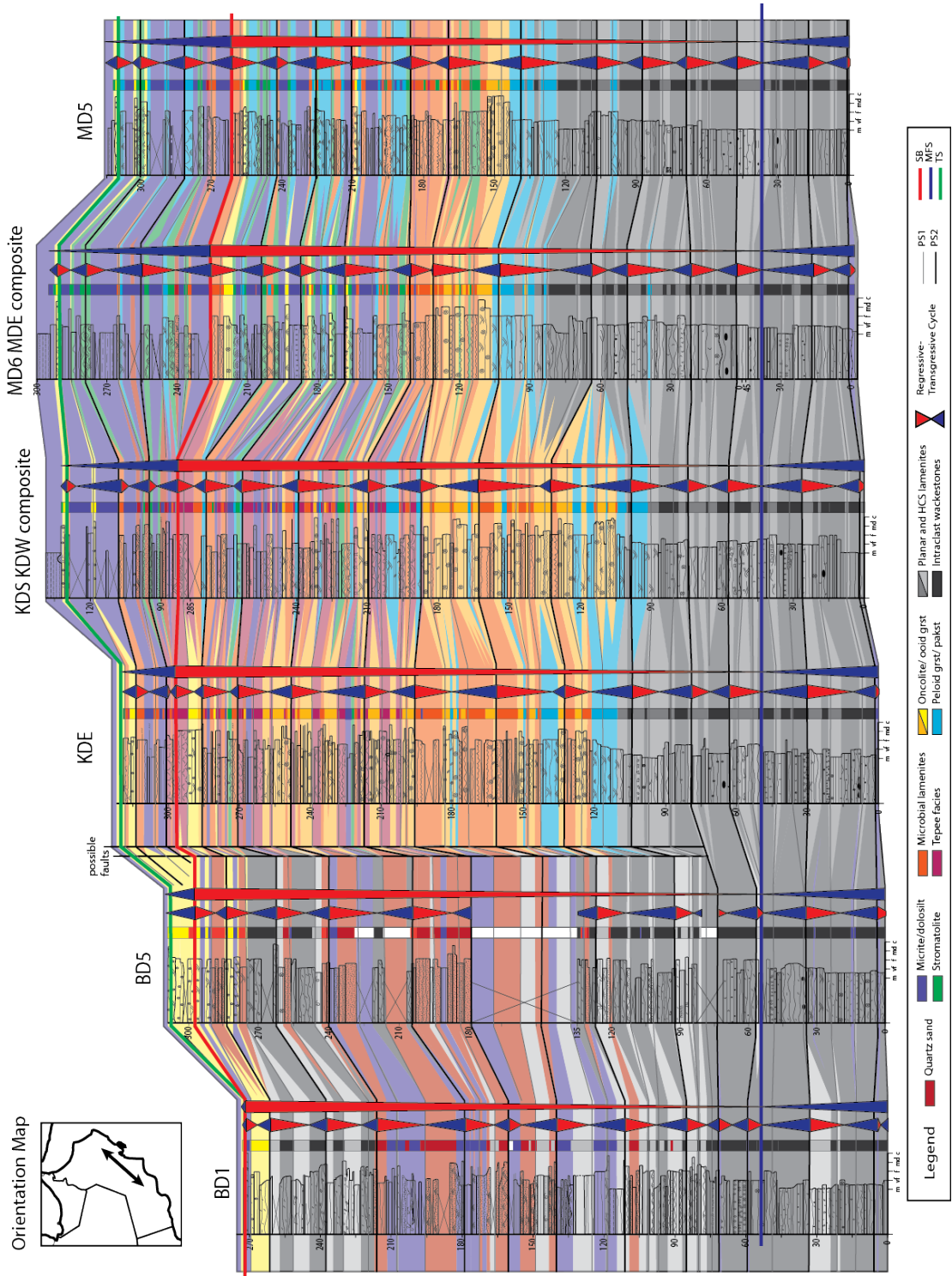
**Figure 14:** **A.** Example stratigraphic sections from early, middle, and late highstand system track illustrating parasequence to parasequence set-scale facies variability. **B.** Facies bars and transgressive-regressive triangles for intervals including sections from A (grey shaded box). Triangle bars are arranged from left to right, parasequence, parasequence set, and composite parasequence set scales. Scales are in meters.

*Parasequence stacking patterns*

Parasequence stacking patterns are documented by plotting transgressive-regressive cycles using blue and red triangles respectively (Figures 14b, 15, 16). Figure 14b illustrates the parasequence, parasequence set (PS1), and composite parasequence set (PS2) for each of the representative parasequences discussed above. This analysis allows for comparison of scales of cyclicity both in a given area through the HST, as well as between domes. General trends include a decrease in parasequence thickness approaching sequence boundaries. Comparison between domes reveals that Khufai Dome has the greatest number of cycles preserved, whereas Buah Dome has fewer, thicker cycles.

Extending this analysis to the whole formation shows longer-term trends (Figures 15 and 16). Figure 15 presents a PS1-scale correlation between stratigraphic sections in the Huqf area and includes PS2 and sequence-scale transgressive-regressive cycles. There is an increase in accommodation up to the maximum flooding interval in the lower Khufai Formation, generally decreasing accommodation up to the main sequence boundary, and increasing accommodation through the Khufai-Shuram transition. A significant PS2-order sequence boundary occurs four cycles below the main SB. While the formation scale sequence boundary was chosen based on the clear accommodation minimum and evidence for subaerial exposure in Khufai Dome, this lower boundary corresponds with an evident facies change including the introduction of lagoonal facies and increased stromatolite growth in both Khufai and Mukhaibah domes, both of which continue to intensify after the main SB.

**Figure 15:** Detailed sequence stratigraphic correlation of stratigraphic sections from Huqf area highlighting transgressive-regressive cycles and facies variability. Colored columns show facies components of each section; colored wedges correlate coarse facies breakdown between sections. Transgressive-regressive cycles are shown at the composite parasequence set and sequence scale. Parasequence-set boundaries are shown in thin black lines, sequence stratigraphic surfaces are showing in thick colored lines, see key.



This analysis is repeated for the Khufai Formation in the Oman Mountains and is illustrated in Figure 16. Despite the 400 km separating the Huqf and Oman Mountains outcrops the MFI occurs in the transitional Masirah Bay-Khufai member of all sections, followed by a PS2-scale SB near the onset of carbonate deposition. A whole PS2 cycle occurs within the carbonate-dominated facies tract up to the main SB, but varies considerably in thickness ranging from 60 to 85 m in Wadi Sahtan (WS1) and Wadi Hajir (WH1) compared to 10 and 15 m in Al Aqor (AQ1) and Wadi Mistal (WM1) respectively. This discrepancy accounts for a large portion of the differences in thickness between the sections and for the very thin bedding and mud dominated deposition of this portion of AQ1 and WM1 respectively. An abrupt transition back to wackestone facies marks the sequence boundary, followed by the transgression into the Shuram Formation.

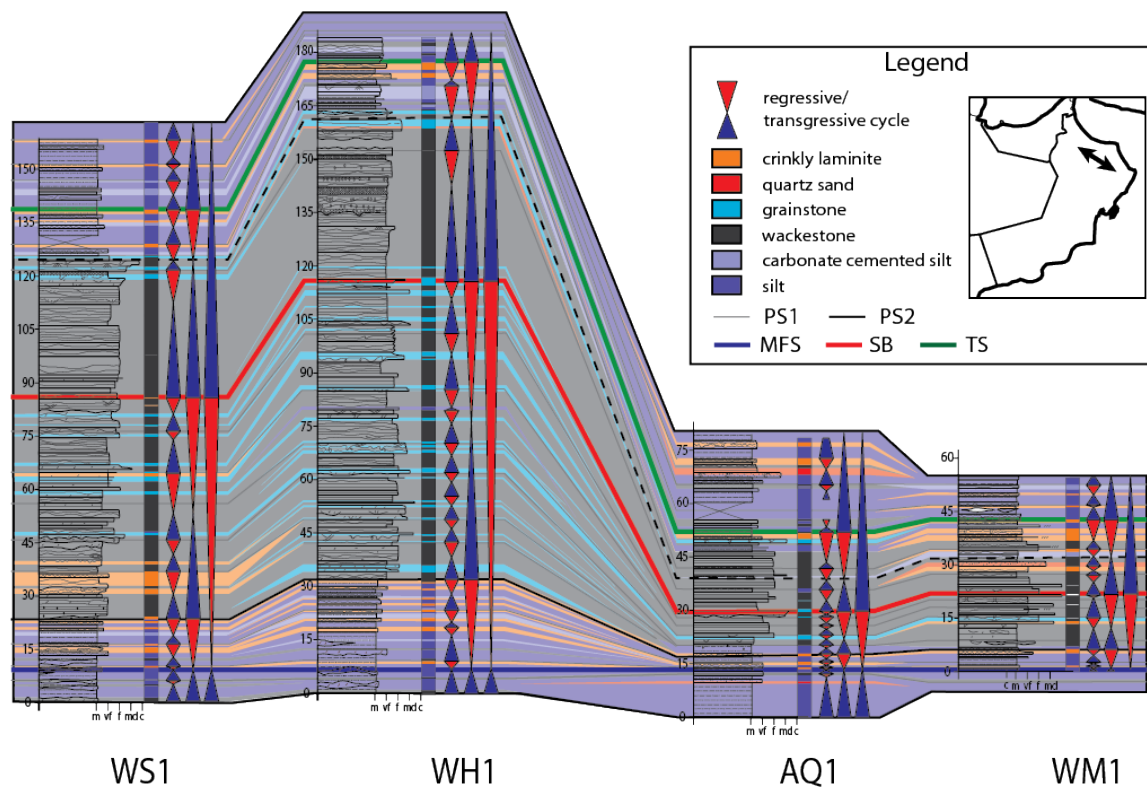


**Figure 16:** Sequence stratigraphic correlation of stratigraphic sections from the Oman Mountains highlighting transgressive-regressive cycles and facies distributions. Colored bars show facies distributions; colored wedges correlate major facies patterns between sections. Sequence scale transgressive-regressive cycles are shown at the parasequence set, composite parasequence set, and sequence scale. Stratigraphic surfaces are given in the key.

## Discussion

In the following section we will discuss the environmental context of Khufai Formation deposition including depositional environment, ramp geometry, eustatic trends, and the source of siliciclastic material. In addition, we will explore the role of syndepositional faulting in producing the unusual facies and stratigraphic geometries present at Buah Dome. Finally, we will address the potential of the Khufai Formation for future hydrocarbon exploration and development.

### ***Depositional Environments***

The Khufai Formation was deposited as a low angle ramp complex on an arid, siliciclastic sediment starved, margin. The Khufai Formation thins significantly in the Oman mountains, matching trends in water depth for the underlying Masirah Bay Formation (Allen and Leather, 2006) which suggest deeper water sedimentation and condensation of the section. The transition between shallow and deep-water sections is not exposed, preventing detailed assessment of the shelf-to-basin transition. While the Khufai has a “layer-cake” appearance, strong lateral facies variability is present. The distribution of the most variable facies is directly dependent on accommodation and the supply of siliciclastic sediment. Where siliciclastics were a minor component, transitions between peritidal grainstone and microbial buildup facies dominated shallow-water sedimentation patterns. Where siliciclastic sedimentation was high, such as at Buah Dome, sands were incorporated into peritidal grainstone intervals and microbial components are absent. Varying levels of restriction in the inner lagoon environment created the extensive tepee belts present in Khufai Dome compared to the stromatolite-dominated Mukhaibah Dome.

### ***Ramp Geometry***

The trends observed in parasequence stacking patterns can be used to extrapolate the geometry of the whole ramp complex for important times in its evolution. A dip-oriented cross-section cartoon is presented in Figure 17 in which the ramp is subdivided into five time intervals (T1-T4) that illustrate its evolution. The solid and dashed boxes indicate the approximate extent of the observable outcrop area in the Huqf and Oman Mountains respectively.

The cross-section begins at the sequence boundary in the Masirah Bay Formation (Allen and Leather, 2006). T1 illustrates the transgressive system tract (TST) between this sequence boundary and the maximum flooding interval in the lower Khufai Formation, showing the simultaneous flooding and decrease in siliciclastic supply. Increased carbonate production and export to down-dip parts of the ramp ensued, resulting in the intraclast wackestone and packstone facies.

T2 illustrates ramp evolution from the maximum flooding surface up to the main SB in the Khufai Formation. This HST includes the majority of the Khufai Formation. The shoal complex is inferred to have had very low relief at the beginning but its relief increased slightly through time. Increased restriction of the ramp as a whole is attributed to decreased circulation from the shoal complex barrier and decreased accommodation within the inner lagoons. Late highstand deposition occurs after the shoal complex prograded beyond the outcrop areas and includes restricted microbial flats and cyclic peritidal deposits. Increasing contributions of restricted lagoonal facies suggest continued expansion of the inner ramp. Parasequence thickness decreases throughout this interval, and approaches a minimum during the late highstand.

T3 shows the time of increasing parasequence thickness up to a TS after the main SB. Lagoonal facies are thick and extensive in this interval and large domal stromatolites appear in Khufai and Mukhaibah domes. The uppermost parasequence capping stromatolites in Mukhaibah Dome become highly elongate, consistent with strong wave currents (cf. Grotzinger, 1986). These changes are likely tied to building of the ramp crest and increased accommodation within the inner ramp. Sediment grain types change significantly as well with the replacement of oncoids with ooids as the dominant coated

grain type along with the influx of siliciclastic sand. While oolites are rare in most of the Khufai Formation their few occurrences are similar to the TS marker bed and foreshadow the transgression.

T4 illustrates the dramatic transgressive surface of the upper Khufai Formation transitioning into the lowermost Shuram Formation. This surface is marked by a very coarse intraclast oolite and associated meter-scale muddy stromatolite bioherms before flooding into HCS-bearing dolomudstone and red Shuram siltstone. The MFS within the lower Shuram Formation is generally not exposed, but where visible contains dark red siltstone.

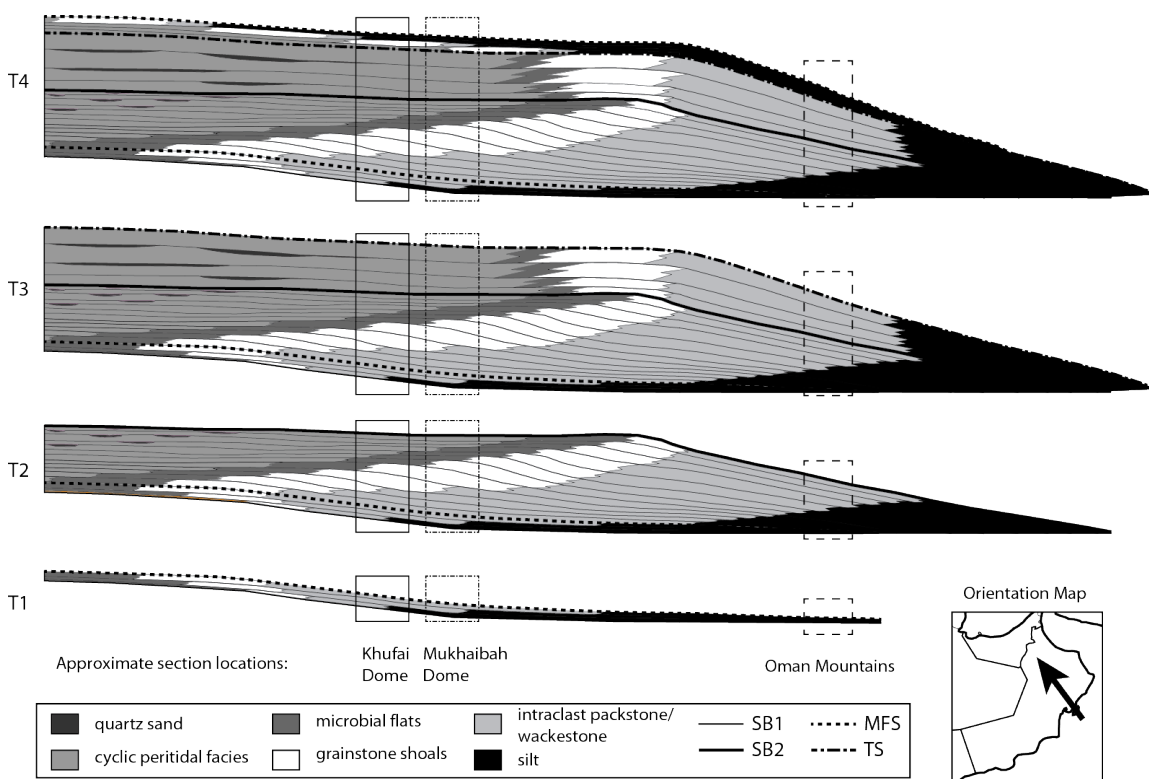


**Figure 17:** Schematic depositional profiles of the Khufai through 4 major time steps. Boxes show approximate zones of Khufai Dome, Mukhaibah Dome, and Oman Mountain outcrop exposures. T1: SB in the Masirah Bay formation up through the MFS in the lower Khufai Formation. T2: MFS up to SB2. T3: SB2 up to the transgressive surface. T4: Flooding into the Shuram formation. Map inset shows approximate primary ramp orientation.

### *Eustatic Trends*

Khufai parasequence stacking patterns vary from high-frequency, low-amplitude trends approaching the sequence boundary, to low-frequency, moderate-amplitude trends afterward. These changes can be interpreted to reflect eustatic variability in greenhouse, vs. icehouse conditions (Read, 1995; Elrick, 1996; Pope and Read, 1998), or alternatively changes in sediment supply and export (Burgess, 2001). Deconvolving these trends can be challenging, but detailed analysis of the facies variability can be helpful. A net decrease in parasequence thickness through the main HST is evident, along with a change in the visually dominant scale of cyclicity to PS from PS1 (Figure 15). The facies variability within each parasequence in this interval generally only includes two or three facies coincident with a relatively small range in water depth (1-3 m). This changes above the sequence boundary where the PS-scale of cyclicity becomes difficult to observe and instead PS1 or PS2 scales of variability dominate outcrop and facies patterns, incorporating much larger numbers of facies and ranges of water depth (Figure 4a, 15); similar trends occur in the Oman Mountains (Figure 16).

The environmental context of the terminal Khufai Formation has significant implications for the Shuram carbon isotopic excursion, specifically whether the end of carbonate deposition relates to flooding by a eustatic mechanism or a more exotic geochemical mechanism (Le Guerroue and Cozzi, 2010; Grotzinger et al., 2011). While this study does not address the potential geochemical causes specifically, data presented here indicate that the Khufai-Shuram boundary is marked by strong transgression with evidence for continued carbonate deposition, similar to what is observed in other globally distributed strata that preserve the Shuram excursion (Grotzinger et al., 2011). This

suggests a eustatic control on flooding, consistent with the return of open marine facies and parasequence stacking patterns indicative of a major increase in accommodation. Strata deposited just prior to the transgression reflect a gradual change to less restricted conditions and do not contain evidence for a significant hiatus. Furthermore, continuation of carbonate deposition (ooids) and cementation into the Shuram Formation is inconsistent with an environmental collapse of the carbonate factory, and instead points to increased siliciclastic sediment supply as the driver of lithological change. Overall we suggest that the transition from the Khufai Formation to the Shuram was a change in the balance between siliciclastic and carbonate deposition reflective of a strong transgressive event.

### *Clastic input*

Quartz sand occurs in three zones within the Khufai stratigraphy: the upper peritidal facies of Khufai and Mukhaibah domes, throughout the calc- to quartz arenites of Buah Dome, and in deformed upper beds of the Oman Mountains. The former two instances were interpreted as tidal channels cutting through the middle-ramp of the Huqf region (McCarron, 1999). In contrast, the Huqf sands were interpreted as inner-ramp tidal channels that cut through carbonate tidal flat deposits (Gorin et al., 1982). A beach origin for the thin sandstones in Khufai and Mukhaibah domes was hypothesized and the grainstone and sandstone at Buah dome were not differentiated in Wright et al. (1990). An eastward source of the sand was interpreted and fed from an onshore zone of deflation where sand was produced and subsequently blown into and reworked in the marine realm (Gorin et al., 1982; McCarron, 1990).

We suggest that termination of distal siliciclastic sedimentation in the lower Khufai Formation resulted from drowning of the source during marine transgression. It is implied that a source area for siliciclastics was exposed updip of the preserved outcrop areas during marine regression. The arid setting is consistent with active aeolian sand dune formation, although all of the sand bodies in the Khufai Formation show evidence of both wave reworking and combination with marine carbonate sediments (ooids, coated sand grains). It is suggested that the sands were deposited in the marine realm, but were likely introduced by eolian and local fluvial processes and reworked during parasequence scale flooding events as in the Permian San Andres Formation (Phelps et al., 2008). The models presented previously describing the small deposits of sand in the southern Huqf as tidal channels are consistent with our observations (Gorin et al., 1982). The non-wave reworked, slumped sands in the Oman Mountains were likely emplaced as mass flows downslope in a deeper environment.

The large accumulations of mixed quartz sand and carbonate grains at Buah Dome require further explanation. Modern arid carbonate producing environments in the Arabian Gulf provide significant insight into the source of siliciclastics in the Khufai ramp. The Holocene leeward coast of the Qatar Peninsula has migrating eolian sand dunes transport sand directly into marine carbonate-producing areas (Shinn, 1973b). These sands are incorporated into carbonate deposits as meter-scale beds of wave-reworked fine to medium sandstone. The description of these deposits is consistent with the sedimentological and depositional patterns observed at Buah Dome. The scale of facies heterogeneity in the Khufai Formation mirrors variation in the modern day Arabian

coast and reflects complex shore line geometries, with strong lateral gradients in sediment supply (Shinn, 1973a, 1973b).

Previous studies of mixed clastic-carbonate systems have demonstrated the stratigraphic controls on sand body accumulation (Kerans et al., 1994; McNeill et al., 2004; Barnaby and Ward, 2007; Phelps et al., 2008). In the Permian Basin of west Texas, bypass of aeolian sand into downslope environments is well documented (Phelps et al., 2008). Sequence boundaries sit directly below packages of siliciclastics, suggesting that Khufai sands also may have accumulated during increases in accommodation. The potential source of this accommodation will be discussed in the following section.

### ***Synsedimentary Faulting***

While Buah Dome is in close proximity to other Huqf exposures, its depositional patterns differ significantly from the simple ramp model and may suggest the influence of syndepositional faulting. This hypothesis is based on circumstantial evidence, but is supported by abrupt lateral facies changes, very coarse, deformed, conglomeratic wackestones in the late HST, and incorporation of larger amounts of siliciclastic material. Figure 15 illustrates the abrupt lateral facies differences between Buah Dome 5 (BD5) and Khufai Dome East (KDE), which are separated by only 13.3 km and lie along a depositional strike-parallel trend. For instance, throughout the Huqf region facies and parasequence stacking patterns at all domes indicate shallowing to an accommodation minimum in the top 60-80 m of section; however, facies and stacking patterns after this point at Buah Dome diverge and contain thick packages of outer- to mid-ramp deposits.

This contrasts with the much greater lateral uniformity of facies between MD5 and KDE that spans a distance of approximately 35 km (Figure 15).

Additional support for synsedimentary-faulting comes from the interpretation of intraclast wackestone facies and soft sediment deformation features at Buah Dome. The intraclast wackestone/packstone facies at Buah Dome frequently contains unusually large clasts (cm- to dm-scale). While this difference is relatively minor in the base of the section, it increases near the top of the formation to include coarse pebble to cobble-size clasts, and breccia layers. These beds are associated with large scale slumping, contorted beds, and fluid escape structures, and resemble seismites produced in carbonates or mixed sedimentary systems (Pope et al., 1997; Onasch and Kahle, 2002). While similar features can be produced by loading, storm or tidal reworking, or gravity driven slumping, the lateral continuity, size, and stratigraphic context of these features suggests faulting (Greb and Denver, 2002; Wheeler, 2002). The presence of early-cemented shallow water carbonates in the intraclast breccias at Buah Dome may indicate a fault-induced depth gradient.

Finally, the presence of thick siliciclastic deposits at Buah Dome also is consistent with synsedimentary faulting. Regional correlation across the Huqf area suggests that sand bodies at Buah Dome accumulated as other parts of the platform experienced extremely low accommodation and sediment bypassing (Figure 15). The parasequence thickness patterns indicate that this does not simply represent a change in position relative to the regional shoreline, but instead increased accommodation and accumulation of eolian sands that would have otherwise bypassed at times of sea level lowstand.

These lines of evidence for synsedimentary-faulting are largely circumstantial as little is known about the nature of the faults themselves. No small-scale growth faults are directly observed in outcrop that might confirm this hypothesis. However, significant thickness and facies variability were noted in the Masirah Bay and Buah formations (Cozzi and J. Grotzinger, 2004; Allen and Leather, 2006). These observations all are consistent with the possibility of local tectonic activity during Khufai Formation deposition. It appears that a long-lived structure that bisects Buah Dome – the Maradi Fault – may have expressed itself during Nafun deposition and influenced sedimentation patterns all through the Phanerozoic history of this part of Oman (Hanna and Nolan, 1989)

#### ***Implications for hydrocarbon exploration***

The Khufai Formation contains facies with both depositional and diagenetic potential as hydrocarbon reservoirs. Dolomitized carbonates worldwide have proven to be very successful reservoirs (Alsharhan and Nairn, 1997; Ahr, 2008). While most are younger than the Khufai Formation, proven plays in the overlying Ara Group suggest excellent preservation and seal quality (Al-Siyabi, 2005).

While very low in total organic carbon (generally <0.05%), the lower Khufai Formation is petroliferous, particularly in zones of extensive recrystallization, which may serve to concentrate mobile hydrocarbon. The facies in the Oman Mountains are fetid (H<sub>2</sub>S rich) rather than petroliferous, but their black color speaks to a history rich in organic carbon. Additional source rock potential comes from the underlying shales of the Masirah Bay Formation that are organic-rich (Terken et al., 2001; Grosjean et al., 2009).

The reservoir potential of the Khufai Formation is considerable, but diagenetic factors such as subsurface cementation history will require more exploration. Coarse oncolite grainstone facies of the middle to late HST are likely reservoir candidates. However, in outcrop significant porosity occluding silicification has occurred; it is not known to what extent silicification has impacted the subsurface. In contrast, recrystallization and dolomitization processes in the lower Khufai Formation were extensive and acted to create pockets of extremely coarsely crystalline, porous material. The degree of interconnectivity of these pockets will be very important for exploration. Perhaps the most promising potential reservoir facies of the Khufai Formation are the quartz sandstones within Buah Dome. These sands are poorly cemented in outcrop and are capped with either tight intraclast wackestone facies or siltstone. The position of these deposits on the margin of an active tectonic system (as at Buah Dome) suggests the possibility of more widespread sand incorporation in other paleo-lows. While the lateral extent of this facies in the subsurface is unknown, owing to structural and environmental complexity, mapping with traditional well techniques may be very informative.

### **Conclusions**

- The Khufai Formation records continuous deposition of a carbonate ramp during the Ediacaran Era. It contains three major sequence stratigraphic surfaces that define one and a half depositional sequences. The majority of the Khufai Formation comprises a highstand system tract and records progradation of the ramp, capturing facies ranging from outer-ramp to supratidal depositional environments. Distal ramp depositional environments are recorded in the Oman Mountains. Parasequence stacking patterns reveal a transition from high-frequency,

low-amplitude to low-frequency, moderate-amplitude sea level oscillation at the sequence boundary

- This carbonate platform displays considerable facies variability and depositional complexity introduced from siliciclastic sediment supply and potentially syndepositional faulting. Siliciclastic input is most prevalent in the northern Huqf where large quantities of quartz sandstone are incorporated with and replace carbonate facies. Discrepancies between this area and the other platform locations along with seismite facies suggest the potential for previously undocumented tectonism concurrent with deposition.
- Potential for hydrocarbon exploration and development exists in the Khufai Formation with potential source (basal mudstone), reservoir (oncolite grainstone, quartz sandstone, diagenetic fabrics), and seal facies (basal mudstones, Shuram Formation siltstones) being identified. However, further investigation of the subsurface cementation history and the connectivity of high porosity facies groups will be required.
- The boundary between the Khufai and Shuram formations is not a major unconformity and is instead marked by rapid transgression and a return to deeper water, siliciclastic-dominated deposition. Accordingly, this boundary cannot account for the missing time between dated intervals of the Huqf Supergroup as suggested previously. While a sequence boundary does occur within the upper Khufai Formation, it is well below the Khufai-Shuram lithostratigraphic boundary and the onset of the Shuram isotopic excursion.

**Acknowledgements:** We would like to thank: William Wilks, Gordon Forbes, Gideon Lopes-Cardozo, Joachim Amthor, and other Petroleum Development Oman personnel for helpful discussions, Salim Al Maskery for field support and logistics, the participants of the 2009 Agouron Advanced Field Course for initial stratigraphic observation, the Ministry of Oil and Gas, Sultanate of Oman for permission to carry out and publish this research, and Michael Pope, Erwin Adams, and Stephan Schroder for helpful and constructive reviews.

#### References Cited

- Ahr, W. M., 2008, *Geology of Carbonate Reservoirs: Wiley-Interscience, Identification, Description, and Characterization of Hydrocarbon Reservoirs in Carbonate Rocks*, p. 296.
- Al-Siyabi, H. A., 2005, Exploration history of the Ara intrasalt carbonate stringers in the South Oman Salt Basin: *GeoArabia*, v. 10, no. 4, p. 39–54.
- Allen, P. A., 2007, The Huqf Supergroup of Oman: Basin development and context for Neoproterozoic glaciation: *Earth-science reviews*, v. 84, p. 139–185.
- Allen, P. A., and J. Leather, 2006, Post-Marinoan marine siliciclastic sedimentation: The Masirah Bay Formation, Neoproterozoic Huqf Supergroup of Oman: *Precambrian Research*, v. 144, no. 3-4, p. 167–198.
- Allen, P. A., J. Leather, M. Brasier, R. Rieu, M. McCarron, E. Le Guerroue, S. Bowring, J. Grotzinger, J. Etienne, and A. Cozzi, 2011, The Abu Mahara Group (Ghubrah and Fiq Formations), Jabal Akhdar, Oman: *Geological Society, London, Memoirs*, v. 36, p. 251–262.
- Alsharhan, A. S., and A. E. M. Nairn, 1997, *Sedimentary Basins And Petroleum Geology Of The Middle East: Elsevier Science*, p. 942.
- Assereto, R. L., and C. Kendall, 1977, Nature, origin and classification of peritidal tepee structures and related breccias: *Sedimentology*, v. 24, p. 153–210.
- Barnaby, R. J., and W. B. Ward, 2007, Outcrop analog for mixed siliciclastic-carbonate ramp reservoirs - Stratigraphic hierarchy, facies architecture, and geologic heterogeneity: Grayburg Formation, Permian basin, USA: *Journal of Sedimentary Research*, v. 77, p. 34–58.

- Betzler, C., J. Reijmer, K. Bernet, G. Eberli, and F. Anselmentti, 1999, Sedimentary patterns and geometries of the Bahamian outer carbonate ramp (Miocene- Lower Pliocene, Great Bahama bank): *Sedimentology*, v. 46, no. 1127–1143.
- Bowring, S. A., J. P. Grotzinger, D. J. Condon, J. Ramezani, M. J. Newall, and P. A. Allen, 2007, Geochronologic constraints on the chronostratigraphic framework of the Neoproterozoic Huqf Supergroup, Sultanate of Oman: *American Journal of Science*, v. 307, no. 10, p. 1097–1145.
- Brasier, M., G. McCarron, R. Tucker, J. Leather, P. Allen, and G. Shields, 2000, New U-Pb zircon dates for the Neoproterozoic Ghubrah glaciation and for the top of the Huqf Supergroup, Oman: *Geology*, v. 28, no. 2, p. 175–178.
- Burgess, P. M., 2001, Modeling carbonate sequence development without relative sea-level oscillations: *Geology*, v. 29, no. 12, p. 1127–1130.
- Burns, S. J., and A. Matter, 1993, Carbon isotopic record of the latest Proterozoic from Oman: *Eclogae geologicae Helvetiae*, v. 86, no. 2, p. 595–607.
- Carto, S. L., and N. Eyles, 2011, The deep-marine glaciogenic Gaskiers Formation, Newfoundland, Canada, *in* The geological record of Neoproterozoic glaciations: Geological Society, London, Memoirs, p. 467–473.
- Cozzi, A., and J. Grotzinger, 2004, Evolution of a terminal Neoproterozoic carbonate ramp system (Buah Formation, Sultanate of Oman): Effects of basement paleotopography: *Geological Society of America Bulletin*, v. 116, no. 11/12, p. 1367–1384.
- Cozzi, A., P. A. Allen, and J. P. Grotzinger, 2004, Understanding carbonate ramp dynamics using  $\delta^{13}\text{C}$  profiles: examples from the Neoproterozoic Buah Formation of Oman: *Terra Nova*, v. 16, no. 2, p. 62–67.
- Dibenedetto, S., and J. Grotzinger, 2005, Geomorphic evolution of a storm-dominated carbonate ramp (c. 549 Ma), Nama Group, Namibia: *Geological Magazine*, v. 142, no. 5, p. 583–604.
- Elrick, M., 1996, Sequence stratigraphy and platform evolution of Lower–Middle Devonian carbonates, eastern Great Basin: *GSA Bulletin*, v. 108, no. 4, p. 392–416.
- Elrick, M., and J. Read, 1991, Cyclic Ramp-to-Basin Carbonate Deposits, Lower Mississippian, Wyoming and Montana: A Combined Field and Computer Modeling Study: *Journal of Sedimentary Research*, v. 61, no. 7, p. 1194–1224.
- Eyles, N., and C. H. Eyles, 2006, Glacially-influenced deep-marine sedimentation of the Late Precambrian Gaskiers Formation, Newfoundland, Canada: *Sedimentology*, v. 36, no. 4, p. 601–620.
- Fairchild, I., 1991, Origins of carbonate in Neoproterozoic stromatolites and the

- identification of modern analogues: *Precambrian Research*, v. 53, p. 281–299.
- Fairchild, I., and P. Herrington, 1989, A tempestite-stromatolite-evaporite association (Late Vendian, East Greenland): a shoreface-lagoon model: *Precambrian Research*, v. 43, p. 101–127.
- Fike, D. A., and J. P. Grotzinger, 2008, A paired sulfate–pyrite  $\delta^{34}\text{S}$  approach to understanding the evolution of the Ediacaran–Cambrian sulfur cycle: *Geochimica et Cosmochimica Acta*, v. 72, p. 2636–2648.
- Fike, D. A., J. P. Grotzinger, L. M. Pratt, and R. E. Summons, 2006, Oxidation of the Ediacaran Ocean: *Nature*, v. 444, no. 7120, p. 744–747.
- Forbes, G., H. Jansen, and J. Schreurs, 2010, *Lexicon of Oman Subsurface Stratigraphy: Manama, Bahrain, GeoArabia Special Publication 5*.
- Goldhammer, R. K., P. A. Dunn, and L. A. Hardie, 1990, Depositional styles, composite sea-level changes, cycle stacking patterns, and the hierarchy of stratigraphic forcing: Examples from Alpine Triassic platform carbonates: *GSA Bulletin*, v. 102, p. 535–562.
- Gorin, G., L. Racz, and M. Walter, 1982, Late Precambrian-Cambrian sediments of the Huqf Supergroup, Sultanate of Oman: *AAPG Bulletin*, v. 66, p. 2209–2627.
- Greb, S. F., and G. R. J. Denver, 2002, Critical evaluation of possible seismites: Examples from the Carboniferous of the Appalachian basin, *in* F. R. Ettensohn, N. Rast, and C. E. Brett, eds., *Ancient Seismites: GSA Bulletin Special Papers*, p. 109–125.
- Grosjean, E., G. D. Love, C. Stalvies, D. A. Fike, and R. E. Summons, 2009, Origin of petroleum in the Neoproterozoic–Cambrian South Oman Salt Basin: *Organic Geochemistry*, v. 40, no. 1, p. 87–110, doi:10.1016/j.orggeochem.2008.09.011.
- Grotzinger, J., 1986, Evolution of early proterozoic passive-margin carbonate platform, Rocknest Formation, Wopmay Orogen, Northwest Territories, Canada: *Journal of Sedimentary Petrology*, v. 56, no. 6, p. 831–847.
- Grotzinger, J., and J. Amthor, 2002, Facies and reservoir architecture of isolated microbial carbonate platforms, terminal Proterozoic-early Cambrian Ara Group, South Oman salt basin, AAPG ACE, Houston, TX.
- Grotzinger, J., H. Al-Siyabi, R. Al-Hashimi, and A. Cozzi, 2002, New model for tectonic evolution of Neoproterozoic-Cambrian Huqf Supergroup basins, Oman, *in* *GeoArabia*: p. 241.
- Grotzinger, J. P., 1986, Cyclicality and paleoenvironmental dynamics, Rocknest platform, northwest Canada: *GSA Bulletin*, v. 97, p. 1208–1231.

- Grotzinger, J. P., 1989, Facies evolution of Precambrian carbonate depositional systems: emergence of the modern platform archetype: *SEPM Special Publication*, p. 79–106.
- Grotzinger, J. P., and A. H. Knoll, 1999, Stromatolites in precambrian carbonates: evolutionary mileposts or environmental dipsticks?: *Annual Review of Earth and Planetary Sciences*, v. 27, p. 313–358.
- Grotzinger, J. P., D. A. Fike, and W. W. Fischer, 2011, Enigmatic origin of the largest-known carbon isotope excursion in Earth's history: *Nature Geoscience*, v. 4, no. 5, p. 285–292.
- Halverson, G., 2005, Toward a Neoproterozoic composite carbon-isotope record: *Geological Society of America Bulletin*, v. 117, no. 9, p. 1181.
- Hanna, S., and S. Nolan, 1989, The Maradi Fault Zone - Evidence of Late Neogene Tectonics in the Oman Mountains: *Journal of the Geological Society*, v. 146, p. 867–871.
- Hebert, C. L., A. J. Kaufman, S. C. Penniston-Dorland, and A. J. Martin, 2010, Radiometric and stratigraphic constraints on terminal Ediacaran (post-Gaskiers) glaciation and metazoan evolution: *Precambrian Research*, v. 182, no. 4, p. 402–412.
- Kendall, C., and J. Warren, 1987, A review of the origin and setting of tepees and their associated fabrics: *Sedimentology*, v. 34, p. 1007–1027.
- Kerans, C., and W. Fitchen, 1995, Sequence Hierarchy and Facies Architecture of a carbonate-ramp system: San Andres Formation of Algerita Escarpment and Western Guadalupe Mountains, West Texas and New Mexico, Report of Investigations No. 235: Austin, Bureau of Economic Geology, UT Austin, 1–86 p.
- Kerans, C., F. Lucia, and R. Senger, 1994, Integrated characterization of carbonate ramp reservoirs using Permian San Andres Formation outcrop analogs: *AAPG Bulletin*, v. 78, no. 2, p. 181–216.
- Knoll, A. H., and K. Swett, 1990, Carbonate deposition during the late Proterozoic Era: and example from Spitsbergen: *American Journal of Science*, v. 290-A, p. 104–132.
- Koerschner, W., and J. Read, 1989, Field and Modeling Studies of Cambrian Carbonate Cycles, Virginia Appalachians: *Journal of Sedimentary Petrology*, v. 59, no. 5, p. 654–687.
- Krinsley, D. H., P. F. Friend, and R. Klimentidis, 1976, Eolian transport textures on the surfaces of sand grains of Early Triassic age: *GSA Bulletin*, v. 87, p. 130–132.
- Le Guerroue, E., and A. Cozzi, 2010, Veracity of Neoproterozoic negative C-isotope values: The termination of the Shuram negative excursion: *Gondwana Research*, v. 17, no. 4, p. 653–661.

- Le Guerroue, E., P. A. Allen, and A. Cozzi, 2006a, Chemostratigraphic and sedimentological framework of the largest negative carbon isotopic excursion in Earth history: The Neoproterozoic Shuram Formation (Nafun Group, Oman): *Precambrian Research*, v. 146, p. 68–92.
- Le Guerroue, E., P. A. Allen, and A. Cozzi, 2006b, Parasequence development in the Ediacaran Shuram Formation (Nafun Group, Oman): high-resolution stratigraphic test for primary origin of negative carbon isotopic ratios: *Basin Research*, v. 18, no. 2, p. 205–219.
- Le Guerroue, E., P. A. Allen, A. Cozzi, J. L. Etienne, and M. Fanning, 2006c, 50 Myr recovery from the largest negative  $\delta^{13}\text{C}$  excursion in the Ediacaran ocean: *Terra Nova*, v. 18, no. 2, p. 147–153.
- Lehrmann, D., Y. Wan, J. Wei, Y. Yu, and J. Xiao, 2001, Lower Triassic peritidal cyclic limestone: an example of anachronistic carbonate facies from the Great Bank of Guizhou, Nanpanjiang Basin, Guizhou province, South China: *Palaeo*, v. 173, p. 103–125.
- Markello, J., 1981, Carbonate ramp-to-deeper shale shelf transitions of an Upper Cambrian intrashelf basin, Nolichucky Formation, Southwest Virginia Appalachians: *Sedimentology*, v. 28, p. 573–597.
- Mattes, B., and S. Conway Morris, 1990, Carbonate/evaporite deposition in the late Precambrian - Early Cambrian Ara Formation of Southern Oman: The Geology and Tectonics of the Oman Region, Geological Society Special Publication, v. 49, p. 617–636.
- McCarron, G. M., 1999, Sedimentology and stratigraphy of the Nafun Group, Huqf Supergroup, Oman: p. 1–302.
- McNeill, D. F., K. J. Cunningham, and L. A. Guertin, 2004, Depositional Themes of Mixed Carbonate-siliciclastics in the South Florida Neogene: Application to Ancient Deposits, *in* Integration of outcrop and modern analogs to reservoir modeling: AAPG Memoir 80, p. 1–21.
- Onasch, C. M., and C. F. Kahle, 2002, Seismically induced soft-sediment deformation in some Silurian carbonates, eastern U.S. midcontinent, *in* F. R. Ertensohn, N. Rast, and C. E. Brett, eds., *Ancient Seismites: GSA Bulletin Special Papers*, p. 165–179.
- Orpin, A., G. Brunskill, I. Zagorskis, and K. Woolfe, 2004, Patterns of mixed siliciclastic-carbonate sedimentation adjacent to a large dry- tropics river on the central Great Barrier Reef shelf, Australia: *Australian Journal of Earth Sciences*, v. 51, p. 665–683.
- Phelps, R. M., C. Kerans, S. Z. Scott, X. Janson, and J. A. Bellian, 2008, Three-dimensional modeling and sequence stratigraphy of a carbonate ramp-to-shelf transition, Permian Upper San Andres Formation: *Sedimentology*, v. 55, p. 1777–

1813.

- Pope, M. C., and J. F. Read, 1998, Ordovician meter-scale cycles: implications for climate and eustatic fluctuations in the central Appalachians during a global greenhouse, non-glacial to glacial transition: *Palaeogeography, Palaeoclimatology, Palaeoecology*, v. 138, p. 27–42.
- Pope, M. C., J. F. Read, R. Bambach, and H. J. Hofmann, 1997, Late Middle to Late Ordovician seismites of Kentucky, southwest Ohio and Virginia: Sedimentary recorders of earthquakes in the Appalachian basin: *GSA Bulletin*, v. 109, no. 4, p. 489–503.
- Read, J., 1985, Carbonate Platform Facies Models: *AAPG Bulletin*, v. 69, p. 1–21.
- Read, J. F., 1995, Overview of Carbonate Platform Sequences, Cycle Stratigraphy and Reservoirs in Greenhouse and Ice House Worlds, *in* J. F. Read, C. Kerans, L. J. Weber, J. F. Sarg, and F. M. Wright, eds., *Milankovitch Sea-Level Changes, Cycles, and Reservoirs on Carbonate Platforms in Greenhouse and Ice-House Worlds: SEPM Short Course*, p. 1–103.
- Riding, R., 2000, Microbial carbonates: the geological record of calcified bacteria-algal mats and biofilms: *Sedimentology*, v. 47, no. 1, p. 179–214.
- Rieu, R., and P. A. Allen, 2008, Siliciclastic sedimentation in the interlude between two Neoproterozoic glaciations, Mirbat area, southern Oman: A missing link in the Huqf Supergroup?: *GeoArabia*, v. 13, no. 4, p. 45–72.
- Sami, T. T., and N. P. James, 1994, Peritidal Carbonate Platform Growth and Cyclicity in an Early Proterozoic Foreland Basin, Upper Pethei Group, Northwest Canada: *Journal of Sedimentary Research*, v. B64, no. 2, p. 111–131.
- Sami, T. T., and N. P. James, 1996, Synsedimentary cements as Paleoproterozoic platform building blocks, Pethei Group, Northwestern Canada: *Journal of Sedimentary Research*, v. 66, no. 1, p. 209–222.
- Schlager, W., J. Reijmer, and A. Droxler, 1994, Highstand shedding of carbonate platforms: *Journal of Sedimentary Research*, v. B64, no. 3, p. 270–281.
- Shinn, E., 1973a, Carbonate coastal accretion in an area of longshore transport, NE Qatar, Persian Gulf, *in* B. H. Purser, ed., *The Persian Gulf*: New York, Heilberg, Berlin, Springer-Verlang, p. 179–191.
- Shinn, E., 1973b, Sedimentary accretion along the Leeward, SE Coast of Qatar Peninsula, Persian Gulf, *in* B. H. Purser, ed., *The Persian Gulf*: New York, Heidelberg, Berlin, Springer-Verlang, p. 199–209.
- Shinn, E., R. Lloyd, and R. Ginsburg, 1969, Anatomy of a modern carbonate tidal-flat, Andros island, Bahamas: *Journal of Sedimentary Research*, v. 39, no. 3, p. 1202–

1228.

- Sumner, D., and W. Corcoran, 2001, Decimeter-thick encrustations of calcite and aragonite on the sea floor and implications for Neoproterozoic and Neoproterozoic ocean chemistry: p. 107–120.
- Terken, J. M. J., N. L. Frewin, and S. L. Indrelid, 2001, Petroleum Systems of Oman: Charge Timing and Risks: AAPG Bulletin, v. 85, no. 0, p. 1817–1845.
- Tinker, S., 1998, Shelf to basin facies distributions and sequence stratigraphy of a steep-rimmed carbonate margin: Capitan depositional system, McKittrick Canyon, New Mexico and Texas: *Journal of Sedimentary Research*, v. 68, no. 6, p. 1146–1174.
- Tucker, M., and V. Wright, 1990, *Carbonate Sedimentology*: Blackwell Science, p. 482.
- Wheeler, R., 2002, Distinguishing seismic from nonseismic soft-sediment structures: Criteria from seismic-hazard analysis, *in* F. R. Ettensohn, N. Rast, and C. E. Brett, eds., *Ancient Seismites*: GSA Special Papers 359.
- Wilson, J., 1975, *Carbonate Facies in Geologic History*: London, Heidelberg, Berlin, Springer-Verlag.
- Wood, R., J. Grotzinger, and J. Dickson, 2002, Proterozoic Modular Biomineralized Metazoan from the Nama Group, Namibia: *Science*, v. 296, no. 5577, p. 2383–2386.
- Wright, V., A. Ries, and S. Munn, 1990, Intraplatformal basin-fill deposits from the Infracambrian Huqf Group, east Central Oman, *in* A. Robertson, M. Searle, and A. Ries, eds., *The geology and tectonics of the Oman region*: Geological Society, p. 1–16.

## *Chapter 4*

In preparation for submission to *Earth and Planetary Science Letters*

### **Dynamic changes in the isotopic record of sulfate preceding the Shuram Excursion**

Magdalena R. Osburn <sup>a\*</sup>, Jeremy Owens <sup>b</sup>, Kristin D. Bergmann <sup>a</sup>, John P. Grotzinger <sup>a</sup>,  
and Timothy W. Lyons <sup>b</sup>

<sup>a</sup> Division of Geological and Planetary Sciences, California Institute of Technology,  
Pasadena, CA 91125, USA

<sup>b</sup> Department of Earth Sciences, University of California, Riverside, CA 92521, USA

*Keywords:* CAS, Neoproterozoic, Shuram Excursion, chemostratigraphy

## ABSTRACT

The Ediacaran Period records substantial changes in ocean chemistry as the result of progressive or episodic oxidation of the deep-ocean. Large excursions in carbon and sulfur isotopic composition record these changes, but often are poorly correlated with one another or insufficiently resolved to create a mechanistic link between the two coupled systems. Here we present a high-resolution record of carbon and sulfur isotopes from the Khufai Formation, directly preceding the Shuram (large, negative) carbon isotope event. We document large coherent excursions in the sulfate-sulfur isotope and concentration records that occur both independently and in conjunction with carbon isotopic trends. These changes appear independent of major stratigraphic surfaces and facies changes, suggesting primary signals. Our data suggest very low marine sulfate concentrations are maintained at least through the middle-Khufai Formation, but require that the burial fraction of pyrite and fractionation factor between sulfate and pyrite necessarily change through deposition. In order to reconcile a simultaneous, up-section increase in marine sulfate concentration and  $\delta^{34}\text{S}$ , our numerical modeling requires the introduction of an additional flux of  $^{34}\text{S}$ -enriched sulfur. Weathering of Cryogenian  $^{34}\text{S}$ -enriched pyrite or sulfate deposits are possible sources, along with potential mixing between separate marine reservoirs. This study presents the highest resolution record yet of carbon and sulfur cycling at the onset of the Shuram carbon isotope anomaly—a critical juncture in Earth History.

## 1. Introduction

The Neoproterozoic Era was an interval of intense environmental and biological variability that included at least two Snowball Earth Glaciations (Hoffman et al., 1998; Macdonald et al., 2010), significant changes in deep ocean chemistry (Fike et al., 2006; Canfield et al., 2007; 2008), and a number of evolutionary advances and extinctions (Amthor et al., 2003; Narbonne, 2005) culminating in the Cambrian explosion. The Ediacaran period is particularly crucial in recording the evolution of the ocean-atmosphere system from a perturbed post-glacial state to one more amenable to animal evolution (Maloof et al., 2010). Environmental changes (e.g., glaciations and extinction events) during this interval are indicated primarily by isotopic (C,O,S, etc) perturbations and inorganic geochemical proxies (REE, iron speciation) measured from sedimentary deposits (Halverson, 2005; Halverson et al., 2010). Chemical proxies suggest that significant oxygenation of the deep ocean occurred during this time (Canfield et al., 2007; Scott et al., 2008; Sahoo et al., 2012), however the relationship between this overturn and isotopic excursions remains stratigraphically ambiguous. Additional ambiguity in absolute timescales, along with incomplete chemostratigraphic records, precludes the formation of mechanistic links between these events.

The Shuram Excursion is the largest negative carbon isotope excursion in both magnitude and duration recorded in Earth history (Grotzinger et al., 2011). It observed globally, including Oman, South China, Death Valley/N. Mexico, Australia, and Namibia (Burns and Matter, 1993; Calver, 2000; Halverson, 2005; Kaufman et al., 2007; McFadden et al., 2008). The excursion itself is defined by a dramatic drop in  $\delta^{13}\text{C}_{\text{carb}}$  from high values (~6 ‰) characteristic of the Ediacaran to as low as -12 ‰. A protracted

recovery period persists for 50 Ma covering a range of sedimentary environments (Le Guerroue et al., 2006b). While a number of diagenetic mechanisms have been suggested, none can account for the global occurrence of strikingly similar excursions across diverse sedimentary environments (Derry, 2010; Knauth, 2009). Primary (non-diagenetic) mechanisms to explain the Shuram Excursion are varied and controversial but broadly center on a large scale oxidation event (Rothman et al., 2003; Fike et al., 2006; Kaufman et al., 2007; McFadden et al., 2008; Grotzinger et al., 2011). Globally, the Shuram Excursion is either recorded as part of an unconformity-based transgressive package or highly condensed section (McFadden et al., 2008), which either miss the initial  $\delta^{13}\text{C}$  decline entirely or lack resolution.

The Khufai Formation, Sultanate of Oman, records both the onset of the Shuram Excursion and a ~300 m-thick continuous carbonate record beforehand. This record is the thickest and most continuous record of pre-excursion carbonate sedimentation described thus far and is therefore an ideal target for detailed observation of the environmental conditions prior to and during the excursion onset. Here we present a high-resolution paired carbon and sulfur isotopic record of the Khufai Formation demonstrating large excursions in sulfur isotope data preceding the better known carbon isotope trends.

## **2. Geological Setting**

The Huqf Supergroup spans the end Cryogenian through earliest Cambrian of Oman, outcropping in the Oman Mountains, Huqf, and Mirbat areas (Wright et al., 1990; Allen, 2007). Formations of the Huqf Supergroup are routinely accessed in the subsurface from hydrocarbon exploration wells (Forbes et al., 2010). In ascending order,

the Huqf Supergroup is composed of the Hadash, Masirah Bay, Khufai, Shuram, and Buah formations capped with the Ara Group (Wright et al., 1990). The lower formations of the Huqf Supergroup comprise the Nafun Group, which consists of two thick siliciclastic-to-carbonate grand cycles. The Khufai Formation is the carbonate phase of the first cycle, bounded above and below by siltstone and shales of the Masirah Bay and Shuram formations.

The Khufai Formation crops out in the Oman Mountains and along the central coast in the Huqf area. Sampling locations for each region are shown in Figure 1. Stratigraphic sections from the Oman Mountains preserve deep-water facies including turbiditic wackestones and packstones, deep-water microbialites, and siliciclastic siltstone (Figure 1). In contrast, the stratigraphy of the Huqf area includes platform carbonate facies ranging from outer ramp to supratidal environments (Osburn et al., 2013). Facies include a diversity of grainstone types, stromatolites, lagoonal facies, and evaporitic facies (Figure 1). Stratigraphic sections are considerably thicker in the Huqf area, ranging from 310 to 340 m compared to 50 to 185 m in the mountains. The sediments from the Huqf area are also better preserved than those of the Oman Mountains owing to shallower burial and a general lack of tectonic deformation. A full stratigraphic characterization of the Khufai Formation is presented in Osburn et al. (2013).

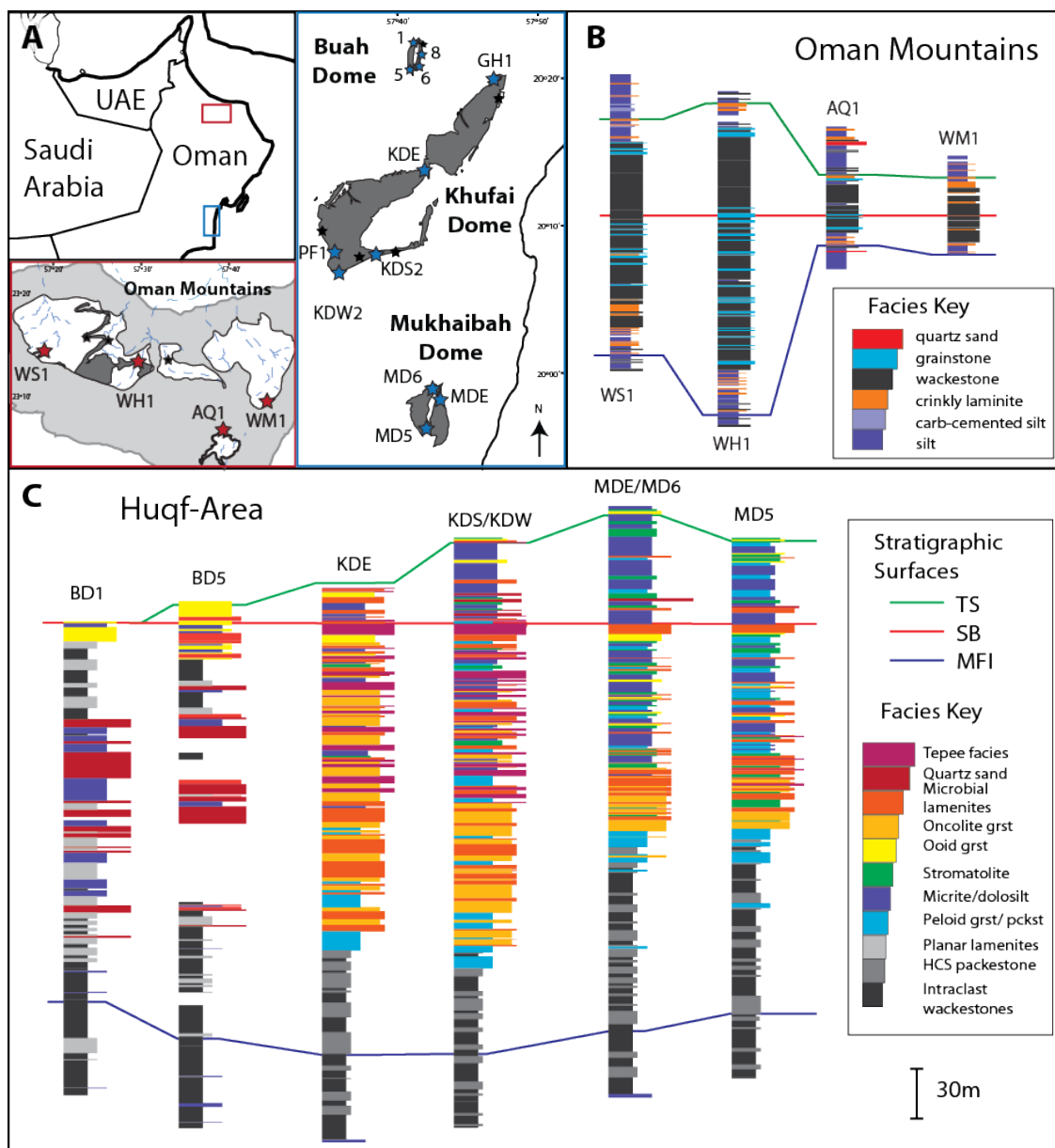


Figure 1: Geographic and stratigraphic information for the Khufai Formation. A. Location map showing the location of the Oman Mountains and Huqf in Oman with expanded panels showing the locations of sections (stars) in the Oman Mountains (top panel) and Huqf areas. B. Summary stratigraphic sections from the Oman Mountains with major sequence stratigraphic surfaces. C. Summary stratigraphic sections from the Huqf with stratigraphic surfaces.

### 3. Background – S-isotopic and concentration proxies

The record of sulfur isotopes through time has come primarily from measurements of marine evaporites, but more recently has included measurements of trace sulfate incorporated into the matrix of carbonate minerals (Claypool et al., 1980; Burdett et al., 1989; Strauss, 1997; 1993; Kampschulte and Strauss, 2004). Development of the carbonate-associated sulfate (CAS) method expanded the available record of Precambrian sulfur isotope data considerably, and in many cases revealed large magnitude isotopic excursions (Hurtgen et al., 2004; Kah et al., 2004; Gellatly and Lyons, 2005). While subject to diagenetic processes, this technique has been shown to faithfully record isotopic compositions from the modern ocean (Kampschulte and Strauss, 2004) and broadly agrees with evaporite records where both are available (Kah et al., 2004). It was demonstrated in a study of modern corals that sulfur isotopic ratios are not significantly altered during recrystallization from aragonite to calcite, although CAS concentration is lowered (Gill et al., 2008). Evaporite and CAS records agree that the latest Precambrian was a time of highly variable, but generally increasing  $\delta^{34}\text{S}_{\text{CAS}}$  preceding the extremely high values observed near the Precambrian-Cambrian boundary (Fike et al., 2006; Fike and Grotzinger, 2008; 2010; Halverson et al., 2010).

Interpretation of the concentration of sulfate in the ocean through time is considerably more complex. On a very general level, the limited occurrence of sulfate evaporites in Precambrian strata suggests significantly lower marine sulfate concentrations than in modern seawater (Strauss, 1997; Kah et al., 2004). Additional constraints come from interpretation of rates of sulfur isotopic change during particular stratigraphic intervals (e.g., Gill et al., 2012). CAS concentrations and rates of  $\delta^{34}\text{S}$

change in Precambrian rocks, and especially post-Marinoan strata, suggest very low marine sulfate concentrations (<1mM) (Hurtgen et al., 2002; Kaufman et al., 2007; Ries et al., 2009; Loyd et al., 2012). However, estimates from evaporite deposits in Oman that span the Precambrian-Cambrian boundary appear to approach roughly modern values (16 to 25 mM) (Brennan et al., 2004; Fike and Grotzinger, 2008). While there is scatter in the record, these bounds require that marine sulfate concentration increased dramatically (at least locally) between 580 and 550 Ma. A trend of increasing marine sulfate reservoir during the latest Precambrian has been suggested previously (Halverson and Hurtgen, 2007) and is supported in greater detail by this study.

#### **4. Materials and Methods**

##### *4.1 Sample collection and correlation*

Samples were collected in 2009, 2010, 2011, and 2012, in concert with stratigraphic and sedimentologic field analysis. Large samples (~500 g) for sulfur isotope analysis were taken at ~2 m intervals, whereas smaller samples (chips to 100 g) for carbon and oxygen isotope analysis were collected at finer resolution. Additional material was collected for slab and petrographic analysis of facies, described previously (Osburn et al., 2013). Section names, locations, heights and isotopic analyses performed are listed in Table 1.

Table 1: Section locations and data

<i>Section Name</i>	<i>Abbr.</i>	<i>Lat</i>	<i>Long</i>	<i>Height (m)</i>	<i>Complete?</i>	<i>C/O</i>	<i>S/CAS</i>
<i>Oman Mountains</i>							
Wadi Sahtan 1	WS1	23.22366	57.31208	204	*	*	*
Wadi Hajir 1	WH1	23.20498	57.5592	181	*	*	*
Wadi Bani Awf	WBA	23.24078	57.40588	30.4		*	
Al Aqor Village 1	AQ1	23.07361	57.66517	76.7	*	*	
Wadi Mistal 1	WM1	23.12724	57.75148	54	*	*	
<i>Huqf</i>							
Buah Dome 1	BD1	20.38214	57.68652	272	*	*	
Buah Dome 8	BD8	20.38358	57.69339	303.5	*	*	
Buah Dome 6	BD6	20.35387	57.68817	91		*	
Buah Dome 5	BD5	20.35182	57.6862	307.8	*	*	*
Goose Chase 1	GH1	20.33477	57.78247	14.7		*	
Khufai Dome East	KDE	20.23195	57.69993	319.1		*	(local)
Khufai Dome South	KDS	20.13538	57.6405	307.8		*	*
Khufai Dome West	KDW	20.11736	57.59718	131.8		*	(local)
Post-Fault 1	PF1	20.13799	57.58743	28.8		*	
Mukhaibah Dome 6	MD6	19.98238	57.71587	260.9		*	(local)
Mukhaibah Dome East	MDE	19.96842	57.71682	293.4		*	(local)
Mukhaibah Dome 5	MD5	19.94093	57.70551	312.1	*	*	*
Nafun 1	NA1	19.87315	57.69944	19.8		*	

\*Local indicates that only local spot measurements were made.

In order to effectively compare chemostratigraphic data, a normalized vertical scale ( $Z_n^*$ ) was created from sequence stratigraphic boundaries defined for the Huqf and Oman Mountain areas. For the Huqf sections, the base and top of carbonate deposition were set to 0 and 320 m, respectively. Sixteen intermediate stratigraphic surfaces were used as tie points between sections and  $Z_n^*$  values for each section were calculated relative to the type section (MD5). As these surfaces are sequence stratigraphic boundaries, and thus timelines, this correlation allows observation of contemporaneous

chemical events. This exercise was repeated for mountain sections using 0 and 120 m as upper and lower boundaries and six intervening surfaces as calibration points.

#### *4.2 CAS extraction*

Hand samples for sulfate extraction were first cleaned and trimmed, removing outer surfaces and visible secondary carbonate phases such as cement filled veins, before crushing and grinding using a chipmunk crusher and shatter box, respectively. All equipment was rinsed with MilliQ water and acetone before use and between samples. Approximately 60 g splits of powdered samples were weighed into 1 L Erlenmeyer flasks for CAS purification and extraction. CAS extraction followed a protocol modified from Burdett et al. (1989) (Gill et al., 2011). Samples were subjected to a series of rinses and soaks, each occurring at least overnight, followed by removal of the overlying solution by decanting. The rinse order was as follows: 10% NaCl, MilliQ, 3% bleach, and MilliQ (2x). After the final MilliQ rinse, samples were dissolved in 4 N HCl and filtered immediately on 0.4  $\mu\text{m}$  nitrocellulose membrane filters (Millipore). The filtrate was adjusted to a known volume, and a 5 ml aliquot was removed for elemental analysis. The remaining sample was returned to a clean flask, and 100 ml of a saturated BaCl solution was added to precipitate dissolved sulfate as barite. The barite were filtered again onto 0.4  $\mu\text{m}$  nitrocellulose membranes, dried, scraped, and stored until isotopic analysis.

#### *4.3 Isotopic analyses*

Carbon and oxygen isotope analyses were performed by standard techniques. Hand samples were prepared by cutting to expose fresh surfaces, followed by microdrilling to produce  $\sim 0.5$  mg of powder. Areas with evidence for recrystallization and clear secondary phases were avoided. Carbon and oxygen isotope analyses were

performed at a number of labs over the course of this study: Washington University in St. Louis, University of Missouri, University of Michigan Stable Isotope Laboratory, University of Riverside, and in house at the California Institute of Technology. Replicate samples were compared among the labs to maintain internal consistency. Samples run at Caltech were analyzed via gas bench coupled to a Thermo Delta V gas sourced IRMS. Powdered samples ~200  $\mu\text{g}$  were reacted with excess anhydrous  $\text{H}_3\text{PO}_4$  at 72 °C in He flushed Extainers. Evolved  $\text{CO}_2$  was then introduced into a Delta V isotope ratio mass spectrometer. Accuracy and precision was monitored via calibration to the Carrera Marble internal standard and by analysis of replicate sample peaks. Combined error on samples and standards averaged 0.03 ‰ for carbon and 0.04 ‰ for oxygen isotopes among all the labs. All analyses are reported relative to Vienna Pee Dee Belemnite (VPDB).

Sulfur isotope analyses were performed at the University of California, Riverside, by EA-IRMS. Barite precipitates were homogenized and weighed into tin capsules with an excess of  $\text{V}_2\text{O}_5$  for combustion via elemental analyzer. The resultant  $\text{SO}_2$  was analyzed on line for  $^{34}\text{S}/^{32}\text{S}$  using a Thermo Delta V gas sourced IRMS. Sulfur isotope composition is reported in permil relative to Vienna Canyon Diablo Troilite (V-CDT) using the standard delta notation. Instrumental error on standards (NBS 127, IAEA SO-5, IAEA SO-6) and replicate samples averaged 0.2 ‰.

#### *4.4 CAS concentration*

The concentration of CAS in each sample was measured from aliquots of known volume taken immediately post dissolution. Samples were analyzed at the Biogeochemistry Laboratory at the University of California, Riverside, using an Agilent

7500ce quadrupole ICP-MS with Xe as the collision cell gas. Sulfate was measured as total S with error on replicates better than 5%. CAS concentration is corrected for the insoluble content of each sample.

#### *4.5 Modeling*

A simple box model of the sulfur cycle was constructed using the Stella software package (isee Systems, 2011). Models were adapted from Kurtz et al. (2003), Kah et al. (2004), and Halverson and Hurtgen, (2007). Governing equations and input parameters are described in detail in the text below.

### **5. Results: Formation-scale chemostratigraphy**

#### *5.1 Data from the Huqf sections*

Isotopic data from the Huqf region show remarkable continuity between stratigraphic sections in both trend and magnitude (Figure 2). Carbon isotope data for the majority of the Khufai Formation are consistently  $^{13}\text{C}$ -enriched. While some scatter is present, agreement between stratigraphic sections is often better than  $\pm 1$  ‰. In ascending stratigraphic order,  $\delta^{13}\text{C}$  values first increase slightly from  $\sim 2$  to  $>5$  ‰. High values are maintained with a very slight negative slope for 250 m before decreasing rapidly to  $\delta^{13}\text{C}$  values approaching  $-10$  ‰ at the formation boundary. This decline defines the falling limb of the Shuram Isotope Excursion and does not recover to positive values until well into the Buah Formation (Burns and Matter, 1993; Le Guerroue et al., 2006b).

Oxygen isotope data show considerably more scatter through the sections, as predicted for rocks of this age, likely because of overprints during burial. Trends are

visually apparent in the data but more likely represent diagenetic process rather than depositional changes (see Evaluation of Trends below). The majority of the Khufai Formation is characterized by relatively high  $\delta^{18}\text{O}$  of -3 to -4 ‰, and we suggest that the bulk signal records relatively little alteration. Samples from Buah Dome as well as data from Fike et al. (2006) are significantly depleted relative to the other sections, most markedly so during the interval of highest  $\delta^{18}\text{O}$  values from 75 to 275 m. Of interest to the Shuram excursion is the relative lack of depletion in oxygen isotopes as the negative carbon excursion reaches its full magnitude (Figure 2, >300 m  $Z_n^*$ ).

Sulfur isotope composition ( $\delta^{34}\text{S}$ ) and CAS concentration ([CAS]) both show considerable, but systematic variability in the Khufai Formation.  $\delta^{34}\text{S}$  values begin at an average of 25 ‰ and decrease slightly over 75 meters to 22 ‰. CAS concentration is broadly constant to slightly declining during this interval. Directly following this decline is a relatively rapid increase in  $\delta^{34}\text{S}$  and [CAS] to 30 ‰ and ~500 ppm respectively, followed by a gradual decline ending at  $Z_n^*$  150 m. The most dramatic signals in both  $\delta^{34}\text{S}$  and [CAS] occur between 150 and 310 m, where a very linear increase in  $\delta^{34}\text{S}$  peaks at 35 ‰ and coincides with dramatic, although highly variable, increases in CAS concentration. We will refer to the first increase-decrease and subsequent increase as Excursion 1 and Excursion 2 for the remainder of this paper.

The formation-scale sequence stratigraphic surfaces identified in (Osburn et al. 2013) are plotted behind the data in colored lines for reference. Blue, red and green lines demarcate the maximum flooding interval, sequence boundary, and transgressive boundary respectively. Isotopic trends are invariant with respect to the maximum flooding surface and sequence boundary. The precipitous initial decline in  $\delta^{13}\text{C}$  at the

Shuram Excursion onset occurs at the transgressive surface (green) and is accompanied by a sharp decrease in  $\delta^{34}\text{S}$ .

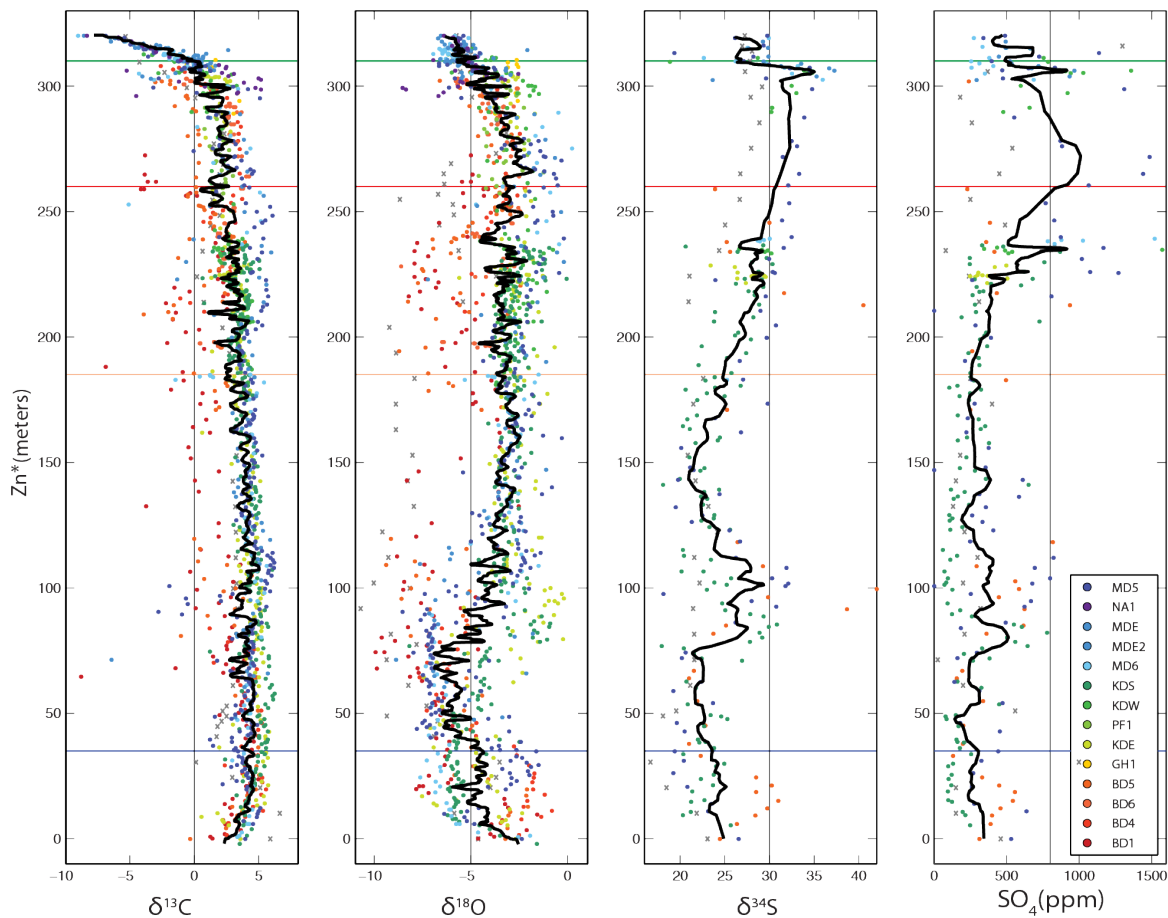


Figure 2: Chemostratigraphic data for Huqf samples plotted against a height scale normalized to sequence stratigraphic surfaces. Data from Fike et al. (2006) are indicated by X symbols for reference. Running averages of data from all areas are shown in solid black lines.

## 5.2 Data from the Oman Mountains

Carbon isotope trends from the Oman Mountains are broadly similar to those of the Huqf area (Figure 3). Carbon isotope composition begins by increasing slightly to a very stable and high  $\delta^{13}\text{C}$  value for a large portion of deposition. Absolute  $\delta^{13}\text{C}$  values

are shifted higher in the Mountains (up to 3 ‰), likely attributable to diagenetic processes (see below). After the sequence boundary,  $\delta^{13}\text{C}$  values begin to decline (as in the Huqf); however, each section takes its own trajectory on this path with some sections producing remarkably depleted final excursion values. Oxygen isotope data for the Oman Mountains are broadly depleted (centering on -10 ‰) relative to the Huqf sections and are similar to the data from Fike et al. (2006).

Trends in  $\delta^{34}\text{S}_{\text{CAS}}$  also are broadly similar between the Huqf and Oman Mountains, although absolute values are depleted in the Oman Mountains. Lower sampling density and more condensed deposition preclude comparison of the small scale excursions observed in the Huqf, but generally an increase from 15 to >30 ‰ is observed. CAS concentrations are considerably lower in the Oman Mountains ranging from ~100 to 500 ppm (Figure 3). These values are consistent with the mean of Huqf data, but do not capture the large increase concurrent with isotopic enrichment.

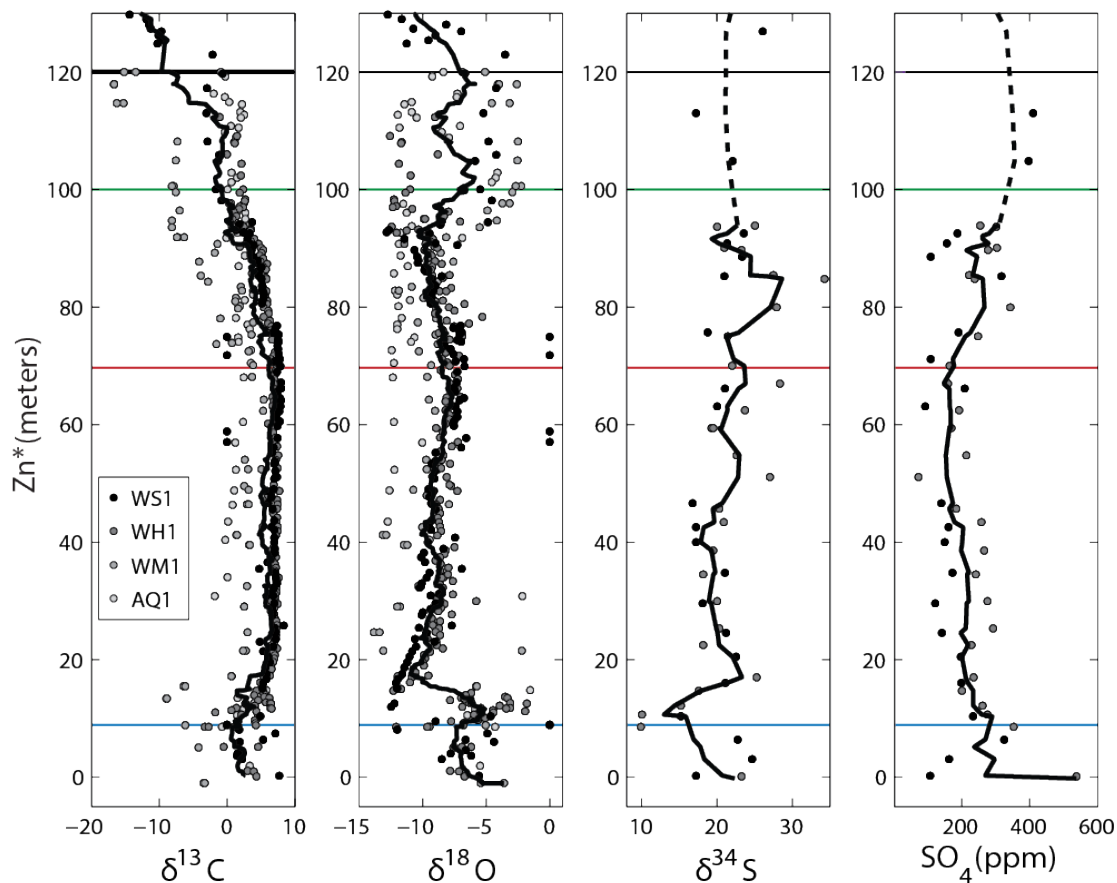


Figure 3: Chemostratigraphic data from the Oman Mountain sections plotted against normalized stratigraphic height. Major stratigraphic surfaces are shown for references. Solid black lines indicate running averages of data from all areas.

## 6. Evaluation of trends

### 6.1 Diagenetic concerns

The depositional and diagenetic environments of the Huqf and Oman Mountain sections introduce different possibilities for alteration of isotopic and compositional information. The Huqf Area generally is well preserved and has experienced only shallow burial and low tectonic stresses (Le Guerroue et al., 2006a). Organic matter from this region maintains low thermal maturity, and primary mineral fabrics are mostly

preserved. The sediments in the Huqf have experienced at least two phases of alteration. The first was pervasive early dolomitization, although retention of primary fabrics suggests that this process took place during lithification. An additional phase of neomorphic recrystallization to calcite after dolomite occurs in pockets in the outer and middle ramp facies, possibly associated with hydrothermal fluids (Osburn et al., 2013). This process produced bands of spar and coarsely crystalline fabrics. Samples were taken and processed to avoid these zones of clear alteration. Despite careful drilling, isotopic evidence for this alteration can be seen in the increased scatter and depletion of oxygen isotope data between 25 and 75 m (Figure 2). Buah Dome, in particular, appears to have experienced a greater degree of alteration than the other Huqf exposures. Significant depletion of carbon and oxygen isotopes from approximately 60 to 250 m coincides with severe recrystallization fabrics. This area may have been more affected than the others by meteoric diagenesis because of fluid flow through its porous quartz sand-dominated facies (Figure 1).

The early diagenetic history of the Oman Mountains was fairly mild due to sustained deep-water conditions; however, subsequent deep burial and tectonic alteration has severely affected the integrity of isotopic signals in these rocks. Major phases of alteration include pre-Permian burial and folding, Cretaceous Ophiolite abduction, and Neogene uplift of the Oman mountains (Forbes et al., 2010; Hanna and Nolan, 1989; Mann et al., 1990). The resultant fabrics of the Khufai Formation in the Oman Mountains range from relatively unaltered to severely recrystallized, with evidence for ductile flow in carbonates, and penetrative cleavage and phyllitic mica growth in siliciclastic sediments. While measurements from these sections are still included for completeness,

emphasis is given to Huqf samples for evaluating trends and mechanisms due to their lower degree of alteration.

Diagenetic processes can differentially affect isotopic systems, and cross plots between proxies can illustrate sample grouping and diagenetic trends (Figure 4). The upper left hand panel shows the relationship between carbon and oxygen isotope data. Most samples occupy a tight cluster with a positive slope between the two isotope systems. Significant divergence from this cluster is seen for the Oman Mountains samples, which show enriched  $\delta^{13}\text{C}$  and depleted  $\delta^{18}\text{O}$  values consistent with recrystallization by basinal brines. A trend of strong  $\delta^{13}\text{C}$  depletion with negligible  $\delta^{18}\text{O}$  depletion is defined by Huqf samples from the Shuram excursion onset. Samples from Wadi Sahtan within the Shuram Formation are strongly depleted in both isotope systems where those from Wadi Mistal are  $^{13}\text{C}$ -depleted and  $^{18}\text{O}$ -enriched (see below). No significant trend is observed between  $\delta^{13}\text{C}$  and  $\delta^{34}\text{S}$  (Figure 4). The upper right hand panel of Figure 4 illustrates the relationship between sulfate concentration and  $\delta^{34}\text{S}$  values. A clear, albeit scattered positive correlation is observed in our samples. This relationship could indicate mixing between marine fluids and an enriched, concentrated end-member. This brine could not have been produced by evaporation of seawater or the precipitation of gypsum directly due to either no fractionation or positive fractionation (Claypool et al., 1980) associated with those processes. However, enriched sulfate brine could be produced through bacterial sulfate reduction concurrent with evaporite deposition as described by Fike (2007) (Fike, 2007). The relationship between sulfate concentration and carbonate oxygen isotopes is shown in the bottom right panel of Figure 4. Covariation between these two measurements might be expected, as they are both

easily altered by meteoric diagenesis (Gill et al., 2008; Marenco et al., 2008). The data follow two trends based on sample location. Samples from the Oman Mountains display consistently low sulfate concentrations with a large range in  $\delta^{18}\text{O}$ . Conversely, Huqf samples show a large range in sulfate concentration but are restricted to a more narrow range in  $\delta^{18}\text{O}$ . Positive correlation between these systems could be suggestive of loss of carbonate-associated sulfate during meteoric diagenesis—similar to Gill et al. (2008). In this case, the samples with high [CAS] are interpreted to be less altered than those with low [CAS].

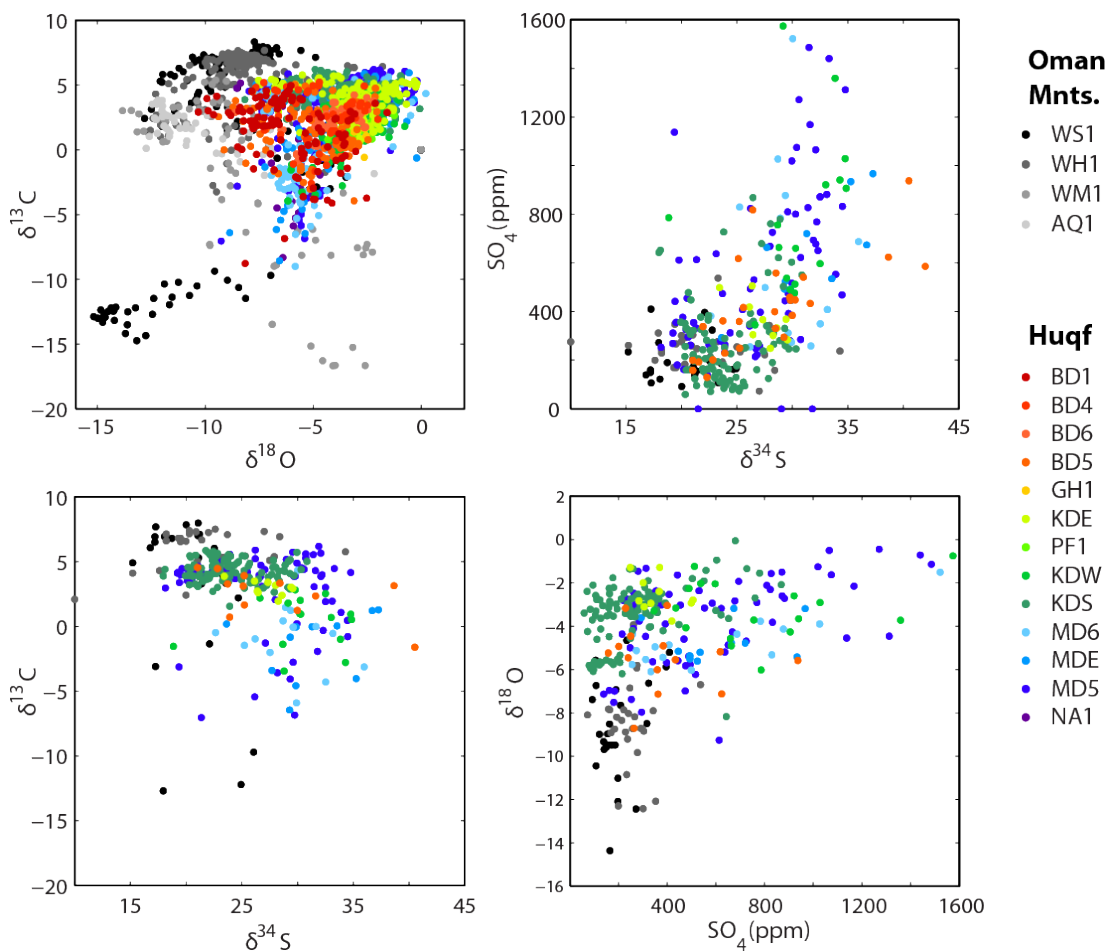


Figure 4: Chemostratigraphic cross plots of selected data from both Huqf and Oman Mountains samples.

Broadly speaking, diagenetic processes do not appear to be the primary source of C and S isotopic variability for the Khufai Formation. Where strong diagenetic signals exist, they can be identified and excluded from interpretation of primary environmental variables.

### *6.1.1 Authigenic Carbonate*

It has recently been suggested that the Shuram carbon isotope excursion was produced through precipitation of  $^{13}\text{C}$ -depleted authigenic carbonate within the stratigraphic horizons interpreted to contain the excursion (Schrag et al., 2013). Authigenic carbonate is defined in Schrag et al. (2013) as an *in situ* precipitated phase, where alkalinity production occurs through diagenetic reactions rather than primary marine DIC. The main carbon isotope decline in the Huqf occurs within a package of oolite followed by micritic carbonates, similar to other sections worldwide (Verdel et al., 2011). Petrographic characteristics are described in detail in Osburn et al. 2013, but the observation most relevant to this discussion is that ooids retain primary radial-concentric fabrics. Ooids are grains that are precipitated directly from seawater with wave agitation: quite different from what is described as *in situ* authigenic carbonate precipitation in the sense of Schrag et al. (2013). Detailed drilling of ooid, cement, and micritic components in these units showed no significant difference in carbon or oxygen isotopes (Osburn et al. 2010, GSA Annual Meeting Abstract # 181278). These observations allow us to conclude that the Shuram Excursion described from Khufai Formation oolites is not the result of secondary mineral precipitation, but rather primary trends in marine DIC.

In contrast, some sections in the Oman Mountains may include a significant amount of authigenic carbonate and are isotopically heterogeneous. Within the upper and lower transitional members of the Khufai Formation (Osburn et al., 2013), carbonates are

restricted to irregular pockets and nodular beds surrounded by siliciclastic siltstone. While some depositional character is preserved (intraclasts and microbial laminations), it is likely that some part of the carbonate here was deposited as a secondary diagenetic phase. In the lower transitional zone, large scatter with significantly depleted  $\delta^{13}\text{C}$  and relatively enriched  $\delta^{18}\text{O}$  values are observed, consistent with the variable inclusion of porewater carbonate into our analyses. In the upper transition zone, one section departs significantly from the others, displaying highly depleted  $\delta^{13}\text{C}$  (down to  $\sim -20$  ‰) and correspondingly enriched  $\delta^{18}\text{O}$ . Interestingly, these extreme enrichments occur synchronously with the decline in other sections related to the Shuram excursion, but are amplified. We suggest that this is consistent with universally depleted marine DIC, and thus porewater starting value, that then evolves with authigenic precipitation from a decreasing baseline.

## *6.2 Statistical evaluation of stratigraphic trends*

A brief statistical evaluation of the data is presented to evaluate the strength of stratigraphic trends as well as correlation between different proxies (Table 2). The section was divided into six key intervals based on visually apparent trends, and statistical analyses were applied to evaluate the strength of these trends. Analysis of trends in carbon isotopic ratios with height statistically supports the presence of a subtle decline in  $\delta^{13}\text{C}$  up to 300 m before the strong decline from 300 to 320 m. Sulfur isotopes display significant trends with stratigraphic height after 25 m alternating from negative to positive slopes twice before ending on a very negative slope at 300 to 320 m. These changes in slope provide statistical support to our identification of two positive

excursions. The most robust trend in CAS concentration is a strong positive slope (4.6 ppm/m) between 150 and 300 m. Less supported negative trends are also present between 75-100 and 300-320 m. The only statistically significant covariation in isotopes for the lower Khufai is a strong negative correlation between carbon and oxygen isotopes from 0-25 m. Covariation between C and O does not reoccur until the 300-320 m interval. A strong negative correlation between C and S isotope values occurs between 150-300 m, as does a strong correlation between  $\delta^{34}\text{S}$  and [CAS]. In total, this statistical treatment suggests that the trends observed for Excursion 2 are stronger than those of Excursion 1, but both are statistically supported.

Table 4.2 Correlation coefficients and statistical analysis

bin ( $Z_n^*$ )	C vs. Z		S vs. Z		CAS vs. Z		C vs. O		C vs. S		S vs. CAS		O vs. CAS	
	slope	r	slope	r	slope	r	r	p	r	p	r	p	r	p
0 to 25	0.078	0.53	0.040	0.080	-7.0	-0.26	-0.93	<b>0.007</b>	-0.30	0.58	0.48	0.34	0.424	0.40
25 to 75	-0.015	-0.14	-0.044	-0.25	-0.14	-0.017	0.33	0.33	-0.11	0.75	-0.13	0.69	-0.042	0.90
75 to 100	-0.015	-0.068	0.14	0.20	-7.1	-0.22	0.083	0.88	0.19	0.72	0.25	0.63	0.031	0.95
100 to 150	-0.0068	-0.071	-0.16	-0.56	-1.4	-0.092	-0.19	0.57	0.34	0.31	0.049	0.89	-0.16	0.65
150 to 300	-0.014	-0.30	0.071	0.66	4.6	0.46	0.13	0.50	-0.77	<b>&lt; 0.0001</b>	0.78	<b>&lt; 0.0001</b>	0.39	<b>0.002</b>
300 to 320	-0.34	-0.73	-0.39	-0.52	-8.1	-0.19	0.80	<b>0.006</b>	0.73	<b>0.018</b>	0.36	0.31	0.25	0.50
total	-0.015	<b>-0.58</b>	0.025	<b>0.52</b>	1.4	<b>0.44</b>	0.42	<b>0.0003</b>	-0.29	<b>0.015</b>	0.71	<b>&lt; 0.0001</b>	0.20	0.10

### 6.3 Deconvolving facies driven signals vs. stratigraphic trends

Facies distributions change with stratigraphic architecture, complicating the differentiation between local facies-driven isotopic signals from global trends in ocean chemistry. Additionally, it is possible that particular intervals or proxies are more sensitive to facies-specific alteration. For instance, CAS concentrations could be particularly effected by local depositional (and thus facies-driven) variability by basin restriction. Also, one might also suspect that high levels of bacterial sulfate reduction

within microbial mats might affect the preserved  $\delta^{34}\text{S}$  values in microbialite facies. We analyzed isotopic trends in terms of stratigraphic packages and facies independently to better understand the relative roles of facies-driven vs. stratigraphic trends in this dataset (Figure 5). Broadly speaking, chemostratigraphic data shows little relationship to the facies of origin, thereby validating our interpretation of observed variability as non-local.

Several facies show distinctive trends worth discussion. The  $\delta^{13}\text{C}$  range of the inner-ramp subtidal facies is exceptionally low and bimodal compared to the section average. Analysis reveals that this facies association contains the intraclast dolosiltite facies that only occurs in the uppermost beds of Mukhaibah Dome and contains much of the isotopic decline into the Shuram Excursion. With the exception of this facies, the remainder of the group is similar to neighboring facies and the section average. This facies occurs at a very specific stratigraphic interval thus giving the illusion of an environmental trend when really it is stratigraphy-driven. Also, the oncolite grainstone facies occupies restricted ranges in all proxies with unusually depleted  $\delta^{34}\text{S}$  values and low [CAS]. We interpret these isotopic distributions as resulting from deposition of this facies in a relatively narrow stratigraphic band that coincidentally intersects a minimum in both sulfur isotopes and [CAS] after Excursion 1. The inner-ramp high energy and lagoonal facies both show exceptionally large ranges in [CAS] and include the highest observed values. These facies groups represent very different environmental conditions, precluding the possibility that this trend reflects a specific local environment. The [CAS]-enrichment of the IR-high energy facies is difficult to explain based on environmental factors, as these facies are not restricted. The [CAS] enrichment of lagoonal facies could be consistent with restricted evaporitic conditions; however, as noted below, the

supratidal facies do not follow this trend. While it may be significant that all very high [CAS] values fall within this group, the group includes many low concentrations as well. The stratigraphic intervals in which this group predominates (>S9) include the highest values, but also have increased lower bounds and means. We suggest that this trend is also primarily stratigraphic.

This data can also be used to ascertain whether the observed signals reflect local processes or larger-scale trends. In the microbial mat scenario proposed above, we would predict a local signal of BSR to enrich the local pool of  $\delta^{34}\text{S}$  through distillation. This hypothesis is not supported by the data that instead show a range  $\delta^{34}\text{S}$  slightly depleted relative to the mean (Figure 5). One might also predict that supratidal facies would reflect concentrated seawater sulfate and, therefore, reflect higher than average CAS concentration. The data do not support this prediction either, instead showing intermediate values for supratidal facies (Figure 5). These observations along with stratigraphic continuity suggest that the trends observed in our data set reflect widespread marine rather than local conditions.

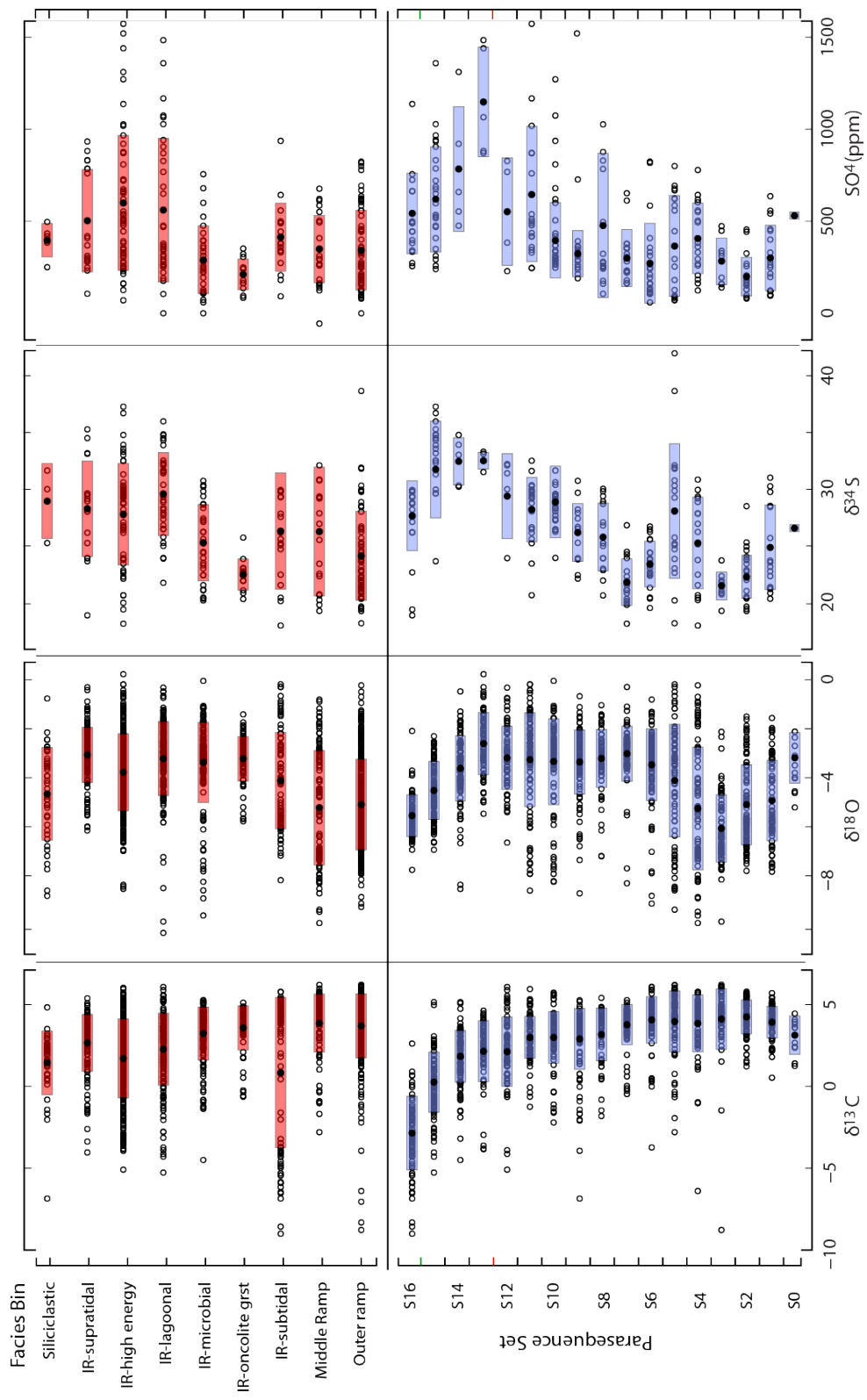


Figure 5: A comparison of chemostratigraphic data binned by facies associations (upper panels) vs. by stratigraphic package (lower panels). Solid circles indicated the mean of each bin where the shade bar shows two standard deviations. Facies and stratigraphic characterization is presented in Osburn et al. (2013).

## 7. Discussion

Chemostratigraphic trends of the Khufai Formation include consistently enriched carbon isotopes, variable sulfur isotopes, and large changes in [CAS], all preceding the Shuram Excursion onset. These changes appear independent of major stratigraphic surfaces and facies changes, suggesting an inheritance from the global ocean rather than local environment. Here we will use mass balance-based modeling of the carbon and sulfur cycles to identify environmental parameters that could have contributed to these changes. Given that most of the observed variability in this study is within the sulfur system, we will begin by evaluating possible mechanisms to account for these trends and then evaluate those options in light of the carbon isotope results.

### *7.1 Estimating timescale*

It is necessary to estimate depositional timescale to convert stratigraphic data points into rates of change. This can be difficult for Precambrian sedimentary sections, particularly one as deficient in direct geochronologic constraints as the Huqf Supergroup (Bowring et al., 2007). The Huqf Supergroup is bounded below by the Hadash cap carbonate, which is interpreted to be equivalent to Marinoan aged cap carbonates worldwide with an approximate age of 635 Ma (Rieu et al., 2006; Bowring et al., 2007). There are no known dateable volcanic materials in the intervening Masirah Bay, Khufai, and Buah formations, although estimates from detrital zircons provide broad constraints. The overlying basal Ara Group is constrained by an ash bed in the A0 unit dated at  $546.72 \pm 0.21$  (Bowring et al., 2007). These lower and upper brackets provide a maximum timescale of  $\sim 100$ Ma for the Nafun Group deposition. More specific estimates

have placed the basal Shuram Formation at 560 Ma or linked the sequence boundary in the upper Khufai formation to the Gaskiers glacial at 580 Ma (Fike et al., 2006).

As these estimates provide relatively poor constraints on deposition of the Khufai Formation, we instead estimate a depositional timescale using cyclostratigraphy and depositional thickness. Applying the conservative accumulation rates of 30 and 50 m/Ma for Precambrian carbonate platforms presented in Kah et al. (2004) yields estimates of 6.3 to 10.5 Ma for deposition of the Khufai Formation. Using accumulation rates calculated for the Paleoproterozoic Rocknest Formation from Grotzinger (1986) and timescale reinterpretation in Bowring and Grotzinger, (1992) produces estimates of 5.6 to 7.6 Ma. Traditional timescale estimates for 4<sup>th</sup> and 5<sup>th</sup> order depositional sequences (Goldhammer et al., 1990) and the number of parasequences and parasequence sets published in Osburn et al. (2013), yield estimates of 2 to 20 Ma. While significantly scattered, there is broad agreement between these estimates and for the remainder of this discussion we will assume a timescale of approximately 10 Ma.

### *7.2 Marine sulfate box model*

In order to evaluate trends in sulfur isotopes, a simple box model was constructed to represent the marine sulfate system including mass and isotopic components. The governing equations used to manipulate these models are fundamentally based in mass balance with the mass of the system representing a balance of input and output fluxes (Kump and Arthur, 1999; Kurtz, 2003). The isotopic evolution of the sulfate reservoir of mass  $M_O$  is governed by the initial isotopic value of the sulfate reservoir ( $\delta_O$ ), isotopic value of the input fluxes ( $F_{in}$ : weathering  $\delta_w, F_w$ ; hydrothermal  $\delta_{ht}, F_{ht}$ ), and the

fractionation ( $\Delta^{34}\text{S}$ ) associated with output fluxes ( $F_{\text{out}}$ : pyrite and sulfate burial  $F_{\text{py}}$ ,  $F_{\text{sulf}}$ ) following the equations calculated previously by Kurtz et al. (2003):

$$(1) \quad M_{\text{O}} = F_{\text{ht}} + F_{\text{W}} - F_{\text{py}} - F_{\text{sulf}}$$

$$(2) \quad d\delta^{34}\text{S}/dt = (F_{\text{in}}(\delta_{\text{in}} - \delta_{\text{O}}) - F_{\text{py}}\Delta^{34}\text{S})/M_{\text{O}}$$

Buried sulfate was modeled as isotopically equivalent to seawater sulfate, despite the fractionation of 1.65 ‰ associated with evaporite formation (Claypool et al., 1980). This offset had very little effect on our results and was excluded for simplicity.

We applied this model in two fundamentally different ways. We first input our data into the model to invert for the solution space of input parameters under different conditions. Second, we used a forward modeling approach to replicate the magnitude and shape of the two observed sulfur isotopic excursions under both steady state and increasing reservoir conditions. Both of these approaches set bounds on the state of the marine sulfate system at the time of deposition.

### 7.2.1 Calculation of reservoir size

We will focus first on the inverse problem and use our data to solve for model parameters, beginning with estimating the size of  $M_{\text{O}}$  and followed by calculation of realistic values for fractionation ( $\Delta^{34}\text{S}$ ) and pyrite burial ( $F_{\text{py}}$ ). Equation 2 suggests that the rate of sulfur isotopic change of marine sulfate is inversely proportional to the mass of the sulfate reservoir. Slight rearrangement of Equation 2 yields an expression for the mass of the sulfate reservoir.

$$(3) \quad M_{\text{O}} = \frac{(F_{\text{in}}(\delta_{\text{in}} - \delta_{\text{O}}) - F_{\text{py}}\Delta^{34}\text{S})}{\frac{d\delta^{34}\text{S}}{dt}}$$

This relationship has been commonly applied to the Precambrian ocean to estimate the size of the marine sulfate reservoir (Hurtgen et al., 2002; Kah et al., 2004; Gellatly and Lyons, 2005; Halverson and Hurtgen, 2007; Loyd et al., 2012). Previous estimates for the Neoproterozoic ocean suggest an extremely small sulfate reservoir (Hurtgen et al., 2002; Kaufman et al., 2007; Loyd et al., 2012), with a possible increase in the latest Ediacaran (Fike et al., 2006; Halverson and Hurtgen, 2007).

Data from the Huqf were binned into 5 m intervals, and running average of this data was taken as the smoothest possible representation of isotopic trends. A rate of change in ‰ / Ma was calculated for each bin and analyzed using Equation 3 (Figure 6). Ranges of  $F_{py}$  from 0.7 to 1.5 and  $\Delta^{34}S$  between 20 and 40 ‰ were applied along with  $F_{in}$  of  $1.5 \text{ moles} \times 10^{18} / \text{Ma}$  and  $\delta_w$  of 8 ‰. No single pair of input values for  $F_{py}$  and  $\Delta^{34}S$  produced positive values of  $M_O$  for all stratigraphic intervals. Loyd et al. (2012) noted that positive reservoir masses were only achieved for their data using  $F_{py} = 1$  and subsequently used this as a constraint on the state of the ocean. This analysis constrains both the reservoir mass and ranges of input parameters at each stratigraphic bin.

The maximum calculated  $M_O$  for any combination of variables was recorded for each interval and plotted in Figure 6. During periods of stable isotopic values, large  $M_O$  are permitted, whereas periods of rapid change require extremely small  $M_O$ . Particularly low sulfate concentrations are required at the end of the Excursion 1 (120 to 150 m) and at the onset of the Shuram excursion (310 to 320 m). Ranges of  $F_{py}$  were used to calculate  $\Delta^{34}S$  and vice versa for  $M_O = 0.288, 4, \text{ and } 8 \times 10^{18} \text{ moles}$  (or 0.2 mM, 2.8 mM and 5.6 mM), and are plotted in Figure 6. Intervals of decreasing isotopic values generally allow only very small ranges of both  $F_{py}$  and  $\Delta^{34}S$ , and only yield solutions for the smallest

reservoir mass, further supporting periodic very low sulfate concentrations throughout the Khufai Formation.

Poor age control is a concern for this type of analysis, but our conclusions do not change for either shorter or longer depositional timescales within the range discussed above. Significantly shorter timescales produce rapid rates of change that further restrict input parameters and require increasingly small sulfate reservoir sizes. Whereas longer depositional timescales are more accommodating to both input values and reservoir sizes.

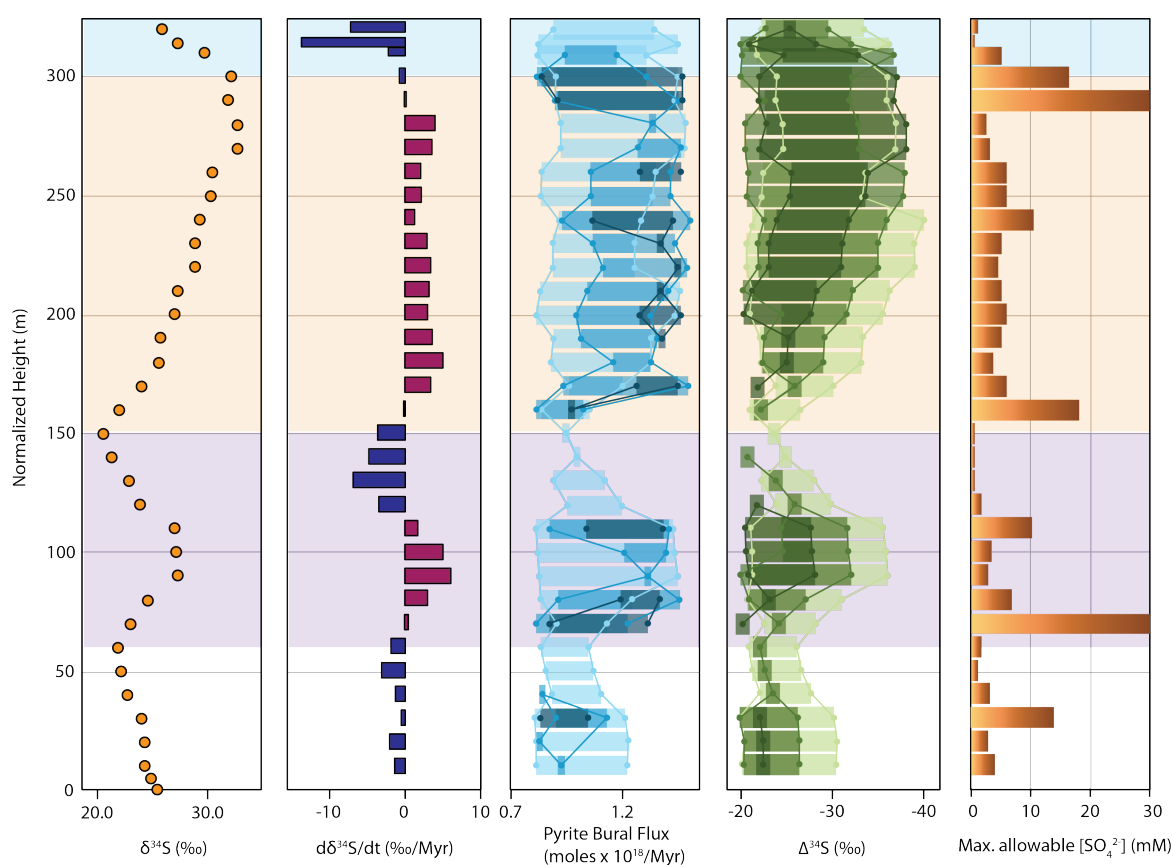


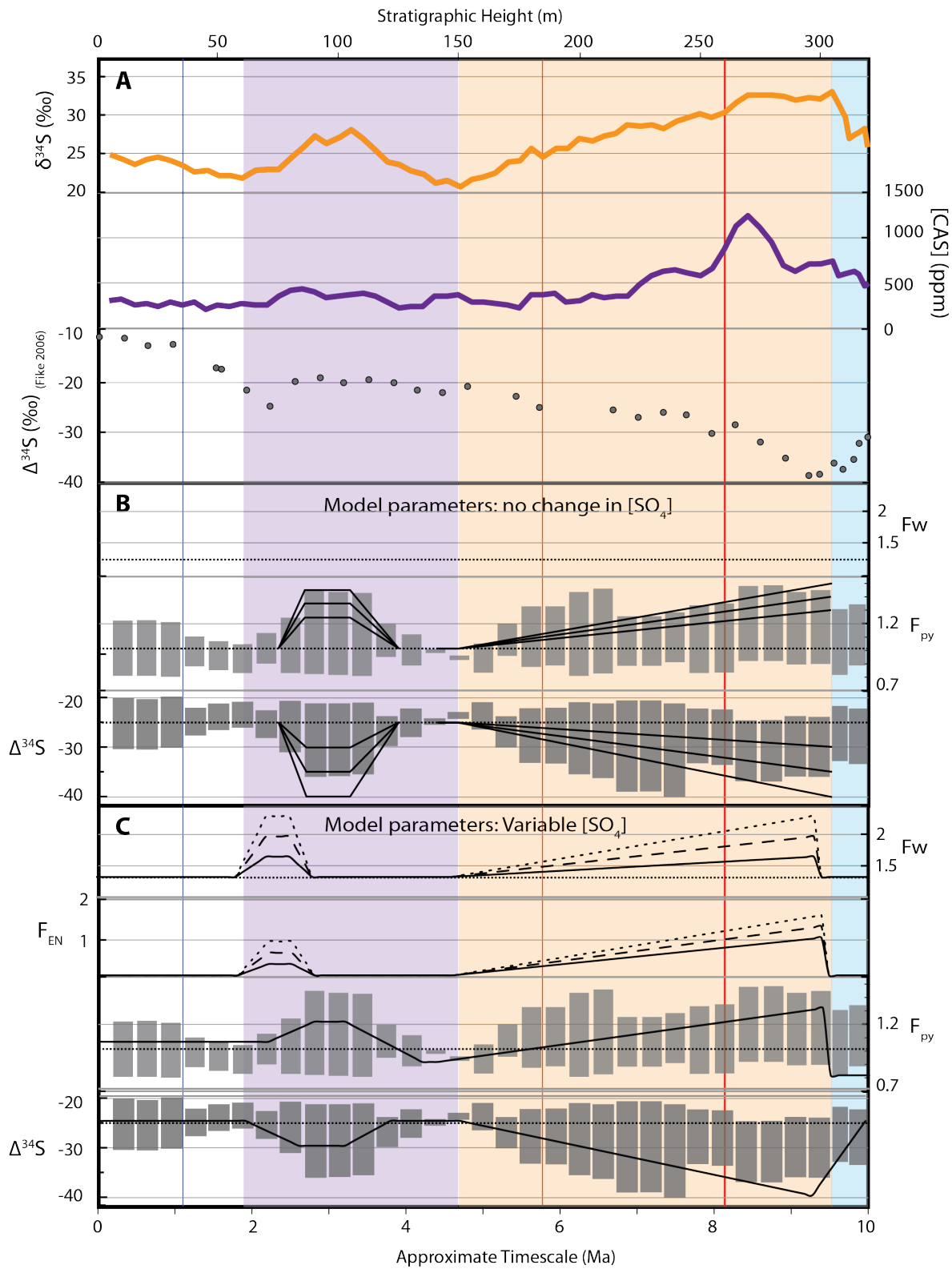
Figure 6: Smoothed sulfur isotope data, rates of change for each bin, and results from the calculation of reservoir size. Pyrite Burial Flux and fractionation plots each show the results from calculation for  $Mo = 0.288, 4, 8 \times 10^{18}$  moles/Ma in the light, medium, and dark shaded tones. Excursion 1, 2, and Shuram onset are shown in the background purple, orange, and blue shaded boxes, respectively

### 7.2.2 Modeling excursions in $\delta^{34}\text{S}$

We have implemented a forward modeling approach to evaluate causal mechanisms for the observed variations in our  $\delta^{34}\text{S}_{\text{CAS}}$ . Excursions 1 and 2 vary in both the magnitude and rates of isotopic change. Excursion 1 can be thought of as a pulsed change and then relaxation to the baseline, rapidly increasing from 22 to 28 ‰ between 75 and 85 m and gradually decrease to 20 ‰ by 145 m. Excursion 2 begins directly afterward, but is larger and opposite in character with a protracted rise in  $\delta^{34}\text{S}$  from 20 to 40 ‰ starting at 155 m to 310 m, then declining rapidly coincident with the major drop in carbon isotopes. Both Excursion 1 and Excursion 2 are accompanied by at least some increase in [CAS] concentration.

We attempt to replicate the basic trends and magnitudes of these excursions using modeling scenarios with either constant or increasing sulfate reservoir mass. The first maintains balanced input and output fluxes and forces the isotopic system by transiently increasing either the ratio of pyrite to sulfate burial ( $f_{\text{py}}$ ) or the fractionation associated with pyrite formation ( $\Delta^{34}\text{S}$ ). The second approach allows the mass of the sulfate reservoir to increase through imbalances in input and output fluxes. Both models are described in detail below and parameters are summarized in Figure 7B and 7C.

Figure 7: Modeling parameters for sulfur geochemical box model. A. Smoothed sulfur isotope and CAS concentration data from this study with  $\Delta^{34}\text{S}$  data from Fike et al. (2006) for comparison. B. Input parameters for modeling with balanced input and output fluxes. Shaded bars are allowable parameters for  $M_0=0.288$  calculated in Section XXX. B. Input parameters for modeling with increasing sulfate concentration. A constant  $F_{\text{sulf}}=0.45$  was used in these trials. C. Input parameters for modeling with changing mass.



### 7.2.3 *Balanced models*

In the model scenario where input and output fluxes are balanced, the primary mechanisms for introducing isotopic changes are variation in the pyrite burial flux ( $F_{py}$ ) relative to sulfate burial and fractionation ( $\Delta^{34}S$ ) terms. Both of these variables have been shown to change throughout Earth history and have been implicated previously in sulfur isotope change (Canfield, 2004; Gill et al., 2011; Jones and Fike, 2013). Calculations presented in the previous section suggest that both of these variables are required to change over the course of Khufai Formation deposition. We investigated model responses to increased  $F_{py}$  and  $\Delta^{34}S$  for sulfate concentrations of 0.2, 0.6, and 1.2 mM with constant input fluxes ( $1.3$  and  $0.2 \times 10^{18}$  moles/Ma,  $\delta_w$  and  $\delta_{hy}$  of 6.5 and 3.5 ‰) (Figure 8).

Figure 8 illustrates the steady-state modeling output for Excursion 1 and Excursion 2 with increased fractionation (top) and pyrite burial (middle) or both (bottom). The observed magnitude ( $\sim 30$  ‰) Excursion 1 can be produced by either  $F_{py}$  or  $\Delta^{34}S$  (or their combination), whereas individual forcing variables were insufficient to replicate the magnitude of Excursion 2, instead requiring a combination. Individual forcing of  $\Delta^{34}S$  of  $>30$  ‰ for a 0.2 mM ocean or  $>40$  ‰ for a 0.6 mM ocean reached sufficient magnitudes to replicate Excursion 1, as did an increase in  $F_{py}$  to  $1.5 \times 10^{18}$  moles/Ma. Excursion 2 is most easily replicated with  $\Delta^{34}S$  increasing to  $>40$  ‰. In combination, increases in  $F_{py}$  and  $\Delta^{34}S$  directly amplify one another and thus most combined trials were successful below 1.2 mM sulfate. Increased reservoir mass mutes the rate and magnitude of isotope change in all cases.

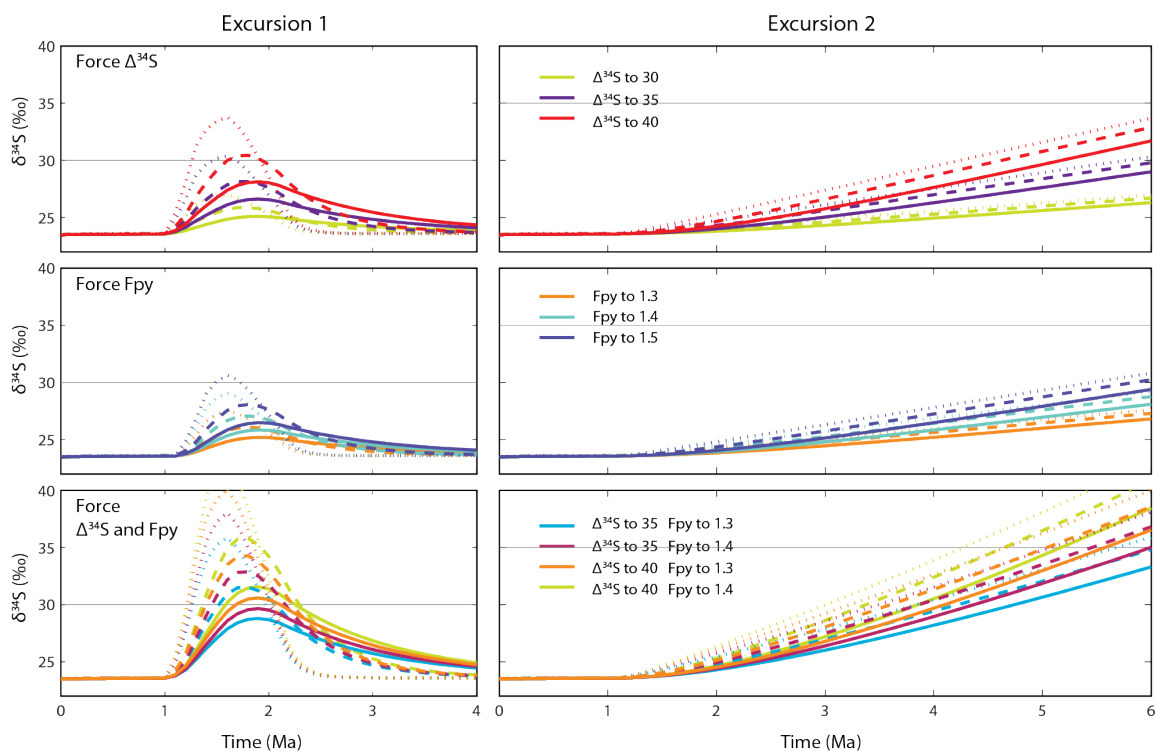


Figure 8: Model output for Section 7.2.3. Excursion 1 and 2 are modeled separately and showing in left and right hand panels respectively. Each set of conditions is shown for marine sulfate concentration of 0.2, 0.6, and 1.2 mM illustrated in dotted, dashed, and solid lines.

We can evaluate the robustness of this model and its predictions through comparison to geological evidence and to parameters calculated in 7.2.1. The difference between  $\delta^{34}\text{S}_{\text{CAS}}$  and  $\delta^{34}\text{S}_{\text{pyr}}$  ( $\Delta^{34}\text{S}$ ) was measured for the Khufai Formation in Fike et al. (2006) (Figure 7). This data suggests little to no increase in  $\Delta^{34}\text{S}$  during Excursion 1, but a protracted increase to up to  $\sim 40$  ‰ during Excursion 2. If fractionation does not change significantly during Excursion 1, then very large pyrite burial fluxes are required, up to a flux equal to the combined input fluxes. While the burial flux of pyrite was likely high at this time (Canfield, 2004), evidence for the presence of sedimentary sulfate minerals and non negligible [CAS] suggest that pyrite burial could not be the exclusive output of sulfur. In contrast, the relatively high values of  $\Delta^{34}\text{S}$  observed for the

Excursion 2 interval reduce the need for large  $F_{py}$ , producing sufficient  $\delta^{34}\text{S}$  values at  $F_{py} \geq 1.3 \times 10^{18}$  moles / Ma. Our model results concur with previous data suggesting that  $\Delta^{34}\text{S}$  increased during the course Khufai Formation deposition, but illustrates that fractionation changes alone are not sufficient to cause the observed  $\delta^{34}\text{S}$  signatures, especial at  $>1\text{mM}$  sulfate.

#### 7.2.4 Increasing $[\text{SO}_4]$

The modeling results presented thus far are robust *only* if the concentration of sulfate in the ocean remained very low and constant during excursion intervals. While direct interpretation  $[\text{CAS}]$  as reflective of the marine  $[\text{SO}_4]$  is unusual, the systematic changes in  $[\text{CAS}]$  coincident with excursion intervals that we observe in the Khufai Formation lack a clear facies-based or diagenetic interpretation. The global record of sulfate concentration through this time period is ambiguous and contradictory, but we do know that the Ediacaran started with extremely low sulfate concentrations (Hurtgen et al., 2002) and, in Oman, ends in a massive sulfate-rich evaporite deposit. In addition, elevated  $[\text{CAS}]$  are replicated in roughly correlative sections from Death Valley, N. Mexico, and South China, supporting a global signal. While this data certainly does not require that  $[\text{SO}_4]$  increased during deposition of the Khufai Formation, it would be consistent with this scenario. To account for this option, we evaluate the model response to increasing the mass of the marine sulfate reservoir through imbalances between input and output fluxes.

It is possible to change the mass of the marine sulfate reservoir by reducing the magnitude of output relative to input fluxes; in this case, decreasing pyrite and/or sulfate burial fluxes. Decreasing pyrite burial is possible, but would result in  $^{34}\text{S}$ -depletion of

marine sulfate, opposite of the observed trend. There is evidence of a very slight decrease in the burial fraction of pyrite ( $f_{py}$ ) during this interval (Halverson and Hurtgen, 2007), but this decrease is minor compared to what is required to increase the reservoir significantly and may also be related in increases in the burial of sulfate minerals. Increasing sulfate mineral content and [CAS] of sedimentary rocks both globally and in the Khufai Formation during this time argue against a decrease in evaporite burial (Wright et al., 1990; Strauss, 1993). In this light, reduction of the output requires unreasonably large decreases in burial fluxes and is not considered further.

Next we use our model to evaluate  $\delta^{34}\text{S}$  change resulting from increasing  $F_w$  during excursion intervals without a corresponding increase in output fluxes (Figure 9A-C). We applied pulsed fluxes of constant isotopic composition, either 6.5 or 12 ‰, (9A, blue and green curves) to the same model system used previously for the steady state discussion. Instead of yielding positive isotope excursions at the intervals of interest, these trials actually produce negative excursions because of the relatively depleted values of  $\delta_w$ . Increasing the bulk value of  $\delta_w$  increases the equilibrium  $\delta^{34}\text{S}$ -value of the system, but does not produce positive excursions. This is true even when the modified weathering fluxes are combined with the changes in  $F_{py}$  and  $\Delta^{34}\text{S}$  suggested from the steady state modeling (9B, blue curves). These trials demonstrate that periodically increasing  $F_w$  cannot account for the observed trends in  $\delta^{34}\text{S}$  with a constant  $\delta_w$ , regardless of the value.

In order to simultaneously account for increases in sulfate concentration and  $\delta^{34}\text{S}$ , we investigated scenarios where  $\delta_w$  and  $F_w$  increased concurrently. While this manipulation alone produces only mild increases in  $\delta^{34}\text{S}$  (Figure 9A, orange curves), its

impact when acting in concert with previously applied  $F_{py}$  and  $\Delta^{34}S$  increases produces large changes in  $\delta^{34}S$  (Figure 9B, orange curves). In these models, modest isotope enrichment (12 ‰) at high flux ( $2.2 \times 10^{18}$  moles / Ma) or more significant enrichment (16‰) at moderate flux ( $1.9 \times 10^{18}$  moles / Ma) were sufficient to reproduce the trend and magnitude of observed  $\delta^{34}S$  excursions. During these trials, the size of the marine sulfate reservoir increased from 0.2 to 2-4 moles  $\times 10^{18}$  in roughly 8 Ma.

To more systematically investigate flux rate and isotopic requirements of an enriched input flux, we created an additional input flux mechanistically decoupled from  $F_W$ . Modeled fluxes ( $F_{EN}$ ) range from 1 to  $1.6 \times 10^{18}$  moles / Ma with isotopic compositions ( $\delta_{EN}$ ) from 30 to 50 ‰, and were evaluated alone and in combination with  $F_{py}$  and  $\Delta^{34}S$  increases (Figure 9D-F). All trials including this flux produced positive excursions roughly approximating the trends in our data. A  $F_{EN}$  greater than or equal to  $F_W$  with  $\delta_{EN}$  of 50‰ is sufficient to explain our data alone, and when applied in combination with  $F_{py}$  and  $\Delta^{34}S$  increases (Figure 9E), even our smallest modeled flux can account for the observed trends. We will discuss potential sources of isotopically enriched sulfate in the following section.

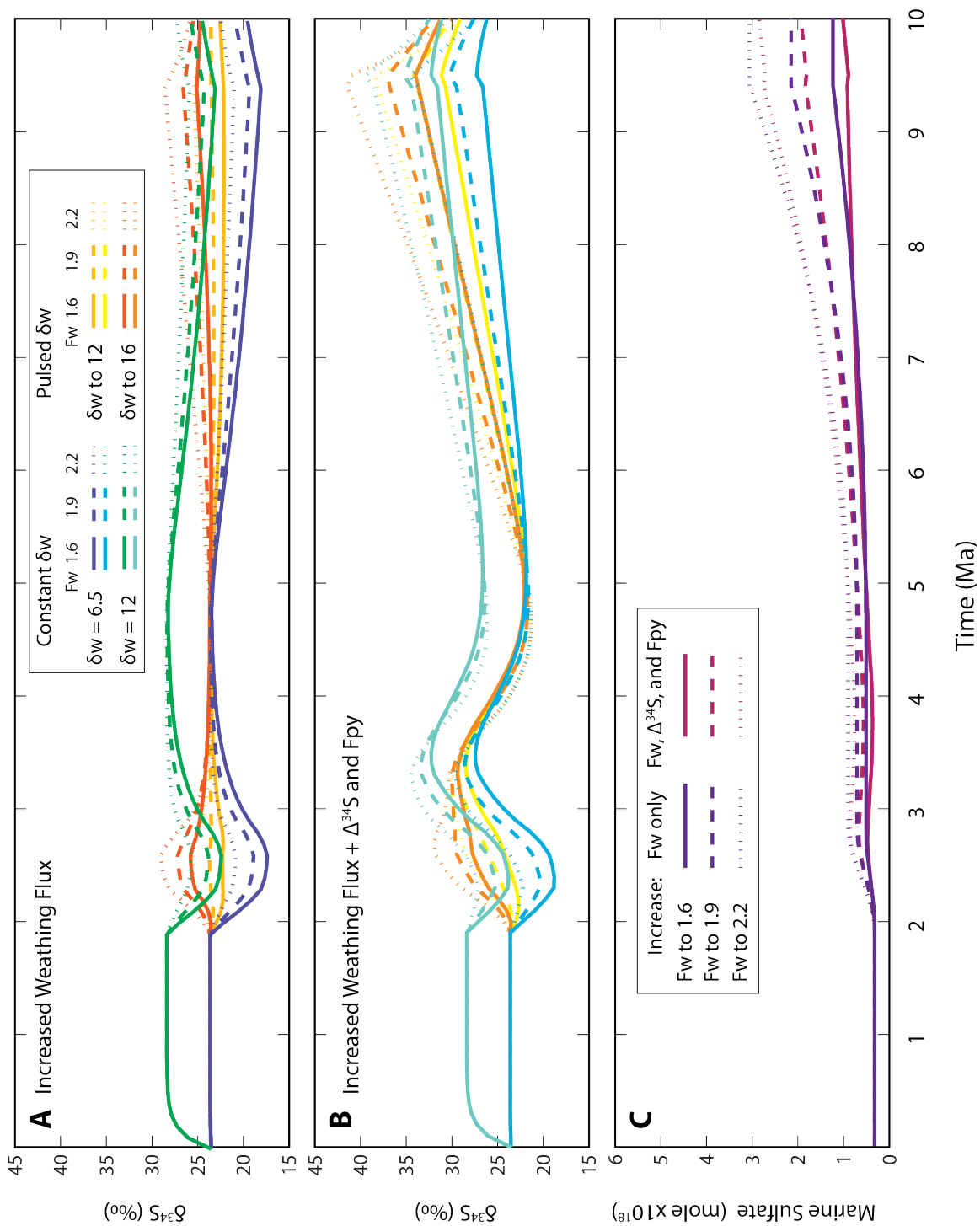


Figure 9A-C: Modeling runs with excess weathering flux. A. The resultant  $\delta^{34}\text{S}$  from increasing  $F_w$  alone for various states of  $\delta w$ . B. The combined effect of excess  $F_w$  with increasing fractionation and pyrite burial (trajectories shown in Figure 7). C. Mass of the marine sulfate reservoir for the various input conditions of  $F_w$ .

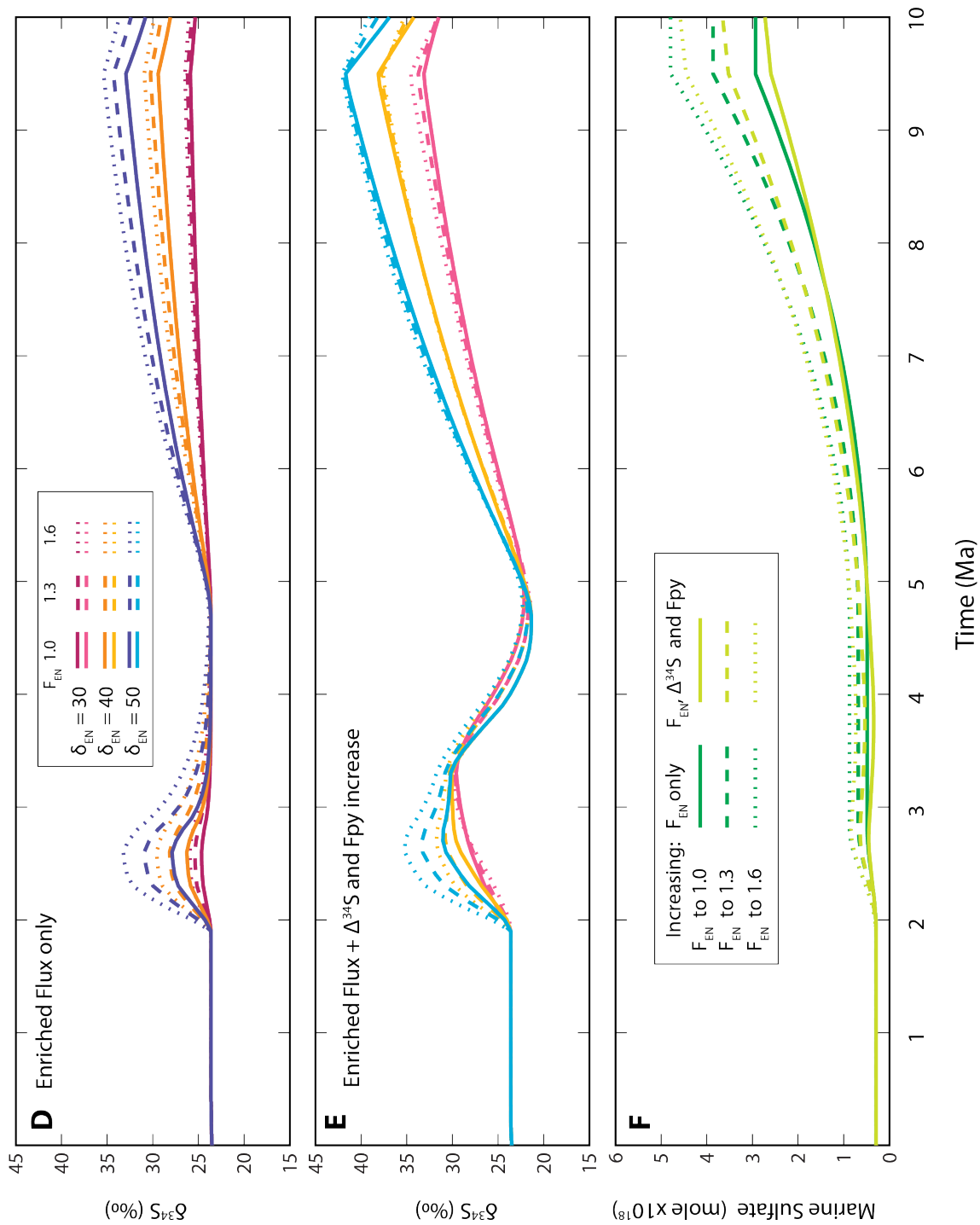


Figure 9D-F: Modeling runs with the addition of an enriched flux of sulfate. D. Resultant  $\delta^{34}\text{S}$  for various enriched fluxes. E. The combined effect of a enriched flux with increasing fractionation and pyrite burial (See Figure 7). F. The increase in the mass of the marine sulfate reservoir from varying inputs of  $F_{\text{EN}}$ .

### *7.3 Sources of enriched sulfate*

In order to produce the observed S-isotopic excursions on a background of increasing marine sulfate concentration, our models require the addition of an enriched flux of sulfate. As weathering is the primary input of sulfur into our model we will explore the possible isotopic variability of weathering inputs during the Neoproterozoic. We will also address possible inputs from other reservoirs of sulfur including hydrothermal fluxes and restricted or stratified basins. How feasible these options are is contingent on both the size of each enriched reservoir and the possibility of periodically introducing material into the marine system.

The weathering flux of sulfate incorporates fluxes, and isotopic signatures, from the dissolution of sulfate minerals and oxidation of sulfide minerals. In the modern, these processes produce enriched and depleted end member inputs from sulfate and sulfides respectively (Claypool et al., 1980). Based on these end members, transiently increasing the ratio of sulfate to sulfide weathering produces a more positive  $\delta_w$ . However, the model runs that most closely approximate our data incorporate  $\delta_w$  of up to 16 ‰, roughly equivalent to Phanerozoic estimates of the sulfate derived flux alone. While this level of enrichment would be difficult to produce given modern reservoirs, Neoproterozoic estimates of the isotopic composition of both sulfate and sulfide make this distinctly more feasible.

The compilation of Neoproterozoic sulfur isotopes presented in Halverson et al. (2010) includes both sulfate and sulfide values and reveals enormous variability in both records through time. Of interest to this discussion is the extreme enrichment of most pyrite data during the Cryogenian ranging mostly from 10 to 50 ‰. Sulfate derived

isotopic estimates also reach very enriched values directly preceding Khufai Formation deposition. If the sedimentary packages analyzed thus far are reflective of those that contributed to the weathering flux during deposition of the Khufai Formation, it is conceivable that a very enriched weathering flux could have been produced.

At any given time, the ratio of sulfide to sulfate weathering fluxes will depend on the area of exposed rocks of each type and the relative intensity of rock weathering in their respective locations. Sulfate evaporite sequences punctuate the rock record with distributions controlled by tectonic configuration and ocean chemistry (Strauss, 1997). Large-scale sulfate evaporites are rare before the Mesoproterozoic, but there is increasing evidence for periodic increases in marine sulfate concentrations even well before this, such as 2.3 to 2.1 Ga associated with the Lomagundi event (Planavsky et al., 2012). While marine sulfate concentration was likely extraordinarily low just prior to the deposition of the Khufai Formation (Hurtgen et al., 2002), it is possible that a sulfate-rich package deposited prior to this time could have been weathered to generate the enriched flux. However, sulfur burial through much of the Meso- and early Neoproterozoic oceans has been proposed to have been dominated by pyrite burial (Canfield, 1998), suggesting, instead, that weathering of sulfidic shales may have dominated sulfur fluxes.

It is also possible that the enriched flux is unrelated to weathering input and instead originates from a chemically isolated layer/ basin within the ocean itself. The concept of a stratified Ediacaran ocean has been proposed previously (Canfield et al., 2008; McFadden et al., 2008; B. Shen et al., 2008; Ader et al., 2009), with support stemming from isotopic, sedimentological, and chemical arguments. Recently Li et al. (2010) proposed a model where a sulfidic wedge is maintained, separating ferruginous

deep waters from oxygenated surface waters (Li et al., 2010). The sulfur isotope composition of the deep reservoirs is presumed to have been driven to very enriched values through Rayleigh distillation of sulfate by removal of the sulfide via pyrite formation (e.g., (Hurtgen et al., 2005; B. Shen et al., 2008)). However, the sulfate concentration of such a reservoir is required to be very low to maintain stratification (B. Shen et al., 2008), greatly reducing the likelihood that such a reservoir could supply sulfate to the surface ocean.

Independent observations of environmental change during the Ediacaran may suggest which processes and fluxes could have been most relevant to the Khufai Formation. Oxidation of the intermediate or deep ocean waters is commonly evoked to explain chemical changes to the surface ocean in this time interval. These observations come primarily from trace element and iron speciation data in Newfoundland, Canada, and China (Canfield et al., 2007; Scott et al., 2008; Y. Y. Shen et al., 2008; Sahoo et al., 2012). These reports document the transition between anoxic and oxic marine intermediate waters, supporting exchange and reaction between separate reservoirs of the ocean. Also, glaciations are known to effect both ocean circulation and terrestrial weathering fluxes. These effects are likely to be enhanced by the global extent of Cryogenian glaciations. If we adopt the rapid cycling model of Berner (Berner, 2006), preferential weathering of enriched sulfides and sulfates deposited before Marinoan (or Gaskiers, but timing is uncertain) is likely. While incorporation of sulfate from weathering can only increase sulfate concentration if the weathering fluxes outpace burial fluxes, we might expect the large, pulsed input from glaciations to behave in this manner.

#### *7.4 Constraints from the carbon isotopic record*

We can further constrain the mechanisms of sulfur isotopic change by comparison to carbon isotope record. For the majority of deposition,  $\delta^{13}\text{C}$  values of carbonate are stable and enriched, hovering around 6-7 ‰. These enriched values are characteristic of the interval between the Marinoan glacial-associated negative excursion and the Shuram Excursion (Halverson, 2005; Halverson et al., 2010), and are interpreted as reflecting high burial flux of OM during this period. Notably,  $\delta^{13}\text{C}$  of carbonate is basically invariant through Excursion 1 and decreases slightly through Excursion 2. At the onset of the Shuram Excursion both  $\delta^{13}\text{C}$  and  $\delta^{34}\text{S}$  decrease rapidly. Mechanistic explanations sulfur isotope change must be consistent with these observations.

In the steady state modeling scenario, changes in  $\delta^{34}\text{S}$  are modeled as resulting from increasing the fractionation associated with pyrite formation and pyrite burial flux. Changes in  $\Delta^{34}\text{S}$  should have no effect on the carbon isotope budget; however, increasing  $F_{\text{py}}$  favors organic carbon burial, thus increasing  $\delta^{13}\text{C}_{\text{carb}}$ . Based on measured values of  $\Delta^{34}\text{S}$ , we expect  $F_{\text{py}}$  to increase more during Excursion 1 than Excursion 2, suggesting that Excursion 1 should be associated with relatively more  $\delta^{13}\text{C}_{\text{carb}}$  increase. In fact,  $\delta^{13}\text{C}_{\text{carb}}$  is constant to decreasing through both excursions, suggesting that any changes in  $F_{\text{py}}$  were not accompanied by major changes in carbon burial.

Changing  $\delta^{34}\text{S}$  with additional fluxes of sulfur could also differentially influence the carbon isotope record. For instance, evaporite deposits are not generally associated with significant quantities of organic carbon, and thus weathering of this pool could produce sulfur isotope excursions independent of carbon isotope excursions. This is not the case for sedimentary sulfide deposits, such as black shales, that are commonly

associated with multiple weight % quantities of organic carbon. Pulsed weathering of sulfidic shales might then be expected to produce a strongly negative carbon isotopic flux. It has also been suggested that the Neoproterozoic deep ocean might contain large quantities of dissolved organic carbon, eliciting a similar response. There is a well-supported negative correlation between carbon and sulfur isotopes during Excursion 2, but the decline in  $\delta^{13}\text{C}$  is very slow. Additional modeling using a linked sulfur-carbon model will be required to evaluate if these possibilities could be consistent with such a decline.

## 8. Conclusions

The Khufai Formation was deposited during a critical interval in Earth history and is uniquely positioned to document the environmental conditions prior to and during the initial Shuram isotopic excursion. We present the highest resolution record of sulfur and carbon isotopes through this interval. We document an extremely slow decline in carbon isotopes compared to rapid and large variability in the sulfur isotopic record. The [CAS] concentration is also highly variable, corresponding to increasing in  $\delta^{34}\text{S}$  and defying simple diagenesis or facies-based explanations. Isotopic and compositional changes do not occur at major stratigraphic surfaces

Our modeling results make predictions of both the general state of the sulfur system during the middle Ediacaran and changes at specific excursion intervals. Low sulfate concentrations (<1mM) are required to permit the high rates of isotopic change observed during the middle Khufai Formation and at the onset of the Shuram excursion. This is consistent with observations of others regarding the size of the Ediacaran sulfate reservoir (Hurtgen et al., 2002; Kaufman et al., 2007; Loyd et al., 2012), but also allows

for a significant increases in concentration between the two intervals. Excursions in  $\delta^{34}\text{S}$  can be explained by transient increases in either fractionation or  $F_{\text{py}}$ , but they cannot account for increases in sulfate concentration. If increases in [CAS] are primary, a flux of enriched sulfate is required to produce synchronous increases in  $\delta^{34}\text{S}$  and [CAS]. Understanding the source of this flux will require a linked mechanistic model of the Ediacaran carbon and sulfur systems to differentiate between multiple options. Answering this question will be critical to unlocking the more elusive mechanism of the Shuram Excursion.

### **Acknowledgements**

This study was labor intensive and required the cooperation of many to be successfully completed. We would like to thank the participants of the 2010 Agouron Advanced Field Course for initial stratigraphic observations and sample collection. Sample preparation was assisted greatly by Haley Barnes, Sean Dembowski, and Emma Dodd. All the sulfur extractions and analyses (concentrations and isotopes) were performed by Angela Gerhardt and Steve Bates at UC Riverside. Carbon and oxygen isotope analyses were performed by Bob Criss, Ken Macleod, and Lora Wingate. This work would not have been possible without generous support from Petroleum development Oman (PDO) for field logistical support and isotopic analyses. Bill Wilks, Gordon Forbes, Zuwaina Al-Rawahi, Joachim Amthor, and Salim Al Maskery (Shuram Oil & Gas) also provided helpful insight. We thank the Ministry of Oil and Gas, Sultanate of Oman, for permission to publish this work. The NSF GRFP supplied additional funding to MRO and KDB.

## References

- Ader, M., Macouin, M., Trindade, R.I.F., Hadrien, M.-H., Yang, Z., Sun, Z., Besse, J., 2009. A multilayered water column in the Ediacaran Yangtze platform? Insights from carbonate and organic matter paired  $\delta^{13}\text{C}$ . *Earth and Planetary Science Letters* 288, 213–227.
- Allen, P.A., 2007. The Huqf Supergroup of Oman: Basin development and context for Neoproterozoic glaciation. *Earth-science reviews* 84, 139–185.
- Amthor, J.E., Grotzinger, J.P., Schroder, S., Bowring, S.A., Ramezani, J., Martin, M.W., Matter, A., 2003. Extinction of Cloudina and Namacalathus at the Precambrian-Cambrian boundary in Oman. *Geology* 31, 431–434.
- Berner, R.A., 2006. GEOCARBSULF: A combined model for Phanerozoic atmospheric  $\text{O}_2$  and  $\text{CO}_2$ . *Geochimica et Cosmochimica Acta* 70, 5653–5664.
- Bowring, S.A., Grotzinger, J.P., 1992. Implications of new chronostratigraphy for tectonic evolution of Wopmay Orogen, Northwest Canadian Shield. *American Journal of Science* 292, 1–20.
- Bowring, S.A., Grotzinger, J.P., Condon, D.J., Ramezani, J., Newall, M.J., Allen, P.A., 2007. Geochronologic constraints on the chronostratigraphic framework of the Neoproterozoic Huqf Supergroup, Sultanate of Oman. *American Journal of Science* 307, 1097–1145.
- Brennan, S.T., Lowenstein, T.K., Horita, J., 2004. Seawater chemistry and the advent of biocalcification. *Geology* 32, 473–476.
- Burdett, J., Arthur, M., Richardson, M., 1989. A Neogene seawater sulfur isotope age curve from calcareous pelagic microfossils. *Earth and Planetary Science Letters* 94, 189–198.
- Burns, S.J., Matter, A., 1993. Carbon isotopic record of the latest Proterozoic from Oman. *Eclogae geologicae Helvetiae* 86, 595–607.
- Calver, C., 2000. ScienceDirect.com - Precambrian Research - Isotope stratigraphy of the Ediacarian (Neoproterozoic III) of the Adelaide Rift Complex, Australia, and the overprint of water column stratification. *Precambrian Research*.
- Canfield, D.E., 1998. A new model for Proterozoic ocean chemistry. *Nature* 395, 450–454.
- Canfield, D.E., 2004. The evolution of the Earth surface sulfur reservoir. *American Journal of Science* 304, 839–861.
- Canfield, D.E., Poulton, S.W., Knoll, A.H., Narbonne, G.M., Ross, G., Goldberg, T., Strauss, H., 2008. Ferruginous Conditions Dominated Later Neoproterozoic Deep-Water Chemistry. *Science* 321, 949–952.
- Canfield, D.E., Poulton, S.W., Narbonne, G.M., 2007. Late-Neoproterozoic Deep-Ocean Oxygenation and the Rise of Animal Life. *Science* 315, 92–95.
- Claypool, G.E., Holser, W.T., Kaplan, I.R., Sakai, H., Zak, I., 1980. The age curves of sulfur and oxygen isotopes in marine sulfate and their mutual interpretation. *Chemical Geology* 28, 199–260.
- Derry, L., 2010. A burial diagenesis origin for the Ediacaran Shuram-Wonoka carbon isotope anomaly. *Earth and Planetary Science Letters* 294, 152.
- Fike, D., 2007. Carbon and Sulfur Isotopic Constraints on Ediacaran Biogeochemical Processes, Huqf Supergroup, Sultanate of Oman. Massachusetts Institute of Technology.

- Fike, D.A., Grotzinger, J.P., 2008. A paired sulfate–pyrite  $\delta^{34}\text{S}$  approach to understanding the evolution of the Ediacaran–Cambrian sulfur cycle. *Geochimica et Cosmochimica Acta* 72, 2636–2648.
- Fike, D.A., Grotzinger, J.P., 2010. A  $^{34}\text{S}/\text{SO}_4$  approach to reconstructing biogenic pyrite burial in carbonate-evaporite basins: An example from the Ara Group, Sultanate of Oman. *Geology* 38, 371–374.
- Fike, D.A., Grotzinger, J.P., Pratt, L.M., Summons, R.E., 2006. Oxidation of the Ediacaran Ocean. *Nature* 444, 744–747.
- Forbes, G., Jansen, H., Schreurs, J., 2010. Lexicon of Oman Subsurface Stratigraphy, *GeoArabia* Special Publication. GeoArabia Special Publication, Manama, Bahrain.
- Gellatly, A.M., Lyons, T.W., 2005. Trace sulfate in mid-Proterozoic carbonates and the sulfur isotope record of biospheric evolution. *Geochimica et Cosmochimica Acta* 69, 3813–3829.
- Gill, B.C., Lyons, T.W., Frank, T.D., 2008. Behavior of carbonate-associated sulfate during meteoric diagenesis and implications for the sulfur isotope paleoproxy. *Geochimica et Cosmochimica Acta* 72, 4699–4711.
- Gill, B.C., Lyons, T.W., Jenkyns, H.C., 2011. A global perturbation to the sulfur cycle during the Toarcian Oceanic Anoxic Event. *Earth and Planetary Science Letters* 312, 484–496.
- Goldhammer, R.K., Dunn, P.A., Hardie, L.A., 1990. Depositional styles, composite sea-level changes, cycle stacking patterns, and the hierarchy of stratigraphic forcing: Examples from Alpine Triassic platform carbonates. *GSA Bulletin* 102, 535–562.
- Grotzinger, J.P., Fike, D.A., Fischer, W.W., 2011. Enigmatic origin of the largest-known carbon isotope excursion in Earth's history. *Nat Geosci* 4, 285–292.
- Habicht, K.S.K., Gade, M.M., Thamdrup, B.B., Berg, P.P., Canfield, D.E.D., 2002. Calibration of sulfate levels in the Archean ocean. *Science* 298, 2372–2374.
- Halverson, G., 2005. Toward a Neoproterozoic composite carbon-isotope record. *Geol Soc America Bull* 117, 1181.
- Halverson, G., Hurtgen, M.T., 2007. Ediacaran growth of the marine sulfate reservoir. *Earth and Planetary Science Letters* 263, 32–44.
- Halverson, G.P., Wade, B.P., Hurtgen, M.T., Barovich, K.M., 2010. Neoproterozoic chemostratigraphy. *Precambrian Research* 182, 337–350.
- Hanna, S., Nolan, S., 1989. The Maradi Fault Zone - Evidence of Late Neogene Tectonics in the Oman Mountains. *J Geol Soc London* 146, 867–871.
- Hoffman, P.F., Kaufman, A.J., Halverson, G.P., Schrag, D.P., 1998. A Neoproterozoic Snowball Earth. *Science* 281, 1342–1346.
- Holser, W.T., 1977. Catastrophic chemical events in the history of the ocean. *Nature* 267, 403–408.
- Hurtgen, Arthur, Suits, Kaufman, 2002. The sulfur isotopic composition of Neoproterozoic seawater sulfate: implications for a snowball Earth? *Earth and Planetary Science Letters* 203, 17–17.
- Hurtgen, M.T., Arthur, M.A., Halverson, G.P., 2005. Neoproterozoic sulfur isotopes, the evolution of microbial sulfur species, and the burial efficiency of sulfide as sedimentary pyrite. *Geology* 33, 41.
- Hurtgen, M.T., Arthur, M.A., Prave, A.R., 2004. The sulfur isotope composition of carbonate-associated sulfate in Mesoproterozoic to Neoproterozoic carbonates from

- Death Valley, California. *Geological Society of America Special Paper* 379, 177–194.
- Jones, D.S., Fike, D.A., 2013. Dynamic sulfur and carbon cycling through the end-Ordovician extinction revealed by paired sulfate–pyrite  $\delta^{34}\text{S}$ . *Earth and Planetary Science Letters* 363, 144–155.
- Kah, L.C., Lyons, T.W., Frank, T.D., 2004. Low marine sulphate and protracted oxygenation of the Proterozoic biosphere. *Nature* 431, 834–838.
- Kampschulte, A., Strauss, H., 2004. The sulfur isotopic evolution of Phanerozoic seawater based on the analysis of structurally substituted sulfate in carbonates. *Chemical Geology* 204, 255–286.
- Kaufman, A.J., Corsetti, F.A., Varni, M.A., 2007. The effect of rising atmospheric oxygen on carbon and sulfur isotope anomalies in the Neoproterozoic Johnnie Formation, Death Valley, USA. *Chemical Geology* 237, 47–63.
- Knauth, L., 2009. The late Precambrian greening of the Earth. *Nature* 460, 728.
- Kump, L.R., Arthur, M.A., 1999. Interpreting carbon-isotope excursions: carbonates and organic matter. *Chemical Geology* 161, 181–198.
- Kurtz, A.C., 2003. Early Cenozoic decoupling of the global carbon and sulfur cycles. *Paleoceanography* 18.
- Le Guerroue, E., Allen, P.A., Cozzi, A., 2006a. Chemostratigraphic and sedimentological framework of the largest negative carbon isotopic excursion in Earth history: The Neoproterozoic Shuram Formation (Nafun Group, Oman). *Precambrian Research* 146, 68–92.
- Le Guerroue, E., Allen, P.A., Cozzi, A., Etienne, J.L., Fanning, M., 2006b. 50 Myr recovery from the largest negative  $\delta^{13}\text{C}$  excursion in the Ediacaran ocean. *Terra Nova* 18, 147–153.
- Li, C.C., Love, G.D.G., Lyons, T.W.T., Fike, D.A.D., Sessions, A.L.A., Chu, X.X., 2010. A stratified redox model for the Ediacaran ocean. *Science* 328, 80–83.
- Lloyd, S.J., Marenco, P.J., Hagadorn, J.W., Lyons, T.W., Kaufman, A.J., Sour-Tovar, F., Corsetti, F.A., 2012. Sustained low marine sulfate concentrations from the Neoproterozoic to the Cambrian Insights from carbonates of northwestern Mexico and eastern California. *Earth and Planetary Science Letters* 339–340, 79–94.
- Macdonald, F.A., Schmitz, M.D., Crowley, J.L., Roots, C.F., Jones, D.S., Maloof, A.C., Strauss, J.V., Cohen, P.A., Johnston, D.T., Schrag, D.P., 2010. Calibrating the Cryogenian. *Science* 327, 1241–1243.
- Maloof, A.C., Porter, S.M., Moore, J.L., Dudas, F.O., Bowring, S.A., Higgins, J.A., Fike, D.A., Eddy, M.P., 2010. The earliest Cambrian record of animals and ocean geochemical change. *Geol Soc America Bull* 122, 1731–1774.
- Mann, A., Hanna, S., Robertson, A., Searle, M., Ries, A., 1990. The tectonic evolution of pre-Permian rocks, Central and Southeastern Oman Mountains. *The Geology and Tectonics of the Oman Region* 307–325.
- Marenco, P.J., Corsetti, F.A., Kaufman, A.J., Bottjer, D.J., 2008. Environmental and diagenetic variations in carbonate associated sulfate: An investigation of CAS in the Lower Triassic of the western USA. *Geochimica et Cosmochimica Acta* 72, 1570–1582.
- McFadden, K.A., Huang, J., Chu, X., Jiang, G., Kaufman, A.J., Zhou, C., Yuan, X., Xiao, S., 2008. Pulsed oxidation and biological evolution in the Ediacaran Doushantuo Formation. *PNAS* 105, 3197–3202.

- Narbonne, G.M., 2005. The Ediacaran Biota: Neoproterozoic Origin of Animals and Their Ecosystems. *Annu. Rev. Earth Planet. Sci.* 33, 421–442.
- Planavsky, N.J.N., Bekker, A.A., Hofmann, A.A., Owens, J.D.J., Lyons, T.W.T., 2012. Sulfur record of rising and falling marine oxygen and sulfate levels during the Lomagundi event. *PNAS* 109, 18300–18305.
- Ries, J.B., Fike, D.A., Pratt, L.M., Lyons, T.W., Grotzinger, J.P., 2009. Superheavy pyrite ( $\delta^{34}\text{S}_{\text{pyr}} > \delta^{34}\text{S}_{\text{SCAS}}$ ) in the terminal Proterozoic Nama Group, southern Namibia: A consequence of low seawater sulfate at the dawn of animal life. *Geology* 37, 743–746.
- Rieu, R., Allen, P., Etienne, J., Cozzi, A., Wiechert, U., 2006. A Neoproterozoic glacially influenced basin margin succession and “atypical” cap carbonate associated with bedrock palaeovalleys, Mirbat area, southern Oman. *Basin Research* 18, 471–496.
- Rothman, D.H., Hayes, J.M., Summons, R.E., 2003. Dynamics of the Neoproterozoic carbon cycle. *PNAS* 100, 8124–8129.
- Sahoo, S.K., Planavsky, N.J., Kendall, B., Wang, X., Shi, X., Scott, C., Anbar, A.D., Lyons, T.W.T., Jiang, G.G., 2012. Ocean oxygenation in the wake of the Marinoan glaciation. *Nature* 489, 546–549.
- Schrag, D.P., Higgins, J.A., Macdonald, F.A., Johnston, D.T., 2013. Authigenic Carbonate and the History of the Global Carbon Cycle. *Science* 339, 533–534.
- Scott, C., Lyons, T.W., Bekker, A., Shen, Y., Poulton, S.W., Chu, X., Anbar, A.D., 2008. Tracing the stepwise oxygenation of the Proterozoic ocean. *Nature* 452, 456–459.
- Shen, B., Xiao, S., Kaufman, A.J., Bao, H., Zhou, C., Wang, H., 2008. Stratification and mixing of a post-glacial Neoproterozoic ocean: Evidence from carbon and sulfur isotopes in a cap dolostone from northwest China. *Earth and Planetary Science Letters* 265, 209–228.
- Shen, Y.Y., Zhang, T.T., Hoffman, P.F.P., 2008. On the coevolution of Ediacaran oceans and animals. *PNAS* 105, 7376–7381.
- Strauss, H., 1993. The sulfur isotopic record of Precambrian sulfates: new data and a critical evaluation of the existing record. *Precambrian Research* 225–246.
- Strauss, H., 1997. The isotopic composition of sedimentary sulfur through time. *Palaeogeography, Palaeoclimatology, Palaeoecology* 132, 97–118.
- Verdel, C., Wernicke, B.P., Bowring, S.A., 2011. The Shuram and subsequent Ediacaran carbon isotope excursions from southwest Laurentia, and implications for environmental stability during the metazoan radiation. *Geol Soc America Bull* 123, 1539–1559.
- Wright, V., Ries, A., Munn, S., 1990. Intraplatformal basin-fill deposits from the Infracambrian Huqf Group, east Central Oman, in: Robertson, A., Searle, M., Ries, A. (Eds.), *The Geology and Tectonics of the Oman Region*. Geological Society, pp. 1–16.

*Appendices*

## Appendix A: Supplementary Tables from electronic annex of Chapter 1

Table A1: Sample locations and descriptions

Sample ID	Mat type	Area	Spring	Park Reference	Latitude	Longitude	Sample Date	Temp. (°C)	pH	Description
B09-1	PS	Sentinel Meadows	Bison Pool	LSMG013	44.56953	110.86511	26-Jun-09	81.5	8.4	pink streamers
B09-2	PS	Sentinel Meadows	Bison Pool	LSMG013	44.56953	110.86511	26-Jun-09	76.6	8.4	yellow streamers
B09-3	YB	Sentinel Meadows	Bison Pool	LSMG013	44.56953	110.86511	26-Jun-09	64.5	8.4	yellow biofilm
B09-4a	OM-LT	Sentinel Meadows	Bison Pool	LSMG013	44.56953	110.86511	26-Jun-09		8.4	upper orange layer from conoform orange mat
B09-4b	OM-LT	Sentinel Meadows	Bison Pool	LSMG013	44.56953	110.86511	26-Jun-09		8.4	green middle layer from conoform orange mat
B09-4c	OM-LT	Sentinel Meadows	Bison Pool	LSMG013	44.56953	110.86511	26-Jun-09		8.4	salmon colored sinter pieces at base of conoform mat
BP09-1	PS	White Creek	"Brain Pool"	LWCG149	44.53225	110.79654	26-Jun-09	85	9.0	pink streamers
BP09-2	PS	White Creek	"Brain Pool"	LWCG149	44.53225	110.79654	26-Jun-09	82.5	7.2	pink streamers with green coatings forming in mixing zone between geyser and creek
BS09-1	SR	Sentinel Meadows	Boulder Spring	NA	44.55873	110.84383	26-Jun-09	81.8	9.2	black gelatious sediment
BS09-2	SR	Sentinel Meadows	Boulder Spring	NA	44.55873	110.84383	26-Jun-09	78.6	6.9	black gelatious sediment
FL08-1	OM-HT	White Creek	"Fallen Log"	LWCGNN O51	NM	NM	13-Jun-08			Planar stratified orange mat with orange, green and salmon layers
IG09-1	YB	Sentinel Meadows	Imperial Geyser	NA	44.53167	110.87643	28-Jun-09	69	9.0	yellow topped stratified mat with orange and green layers below
IG09-2a	OM-HT	Sentinel Meadows	Imperial Geyser	NA	44.53167	110.87643	28-Jun-09	64.2	9.1	<1mm thick upper orange and green layer of stratified mat
IG09-2b	OM-HT	Sentinel Meadows	Imperial Geyser	NA	NM	NM	28-Jun-09	64.2	9.1	bright salmon color layers in stratified mat
IG09-2c	OM-HT	Sentinel Meadows	Imperial Geyser	NA	NM	NM	28-Jun-09	64.2	9.1	thick grey soft mat
IG09-3	OM-HT	Sentinel Meadows	Imperial Geyser	NA	44.53167	110.87643	28-Jun-09	62.5	9.0	thick green filaments growing off of stratified orange mat
LJ08-1	YB	White Creek	"Log Jam"	NA	NM	NM	13-Jun-08			yellow biofilm
NG09-1	Carb	Mammoth Hot Spring	Narrow Gauge	MA042	44.96933	110.71044	25-Jun-09	46.5	7.9	floating pieces of mat from terrace pool
NG09-2	Carb	Mammoth Hot Spring	Narrow Gauge	MA042	44.96933	110.71044	25-Jun-09	46.5	7.9	thin orange mat from terrace edge
NG09-3	Carb	Mammoth Hot Spring	Narrow Gauge	MA042	44.96933	110.71044	25-Jun-09	46.5	7.9	thin orange mat from terrace overflow
NG09-4	PS	Mammoth Hot Spring	Old Narrow Gauge	MA041	44.96983	110.7103	25-Jun-09	58.2	6.3	white opaque streamers from source old Narrow Gauge (carbonate system)
NG09-5	Carb	Mammoth Hot Spring	Old Narrow Gauge	MA041	NM	NM	25-Jun-09			orange mat from runoff channel
NG09-6	Carb	Mammoth Hot Spring	Old Narrow Gauge	MA041	NM	NM	25-Jun-09			white carbonate from spring source

NG09-7	Carb	Mammoth Hot Spring	Old Narrow Gauge	MA041	NM	NM	25-Jun-09			thin white streamers in source pool
NG09-8	Carb	Mammoth Hot Spring	Old Narrow Gauge	MA041	NM	NM	25-Jun-09			orange mat from runoff channel
NR08-1	SR	Norris Geyser Basin	unnamed mat	NA	NM	NM	13-Jun-08			zygogonium mat
NR09-1	SR	Norris Geyser Basin	unnamed mat	NA	44.72885	110.71178	25-Jun-09	25.2	2.3	zygogonium mat
NR09-2	SR	Norris Geyser Basin	unnamed mat	NA	44.72885	110.71178	25-Jun-09	25.2	2.3	elemental sulfur colored white mat from zygogonium mat source spring
NR09-3	SR	Norris Geyser Basin	unnamed outflow channel	NA	44.72747	110.7162	25-Jun-09	36.6	3.2	bright green biofilm encrusting center in runoff channel
OC09-1	PS	Sentinel Meadows	Ojo Caliente	LR001	NM	NM	26-Jun-09	80.2	8.4	pink streamers
OS08-1	PS	White Creek	Octopus Spring	LWCGG138	NM	NM	13-Jun-08			pink streamers
OS08-2	YB	White Creek	Octopus Spring	LWCGG138	NM	NM	13-Jun-08			yellow biofilm
OS08-3	OM-LT	White Creek	Octopus Spring	LWCGG138	NM	NM	13-Jun-08			coniform orange mat
OS09-1	PS	White Creek	Octopus Spring	LWCGG138	44.53405	110.79784	26-Jun-09	86.7	8.4	pink streamers
OS09-2	YB	White Creek	Octopus Spring	LWCGG138	44.53405	110.79784	26-Jun-09	74.1	8.4	yellow biofilm
OS09-3	OM-HT	White Creek	Octopus Spring	LWCGG138	44.53405	110.79784	26-Jun-09	63.1	8.4	thick green filaments growing off of stratified orange mat
OS09-4a	OM-LT	White Creek	Octopus Spring	LWCGG138	44.53405	110.79784	26-Jun-09	37.9	8.4	upper orange layer from coniform orange mat
OS09-4b	OM-LT	White Creek	Octopus Spring	LWCGG138	44.53405	110.79784	26-Jun-09	37.9	8.4	green middle layer from coniform orange mat
OS09-4c	OM-LT	White Creek	Octopus Spring	LWCGG138	44.53405	110.79784	26-Jun-09	37.9	8.4	salmon colored sinter pieces at base of coniform mat
SK08-1	PS	White Creek	"Spent Kleenex"	NA	NM	NM	13-Jun-08			grey streamers
SK09-1	PS	White Creek	"Spent Kleenex"	NA	44.53247	110.79757	26-Jun-09	86.9	9.0	white streamers
WB09-1	SR	Washburn Hot Spring	Boomerang	WHSNN014	44.75573	110.43007	27-Jun-09	76.1	3.3	black gelatinous sediment
WB09-2	SR	Washburn Hot Spring	"DEDS"	NA	44.75573	110.43007	27-Jun-09	73.5	5.0	black sediment
WC08-1	OM-LT	White Creek	White Creek	NA	NM	NM	13-Jun-08			green streamers from warm creek channel

### Notes

1. Spring names given in quotations are unofficial names
2. Mat type abbreviations are: PS - streamers, YB - yellow biofilm, OM-HT - orange mat high temperature, OM-LT - orange mat low temperature, Carb - carbonate, SR - sulfur rich
3. Precise GPS coordinates, temperature, and pH were not measured for springs in 2008.

Table A2: Identification of measured fatty acids

<b>Compound ID</b>	<b>IUPAC name</b>	<b>GC/MS retention time</b>	<b>IRMS retention time</b>
<b>12:0</b>	dodecanoic acid	14.43	
<b>13:0</b>	tridecanoic acid	17.4	
<b>14:0</b>	tetradecanoic acid	20.56	12.96
<b>i-15:0</b>	13-methyltetradecanoic acid	22.57	14.5
<b>a-15:0</b>	12-methyltetradecanoic acid	22.82	14.73
<b>15:1</b>	?-pentadecenoic acid	23.1	15.06
<b>15:0</b>	pentadecanoic acid	23.75	15.59
<b>i-16:0</b>	14-methylpentadecanoic acid	25.76	17.66
<b>16:1</b>	?-hexadecenoic acid	26.13-26.47	18.4
<b>16:0</b>	hexadecanoic acid	27.07	19.19
<b>me-17:0</b>	?-methylhexadecanoic acid	28.3	
<b>i-17:0</b>	15-methylhexadecanoic acid	28.91	21.62
<b>a-17:0</b>	14-methylhexadecanoic acid	29.21	22.02
<b>cy-17:0(a)</b>	?,?-methylene-hexadecanoic acid	29.36	
<b>cy-17:0(b)</b>	?,?-methylene-hexadecanoic acid	29.61	22.25
<b>17:0</b>	heptadecanoic acid	30.09	23.3
<b>18:3</b>	?,?,?-octadecatrienoic acid	31.63	
<b>18:2</b>	?,?-octadecadienoic acid	32.1	
<b>18:1</b>	?-octadecenoic acid	32.3-32.5	26.95
<b>18:0</b>	octadecanoic acid	33.14	27.52
<b>me-19:0(a)</b>	?-methyloctadecanoic acid	34.25	
<b>cy-19:0(a)</b>	?,?-methylene-octadecanoic acid	34.57	
<b>me-19:0(b)</b>	?-methyloctadecanoic acid	34.99	29.22
<b>cy-19:0(b)</b>	?,?-methylene-octadecanoic acid	35.54	29.86
<b>19:1</b>	?-nonadecenoic acid	35.6	
<b>19:0</b>	nonadecanoic acid	36.01	30.1
<b>20:4</b>	?,?,?,?-icosatetraenoic acid	36.82	
<b>20:5</b>	?,?,?,?,?-icosapentaenoic acid	37.09	
<b>20:2</b>	?,?-icosadienoic acid	37.98	31.56
<b>20:1(a)</b>	?-icosenoic acid	38.13	31.82
<b>20:1(b)</b>	icosenoic acid	38.33	
<b>20:0</b>	icosanoic acid	38.83	32.02
<b>cy-21</b>	?,?-methylene-icosanoic acid	41.19	33.5
<b>21:0</b>	heneicosanoic acid	41.49	33.58
<b>22:1</b>	?-docosenoic acid	42.69	
<b>22:0</b>	docosanoic acid	43.02	34.98
<b>23:0</b>	tricosanoic acid	44.1	
<b>24:0</b>	tetracosanoic acid	45.12	36.18
<b>25:0</b>	pentacosanoic acid	46.17	
<b>26:0</b>	hexacosanoic acid	47.29	39.6
<b>27:0</b>	heptacosanoic acid	48.51	
<b>28:0</b>	octacosanoic acid	49.94	

Table A3a: Relative Abundances of Fatty Acids (%), low retention time

Sample ID	Fatty Acid ID Mat Type	12:0	13:0	14:0	i- 15:0	a- 15:0	15:1	15:0	i- 16:0	16:1	16:0	me- 17:0	i- 17:0	a- 17:0	cy- 17:0(a)
B09-1	PS	0	0	0	0	0	0	0	0	7.4	0	6.1	0	0	
B09-2	PS	0	1.1	0	3.5	0	0	0	1.8	0.8	3.4	0	10.2	0.9	0
B09-3	YB	0	0	0.5	1.4	0.2	0	0.6	2.3	0.2	31.8	0	2.8	1	0
B09-4a	OM-LT	0	0	0.4	2.5	0.1	1.2	3.2	0.5	16.3	34.8	0.9	1	0.5	0.7
B09-4b	OM-LT	0	0	0.9	1.9	0	0.5	6.6	0.6	11.8	37.6	0.9	1	0	0
B09-4c	OM-LT	0	0	0.9	2.8	0.9	7	15.4	3	6.8	26.4	3.7	4.1	0	0
BP09-1	PS	0	0	0	0	0	0	0	0	2.2	0	12	0.6	0	0
BP09-2	PS	0	0.5	0.4	2.9	0.6	0	0	1.2	5.7	34.8	5	4.8	1.7	0
BS09-1	SR	0	0	3.7	0	0	0	0.5	0	7.7	20.9	0	0	0	0
BS09-2	SR	0	0	4.3	0.7	0	0	0.9	0.5	14.4	27.9	0	1.2	0.5	0
FL08-1	OM-HT	0	0	0	16.9	0	0	0	2.3	0.6	39.1	0	0	0	0
IG09-1	YB	0	0	0.4	0.8	0.1	0	6.2	0.8	0	34.5	0	2.1	0.5	0.2
IG09-2a	OM-HT	0	0	0.1	0.9	0	0	4.1	0.4	0	34.6	0	1.2	0	0
IG09-2b	OM-HT	0	0	0	1	0	0	12	1.3	0	35.8	0	5.6	0	0
IG09-2c	OM-HT	0	0	0	0	0	0	0	0	0	27.5	0	0	0	0
IG09-3	OM-HT	0	0	0.3	2.3	2.4	0	0	0.5	3.3	45.2	0	2.3	0.2	0.2
LJ08-1	YB	0	0	0	1.3	0	0	0.9	2.3	0	40.1	0.4	0	0	0
NG09-1	Carb	0	0	4	0.7	0	0	0.1	0.8	13.4	44	0	0.2	0.1	0
NG09-2	Carb	0	0	13.2	0.5	0	0	0.1	0.2	9.7	29.2	0	0.2	0	0.1
NG09-3	Carb	0	0	9.8	0.9	0	0	0.1	0.5	6.9	37.3	0	0.1	0	0.1
NG09-4	PS	0	0	0.2	1.3	0.5	0	0.6	1.4	1.3	20.7	0	2.8	1.5	0.2
NG09-6	Carb	NM	NM	NM	NM	NM	NM	NM	NM	NM	NM	NM	NM	NM	NM
NG09-5	Carb	0	0	6.8	0.7	0	0	0.3	0	22	34.6	2.4	0.2	0	0.2
NG09-7	Carb	NM	NM	NM	NM	NM	NM	NM	NM	NM	NM	NM	NM	NM	NM
NG09-8	Carb	NM	NM	NM	NM	NM	NM	NM	NM	NM	NM	NM	NM	NM	NM
NR08-1	SR	0	0	0.8	0	0	0	0	0.1	5.7	27.1	0	0	0	0
NR09-1	SR	0.2	1.1	3.3	0	0.1	0	0.9	0.2	15.3	35.7	0	0.5	0.2	0.1
NR09-2	SR	0.4	3.9	5.5	0	0.3	0	2.5	0.3	0.9	29.2	0	0	0.7	0
NR09-3	SR	0	0	3.5	0.2	0	0	0.5	1	17.4	49.3	0	0.1	0.1	0
OC09-1	PS	0	0	0	0	0	0	0	0	0	7.3	0	2.7	0	0
OS08-1	PS	0	0	0	0	0	0	0.3	3.2	0	2.6	0	22.6	0	0
OS08-2	YB	0	0	0.2	1	0	0	5	0	0	37.8	0	2.1	0	0
OS08-3	OM-LT	0	0	0.6	3.4	0	0	2.7	1.7	9.3	37.8	0	0	0	0.8
OS09-1	PS	0	0	0	0	0	0	0	0	0	10	0	27.9	0.4	0
OS09-2	YB	0	0	0.2	0.1	0	0	0.1	1.8	0	37.8	0	1.7	0.5	0
OS09-3	OM-HT	0	0	0	1.8	0	0	1.6	0.9	0	42.3	0	2.4	0.3	0
OS09-4a	OM-LT	0	0	1.1	2.6	0	0.7	0.7	0.5	5.6	41.6	0.2	0.6	0	0.3
OS09-4b	OM-LT	0	0.2	0.8	1.9	0.2	0.5	1.4	0.2	3.3	40.7	0	0.3	0.1	0.2
OS09-4c	OM-LT	0	0	2.4	2.1	0.7	1.2	5.7	0.7	5.5	35.4	0.9	1	0	0.4
SK08-1	PS	0	0	0	0	0	0	0	1.1	0.9	5.7	0	0	0	0
SK09-1	PS	0	0	0	0	0	0	0	0	0	9.7	0	10	0	0
WB09-1	SR	0	0	1.2	0	0	0	0.3	0.4	1.9	24.7	0	0.2	0.4	0
WB09-2	SR	0	0	1.7	0.4	0.4	0	0.4	1	5.8	26.8	0	0.5	0.6	0
WC08-1	OM-LT	0	0	0.2	2.3	0	0	0.1	0	4.6	48.7	0	1.1	0	0.4

Table A3b: Relative Abundances of Fatty Acids (%), medium retention time

Sample ID	Fatty Acid ID	cy-17:0(b)	17:0	18:3	18:2	18:1	18:0	me-19:0(a)	cy-19:0(a)	me-19:0(b)	cy-19:0(b)	19:1	19:0
Sample ID	Mat Type												
B09-1	PS	0	0	0	0	0	31.3	0	0	6.9	0	0	0
B09-2	PS	0	0	0	0.5	4.3	12.7	0	0	0.8	0	0	0.5
B09-3	YB	0	2.7	0	0.6	1.5	28.8	0.4	0.3	0.2	19.6	0	0.3
B09-4a	OM-LT	1.2	4.1	0	7.4	14.5	5.6	0	0	0.2	1.9	0.6	0.2
B09-4b	OM-LT	0	5.2	0	6.9	18	5.1	0	0	0	0.6	0.6	0
B09-4c	OM-LT	0	12.5	0	0.4	8.5	5.6	0.4	0	0	0	0	0.2
BP09-1	PS	0	0.9	0	1	2.6	13.4	0	0	10.8	1.8	0	3.9
BP09-2	PS	0.3	0.7	0	0.5	18.7	9.7	0	0	0	4.1	0	0.6
BS09-1	SR	0	0.6	0	6.6	29.7	10	0	0	1.4	0	0	0
BS09-2	SR	0	0.8	0	3.4	25.4	6.2	0	0	0.5	0.3	0	0.3
FL08-1	OM-HT	0	19.7	0	0	0.5	10.7	0.4	0	0	5.9	0	0.9
IG09-1	YB	0	18	0	0	1	19.7	0.2	0	0.1	14.3	0	0.7
IG09-2a	OM-HT	0	14.4	0	0	0.7	24.3	0.2	0.3	0	17.1	0	1.1
IG09-2b	OM-HT	0	30.7	0	0.4	0	7.2	0.9	0	0	2.7	0	1.3
IG09-2c	OM-HT	0	24.2	0	0	0	44.2	0	0	0	4.2	0	0
IG09-3	OM-HT	0	8	0	0	3.7	20.7	0	3.1	0	0	5.7	1.2
LJ08-1	YB	0	5.2	0	0	0.5	34.4	0	0	0	13.4	0	0.8
NG09-1	Carb	0	0.1	0	14.8	18.6	1.9	0	0	0.3	0	0	0
NG09-2	Carb	0	0.1	0.1	10.7	32.5	1.6	0	0	0.3	0	0	0
NG09-3	Carb	0	0.1	0	14.5	26	1.2	0	0	0.4	0	0	0
NG09-4	PS	0	5.2	0	0.4	12.7	19.2	0	0.3	0.2	12.2	0	1.2
NG09-6	Carb	NM	NM	NM	NM	NM	NM	NM	NM	NM	NM	NM	NM
NG09-5	Carb	0	0.3	0	10.6	18	1.5	0	0	0.3	0	0	0
NG09-7	Carb	NM	NM	NM	NM	NM	NM	NM	NM	NM	NM	NM	NM
NG09-8	Carb	NM	NM	NM	NM	NM	NM	NM	NM	NM	NM	NM	NM
NR08-1	SR	0	0.1	0.8	19.1	35.3	0.7	0	0	0	0.9	0	0
NR09-1	SR	0	0.3	0.9	11	19.4	0.8	0	0	0.2	1.4	0	0
NR09-2	SR	0.1	0.9	0	6.4	17.8	3.6	0	0	0.3	7.2	0	0
NR09-3	SR	0	0.4	0.3	4.8	13.7	3.7	0	0.2	0	0	0	0
OC09-1	PS	0	0.5	0	0	7.2	21.3	0	0	3.1	1	0	1.8
OS08-1	PS	0	0.8	0	0	0	16.4	0.5	0	0	0.8	0	21.3
OS08-2	YB	0	12.4	0	0	0	24.8	0.3	0	0	14.3	0	1.2
OS08-3	OM-LT	0	3.7	0	9.2	21.5	4.6	0	0	0	3.7	0	0
OS09-1	PS	0	1.8	0	7.3	4.4	18.8	0	0	2	0	0	1.6
OS09-2	YB	0	0.9	0	0.3	0.6	40.5	0	0	0	14.3	0	0.3
OS09-3	OM-HT	0	6	0	0.2	4.3	23.1	0	0.3	0	15.5	0	0.4
OS09-4a	OM-LT	0.2	1.2	0	20.6	14	5.2	0	0	0.4	0.5	0.3	0.1
OS09-4b	OM-LT	0.1	1.7	0	21.8	17.5	5.2	0	0	0.5	0.1	0.7	0.1
OS09-4c	OM-LT	0.7	7.1	0	3.4	22.5	6.5	0.3	0	0	0	2.5	0
SK08-1	PS	0	8	0	6.6	8.9	15.8	5.4	0	0	0	0	1
SK09-1	PS	0	0	0	1.2	4.3	24.8	0	0	6.5	0	0	1
WB09-1	SR	0	0.4	0	15.4	38.1	6.5	0	0	1.1	0.8	0	0
WB09-2	SR	0	0	0	7.4	34.3	8.8	0	0	0	3.3	0	0
WC08-1	OM-LT	0	2.3	0	6.1	21.5	8.6	0	0	0	3.4	0	0.2



Table A4: Measured  $\delta D$  values for spring water and fatty acids

Sample ID	Fatty Acid ID	water	14:0	i-15:0	a-15:0	15:1	15:0	i-16:0	16:1	16:0	i-17:0	a-17:0	cy-17:0	17:0
Sample ID	Mat type													
B09-1	PS	-140.3								-174				
B09-2	PS	-141.3	-166					-203	-210	-221				
B09-3	YB	-141.4	-165					-217	-343	-185				-247
B09-4a	OM-LT	-141.4	-191	-155		-191	-216	-162	-262	-247	-124		-195	-223
B09-4b	OM-LT	-141.4	-125			-170	-209		-232	-233				-202
B09-4c	OM-LT	-141.4	-178			-176	-213	-228	-211	-237	-180			-223
BP09-1	PS	-141.4								-203	-255			
BP09-2	PS	-141.4	-169					-224	-268	-283	-188	-249		
BS09-1	SR	-141.1	-253						-284	-241				
BS09-2	SR	-140.8	-254						-286	-261				
FL08-1	OM-HT	-133.5							-226	-275				-241
IG09-1	OM-HT	-139.0								-305				-245
IG09-2a	OM-HT	-140.7				-253	-171		-331	-192				-258
IG09-2b	OM-HT	-140.7												
IG09-2c	OM-HT	-140.7												
IG09-3	OM-HT	-140.7	-198			-251	-185	-247	-304	-189				
LJ08-1	YB	-133.1	-160			-222	-191		-335					-261
NG09-1	Carb	-142.3	-307	-194				-186	-311	-296				
NG09-2	Carb	-142.3	-320	-170				-165	-308	-293				
NG09-3	Carb	-142.3	-321	-176				-177	-300	-293				
NG09-4	PS	-145.6	-257					-285	-266	-308	-342	-277	-256	-322
NG09-6	Carb													
NG09-5	Carb	-145.6	-313	-154					-307	-279				
NG09-7	Carb													
NG09-8	Carb													
NR08-1	SR	-130.0	-267			-193		-293	-283					
NR09-1	SR	-125.6	-257			-246		-305	-280					
NR09-2	SR	-125.6	-224			-238			-264					
NR09-3	SR	-137.2	-314			-261	-278	-335	-269					
OC09-1	PS	-140.3							-219	-173				
OS08-1	PS	-134.8							-237	-258				
OS08-2	YB	-134.8		-244				-327	-202			-264		-330
OS08-3	OM-LT	-134.8	-159			-205	-230	-263	-241			-226		-262
OS09-1	PS	-141.6							-217	-237				
OS09-2	YB	-141.6	-173					-213	-353	-184	-179			-286
OS09-3	OM-HT	-141.6	-166			-224			-319	-157				-240
OS09-4a	OM-LT	-140.2	-241	-142		-200	-146	-260	-250	-105				-201
OS09-4b	OM-LT	-140.2	-206	-131		-230		-251	-225					-192
OS09-4c	OM-LT	-140.2	-216	-143		-237		-273	-248					-240
SK08-1	PS	-137.8							-230					-206
SK09-1	PS	-142.2							-221	-204				
WB09-1	SR	-117.1	-240						-243	-244				
WB09-2	SR	-116.7	-218	-151	-180			-166	-259	-222	-188	-197		
WC08-1	OM-LT	-133.5	-207	-205				-222	-272	-270	-188			-227

Table A4b: Measured  $\delta D$  values for spring water and fatty acids cont.

Sample ID	Mat type	Fatty Acid ID	18:X	18:0	m-19:0	cy-19:0	19:0	20:2	20:1	20:0	cy-21:0	21:0	22:0	24:0	26:0
B09-1	PS		-242	-314						-432	-432	-350			
B09-2	PS		-317	-360						-443	-447				
B09-3	YB		-274	-329		-346					-269				
B09-4a	OM-LT		-258	-197		-285		-300							
B09-4b	OM-LT		-292	-198		-249									
B09-4c	OM-LT		-278	-196											
BP09-1	PS			-323	-254		-309	-371	-377	-357	-360				
BP09-2	PS		-295	-241		-314			-360	-240	-329				
BS09-1	SR		-215	-199						-222			-210	-182	-186
BS09-2	SR		-219	-206						-200			-172		-175
FL08-1	OM-HT			-279		-333									
IG09-1	OM-HT			-308		-328									
IG09-2a	OM-HT			-318		-349		-285		-245					
IG09-2b	OM-HT														
IG09-2c	OM-HT														
IG09-3	OM-HT		-295	-299	-295	-349	-268			-188					
LJ08-1	YB			-322		-333									
NG09-1	Carb		-266	-209											
NG09-2	Carb		-270	-243				-283							
NG09-3	Carb		-285	-226	-251			-301					-178		
NG09-4	PS		-409	-341		-335	-331		-465	-397	-263				
NG09-6	Carb														
NG09-5	Carb		-288	-192				-314							
NG09-7	Carb														
NG09-8	Carb														
NR08-1	SR		-269	-208		-230							-227	-229	-210
NR09-1	SR		-252	-201		-243							-187	-177	-197
NR09-2	SR		-254	-219		-290				-188		-190	-212	-187	-214
NR09-3	SR		-215	-220						-193					-198
OC09-1	PS		-259	-284	-199	-308	-254		-415	-372					
OS08-1	PS			-349	-233		-264		-369	-362	-386				
OS08-2	YB			-344	-310					-205					
OS08-3	OM-LT		-192		-285										
OS09-1	PS		-199	-278	-236					-284	-298	-348			
OS09-2	YB			-337		-318					-242				
OS09-3	OM-HT			-303		-334	-339								
OS09-4a	OM-LT		-256	-183	-230	-286		-339							
OS09-4b	OM-LT		-249	-167	-227	-217		-336							
OS09-4c	OM-LT		-257	-201		-257									
SK08-1	PS			-314	-216					-391	-372	-343			
SK09-1	PS			-252	-187					-381	-359				
WB09-1	SR		-234	-188	-202	-223				-194			-188	-235	-186
WB09-2	SR		-212	-218	-174	-251		-306		-253			-205	-229	
WC08-1	OM-LT		-276	-202		-318							-175		

Table A5: Calculated fractionations (‰) between fatty acid and water

Sample ID	Mat type	Fatty Acid ID	14:0	i-15:0	a-15:0	15:1	15:0	i-16:0	16:1	16:0	i-17:0	a-17:0	cy-17:0	17:0	18:X	18:0			
B09-1	PS									-38					-118	-201			
B09-2	PS		-29					-72		-80	-93				-204	-254			
B09-3	YB		-28					-88		-235	-51				-123	-154	-218		
B09-4a	OM-LT		-57	-16		-58	-87	-24		-141	-123	20		-63	-95	-136	-65		
B09-4b	OM-LT		20			-33	-79			-106	-107				-71	-176	-66		
B09-4c	OM-LT		-43			-40	-84	-101		-81	-111	-45			-95	-160	-64		
BP09-1	PS									-73	-133						-213		
BP09-2	PS		-33					-96		-148	-165	-54		-126			-179	-116	
BS09-1	SR		-130							-166	-117						-85	-67	
BS09-2	SR		-131							-169	-140						-91	-75	
FL08-1	OM-HT									-107	-164						-124	-168	
IG09-1	YB										-193						-123	-197	
IG09-2a	OM-HT					-131	-35			-221	-60						-136	-207	
IG09-2b	OM-HT																		
IG09-2c	OM-HT																		
IG09-3	OM-HT		-67			-129	-51			-124	-189	-57					-180	-184	
LJ08-1	YB		-31			-103	-67			-233							-147	-218	
NG09-1	Carb		-192	-60				-51		-197	-179						-145	-78	
NG09-2	Carb		-207	-32				-27		-193	-175						-149	-118	
NG09-3	Carb		-209	-40				-40		-184	-175						-166	-98	
NG09-4	PS		-130			-163	-141			-190	-230	-154		-129			-206	-309	-229
NG09-6	Carb																		
NG09-5	Carb		-196	-9						-189	-157						-167	-55	
NG09-7	Carb																		
NG09-8	Carb																		
NR08-1	SR		-158					-72		-187	-176						-159	-90	
NR09-1	SR		-150					-137		-206	-177						-144	-86	
NR09-2	SR		-113					-129			-158						-147	-107	
NR09-3	SR		-205					-144	-163		-229	-153					-91	-96	
OC09-1	PS									-91	-38						-139	-167	
OS08-1	PS									-118	-143								-247
OS08-2	YB		-44					-127		-222	-78						-150	-225	
OS08-3	OM-LT		-90	-28				-82	-109		-148	-123					-106	-147	-66
OS09-1	PS									-88	-111						-67	-159	
OS09-2	YB		-37					-84		-246	-49			-44			-168	-228	
OS09-3	OM-HT		-29					-96		-207	-18						-115	-188	
OS09-4a	OM-LT		-118	-2				-70	-7	-140	-128	41					-70	-135	-49
OS09-4b	OM-LT		-76	11				-104		-129	-99						-61	-127	-31
OS09-4c	OM-LT		-88	-3				-113		-154	-125						-116	-136	-71
SK08-1	PS									-107							-79		-205
SK09-1	PS									-92	-72								-128
WB09-1	SR		-139							-143	-144						-133	-81	
WB09-2	SR		-114	-38	-72			-56		-161	-119	-81		-91			-108	-114	
WC08-1	OM-LT		-85	-82				-102		-160	-158	-63					-108	-164	-79
	min:		-209	-130	-72		-58	-163	-163	-229	-246	-154	-129	-63			-206	-309	-254
	max:		-57	20	-72		-33	-70	-7	-81	-38	41	-44	-63			-61	-67	-31
	mean:		-137	-34	-72		-44	-108	-71	-159	-150	-65	-98	-63			-116	-147	-136









## Appendix B Lipid composition and Abundance

**Table B1a:** Lipid distribution of *D. autotrophicum*

ID	14:0	15:1	15:0	m-16	m-16	16:1	16:1	16:0	i-17	cis-9,10	cy-17	17:0
RT	17.19	20.35	20.85	22.31	22.82	23.3	23.45	23.96	25.28	26.28	26.52	26.99
DA_A_A	2.3	0.0	0.3	0.0	0.0	51.3	1.1	23.3	8.7	0.0	1.8	0.8
DA_A_B	1.9	0.2	0.3	0.0	0.0	49.7	0.9	21.4	10.4	0.2	1.9	0.8
DA_S_A	2.1	4.4	4.7	0.4	0.0	35.5	0.5	15.2	8.6	2.2	12.6	6.9
DA_S_B	2.0	4.3	4.8	0.4	0.0	34.2	0.5	14.8	9.4	2.5	12.6	7.9
DA_P_A	2.5	2.9	2.9	0.1	0.0	46.1	0.6	17.1	4.8	1.8	8.3	4.6
DA_P_B	2.5	3.5	3.0	0.1	0.0	43.3	0.9	17.1	4.5	1.4	9.2	5.1
DA_G_A	1.8	0.3	0.3	0.0	0.0	44.5	0.7	24.3	15.7	0.0	2.6	1.5
DA_G_B	2.2	0.3	0.6	0.0	0.0	39.6	0.6	25.2	15.3	0.3	2.4	1.4
DA_H_A	1.2	0.8	2.7	0.3	0.0	27.4	0.0	23.5	17.8	2.2	8.6	5.0
DA_H_B	5.2	3.1	4.1	0.6	0.4	30.0	0.5	23.2	13.7	1.3	6.6	3.5
DA_F_A	2.8	2.9	3.4	0.3	0.3	32.4	0.2	24.8	8.9	1.2	5.6	3.8
DA_F_B	3.4	3.0	3.4	0.3	0.3	30.8	0.5	23.1	10.3	1.3	5.6	3.4

ID	m-18	m-18	18:1	18:1	18:0	m-19	19:0	20:0	21:0	22:0	24:0
RT	28.24	28.9	29.2	29.36	29.96	30.18	32.88	35.66	38.46	41.04	43.69
DA_A_A	0.0	0.0	0.7	8.4	1.3	0.0	0.0	0.0	0.0	0.0	0.0
DA_A_B	0.0	0.0	0.9	9.1	1.8	0.5	0.0	0.0	0.0	0.0	0.0
DA_S_A	0.2	0.0	0.7	4.6	1.1	0.1	0.0	0.0	0.0	0.0	0.0
DA_S_B	0.3	0.0	0.7	4.5	1.3	0.0	0.0	0.0	0.0	0.0	0.0
DA_P_A	0.0	0.0	0.7	6.2	1.4	0.0	0.0	0.0	0.0	0.0	0.0
DA_P_B	0.0	0.0	0.7	6.9	1.6	0.1	0.0	0.0	0.0	0.0	0.0
DA_G_A	0.0	0.0	0.5	6.5	1.3	0.0	0.0	0.0	0.0	0.0	0.0
DA_G_B	0.0	0.0	1.1	8.1	2.6	0.4	0.0	0.0	0.0	0.0	0.0
DA_H_A	0.0	0.0	1.6	5.7	3.1	0.0	0.0	0.0	0.0	0.0	0.0
DA_H_B	0.3	0.0	0.8	3.9	2.5	0.1	0.0	0.0	0.0	0.0	0.0
DA_F_A	0.0	0.2	0.7	3.6	6.7	0.2	0.2	1.5	0.0	0.5	0.1
DA_F_B	0.1	0.1	1.0	4.0	6.2	0.2	0.3	1.8	0.1	0.6	0.2

**Table B1b:** Lipid distribution of *D. hydrogenophilus*

ID	14:1	14:0	15:1	i-15:0	15:0	16:1	16:0	17:0	cy-17	18:1
RT	24.65	25.18	26.54	27.19	28.32	30.34	31.43	32.69	33.68	36.51
DH_A_0	0.4	12.3	0.1	3.5	0.3	15.6	43.1	6.7	14.9	2.4
DH_H_0	0.4	15.0	0.3	1.4	3.3	17.4	35.5	6.1	17.8	2.6

**Table B1c:** Lipid distribution of *E. coli*

ID	12:0	14:0	15:0	16:1	16:1	16:1	16:0	cy17	17:0	18:1	18:1	18:0	cy19
RT	11.3	17.0	20.0	22.5	22.8	22.9	23.0	25.6	26.1	28.4	28.5	29.3	31.6
	8	7	3	7	8	2	9	7	7	6	7	2	4
EC_A_0	0.4	3.8	0.0	0.0	16.4	0.0	41.1	18.5	0.0	0.2	17.1	0.2	2.3
EC_An_0	0.0	6.4	0.0	0.0	18.6	0.0	52.3	15.0	0.0	7.0	0.0	0.2	0.5
EC_An_10	0.0	2.7	0.0	0.0	0.0	0.0	53.9	37.9	0.0	0.0	0.0	0.8	4.7
EC_S_0	0.9	4.4	0.8	0.0	18.3	0.0	40.2	15.3	0.4	0.3	18.0	0.2	1.0
EC_Sn_0	0.0	2.5	9.9	0.0	13.5	0.0	37.6	22.4	2.3	10.7	0.0	0.3	0.8
EC_P_0	0.0	3.5	0.0	0.0	1.2	0.0	46.2	35.7	0.0	0.0	4.3	0.0	9.0
EC_Pn_10	0.0	1.7	0.0	0.0	8.3	0.0	42.7	22.0	0.0	21.0	0.0	0.3	4.0

0													
EC_L_0	0.0	3.3	0.0	0.0	16.8	0.0	40.5	13.6	0.0	0.3	24.1	0.2	1.2
EC_Ln_0	0.5	3.6	0.0	0.0	0.0	0.0	51.1	39.5	0.0	0.0	0.3	0.2	4.9
EC_G_0	0.0	6.1	0.0	0.0	2.2	0.0	51.4	31.4	0.0	0.3	2.5	0.6	5.5
EC_Gn_0	1.4	7.9	0.6	0.2	1.6	0.1	44.2	28.1	0.3	5.0	0.0	0.2	10.3

**Table B1d:** Lipid distribution of *P. denitrificans*

ID	cy-12	C16:1	C16:0	cy-17	C17:0	C18:1	C18:1	C18:0	C19:1	cy-19
RT	11.6	23.4	24.1	26.4	27.1	29.5	29.8	30.1	32.3	32.6
PD_A_0	0.5	0.2	4.8	0.1	0.5	9.0	82.4	1.9	0.1	0.0
PD_A_01	0.1	0.2	8.8	0.0	0.8	19.9	67.3	2.9	0.0	0.0
PD_A_200	0.0	0.1	5.3	0.0	0.5	0.0	92.3	1.8	0.0	0.0
PD_A_400	0.0	0.0	4.9	0.0	0.4	0.0	93.3	1.4	0.0	0.0
PD_An_0	0.0	0.0	4.8	0.0	0.2	0.8	87.5	6.5	0.0	0.0
PD_S_0	0.0	0.1	4.1	0.0	0.0	3.8	90.1	1.9	0.0	0.1
PD_S_01	0.5	0.1	6.4	0.0	0.0	0.0	90.9	2.0	0.0	0.0
PD_S_200	0.7	0.3	7.3	0.0	0.1	2.3	87.3	2.1	0.0	0.0
PD_S_400	0.2	0.3	7.7	0.0	0.1	0.0	89.6	2.1	0.0	0.0
PD_Sn_0	0.8	0.3	6.7	0.0	0.0	3.7	86.8	1.8	0.0	0.0
PD_Sn_200	0.0	0.2	8.9	0.0	0.0	13.0	75.0	2.8	0.0	0.0
PD_Sn_400	0.1	0.3	18.0	0.0	0.0	0.4	75.3	5.9	0.0	0.0
PD_P_0	0.0	0.0	4.1	0.0	0.0	1.2	92.5	2.3	0.0	0.0
PD_L_0	0.0	0.0	3.4	0.1	0.0	0.0	95.1	0.0	1.3	0.0
PD_L_0SP	0.3	0.2	13.1	0.1	0.1	0.0	83.7	2.0	0.6	0.0
PD_Ln_0	0.0	0.6	16.2	0.0	0.0	0.0	79.0	3.6	0.6	0.0
PD_G_0	0.2	0.1	6.2	0.0	0.0	7.6	82.4	3.1	0.0	0.4
PD_G_200	0.3	0.1	5.0	0.0	0.0	0.3	91.9	2.4	0.0	0.0
PD_G_400	0.0	0.0	2.8	0.0	0.0	0.0	94.4	2.8	0.0	0.0
PD_Gn_0	1.0	0.4	8.5	0.0	0.0	3.8	83.2	2.9	0.0	0.2
PD_M_0	0.0	0.0	15.5	0.0	0.0	1.3	59.3	2.4	0.0	20.4
PD_H_0	0.0	0.0	5.5	1.0	0.0	0.0	87.1	5.4	1.0	0.0
PD_H_50	0.0	0.0	5.6	1.3	0.0	0.0	88.6	3.7	0.8	0.0
PD_H_100	0.0	0.0	8.9	0.8	0.0	0.0	82.3	7.1	0.8	0.0
PD_Hn_0	0.0	0.0	10.2	0.0	0.0	1.7	83.6	3.6	0.0	1.0
PD_Hn_50	0.0	0.0	10.9	0.0	0.0	0.0	81.6	7.5	0.0	0.0
PD_Hn_200	0.0	0.0	14.0	0.0	0.0	27.2	47.7	10.5	0.0	0.0
PD_Hn_400	0.0	0.0	14.8	0.0	0.0	0.0	80.1	4.3	0.8	0.0
PD_T_0	0.0	0.0	8.6	0.0	0.0	0.0	81.7	9.6	0.0	0.0
PD_T_50	0.0	0.0	5.5	0.0	0.0	0.0	87.8	6.8	0.0	0.0
PD_T_100	0.0	0.0	4.7	0.0	0.0	0.0	87.3	8.0	0.0	0.0
PD_T_150	0.0	0.0	5.8	0.0	0.0	0.0	86.0	8.2	0.0	0.0
PD_T_200	0.0	0.0	5.2	0.0	0.0	0.0	87.8	7.1	0.0	0.0
PD_Tn_0	0.0	0.0	12.2	0.0	0.0	0.0	77.2	10.6	0.0	0.0
PD_S_1	0.0	0.0	8.8	0.0	0.0	0.0	86.3	4.8	0.0	0.0
PD_S_2	0.4	0.5	8.6	0.0	0.2	0.0	85.6	4.8	0.0	0.0
PD_S_3	0.8	0.6	11.8	0.0	0.2	0.0	82.2	4.4	0.0	0.0
PD_S_4	0.9	0.7	11.5	0.0	0.2	0.0	82.6	4.0	0.0	0.0
PD_S_5	0.6	0.4	12.3	0.0	0.1	0.0	82.8	3.8	0.0	0.0
PD_S_6	0.5	0.4	12.5	0.0	0.1	0.0	82.8	3.6	0.0	0.0
PD_Sn_1	0.0	0.0	23.6	0.0	0.0	0.0	67.5	6.3	0.0	2.6
PD_Sn_2	2.0	0.5	21.0	0.0	0.0	0.0	66.1	7.2	0.0	3.3
PD_Sn_3	0.0	0.0	19.7	0.0	0.0	0.0	67.8	7.7	0.0	4.8
PD_Sn_4	0.0	0.0	21.5	0.0	0.0	0.0	65.9	7.9	0.0	4.7
PD_Sn-5	0.9	0.0	19.0	0.0	0.0	0.0	62.7	11.2	0.0	6.1
PD_Sn_6	0.6	0.1	21.0	0.0	0.0	0.0	66.0	8.1	0.0	4.3

**Table B2a1:** Isotopic fractionation of *D. autotrophicum*

ID	14:0	15:1	15:0	m-16	m-16	16:1comb	16:0	i-17:0	cis-9-10
RT	805.9	953.7	982.3	1075.9	1117.1	1186	1229.5	1342.6	1441.7
DA_A_A	-238		-191			-295	-274	-251	
DA_A_B	-207	-121	-86			-299	-273	-249	-209
DA_S_A	-254	-242	-237	-223		-289	-275	-248	-165
DA_S_B	-239	-214	-225	-196		-296	-280	-258	-157
DA_P_A	-252	-249	-241	-259		-297	-271	-244	-158
DA_P_B	-243	-212	-229			-287	-284	-258	-152
DA_G_A	-250	-215	-211			-299	-285	-261	
DA_G_B	-230	-134	-167			-301	-284	-261	
DA_H_A	-211	-201	-252	-226	-140	-303	-242	-263	-156
DA_H_B	-190	-258	-231	-180	-100	-294	-228	-266	-200
DA_F_A	-189	-248	-220	-214	-170	-297	-193	-245	-191
DA_F_B	-198	-218	-212	-181	-115	-288	-210	-262	-163
Mean	-225	-210	-209	-211	-131	-295	-258	-255	-172

ID	cis-9-10	cy-17	17:0	18:1(a)	18:1(b)	18:1comb	18:0	mean
RT	1470.9	1463.4	1512.3	1780	1810	1802	1883.1	
DA_A_A	-214		-245	-256	-299	-294	-237	-254
DA_A_B	-201	-164	-194	-162	-291	-274	-179	-208
DA_S_A	-232	-212	-260	-247	-296	-289	-243	-248
DA_S_B	-233	-188	-262	-177	-285	-269	-195	-232
DA_P_A	-230	-221	-268	-189	-282	-271	-260	-246
DA_P_B	-230	-177	-267	-225	-298	-290	-231	-242
DA_G_A	-241	-232	-258	-251	-305	-299	-241	-258
DA_G_B	-213	-184	-230	-173	-294	-279	-196	-227
DA_H_A	-242	-200	-267	-192	-292	-265	-172	-226
DA_H_B	-251	-181	-256	-258	-307	-297	-134	-227
DA_F_A	-238	-200	-209	-181	-275	-254	-164	-218
DA_F_B	-230	-195	-216	-252	-303	-292	-165	-219
Mean	-229	-196	-244	-214	-294	-281	-201	

**Table B2a2:** Isotopic fractionation of *D. autotrophicum* error

ID	14:0	15:1	15:0	m-16	m-16	16:1comb	16:0	i-17:0	cis-9-10
RT	805.9	953.7	982.3	1075.9	1117.1	1186	1229.5	1342.6	1441.7
DA_A_A	2.2		24.6			0.4	1.2	3.0	
DA_A_B	20.2		18.0			3.2	3.8	5.0	
DA_S_A	4.9	5.2	5.1	5.5		2.0	5.1	4.7	8.2
DA_S_B	12.2	19.6	7.8	14.2		1.2	4.4	6.0	1.2
DA_P_A	1.5	2.6	2.0			1.8	1.9	1.4	5.9
DA_P_B	2.0	6.0	1.8			0.6	1.3	1.8	2.1
DA_G_A	6.1	19.4	10.6			1.5	5.1	7.6	
DA_G_B	9.1	2.1	15.3			2.0	3.0	4.2	
DA_H_A	12.0	3.8	2.9	19.0	3.2	1.7	8.5	4.2	2.0
DA_H_B	4.9	5.3	4.9	8.1	21.1	1.5	5.9	6.8	17.4
DA_F_A	1.8	2.1	1.8	5.4	29.7	5.4	2.4	3.5	8.5
DA_F_B	1.7	24.6	1.1	8.8	0.7	0.8	2.7	3.3	2.0

ID	cis-9-10	cy-17	17:0	18:1(a)	18:1(b)	18:1comb	18:0
RT	1470.9	1463.4	1512.3	1780	1810	1802	1883.1
DA_A_A	10.5		20.1	9.8	3.0	3.6	6.5
DA_A_B		1.1	2.4	22.5	1.8	1.4	7.6
DA_S_A	6.6	7.0	5.6	14.8	1.8	3.8	12.0
DA_S_B	9.2	11.8	6.0	0.5	2.0	1.0	12.5
DA_P_A	3.6	8.8	6.9	3.5	0.9	3.0	1.6
DA_P_B	4.0	17.8	2.2	36.2	2.5	2.5	1.5
DA_G_A	5.1	12.4	10.4	25.3	1.7	2.8	7.3
DA_G_B	6.0	4.3	16.8	4.3	1.8	0.7	11.0
DA_H_A	6.8	2.0	3.9	6.6	3.4	1.3	2.3
DA_H_B	7.9	5.6	9.8	7.5	1.2	1.6	6.2
DA_F_A	4.9	3.1	9.9	8.2	7.2	6.1	3.7
DA_F_B	12.6	11.5	3.0	0.6	2.4	1.0	3.4

**Table B2b1:** Isotopic fractionation of *D. hydrogenophilus*

ID	14:1	15:1	14:0	i-15	15:0	16:1	16:1	16:0	17:0	cy-17	18:1	mean
RT	660.4	764.9	794.8	833.7	962.2	1145.3	1162.5	1198.4	1301	1439	1753.5	
DH_A_0	-165	-165	-202	-208	-86	-165	-212	-183	-153	-136	-160	-167
DH_H_0	-217	-171	-251	-216	-205	-231	-268	-250	-227	-211	-243	-226

**Table B2b2:** Isotopic fractionation of *D. hydrogenophilus* error

ID	14:1	15:1	14:0	i-15	15:0	16:1	16:1	16:0	17:0	cy-17	18:1
RT	660.4	764.9	794.8	833.7	962.2	1145.3	1162.5	1198.4	1301	1439	1753.5
DH_A_0		15.9	3.6	3.4	12.0	3.3	4.6	5.3	4.5	4.8	11.0
DH_H_0	6.8	13.4	5.5	8.7	6.6	7.8	12.5	4.1	5.0	2.8	9.5

**Table B2c1:** Isotopic fractionation of *E. coli*

ID	?F2	C12:0	C14:0	C15:0	C16:1	C16:0	cy-17	C18:1	cy-19	
RT	489.3	565.3	781.2	955.1	1123.6	1177.1	1421	1742	2017.5	mean
EC_A_0	37	37	31		24	31	31	36	68	37
EC_An_0	-22		7		-24	-15	6	2		-7
EC_An_100			-37			-62	-76		-88	-66
EC_S_0	-16	-12	-20	-48	-18	2	-4	-7	23	-11
EC_Sn_0	-74		-35	-86	-66	-62	-51	-59		-62
EC_P_0			-61		-71	-55	-54	-55	-29	-54
EC_Pn_100			-138		-181	-159	-156	-171	-118	-154
EC_L_0	-14		-19		-38	-30	-29	-25		-26
EC_Ln_0			-102	-113		-105	-87		-58	-93
EC_G_0	-142		-129		-143	-137	-126	-141	-91	-130
EC_Gn_0		-166	-174	-177	-176	-147	-138	-159	-123	-157
EC_Gf_0			-142		-203	-180	-167	-195	-103	-165
EC_Gn_100	-186		-190		-209	-196	-197	-204	-173	-194
EC_Gn_200			-211		-233	-213	-225	-229	-210	-220

**Table B2c2:** Isotopic fractionation of *E. coli* error

ID	?F2	C12:0	C14:0	C15:0	C16:1	C16:0	cy-17	C18:1	cy-19	
RT	489.3	565.3	781.2	955.1	1123.6	1177.1	1421	1742	2017.5	
EC_A_0	1.4	5.9	1.5		1.2	1.3	1.3	1.6	2.4	
EC_An_0	3.0		3.8		8.7	5.3	8.6	6.0		
EC_An_100			3.1			1.9	0.9		3.9	
EC_S_0	6.0	3.0	1.5	6.5	3.2	1.4	2.1	3.2	4.2	
EC_Sn_0	6.9		13.4	8.1	3.1	5.5	9.9	6.2		
EC_P_0			5.0		10.0	2.4	1.8	7.0	2.4	
EC_Pn_100			4.5		4.0	3.8	4.5	4.9	4.1	
EC_L_0	4.8		5.3		6.4	4.9	8.3	7.4		
EC_Ln_0			4.0	5.5		1.8	2.0		2.1	
EC_G_0	4.9		5.2		8.3	1.4	0.6	6.8	4.8	
EC_Gn_0		3.4	2.5	7.1	7.2	2.5	2.5	4.2	2.5	
EC_Gf_0			7.6		1.8	2.5	1.9	1.8	6.5	
EC_Gn_100	5.8		14.7		6.0	6.7	5.5	6.5	6.2	
EC_Gn_200			1.1		2.4	1.9	6.8	6.9	1.8	

**Table B2d1:** Isotopic fractionation of *P. denitrificans*

ID	16:0	17:0	18:1	18:1	18:1	18:0	cy-19	
RT	1214.1	1505	1802	1802	1841.7	1873.3	2037.1	mean
PD_A_0	-29	-32	-35	-33	0	-70		-33
PD_A_01	-75	-73	-66	-46		-46		-61
PD_A_200	-161		-156	-130		-138		-146
PD_A_400	-183	-183		-166		-179		-177
PD_An_0	-128		-159	-94		-97		-120
PD_S_0	-81		-70	-58	-26	-85		-64
PD_S_01	-85			-53		-78		-72
PD_S_200	-188			-156		-162		-169
PD_S_400	-204			-189		-203		-198
PD_Sn_0	-102		-114	-74		-80		-93
PD_Sn_200	-173			-153		-163		-163
PD_Sn_400	-238		-232	-203		-211		-221
PD_P_0	-118		-90	-93		-44		-86
PD_L_0	-161		-147	-167		-126		-150
PD_L_0SP	-168	-119	-144	-182		-133	-116	-144
PD_Ln_0	-170		-142			-131		-148
PD_G_0	-155		-140	-136	-122	-132	-98	-130
PD_G_200	-204			-183		-180		-189
PD_G_400	-249			-232		-294		-258
PD_Gn_0	-179		-158	-116		-121		-144
PD_T_0	-219		-204			-194		-205
PD_T_50	-196		-172			-172		-180
PD_T_100	-196		-182			-171		-183
PD_T_150	-221		-187			-201		-203
PD_T_200	-266		-201	-240		-257		-241
PD_Tn_0	-201		-187			-178		-189
PD_M_0	-267		-262	-227	-251	-193	-192	-232
PD_H_0	-215		-219			-171		-202
PD_H_50	-251		-243			-211		-235
PD_H_100	-250		-251			-226		-242
PD_Hn_0	-165		-153	-141		-134		-148
PD_Hn_50			-210					-210
PD_Hn_200	-240			-227		-229		-232
PD_Hn_400	-281			-245		-278		-268
PD_S_1	-115		-85			-132		-111
PD_S_2	-161		-129			-164		-151
PD_S_3	-191		-160			-142		-164
PD_S_4	-212		-183			-219		-205
PD_S_5	-233		-207			-235		-225
PD_S_6	-235		-206			-232		-225
PD_Sn_1	-213		-201			-218	-168	-200
PD_Sn_2	-246		-235			-242	-205	-232
PD_Sn_3	-286		-279			-274	-271	-277
PD_Sn_4	-285		-282			-283	-263	-278
PD_Sn_5	-305		-299			-319	-291	-304
PD_Sn_6	-292		-295			-289	-296	-293

**Table B2d2:** Isotopic fractionation of *P. denitrificans* error

ID	16:0	17:0	18:1	18:1	18:1	18:0	cy-19
RT	1214.1	1505	1802	1802	1841.7	1873.3	2037.1
PD_A_0	6.9	3.3	4.3	4.1	4.3	50.5	
PD_A_01	6.4	2.2	2.2	1.8		2.0	
PD_A_200	7.5		6.6	8.6		10.9	
PD_A_400	18.4	16.3		16.7		19.8	
PD_An_0	3.1		23.5	3.4		5.2	
PD_S_0	4.7		17.1	14.4	4.0	38.9	
PD_S_01	5.3			3.0		19.9	
PD_S_200	8.5			6.7		12.2	
PD_S_400	19.0			4.9		23.4	
PD_Sn_0	5.0		9.3	6.4		7.7	
PD_Sn_200	14.6			8.3		11.8	
PD_Sn_400	2.3		3.3	2.7		2.3	
PD_P_0	2.0		5.2	4.8		6.5	
PD_L_0	2.9		3.2	2.3		2.4	
PD_L_0SP	1.6	3.1	1.2	1.4		0.9	0.7
PD_Ln_0	3.5		1.4			4.8	
PD_G_0	9.6		8.4	3.8	3.6	5.7	5.0
PD_G_200	2.3			9.7		3.0	
PD_G_400	20.7			16.6		17.9	
PD_Gn_0	1.9		1.0	4.2		4.3	
PD_T_0	7.6		7.5			8.1	
PD_T_50	30.9		3.2			31.8	
PD_T_100	31.1		2.8			35.8	
PD_T_150	23.8		1.9			29.8	
PD_T_200	13.9		2.4	2.1		23.4	
PD_Tn_0	2.1		3.9			6.3	
PD_M_0	7.7		3.1	2.3	3.5	25.7	2.3
PD_H_0	2.0		3.2			2.5	
PD_H_50	2.6		1.9			2.5	
PD_H_100	4.6		3.1			10.4	
PD_Hn_0	3.6		29.2	5.6		10.1	
PD_Hn_50				1.1			
PD_Hn_200	16.3			7.6		28.6	
PD_Hn_400	32.2			10.8			
PD_S_1	4.6		3.8			3.9	
PD_S_2	5.3		5.2			6.7	
PD_S_3	2.6		2.6			7.7	
PD_S_4	3.6		2.0			4.7	
PD_S_5	10.2		6.5			9.7	
PD_S_6	6.6		8.3			11.3	
PD_Sn_1	2.0		2.4			8.6	8.1
PD_Sn_2	2.3		2.6			5.0	4.7
PD_Sn_3	5.7		3.0			5.2	6.4
PD_Sn_4	3.7		4.4			13.0	7.1
PD_Sn_5	5.6		3.8			4.0	9.6
PD_Sn_6	8.0		5.9			16.5	15.0

### Appendix C: Chemostratigraphic data for the Khufai Formation, Chapter 4

Table C1  
Chemostratigraphic data for the Huqf

Section	Stratigraphic Height (m)	Normalized Height Z* (m)	$\delta^{13}\text{C}$	$\delta^{18}\text{O}$	$\delta^{34}\text{S}$	$\text{SO}_4$ (ppm)
BD1	272.2	272.4	-3.81	-4.99		
BD1	271.4	264.8	-3.84	-4.92		
BD1	271.1	261.9	-2.96	-5.00		
BD1	271.1	261.9	-3.62	-5.47		
BD1	270.3	258.8	-4.12	-4.12		
BD1	270.3	258.8	-3.89	-4.34		
BD1	269.5	257.3	-0.32	-5.41		
BD1	269.0	256.3	-0.64	-3.67		
BD1	269.0	256.3	0.21	-4.33		
BD1	266.7	251.9	1.29	-5.35		
BD1	263.4	245.6	3.18	-6.65		
BD1	260.4	239.9	2.38	-5.17		
BD1	256.5	237.5	1.63	-7.77		
BD1	251.4	234.3	2.21	-7.92		
BD1	248.1	232.2	1.86	-7.20		
BD1	243.6	229.3	2.24	-7.91		
BD1	239.0	226.4	1.91	-6.87		
BD1	235.2	223.9	3.00	-7.92		
BD1	234.0	223.1	1.82	-7.33		
BD1	232.1	221.7	2.25	-6.69		
BD1	229.2	219.7	-1.54	-6.81		
BD1	227.0	218.1	-0.36	-7.62		
BD1	224.2	216.2	2.25	-8.22		
BD1	220.3	213.4	-2.20	-5.70		
BD1	217.0	211.1	2.54	-7.56		
BD1	215.0	209.7	-1.42	-3.42		
BD1	211.0	207.0	-1.68	-4.79		
BD1	205.0	202.9	0.37	-5.23		
BD1	203.4	201.8	-0.66	-5.48		
BD1	197.0	197.5	-2.09	-5.80		
BD1	193.6	195.2	0.75	-6.50		
BD1	183.0	188.1	-6.85	-6.32		
BD1	180.0	186.1	-0.90	-4.79		
BD1	175.5	182.6	-0.81	-3.94		
BD1	171.0	179.0	-1.81	-3.73		
BD1	169.4	177.7	0.63	-4.89		
BD1	165.0	174.1	1.68	-4.75		
BD1	164.0	173.3	0.48	-4.89		
BD1	158.0	167.1	0.91	-3.64		
BD1	156.0	164.1	-0.12	-3.03		
BD1	154.5	161.9	1.20	-3.52		
BD1	150.5	156.0	-0.46	-3.52		
BD1	147.5	151.6	-0.26	-5.52		
BD1	144.0	146.5	1.92	-7.70		

Section	Stratigraphic Height (m)	Normalized Height Z* (m)	$\delta^{13}\text{C}$	$\delta^{18}\text{O}$	$\delta^{34}\text{S}$	$\text{SO}_4$ (ppm)
BD1	141.5	142.8	0.04	-8.31		
BD1	138.1	138.4	0.35	-3.58		
BD1	132.5	132.6	-3.73	-2.53		
BD1	126.0	125.7	1.89	-7.02		
BD1	121.0	120.5	1.87	-7.83		
BD1	116.0	115.2	0.50	-3.53		
BD1	113.4	112.5	2.65	-8.82		
BD1	110.0	109.2	3.56	-7.40		
BD1	106.3	106.4	-0.33	-6.97		
BD1	101.0	102.4	3.01	-8.44		
BD1	97.0	99.3	0.21	-8.50		
BD1	93.0	96.3	2.83	-4.75		
BD1	90.0	94.0	1.90	-7.58		
BD1	87.3	91.9	0.10	-5.54		
BD1	84.0	88.8	2.35	-6.93		
BD1	81.0	84.4	2.92	-8.25		
BD1	78.2	80.2	2.71	-9.62		
BD1	77.3	78.9	2.87	-8.92		
BD1	76.0	77.0	2.48	-7.28		
BD1	75.0	75.5	2.53	-4.64		
BD1	74.2	74.3	3.96	-9.92		
BD1	74.2	74.3	4.15	-9.47		
BD1	73.1	72.7	1.47	-8.23		
BD1	72.0	71.0	3.86	-5.51		
BD1	72.0	71.0	3.96	-5.60		
BD1	71.0	69.5	2.47	-6.11		
BD1	70.1	68.0	-1.46	-7.76		
BD1	70.0	67.9	3.03	-9.87		
BD1	70.0	67.9	2.91	-10.33		
BD1	69.0	66.2	2.23	-7.71		
BD1	68.0	64.5	-8.77	-8.15		
BD1	67.0	62.9	3.36	-7.53		
BD1	67.0	62.9	3.29	-8.39		
BD1	64.0	57.9	3.87	-6.48		
BD1	63.0	56.3	3.95	-6.39		
BD1	62.0	54.6	3.70	-6.88		
BD1	62.0	54.6	3.67	-6.93		
BD1	61.2	53.3	3.64	-6.83		
BD1	60.0	51.3	3.95	-6.45		
BD1	59.3	50.2	3.45	-6.44		
BD1	59.3	50.2	3.60	-6.63		
BD1	58.4	49.2	1.96	-6.57		
BD1	56.6	47.5	3.79	-5.99		
BD1	54.0	45.1	4.06	-5.95		
BD1	48.8	40.1	3.97	-6.78		
BD1	47.4	38.8	4.62	-6.11		
BD1	44.0	35.6	4.44	-6.22		
BD1	41.1	32.8	4.28	-6.33		
BD1	37.5	29.4	3.90	-6.37		
BD1	33.0	25.1	4.57	-7.17		

Section	Stratigraphic Height (m)	Normalized Height Z* (m)	$\delta^{13}\text{C}$	$\delta^{18}\text{O}$	$\delta^{34}\text{S}$	$\text{SO}_4$ (ppm)
BD1	31.1	23.7	4.97	-6.03		
BD1	29.0	22.3	4.34	-6.18		
BD1	27.2	21.0	4.10	-7.47		
BD1	27.2	21.0	4.01	-7.67		
BD1	25.5	19.8	4.52	-7.84		
BD1	23.2	18.2	4.19	-7.19		
BD1	20.0	15.9	2.96	-3.27		
BD1	17.0	13.8	2.35	-3.24		
BD1	15.0	12.4	2.77	-3.08		
BD1	11.0	9.6	2.88	-1.57		
BD1	8.0	7.5	2.23	-3.37		
BD1	5.5	5.8	2.42	-3.94		
BD1	3.0	3.4	3.60	-2.12		
BD1	1.7	1.9	2.37	-3.99		
BD1	0.7	0.8	1.25	-3.81		
BD1	0.1	0.1	1.40	-4.62		
BD4	303.0	308.0	-2.60	-5.08		
BD4	302.7	307.4	-1.19	-4.38		
BD4	302.3	306.6	-1.65	-4.90		
BD4	301.8	305.6	-0.74	-5.04		
BD4	300.2	302.4	0.36	-5.23		
BD4	299.4	300.8	0.86	-5.21		
BD4	299.2	300.4	0.53	-4.82		
BD4	298.4	298.6	1.28	-3.64		
BD4	297.0	295.2	2.54	-3.67		
BD4	294.0	288.1	2.68	-3.49		
BD4	293.0	285.7	3.36	-3.44		
BD4	292.2	283.8	3.60	-3.28		
BD4	291.0	281.0	3.44	-2.48		
BD4	290.0	278.1	3.38	-2.84		
BD4	289.0	274.8	3.52	-2.82		
BD4	288.0	271.6	2.63	-3.51		
BD4	286.0	265.2	3.52	-3.20		
BD4	282.0	256.4	3.02	-2.60		
BD4	281.0	254.9	3.72	-3.18		
BD4	280.0	253.4	2.87	-3.32		
BD4	279.0	251.9	2.46	-3.05		
BD4	278.0	250.4	2.22	-3.73		
BD4	277.4	249.6	1.47	-3.98		
BD4	276.1	247.6	1.29	-4.19		
BD4	275.0	246.0	0.70	-3.93		
BD4	273.0	243.0	1.47	-4.12		
BD4	252.8	228.7	3.36	-3.39		
BD4	251.1	227.7	2.81	-3.17		
BD4	248.5	226.1	2.75	-4.07		
BD4	247.1	225.2	2.78	-4.97		
BD4	239.8	216.9	2.59	-4.38		
BD4	238.5	215.4	-1.10	-5.92		
BD4	236.9	213.6	-0.32	-4.72		
BD4	233.9	210.1	0.77	-5.32		

Section	Stratigraphic Height (m)	Normalized Height Z* (m)	$\delta^{13}\text{C}$	$\delta^{18}\text{O}$	$\delta^{34}\text{S}$	$\text{SO}_4$ (ppm)
BD4	84.5	87.1	4.56	-5.23		
BD4	81.6	83.8	1.18	-6.51		
BD4	80.1	82.1	4.44	-5.28		
BD4	76.9	78.4	2.59	-6.61		
BD4	74.4	75.5	4.64	-5.69		
BD4	69.8	70.2	1.52	-7.26		
BD4	67.3	67.5	4.86	-6.23		
BD4	64.3	64.3	4.82	-7.66		
BD4	61.5	61.3	3.58	-5.80		
BD4	58.0	57.5	4.62	-6.78		
BD4	55.7	55.1	4.52	-6.67		
BD4	52.0	51.1	5.19	-7.28		
BD4	47.7	46.1	5.23	-4.72		
BD4	45.4	43.4	4.94	-5.01		
BD4	43.4	41.0	4.96	-4.74		
BD4	39.8	36.8	3.65	-2.77		
BD4	36.9	33.4	4.94	-2.63		
BD4	33.5	29.4	2.35	-2.00		
BD4	30.7	26.1	3.75	-1.71		
BD4	28.8	24.3	5.26	-1.76		
BD4	26.4	22.6	5.26	-1.83		
BD4	22.5	19.7	5.54	-1.78		
BD4	19.5	17.6	5.20	-1.18		
BD4	16.0	15.1	3.96	-2.09		
BD4	12.8	12.8	4.56	-2.28		
BD4	10.6	11.2	5.32	-0.81		
BD4	7.3	8.8	3.95	-1.36		
BD4	5.8	7.7	3.19	-2.39		
BD4	3.8	6.3	2.65	-3.46		
BD4	0.6	1.5	2.52	-2.52		
BD5	307.8	302.2	-1.85	-6.61		
BD5	307.6	301.9	-2.52	-5.46		240
BD5	307.4	301.5	-3.02	-5.15		
BD5	307.0	300.7	-1.89	-5.19		
BD5	306.3	299.3	-1.47	-5.56		
BD5	305.0	296.1	-0.59	-4.55		
BD5	304.9	295.9	-0.67	-4.39		
BD5	304.5	294.9	-0.51	-4.05		
BD5	303.3	292.0	-1.52	-5.07		
BD5	302.8	290.8	-0.10	-4.16		
BD5	302.4	289.9	0.13	-4.49		
BD5	299.4	282.7	0.32	-3.36		
BD5	298.6	280.7	0.31	-2.89		
BD5	298.3	280.0	-0.49	-4.64		
BD5	298.0	276.5	0.42	-3.95		
BD5	297.4	269.4	0.33	-3.82		
BD5	296.9	263.5	0.13	-3.23		
BD5	296.4	259.7	0.14	-3.72		
BD5	295.9	258.9	0.73	-3.17	23.9	229
BD5	295.0	257.6	0.16	-3.52		

Section	Stratigraphic Height (m)	Normalized Height Z* (m)	$\delta^{13}\text{C}$	$\delta^{18}\text{O}$	$\delta^{34}\text{S}$	$\text{SO}_4$ (ppm)
BD5	294.5	256.8	-0.48	-3.34		
BD5	293.9	255.9	-0.51	-3.74		
BD5	291.6	252.5	0.34	-3.24		
BD5	291.4	252.2	0.49	-2.92		
BD5	291.0	251.6	0.72	-3.75		
BD5	290.3	250.5	0.81	-3.37		
BD5	289.2	248.9	1.56	-2.96		
BD5	289.2	248.9	1.65	-3.67		
BD5	287.0	245.6	1.22	-4.91	30.0	384
BD5	286.0	244.1	1.55	-5.12		
BD5	284.5	241.8	2.51	-5.22		
BD5	283.5	240.3	2.80	-5.41		
BD5	283.2	239.9	3.05	-4.81		
BD5	282.4	239.4	2.80	-5.87		
BD5	281.9	239.1	-0.37	-5.75		
BD5	281.5	238.8	0.66	-6.98		
BD5	280.0	237.9	3.92	-6.01	25.2	359
BD5	276.0	235.3	3.51	-6.95		
BD5	272.3	234.0			25.6	416
BD5	271.4	233.3	3.13	-6.04		
BD5	268.9	231.5	-1.25	-5.58		
BD5	263.0	227.1	1.90	-7.52		
BD5	262.0	226.3	1.22	-7.46		
BD5	255.5	221.5	3.22	-7.73		
BD5	254.1	220.5	0.77	-2.45		
BD5	250.1	217.5	2.35	-5.55	31.6	433
BD5	245.5	214.1	2.20	-8.24		
BD5	243.5	212.6	-1.60	-5.59	40.5	937
BD5	240.0	210.0	-2.02	-5.09		
BD5	238.6	209.0	-3.94	-3.10		
BD5	236.0	207.2	-1.66	-6.80		
BD5	219.9	195.8	2.12	-7.36		
BD5	217.8	194.3	3.29	-8.71		264
BD5	205.4	185.6	-0.02	-7.20		
BD5	199.0	181.6	2.43	-6.15		
BD5	197.1	180.4	2.58	-5.92		
BD5	193.9	178.5	1.58	-7.19		
BD5	183.4	172.1	1.92	-3.44		
BD5	181.7	171.0	1.67	-4.46	25.2	250
BD5	134.3	119.5	-0.01	-9.13		
BD5	133.3	118.2			26.4	817
BD5	131.2	115.5	0.44	-5.23		
BD5	127.5	110.7	0.28	-7.89		
BD5	125.6	109.2	2.55	-9.38		
BD5	124.7	108.6			29.2	294
BD5	118.5	104.9	4.46	-7.82		
BD5	116.2	103.5	0.76	-7.18		
BD5	114.7	102.6				559
BD5	110.1	99.8	3.21	-8.09		
BD5	109.5	99.5			42.0	586

Section	Stratigraphic Height (m)	Normalized Height Z* (m)	$\delta^{13}\text{C}$	$\delta^{18}\text{O}$	$\delta^{34}\text{S}$	$\text{SO}_4$ (ppm)
BD5	108.1	98.6	2.27	-5.07		
BD5	104.1	96.2			29.8	446
BD5	103.1	95.6	3.79	-8.59		
BD5	96.1	91.4	3.14	-7.13	38.7	624
BD5	92.5	89.0	1.03	-5.41		
BD5	88.0	85.0	3.11	-5.18	25.1	617
BD5	84.2	81.7	3.27	-7.14	23.7	362
BD5	83.1	80.8	-1.03	-8.12		
BD5	70.4	69.7	4.07	-6.41		
BD5	68.2	66.9			21.5	193
BD5	65.8	64.0	4.55	-5.24	21.0	158
BD5	60.2	57.0	3.18	-4.42		
BD5	58.4	54.8			21.9	339
BD5	55.4	51.1	4.92	-5.36		
BD5	50.5	45.2	4.47	-4.93	22.8	201
BD5	44.4	37.8			21.0	200
BD5	43.3	36.5	4.95	-4.99		
BD5	40.5	33.1			22.3	129
BD5	37.0	28.9	4.84	-4.87		
BD5	34.1	25.4	5.03	-5.85		
BD5	33.1	24.5			28.5	330
BD5	31.8	23.7	4.58	-4.09		
BD5	28.2	21.3			30.3	448
BD5	25.7	19.6	4.76	-2.11		
BD5	24.3	18.7			28.5	558
BD5	22.1	17.3	4.12	-2.14		
BD5	19.0	15.2			31.0	542
BD5	15.3	12.7	2.93	-2.05		
BD5	14.4	12.2			29.7	458
BD5	12.2	10.7	3.70	-2.97		
BD5	10.0	9.2	3.33	-3.05	28.4	400
BD5	6.5	6.9	3.25	-3.37		
BD5	5.0	5.9			26.4	390
BD5	3.0	4.2	2.46	-3.10		
BD5	0.0	0.0	-0.33	-3.21	24.4	313
BD6	91.0	302.9	-0.64	-5.66		
BD6	91.0	302.9	-0.58	-5.69		
BD6	90.5	302.0	-0.33	-5.78		
BD6	90.5	302.0	-0.24	-5.47		
BD6	90.1	301.2	0.25	-4.82		
BD6	90.1	301.2	0.31	-4.94		
BD6	89.8	300.7	-0.84	-5.69		
BD6	89.8	300.7	-0.76	-5.69		
BD6	89.0	299.0	1.76	-2.58		
BD6	89.0	299.0	1.73	-2.63		
BD6	88.3	297.4	1.77	-4.36		
BD6	88.3	297.4	1.75	-4.27		
BD6	86.5	293.1	2.76	-4.40		
BD6	86.5	293.1	2.69	-4.10		
BD6	86.0	291.9	2.77	-2.79		

Section	Stratigraphic Height (m)	Normalized Height Z* (m)	$\delta^{13}\text{C}$	$\delta^{18}\text{O}$	$\delta^{34}\text{S}$	$\text{SO}_4$ (ppm)
BD6	86.0	291.9	2.47	-3.32		
BD6	85.9	291.7	3.17	-3.67		
BD6	85.9	291.7	3.05	-3.34		
BD6	85.0	289.5	3.66	-3.97		
BD6	85.0	289.5	3.30	-3.37		
BD6	84.1	287.4	2.64	-4.28		
BD6	84.1	287.4	2.39	-3.63		
BD6	83.0	284.8	3.08	-3.62		
BD6	83.0	284.8	2.88	-3.93		
BD6	81.3	280.7	3.07	-4.07		
BD6	81.3	280.7	2.73	-4.13		
BD6	80.7	277.6	3.31	-3.16		
BD6	80.7	277.6	3.08	-2.84		
BD6	80.0	272.0	3.67	-4.09		
BD6	80.0	272.0	3.40	-2.94		
BD6	79.0	264.0	4.23	-3.09		
BD6	79.0	264.0	4.02	-2.52		
BD6	78.0	259.2	3.78	-2.21		
BD6	78.0	259.2	3.62	-2.22		
BD6	73.2	251.5	3.06	-3.00		
BD6	73.2	251.5	3.12	-2.55		
BD6	72.3	250.1	2.97	-2.73		
BD6	72.3	250.1	3.09	-2.46		
BD6	69.3	245.3	2.38	-2.90		
BD6	69.3	245.3	2.34	-2.86		
BD6	66.8	241.3	1.82	-4.91		
BD6	66.8	241.3	2.01	-4.70		
BD6	65.9	239.9	1.79	-4.56		
BD6	65.9	239.9	1.95	-4.11		
BD6	55.5	231.2	2.25	-2.93		
BD6	55.5	231.2	2.39	-3.33		
BD6	51.8	228.2	2.17	-2.75		
BD6	51.8	228.2	2.89	-8.60		
BD6	46.1	223.9	2.36	-4.77		
BD6	46.1	223.9	2.31	-4.23		
BD6	5.0	198.0	1.53	-6.48		
BD6	5.0	198.0	1.55	-6.41		
BD6	4.2	197.4	0.43	-4.84		
BD6	4.2	197.4	0.47	-4.81		
BD6	2.7	196.4	1.83	-4.24		
BD6	2.7	196.4	1.82	-4.04		
BD6	1.9	195.8	2.05	-4.66		
GH1	13.3	310.4	1.65	-2.63		
GH1	12.6	309.4	0.21	-3.09		
GH1	11.8	308.6	-0.58	-2.63		
GH1	10.8	307.6	1.08	-2.55		
GH1	10.6	307.4	1.37	-3.10		
GH1	3.4	300.3	2.59	-3.23		
GH1	2.4	297.3	3.36	-2.69		
GH1	1.6	294.1	3.49	-2.58		

Section	Stratigraphic Height (m)	Normalized Height Z* (m)	$\delta^{13}\text{C}$	$\delta^{18}\text{O}$	$\delta^{34}\text{S}$	$\text{SO}_4$ (ppm)
GH1	0.3	289.0	3.03	-3.75		
KDE	319.4	304.0	0.88	-2.84		
KDE	319.2	303.8	0.91	-2.85		
KDE	318.8	303.6	1.92	-2.58		
KDE	319.2	303.8	1.09	-3.52		
KDE	319.0	303.7	1.69	-4.28		
KDE	318.7	303.5	1.59	-3.75		
KDE	318.1	303.1	1.32	-3.81		
KDE	317.5	302.7	2.38	-2.69		
KDE	316.5	302.1	2.78	-3.08		
KDE	316.0	301.7	2.54	-3.35		
KDE	313.5	300.1	2.23	-3.95		
KDE	311.3	296.8	1.40	-4.22		
KDE	310.8	296.1	1.78	-3.17		
KDE	308.8	293.0	1.99	-2.96		
KDE	307.8	291.5	1.40	-3.79		
KDE	306.2	289.1	2.21	-1.70		
KDE	305.2	287.6	1.64	-2.59		
KDE	304.0	285.8	2.32	-2.94		
KDE	303.1	284.4	2.49	-3.12		
KDE	302.6	283.6	2.25	-2.64		
KDE	301.4	281.8	2.81	-3.46		
KDE	300.1	279.4	0.89	-2.58		
KDE	299.3	274.7	1.35	-2.24		
KDE	295.8	258.3	1.44	-2.17		
KDE	293.5	254.3	1.59	-1.90		
KDE	290.0	248.2	2.20	-2.14		
KDE	287.2	243.3	2.02	-3.58		
KDE	284.3	239.0	2.41	-3.40		
KDE	283.0	237.7	2.83	-2.22		
KDE	281.2	235.8	2.35	-2.84		
KDE	280.0	234.6	2.84	-3.10		
KDE	278.5	233.1	2.94	-2.99		
KDE	276.3	230.9	3.39	-1.81		
KDE	274.3	228.9	4.27	-2.97		
KDE	274.0	228.5	3.86	-2.93	23.4	499.16
KDE	273.3	227.8	3.50	-3.76	26.1	418.82
KDE	272.3	226.8	3.16	-3.45		
KDE	271.1	225.6	2.61	-3.11	26.5	305.12
KDE	270.3	224.9	2.31	-2.13		
KDE	270.1	224.7	1.96	-2.00	28.3	300.80
KDE	269.8	224.5	2.40	-2.94	28.6	332.42
KDE	269.5	224.3	3.04	-1.29	29.4	368.91
KDE	269.3	224.2	3.18	-1.29	28.0	248.48
KDE	269.0	224.0	2.93	-2.83	29.6	284.15
KDE	268.3	223.5	1.31	-5.61		
KDE	267.9	223.3	2.74	-2.79	26.4	505.37
KDE	266.1	222.1	2.90	-2.59		
KDE	265.2	221.5	3.40	-2.39	27.3	367.18
KDE	264.0	220.7	3.59	-3.67		

Section	Stratigraphic Height (m)	Normalized Height Z* (m)	$\delta^{13}\text{C}$	$\delta^{18}\text{O}$	$\delta^{34}\text{S}$	$\text{SO}_4$ (ppm)
KDE	261.5	219.0	3.64	-2.82		
KDE	259.8	217.9	3.12	-2.76		
KDE	257.4	216.3	3.97	-2.52		
KDE	255.4	215.0	3.93	-2.88		
KDE	252.7	213.2	3.14	-3.53		
KDE	251.1	212.1	3.61	-2.95		
KDE	249.0	210.7	3.86	-2.81		
KDE	247.9	210.0	3.03	-1.51		
KDE	244.0	206.8	3.78	-2.76		
KDE	242.1	205.3	3.47	-3.00		
KDE	239.9	203.5	3.73	-3.26		
KDE	237.1	201.3	3.56	-2.67		
KDE	235.4	199.9	3.42	-2.29		
KDE	234.3	199.0	3.64	-3.47		
KDE	233.4	198.3	3.55	-3.65		
KDE	230.5	195.9	3.53	-0.68		
KDE	228.4	194.2	1.36	-3.76		
KDE	226.1	192.4	3.89	-1.58		
KDE	224.1	190.7				
KDE	223.6	190.3	4.13	-2.97		
KDE	220.0	187.4	3.30	-2.00		
KDE	218.7	186.4	1.40	-2.93		
KDE	216.0	184.3	3.09	-2.51		
KDE	213.8	182.7	2.70	-2.24		
KDE	211.2	180.9	3.15	-2.75		
KDE	208.0	178.6	4.31	-2.59		
KDE	206.3	177.4	4.33	-1.05		
KDE	204.5	176.1	3.71	-3.44		
KDE	203.8	175.6	3.54	-2.87		
KDE	200.5	173.3	3.22	-1.43		
KDE	198.6	171.9	3.34	-3.30		
KDE	195.6	169.7	4.22	-1.74		
KDE	186.5	161.8	0.60	-2.85		
KDE	180.9	157.0	4.08	-2.41		
KDE	178.8	155.1	3.62	-3.40		
KDE	177.8	154.3	4.12	-3.32		
KDE	175.8	152.5	4.44	-3.74		
KDE	172.3	149.5	2.88	-4.03		
KDE	171.2	148.5	4.73	-3.52		
KDE	168.4	146.1	4.56	-3.23		
KDE	166.1	144.1	4.60	-3.13		
KDE	164.3	142.5	5.10	-1.64		
KDE	161.0	139.6	4.67	-1.68		
KDE	160.0	138.5	4.19	-2.48		
KDE	158.8	137.3	4.05	-2.98		
KDE	155.4	133.7	4.26	-3.78		
KDE	150.7	128.8	4.23	-3.63		
KDE	149.9	128.0	4.68	-3.17		
KDE	147.5	125.5	4.83	-2.92		
KDE	145.2	123.1	3.53	-3.95		

Section	Stratigraphic Height (m)	Normalized Height Z* (m)	$\delta^{13}\text{C}$	$\delta^{18}\text{O}$	$\delta^{34}\text{S}$	$\text{SO}_4$ (ppm)
KDE	142.3	120.0	4.87	-1.34		
KDE	142.3	120.0	4.78	-1.49		
KDE	141.3	119.0	3.37	-2.64		
KDE	139.7	117.3	4.59	-2.89		
KDE	139.7	117.3	4.56	-2.89		
KDE	137.5	115.0	4.09	-1.84		
KDE	136.0	113.4	4.07	-2.68		
KDE	134.0	111.4	3.87	-3.16		
KDE	132.5	109.9	4.22	-3.16		
KDE	130.9	108.7	3.47	-3.15		
KDE	128.0	106.7	3.60	-3.91		
KDE	126.5	105.7	4.06	-4.10		
KDE	123.9	103.8	4.20	-3.29		
KDE	121.6	102.2	3.57	-3.83		
KDE	120.7	101.6	4.82	-1.99		
KDE	118.3	99.9	5.28	-0.89		
KDE	116.9	99.0	5.12	-1.18		
KDE	114.9	97.6	5.32	-0.31		
KDE	112.3	95.7	5.12	-0.20		
KDE	111.0	94.8	4.19	-0.97		
KDE	110.8	94.7	4.33	-0.67		
KDE	109.5	93.8	5.08	-0.50		
KDE	108.5	93.1	4.76	-1.19		
KDE	107.1	92.1	4.86	-5.37		
KDE	105.2	90.8	5.12	-2.20		
KDE	103.0	89.1	5.17	-0.71		
KDE	102.2	88.5	4.66	-1.47		
KDE	99.2	86.1	4.33	-1.26		
KDE	97.0	84.3	5.25	-4.73		
KDE	95.0	82.7	5.19	-2.85		
KDE	93.1	81.2	4.88	-5.99		
KDE	91.0	79.6	4.85	-0.24		
KDE	89.7	78.5	4.43	-1.55		
KDE	86.0	75.6	4.93	-2.94		
KDE	84.0	74.0	5.21	-5.16		
KDE	81.3	71.8	4.04	-2.45		
KDE	79.4	70.3	5.34	-6.76		
KDE	76.0	66.2	4.72	-2.34		
KDE	74.5	64.3	5.02	-7.43		
KDE	73.0	62.4	4.65	-2.81		
KDE	71.8	60.9	5.01	-5.20		
KDE	68.8	57.1	4.85	-5.67		
KDE	65.3	52.7	4.93	-6.48		
KDE	62.0	49.1	5.05	-5.82		
KDE	59.6	47.3	5.13	-6.41		
KDE	57.3	45.5	2.98	-6.61		
KDE	55.5	44.1	4.46	-7.11		
KDE	53.5	42.6	5.79	-5.50		
KDE	51.2	40.9	5.52	-3.71		
KDE	49.7	39.7	5.53	-4.72		

Section	Stratigraphic Height (m)	Normalized Height Z* (m)	$\delta^{13}\text{C}$	$\delta^{18}\text{O}$	$\delta^{34}\text{S}$	$\text{SO}_4$ (ppm)
KDE	45.4	36.5	1.93	-6.92		
KDE	42.5	34.3	5.56	-4.74		
KDE	39.8	32.2	5.70	-3.83		
KDE	37.9	30.8	5.32	-4.57		
KDE	35.6	29.0	5.43	-4.77		
KDE	33.7	27.6	4.34	-4.58		
KDE	31.1	25.6	5.08	-4.40		
KDE	30.4	25.1	3.84	-3.93		
KDE	27.2	22.8	5.22	-4.16		
KDE	25.0	21.3	5.71	-4.05		
KDE	21.5	18.9	4.40	-3.64		
KDE	18.7	16.9	5.38	-7.53		
KDE	16.5	15.4	4.79	-5.75		
KDE	14.6	14.1	5.44	-6.92		
KDE	13.5	13.3	4.87	-6.77		
KDE	11.3	11.8	3.75	-3.00		
KDE	9.0	10.2	1.80	-2.35		
KDE	7.0	8.8	0.54	-3.55		
KDE	5.1	7.5	2.17	-3.20		
KDE	4.0	6.7	2.28	-3.41		
KDE	2.0	5.3	2.66	-3.11		
KDE	0.0	0.0	3.58	-2.71		
KDS	274.3	236.5	4.09	-3.50	29.3	330
KDS	273.8	236.0	3.88	-2.24	20.6	478
KDS	273.3	235.5	3.75	-0.95		
KDS	272.5	234.7	3.80	-1.75		
KDS	271.9	234.1	1.43	-1.44		
KDS	271.7	233.9	2.89	-2.08	26.4	869
KDS	270.8	233.1	2.34	-2.74		
KDS	270.3	232.6	3.91	-2.00		
KDS	269.8	232.1	2.82	-1.41		
KDS	269.4	231.7	3.96	-1.81		
KDS	269.2	231.5	3.91	-2.29	29.7	246
KDS	269.0	231.3	2.64	-1.96		
KDS	268.5	230.8	4.03	-1.17		
KDS	268.4	230.7	5.00	-2.67		
KDS	268.0	230.3	5.03	-3.41		
KDS	267.5	229.8	4.56	-2.69	28.0	761
KDS	267.1	229.5	3.89	-1.54		
KDS	266.8	229.2	2.37	-1.19		
KDS	266.6	229.0	4.39	-1.37	30.3	246
KDS	265.1	227.5	4.08	-2.42		
KDS	264.6	227.0	5.07	-3.26		
KDS	264.2	226.6	4.32	-1.33		
KDS	263.6	226.1	4.30	-3.48	28.8	621
KDS	263.1	225.6	3.84	-2.58		
KDS	262.6	225.1	3.21	-3.02		
KDS	262.1	224.7	2.76	-2.69		
KDS	261.4	224.3	1.62	-2.43		
KDS	260.6	223.8	2.51	-1.18		

Section	Stratigraphic Height (m)	Normalized Height Z* (m)	$\delta^{13}\text{C}$	$\delta^{18}\text{O}$	$\delta^{34}\text{S}$	$\text{SO}_4$ (ppm)
KDS	260.1	223.5	0.63	-2.87		
KDS	259.6	223.1	3.17	-0.06	27.2	680
KDS	259.2	222.9	3.01	-2.52	29.1	280
KDS	258.7	222.6	3.04	-1.14		
KDS	258.6	222.5	4.09	-3.50		
KDS	258.1	222.2	2.74	-2.51		
KDS	257.7	221.9	2.88	-2.97		
KDS	257.6	221.9	2.80	-2.91		
KDS	256.9	221.4	2.75	-2.15		
KDS	256.6	221.2	3.42	-2.93	26.2	392
KDS	255.6	220.6	3.20	-3.27		600
KDS	254.6	219.9	2.89	-2.68	29.3	292
KDS	253.1	219.0	2.88	-3.03		
KDS	251.9	218.2	4.02	-2.63	27.7	341
KDS	251.5	218.0	3.54	-3.35	28.3	312
KDS	251.2	217.8	3.30	-3.30		
KDS	250.7	217.4	3.38	-2.47		
KDS	249.6	216.7	4.27	-3.46	28.3	266
KDS	248.3	215.9	4.12	-2.09		
KDS	248.2	215.8	4.17	-2.73		
KDS	246.5	214.8	4.20	-3.19		
KDS	245.5	214.2	4.04	-2.83		
KDS	244.7	213.7	3.36	-3.64		
KDS	244.3	213.4	0.78	-3.25		
KDS	243.5	212.9	4.25	-3.26	28.8	281
KDS	242.5	212.3	3.74	-2.93		
KDS	242.1	212.0	3.87	-3.34		
KDS	241.3	211.5	4.15	-2.88		
KDS	240.5	211.0	3.23	-2.10		
KDS	239.6	210.4	3.33	-3.09		
KDS	238.9	209.9	1.56	-2.98	23.9	289
KDS	237.9	209.1	3.61	-3.71		
KDS	237.5	208.8	3.16	-2.15		
KDS	236.5	207.9	3.84	-2.98	28.2	190
KDS	235.5	207.1	4.17	-2.88		
KDS	234.4	206.1	3.40	-1.35	23.8	728
KDS	233.0	205.0	3.46	-3.42		
KDS	231.8	203.9	3.76	-2.51		
KDS	230.8	203.1	3.89	-3.30		
KDS	229.2	201.7	3.64	-3.37	26.5	360
KDS	227.8	200.6	3.36	-2.95	26.1	347
KDS	227.0	199.9	3.27	-3.77		
KDS	226.0	199.0	2.64	-2.70	27.9	317
KDS	225.0	198.2	2.90	-2.98		
KDS	223.8	197.2	2.80	-3.16		
KDS	222.8	196.3	2.71	-2.75	22.4	366
KDS	221.8	195.5	3.45	-3.15		
KDS	220.5	194.4	3.46	-2.53		
KDS	219.5	193.5	3.82	-2.97	27.4	238
KDS	218.3	192.5	3.11	-4.00		

Section	Stratigraphic Height (m)	Normalized Height Z* (m)	$\delta^{13}\text{C}$	$\delta^{18}\text{O}$	$\delta^{34}\text{S}$	$\text{SO}_4$ (ppm)
KDS	218.3	192.5	2.70	-2.87		
KDS	217.2	191.6	2.96	-2.20	25.2	308
KDS	217.1	191.5	3.45	-2.73		
KDS	216.4	190.9	2.71	-2.75		
KDS	216.3	190.8	3.45	-3.15		
KDS	215.5	190.1	3.46	-2.53		
KDS	215.4	190.1				
KDS	213.8	188.7	3.71	-3.40	22.1	312
KDS	212.8	187.9	4.31	-2.03		
KDS	212.0	187.2	2.70	-3.17		
KDS	210.1	185.6	3.35	-3.54	25.8	251
KDS	208.9	184.7	4.26	-2.79		
KDS	208.0	184.0	3.91	-2.73	23.9	253
KDS	207.0	183.4	3.73	-3.01		
KDS	205.9	182.6	3.03	-2.60	22.8	273
KDS	204.2	181.5	3.59	-3.53		
KDS	203.9	181.3	4.00	-3.20		
KDS	202.8	180.6	4.15	-2.26	26.8	161
KDS	201.7	179.8	3.85	-2.58	23.9	106
KDS	200.6	179.0	3.87	-2.42	20.6	323
KDS	199.6	178.4	3.85	-2.73		
KDS	198.5	177.7	4.22	-3.26	23.0	249
KDS	197.0	176.6	4.52	-2.91		
KDS	196.8	176.5	3.59	-1.77	25.0	177
KDS	195.5	175.7	3.90	-3.19		
KDS	194.4	174.9	4.06	-3.05	21.9	243
KDS	186.1	168.7	3.64	-2.85	21.9	164
KDS	184.8	167.2	3.28	-3.00	20.8	306
KDS	183.5	165.6	3.52	-4.11		
KDS	182.6	164.4	3.22	-2.61	20.3	351
KDS	181.7	163.3	3.08	-1.89	21.0	322
KDS	180.8	162.2	3.60	-3.01		
KDS	179.9	161.1	4.37	-2.61		
KDS	179.0	159.9	4.15	-3.40	24.5	227
KDS	178.0	158.8	4.21	-3.46	24.2	163
KDS	177.1	157.7	3.66	-2.49	21.7	377
KDS	176.0	156.3	4.62	-2.59		
KDS	174.0	153.8	4.70	-1.87		
KDS	172.5	152.0	3.17	-2.50	21.0	223
KDS	171.6	150.9	4.62	-3.57		
KDS	170.5	149.5	4.60	-2.21		
KDS	169.6	148.4	4.90	-3.45		
KDS	169.1	147.7	4.08	-3.54	22.7	179
KDS	168.2	146.6	4.00	-2.77	22.3	283
KDS	166.5	144.5	3.59	-2.65		
KDS	165.5	143.4	3.90	-3.24	19.9	357
KDS	164.6	142.3				
KDS	163.7	141.1	4.40	-3.64	18.1	652
KDS	162.9	140.1	4.72	-3.77		
KDS	161.9	139.1	4.75	-2.76	24.4	116

Section	Stratigraphic Height (m)	Normalized Height Z* (m)	$\delta^{13}\text{C}$	$\delta^{18}\text{O}$	$\delta^{34}\text{S}$	$\text{SO}_4$ (ppm)
KDS	161.0	138.2	4.80	-2.75	22.7	211
KDS	159.1	136.4	5.12	-2.98	22.3	164
KDS	158.2	135.5	4.60	-3.06	23.0	136
KDS	157.3	134.6	5.08	-2.58		
KDS	157.2	134.5	5.10	-2.89		
KDS	155.9	133.2	4.44	-3.43	22.6	241
KDS	155.1	132.5	4.80	-3.06		
KDS	154.2	131.6	4.71	-2.53		
KDS	152.3	129.8	4.97	-3.45		
KDS	151.6	129.1	4.78	-3.50	23.9	104
KDS	150.2	127.7	3.95	-3.63	23.7	127
KDS	149.3	126.8	4.06	-3.30	22.4	107
KDS	147.6	125.1	3.04	-4.02		
KDS	146.7	124.2	3.52	-3.20	23.3	194
KDS	145.6	123.2	4.66	-2.78	25.6	111
KDS	144.7	122.3	3.79	-2.78		
KDS	142.5	120.2				
KDS	140.6	118.3	4.73	-3.04		
KDS	137.3	115.1	4.06	-3.39	20.3	59
KDS	136.7	114.5	3.36	-3.81		
KDS	135.9	113.7	4.98	-3.59		
KDS	135.0	112.8	4.47	-3.15	20.4	159
KDS	133.6	111.4	4.84	-3.29		
KDS	133.4	111.2	5.18	-4.60	23.5	112
KDS	131.7	109.8	4.80	-3.81		
KDS	130.8	109.2	4.46	-3.29		
KDS	127.3	107.2	6.03	-3.44		
KDS	126.4	106.6	4.91	-2.39	22.6	71
KDS	126.3	106.6	4.56	-3.34	20.2	
KDS	125.6	106.1	4.44	-3.53		
KDS	123.7	105.0	4.25	-3.72		
KDS	121.7	103.8	4.88	-2.10	25.7	95
KDS	120.2	103.0	4.29	-3.28		
KDS	118.8	102.1	4.60	-3.22	23.8	84
KDS	117.8	101.5	4.14	-4.22		
KDS	117.6	101.4	4.27	-3.43		
KDS	117.3	101.2	4.31	-4.25	25.2	73
KDS	116.4	100.7	4.05	-2.83		
KDS	115.0	99.8	5.05	-2.25		
KDS	113.9	99.2	4.23	-4.13	23.0	127
KDS	112.9	98.6	4.35	-3.42		
KDS	111.8	98.0	4.97	-2.19		
KDS	104.8	93.8	5.00	-3.72	24.7	92
KDS	100.2	91.1	5.46	-2.22	25.1	181
KDS	97.8	89.5	5.10	-2.80	27.8	125
KDS	96.7	88.6	5.15	-1.35	29.3	259
KDS	94.4	86.7	4.89	-1.73		
KDS	93.3	85.8	5.62	-0.91		
KDS	92.8	85.3	5.01	-1.91	30.8	550
KDS	91.7	84.4	5.72	-0.95	29.9	603

Section	Stratigraphic Height (m)	Normalized Height Z* (m)	$\delta^{13}\text{C}$	$\delta^{18}\text{O}$	$\delta^{34}\text{S}$	$\text{SO}_4$ (ppm)
KDS	91.1	83.9	4.45	-3.10		
KDS	90.0	83.0	4.27	-1.73		
KDS	88.9	82.1	4.75	-1.55	28.9	779
KDS	87.8	81.2	4.19	-2.97		
KDS	86.5	80.2	5.03	-1.81	29.2	503
KDS	85.6	79.4	5.23	-1.06		
KDS	84.5	78.5	4.57	-1.43	27.8	559
KDS	82.4	76.8	3.88	-8.17	18.0	643
KDS	81.3	75.9	5.34	-4.02	20.4	332
KDS	79.7	74.6	1.22	-4.19		
KDS	78.7	73.7	3.49	-5.34	21.5	206
KDS	77.6	72.8	5.78	-4.28		
KDS	76.5	71.9	5.78	-4.21	22.4	383
KDS	75.9	71.4	4.78	-4.42		
KDS	75.3	70.9	2.97	-3.57	26.9	268
KDS	74.7	70.4	4.44	-4.52		
KDS	73.2	68.7	5.81	-4.54		
KDS	69.1	63.9	5.54	-4.31		
KDS	68.1	62.6	4.76	-4.48	20.7	161
KDS	67.0	61.4	6.00	-4.33		
KDS	66.0	60.1	5.86	-4.05	21.8	327
KDS	64.9	58.9	3.67	-4.52		
KDS	64.1	57.9	6.21	-4.91		
KDS	63.3	57.0	6.07	-4.64		
KDS	62.1	55.5	6.13	-4.65		
KDS	60.4	53.5	5.50	-3.93	20.8	448
KDS	59.3	52.1	5.73	-4.61		
KDS	58.6	51.4	4.31	-4.47		
KDS	57.5	50.0	4.18	-5.90		
KDS	56.5	49.2	5.04	-5.57	23.4	149
KDS	55.9	48.7	4.91	-5.81	24.6	80
KDS	54.6	47.7	5.43	-5.95	25.3	86
KDS	53.1	46.5	5.17	-5.86		
KDS	51.7	45.4	5.51	-5.68		
KDS	51.1	44.9	5.39	-5.65	22.7	168
KDS	49.7	43.7	3.48	-5.23		
KDS	48.6	42.8	5.68	-4.90		
KDS	46.2	41.0	5.04	-5.65		
KDS	45.3	40.2	5.04	-5.67		
KDS	44.5	39.5	5.70	-3.52	22.0	153
KDS	43.6	38.8	4.24	-5.86		
KDS	43.3	38.6	5.63	-2.50	22.8	163
KDS	43.0	38.4	5.52	-5.68	22.2	206
KDS	42.1	37.7	5.22	-5.73		
KDS	40.3	36.2	5.54	-5.77	23.8	179
KDS	38.4	34.7	5.21	-6.08		
KDS	37.1	33.7	5.45	-4.21	20.3	256
KDS	36.1	32.9	4.91	-6.17		
KDS	34.6	31.7	2.38	-6.23		
KDS	33.4	30.7	4.93	-5.71		

Section	Stratigraphic Height (m)	Normalized Height Z* (m)	$\delta^{13}\text{C}$	$\delta^{18}\text{O}$	$\delta^{34}\text{S}$	$\text{SO}_4$ (ppm)
KDS	32.5	30.0	3.85	-5.71	24.9	130
KDS	31.1	28.8	5.43	-6.01	24.0	98
KDS	29.8	27.8	4.78	-5.93		
KDS	28.3	26.6	4.71	-5.67		
KDS	26.9	25.5	5.14	-5.79	23.7	122
KDS	24.9	23.8	4.64	-5.63	22.3	100
KDS	23.9	23.0	3.77	-5.39		
KDS	22.8	22.2	4.68	-5.49		
KDS	21.8	21.3	4.67	-5.73	23.7	120
KDS	20.7	20.4	4.49	-6.06		
KDS	20.0	19.8	4.44	-6.17		
KDS	18.9	18.9	4.49	-6.09	21.4	96
KDS	17.0	17.3	3.29	-5.40		
KDS	15.7	16.2	4.18	-5.87		
KDS	14.7	15.4	4.16	-5.80	22.7	97
KDS	13.8	14.7	4.03	-5.66	21.2	124
KDS	12.7	13.8	3.97	-5.79		
KDS	11.3	12.7	3.60	-5.86		
KDS	8.9	10.7	3.83	-5.52	21.2	196
KDS	7.4	9.4	3.92	-6.20	20.3	214
KDS	5.7	8.0	3.44	-5.78		
KDS	5.5	7.8	3.29	-5.93		
KDS	4.3	6.9	3.85	-5.61		
KDS	2.5	5.4	3.80	-4.56	25.7	249
KDS	1.5	3.8	4.45	-4.03		
KDS	0.5	1.3	4.09	-3.50		
KDS	-0.8	-2.0	3.51	-1.59		
KDW	131.8	315.0	-3.45	-4.91	28.8	664
KDW	131.0	312.6	-3.93	-6.17		
KDW	130.9	312.4	-3.27	-5.52		
KDW	130.6	311.5	-0.82	-3.91		
KDW	130.5	311.2	-1.38	-3.71	28.7	756
KDW	130.2	310.3	-0.99	-4.24		
KDW	130.2	310.3	-0.13	-3.98		
KDW	129.5	309.7	-1.55	-6.02	18.8	786
KDW	121.3	306.2	-0.99	-3.72	33.9	1359
KDW	120.7	305.9	0.52	-4.27	34.8	906
KDW	120.5	305.8	0.60	-4.89		
KDW	119.5	305.4	-1.37	-5.02		
KDW	119.5	305.4	-1.15	-5.99		
KDW	119.1	305.2	0.94	-2.91	34.8	1028
KDW	119.0	305.2	-2.79	-3.65	34.3	941
KDW	119.0	305.2	0.89	-3.17		
KDW	117.5	304.5	2.88	-3.89		
KDW	112.0	302.2	1.27	-2.31		
KDW	107.6	300.3	1.11	-3.28		
KDW	107.3	300.1	2.53	-2.04	32.5	597
KDW	107.3	300.1	2.38	-2.00		
KDW	107.3	300.1	3.28	-1.86		
KDW	106.9	299.8	2.83	-1.67		

Section	Stratigraphic Height (m)	Normalized Height Z* (m)	$\delta^{13}\text{C}$	$\delta^{18}\text{O}$	$\delta^{34}\text{S}$	$\text{SO}_4$ (ppm)
KDW	106.0	298.3	1.49	-1.77		
KDW	105.4	297.2	0.68	-2.60	33.0	921
KDW	105.2	296.9	0.97	-1.48		
KDW	104.8	296.2	1.79	-1.96		
KDW	102.0	291.4	0.93	-4.58	30.3	659
KDW	102.0	291.4	0.98	-3.59		
KDW	101.9	291.2	1.42	-3.13		
KDW	101.0	289.7	0.97	-4.08	30.2	476
KDW	101.0	289.7	-0.22	-3.74		
KDW	97.2	283.1	2.16	-2.16		
KDW	97.1	282.9	2.06	-3.67		
KDW	95.1	279.5	1.82	-3.09		
KDW	92.1	274.5	1.70	-3.16		
KDW	89.5	270.2	2.20	-4.15		
KDW	89.4	270.1	2.31	-3.66		
KDW	87.0	266.1	1.35	-1.78		
KDW	84.1	261.3	1.34	-2.06		
KDW	80.4	255.0	2.15	-1.68		
KDW	79.2	252.9	3.04	-2.99		
KDW	77.7	250.3	2.80	-3.66		
KDW	73.2	242.6	1.59	-2.04		
KDW	72.3	241.0	2.65	-3.23		
KDW	70.9	239.2	3.74	-3.02		
KDW	70.6	238.9	2.64	-2.55		
KDW	69.9	238.2	3.35	-4.52		
KDW	69.6	237.9	3.45	-4.26		
KDW	68.6	237.0	2.65	-3.76		
KDW	67.5	235.9	3.35	-3.02		
KDW	67.2	235.6	1.53	-3.16		436
KDW	67.1	235.5	1.88	-3.09		
KDW	66.8	235.2	2.19	-3.29	26.6	345
KDW	66.5	234.9	1.86	-3.13		
KDW	66.4	234.8	1.80	-0.76	29.2	1574
KDW	66.0	234.4	2.81	-2.26	29.8	490
KDW	65.5	233.9	2.91	-2.02	29.5	538
KDW			1.87	-3.37		
KDW	65.0	233.4	2.76	-3.03		
KDW	64.8	233.2	2.02	-1.24	30.2	512
KDW	63.9	232.4	2.10	-2.83		
KDW	63.0	231.5	2.73	-2.73		
KDW	62.0	230.5	1.95	-2.61		
KDW	61.0	229.5	2.10	-1.75		
KDW	60.1	228.6	3.06	-2.32		
KDW	58.4	227.0	4.38	-4.09		
KDW	58.0	226.6	3.67	-2.98		
KDW	57.0	225.6	3.63	-3.60		
KDW	55.7	224.6	2.89	-2.68		
KDW	53.2	222.9	2.28	-2.04		
KDW	52.8	222.7	2.49	-1.81		
KDW	51.0	221.5	3.07	-1.60		

Section	Stratigraphic Height (m)	Normalized Height Z* (m)	$\delta^{13}\text{C}$	$\delta^{18}\text{O}$	$\delta^{34}\text{S}$	$\text{SO}_4$ (ppm)
KDW	48.8	220.1	2.90	-2.78		
KDW	47.9	219.6	3.13	-3.09		
KDW	46.5	218.7	4.06	-3.11		
KDW	46.4	218.6	4.03	-3.12		
KDW	45.5	218.0	3.85	-1.08		
KDW	45.1	217.8	3.81	-3.48		
KDW	43.7	216.9	3.34	-2.91		
KDW	41.8	215.6	3.93	-3.64		
KDW	39.9	214.4	4.48	-2.58		
KDW	39.0	213.8	4.31	-1.83		
KDW	38.3	213.4	2.53	-2.04		
KDW	38.2	213.3	4.16	-2.29		
KDW	36.6	212.3	4.18	-3.80		
KDW	35.5	211.6	3.67	-2.49		
KDW	34.5	211.0	4.04	-3.27		
KDW	32.1	209.2	3.71	-2.71		
KDW	31.8	208.9	2.84	-3.48		
KDW	31.0	208.1	3.53	-3.43		
KDW	31.0	208.1	4.13	-3.28		
KDW	30.2	207.4	3.77	-3.08		
KDW	30.0	207.2	4.25	-2.74		
KDW	29.5	206.8	4.08	-2.68		
KDW	29.5	206.8	4.14	-2.47		
KDW	29.2	206.5	4.04	-2.77		
KDW	28.9	206.2	4.53	-1.77		
KDW	28.8	206.1	4.32	-2.85		
KDW	28.5	205.8	4.24	-2.05		
KDW	28.4	205.7	4.28	-3.63		
KDW	28.1	205.5	4.02	-3.01		
KDW	27.5	204.9				
KDW	26.5	204.0	3.88	-3.32		
KDW	25.0	202.6	3.63	-3.74		
KDW	23.3	201.0	3.36	-2.96		
KDW	21.5	199.4	3.82	-2.98		
KDW	20.5	198.4	3.18	-2.71		
KDW	19.5	197.5	3.35	-2.59		
KDW	18.4	196.5	3.36	-3.22		
KDW	16.9	195.1	3.54	-1.74		
KDW	15.2	193.5	3.47	-3.21		
KDW	15.0	193.3	3.54	-3.36		
KDW	14.1	192.5	3.71	-3.54		
KDW	12.1	190.6	3.95	-3.33		
KDW	10.5	189.2	4.17	-3.17		
KDW	8.2	187.0	4.43	-2.99		
KDW	7.0	185.9	3.60	-3.29		
KDW	1.4	181.9	4.17	-3.68		
KDW	0.0	181.0	3.84	-3.71		
MD5	323.0	330.0	-7.04	-9.26	21.4	614
MD5	306.2	320.0	-6.85	-5.39	29.7	489
MD5	305.8	319.1	-5.44	-5.65	26.2	341

Section	Stratigraphic Height (m)	Normalized Height Z* (m)	$\delta^{13}\text{C}$	$\delta^{18}\text{O}$	$\delta^{34}\text{S}$	$\text{SO}_4$ (ppm)
MD5	305.7	318.9	-5.85	-5.55		
MD5	304.7	316.6	-4.96	-5.55		
MD5	304.5	316.1	-4.07	-5.59	29.3	444
MD5	303.9	314.5	-3.76	-5.33		
MD5	303.9	314.5	-3.93	-5.54		
MD5	303.8	314.1	-3.08	-5.17		
MD5	303.7	313.6	-3.14	-5.77		
MD5	303.6	313.2	-3.13	-4.55	19.4	1137
MD5	303.3	311.8	-3.58	-4.70	28.2	725
MD5	302.8	309.9	-1.29	-5.69	27.1	397
MD5	302.7	309.8	-1.20	-5.73		
MD5	302.3	309.3	-0.54	-4.95		
MD5	302.0	309.0	0.14	-6.64		
MD5	301.5	308.5	0.20	-6.22	29.9	516
MD5	301.0	307.9	0.88	-6.64		
MD5	300.5	307.4	-0.78	-3.81	34.5	832
MD5	300.2	307.1	-0.32	-4.86	32.3	650
MD5	299.7	306.5	-0.97	-3.75		
MD5	299.5	306.3	0.45	-4.59	34.5	469
MD5	299.2	306.0	1.24	-4.91		
MD5	296.5	303.0	-2.77	-5.83	29.6	476
MD5	293.5	299.8	3.03	-5.00		
MD5	293.1	299.4	-3.18	-6.13		
MD5	292.5	298.7	4.16	-4.46	34.8	1312
MD5	291.2	297.3	0.17	-4.28		
MD5	289.3	295.3	1.47	-5.49		
MD5	289.2	295.2	5.08	-3.76		
MD5	289.0	288.6	1.70	-3.20		
MD5	288.0	287.5	1.09	-3.15	33.9	553
MD5	280.0	279.0	1.98	-2.26		
MD5	279.1	278.1	3.02	-1.50	32.5	871
MD5	277.8	276.8	3.19	-1.92		
MD5	277.5	276.5	1.97	-3.26		
MD5	277.0	276.0	1.96	-2.72	33.1	882
MD5	276.2	275.2	1.42	-3.40		
MD5	275.1	274.1	-0.05	-1.42		
MD5	273.1	272.1	2.17	-2.26		
MD5	273.0	272.0	3.15	-1.25		
MD5	272.8	271.8	3.06	-1.15	31.5	1485
MD5	271.3	270.3	3.65	-0.32		
MD5	269.3	268.3	2.60	-2.44		
MD5	268.5	267.5	3.29	-2.17		
MD5	267.8	266.8	4.35	-1.68		
MD5	267.0	266.0	4.62	-1.21		
MD5	266.0	265.0	4.47	-0.71	33.3	1440
MD5	264.2	263.2	3.67	-0.60		
MD5	261.5	260.5	3.85	-0.51	32.1	1065
MD5	260.6	259.6	4.27	-1.25		
MD5	259.1	258.0	1.71	-1.98		
MD5	254.6	253.3	3.99	-2.91	32.2	769

Section	Stratigraphic Height (m)	Normalized Height Z* (m)	$\delta^{13}\text{C}$	$\delta^{18}\text{O}$	$\delta^{34}\text{S}$	$\text{SO}_4$ (ppm)
MD5	253.3	251.9	5.88	-1.79		
MD5	251.5	250.0	4.84	-0.77		
MD5	249.9	248.3	6.08	-0.75		
MD5	248.1	246.4	5.52	-1.56	31.4	828
MD5	247.2	245.5	5.28	-1.69		
MD5	245.5	243.7	4.66	-3.29		
MD5	241.7	239.7	1.93	-2.60	32.5	873
MD5	241.2	239.3	5.33	-0.20		
MD5	237.0	235.5	4.31	-2.15	31.6	1168
MD5	235.0	233.7	5.25	-2.57		
MD5	232.2	231.1	4.89	-1.26	30.0	1019
MD5	229.9	229.1	3.35	-1.47		
MD5	226.4	225.9	4.52	-1.63	30.4	1075
MD5	226.0	225.5	4.41	-0.44	30.6	1271
MD5	223.0	222.6	5.57	-2.48	23.9	264
MD5	219.2	218.8	5.59	-1.91		
MD5	216.5	216.1	5.73	-2.12	29.6	809
MD5	213.3	212.9	5.64	-2.02		
MD5	212.4	212.0	5.32	-1.92		
MD5	210.9	210.5	5.18	-3.21	29.0	0
MD5	206.5	206.1	4.93	-2.09		
MD5	205.0	204.6	5.27	-3.76	30.7	285
MD5	203.5	203.1	4.76	-3.43		
MD5	202.8	202.4	4.08	-3.83		
MD5	201.7	201.3	4.12	-2.39		
MD5	200.1	199.7	3.87	-3.89	29.7	392
MD5	196.8	196.3	3.49	-2.32		
MD5	195.0	194.5	3.66	-2.31		
MD5	194.3	193.8	3.73	-2.27		
MD5	192.2	191.7	3.48	-3.81		
MD5	191.0	190.5	3.82	-4.36	26.7	214
MD5	189.4	188.9	3.51	-3.27		
MD5	187.8	187.3	3.60	-2.70		
MD5	186.3	185.8	3.96	-2.76		
MD5	183.4	183.0	4.39	-3.26	27.1	258
MD5	182.0	181.7	4.52	-3.07		
MD5	180.8	180.6	3.96	-3.16		
MD5	179.5	179.4	3.00	-3.59		
MD5	178.0	178.0	4.03	-3.19		
MD5	177.0	177.0	4.14	-1.85		
MD5	175.2	175.3	4.59	-2.87		
MD5	173.2	173.5	3.86	-1.47	29.8	280
MD5	170.6	171.0	4.70	-2.01		
MD5	168.6	169.1	4.54	-2.17		
MD5	168.0	168.5	4.63	-1.86		
MD5	167.0	167.5	4.61	-2.73	23.9	233
MD5	166.5	167.1	4.51	-2.75		
MD5	165.3	165.9	4.24	-2.68		
MD5	164.8	165.4	4.35	-2.65		
MD5	164.0	164.6	4.01	-2.87		

Section	Stratigraphic Height (m)	Normalized Height Z* (m)	$\delta^{13}\text{C}$	$\delta^{18}\text{O}$	$\delta^{34}\text{S}$	$\text{SO}_4$ (ppm)
MD5	162.8	163.4	3.30	-2.40		
MD5	162.3	162.9	3.23	-2.32		
MD5	161.3	162.0	3.07	-2.82	26.8	222
MD5	161.0	161.7	4.01	-2.71		
MD5	160.0	160.7	4.22	-1.28		
MD5	159.0	159.7	4.63	-0.31		
MD5	157.2	157.9	4.76	-3.44		
MD5	155.0	155.8	3.54	-3.01	20.1	376
MD5	154.0	154.8	4.88	-2.83		
MD5	152.0	152.8	5.27	-3.10		
MD5	150.0	150.9	4.48	-3.28		
MD5	149.0	149.9	4.68	-3.52		
MD5	148.0	148.9	3.87	-3.43		
MD5	147.1	148.0	4.62	-2.37	21.1	355
MD5	146.0	147.0	4.04	-2.74	21.5	0
MD5	145.0	146.0	4.08	-5.41		
MD5	143.0	144.0	4.25	-2.50		
MD5	143.0	144.0	4.63	-2.56		
MD5	142.0	143.0			19.8	612
MD5	141.0	142.1	4.41	-3.50		
MD5	140.0	141.1	4.08	-3.37		
MD5	139.0	140.1	4.36	-0.81		
MD5	138.0	139.2	4.04	-2.94		
MD5	136.0	137.3	3.67	-1.33	24.4	313
MD5	135.0	136.3	4.17	-2.94		586
MD5	134.0	135.4	4.14	-3.56		
MD5	130.6	132.2	3.99	-2.92	19.5	356
MD5	129.0	130.7	3.75	-3.41		
MD5	128.0	129.8	3.65	-4.94		
MD5	127.0	128.8	4.45	-3.27	22.5	264
MD5	127.0	128.8	3.69	-4.56		
MD5	126.4	128.3	4.18	-2.42		
MD5	125.0	127.0	3.27	-3.65		
MD5	124.3	126.3	4.26	-2.49	21.3	332
MD5	123.5	125.6	4.24	-4.04		
MD5	122.5	124.6	4.66	-4.46		
MD5	120.7	122.9	4.19	-2.53	25.5	408
MD5	120.3	122.6	4.25	-2.18		
MD5	119.2	121.5	4.51	-4.40		
MD5	116.0	118.5	4.73	-5.00	26.7	248
MD5	115.0	117.6	4.29	-2.56		
MD5	114.2	116.8	4.65	-3.64		
MD5	113.0	115.7	4.85	-2.55		
MD5	112.0	114.8	5.25	-2.14		
MD5	111.1	113.9	6.06	-1.40		
MD5	110.0	112.9	5.67	-1.71		
MD5	109.0	112.0	5.90	-2.32	26.2	824
MD5	108.0	111.0	6.09	-2.24		
MD5	107.0	110.1	6.20	-2.20		
MD5	106.0	109.1	5.92	-2.39		

Section	Stratigraphic Height (m)	Normalized Height Z* (m)	$\delta^{13}\text{C}$	$\delta^{18}\text{O}$	$\delta^{34}\text{S}$	$\text{SO}_4$ (ppm)
MD5	105.0	108.0	6.18	-1.93	31.9	693
MD5	104.0	107.0	5.76	-2.46		
MD5	103.0	106.0	5.72	-2.91		
MD5	102.0	104.9	5.98	-2.60		
MD5	100.9	103.8			30.3	800
MD5	100.0	102.8	5.52	-3.49		
MD5	99.0	101.8	5.65	-2.83	32.1	678
MD5	98.0	100.8	-1.94	-5.76	31.8	0
MD5	97.0	99.7	5.48	-2.00		
MD5	96.0	98.7	5.87	-6.16		
MD5	95.0	97.7	2.97	-7.38	18.1	253
MD5	94.2	96.8	1.99	-5.77		
MD5	93.2	95.8	-0.65	-4.63		
MD5	92.2	94.8	2.06	-4.27	28.0	668
MD5	91.0	93.5	-0.49	-4.79		
MD5	90.0	92.5	5.60	-3.18	30.8	622
MD5	89.0	91.5	5.07	-7.27		
MD5	88.0	90.4	-2.80	-8.52		
MD5	87.0	89.4	-0.96	-7.38		
MD5	86.0	88.3	3.31	-3.31		
MD5	85.0	87.2	4.70	-7.60		
MD5	84.0	86.1	5.23	-5.77	26.2	493
MD5	83.1	85.1	4.58	-6.89		
MD5	82.0	83.9	4.53	-7.01		184
MD5	81.0	82.9	4.43	-7.30		
MD5	80.0	81.8	4.50	-7.11		
MD5	79.0	80.7	3.99	-7.18		
MD5	78.0	79.6	2.94	-6.99		
MD5	77.0	78.5	4.42	-7.02		
MD5	76.0	77.5	4.60	-7.22		
MD5	75.0	76.4	4.58	-6.99		
MD5	74.0	75.3	4.30	-7.17		
MD5	73.0	74.2	4.51	-7.98	20.6	295
MD5	72.0	73.1	4.21	-7.08		
MD5	71.0	72.1	4.31	-6.96	20.2	162
MD5	70.0	71.0	1.77	-4.07		
MD5	69.0	69.9	4.53	-7.10		
MD5	68.0	69.0	4.63	-6.81		
MD5	67.0	68.0	4.24	-7.03		
MD5	65.8	66.9	2.80	-5.09		
MD5	65.0	66.2	3.01	-6.02		
MD5	64.0	65.3	4.30	-7.46		
MD5	63.0	64.3	3.70	-4.74		
MD5	62.0	63.4	4.01	-7.28		
MD5	61.0	62.5	4.23	-7.14	22.3	140
MD5	60.0	61.5	4.38	-7.06		
MD5	59.2	60.8	4.46	-7.16		
MD5	58.2	59.9	4.54	-5.34		
MD5	57.1	58.8	4.16	-4.47	19.2	312
MD5	56.0	57.8	4.72	-7.13		

Section	Stratigraphic Height (m)	Normalized Height Z* (m)	$\delta^{13}\text{C}$	$\delta^{18}\text{O}$	$\delta^{34}\text{S}$	$\text{SO}_4$ (ppm)
MD5	55.0	56.9	3.88	-5.82		
MD5	54.0	56.0	4.62	-6.70		
MD5	52.9	54.9	4.44	-6.50		
MD5	52.0	54.1	4.46	-6.99	23.7	474
MD5	51.0	53.2	3.19	-5.32		
MD5	50.0	52.2	4.44	-7.08		
MD5	49.0	51.3	3.60	-6.62		
MD5	48.0	50.4	3.95	-6.83		
MD5	47.1	49.6	3.17	-7.04		
MD5	46.0	48.7	1.58	-3.02		
MD5	45.0	47.8	2.89	-4.10		
MD5	44.0	47.0	4.05	-7.39		
MD5	43.0	46.2	4.46	-7.51	19.6	180
MD5	42.0	45.3	4.87	-7.12		
MD5	41.0	44.5	4.45	-7.27		
MD5	40.2	43.8	4.46	-7.79		
MD5	39.0	42.8	3.53	-3.02	20.5	455
MD5	38.0	42.0	4.40	-6.79		
MD5	37.2	41.3	4.17	-6.46		
MD5	36.0	40.3	2.91	-7.08		
MD5	35.0	39.5	1.23	-4.14		
MD5	34.0	38.7	2.91	-2.43		
MD5	32.1	37.1	1.46	-3.56		
MD5	31.0	36.2	3.20	-3.93		
MD5	30.0	35.3	3.15	-3.50		
MD5	30.0	35.3	3.09	-2.64		
MD5	29.5	34.9	3.38	-1.64	19.4	442
MD5	27.0	32.8	3.44	-2.66		
MD5	26.3	32.3	3.70	-2.34		
MD5	25.0	31.2	3.78	-2.95	20.4	326
MD5	24.0	30.3	3.74	-2.13		
MD5	23.0	29.5	3.31	-1.51		
MD5	22.0	28.7	2.86	-1.89		
MD5	21.0	27.8	3.91	-3.37		
MD5	20.0	27.0	3.71	-2.05		
MD5	19.0	26.2	4.12	-2.99	19.2	269
MD5	18.0	25.3	4.03	-1.99		
MD5	17.0	24.3	4.19	-2.90		
MD5	16.0	23.0	3.30	-2.63		
MD5	15.0	21.8	2.19	-2.93		
MD5	14.1	20.7	4.13	-4.11	20.8	262
MD5	13.3	19.7	4.05	-3.20		
MD5	8.6	14.0			23.5	278
MD5	7.2	12.2	5.12	-4.59		
MD5	6.2	11.0	4.99	-5.19	23.1	637
MD5	5.3	9.9	4.91	-6.38		
MD5	4.3	8.7	4.84	-5.34		
MD5	3.0	7.1	3.82	-5.21		
MD5	2.0	5.9	4.55	-4.83		
MD5	0.0	0.0	3.94	-2.37	26.5	531

Section	Stratigraphic Height (m)	Normalized Height Z* (m)	$\delta^{13}\text{C}$	$\delta^{18}\text{O}$	$\delta^{34}\text{S}$	$\text{SO}_4$ (ppm)
MD6	260.9	320.0	-9.00	-5.83		
MD6	260.5	319.1	-6.53	-5.81		
MD6	260.5	319.1	-5.89	-5.13	29.9	273
MD6	259.9	317.7	-5.30	-5.76		
MD6	259.5	316.8	-4.27	-6.07		
MD6	259.0	315.7	-4.13	-5.58		
MD6	259.0	315.7	-3.70	-6.10		333
MD6	258.8	315.2	-2.01	-6.03	27.5	499
MD6	258.8	315.2	-3.98	-5.62		
MD6	258.7	315.0	-3.46	-5.69		
MD6	258.7	315.0	-3.21	-5.34		
MD6	258.7	314.9	-2.98	-6.14		
MD6	258.7	314.8	-2.62	-6.62		
MD6	258.7	314.8	-3.01	-5.83		
MD6	258.6	314.6	-3.06	-6.34		
MD6	258.6	314.5	-2.85	-5.96		
MD6	258.6	314.5	-2.94	-6.55		
MD6	258.4	313.8	-1.62	-6.35		
MD6	258.4	313.8	-1.86	-6.46		
MD6	258.2	313.0	-1.80	-6.14		
MD6	258.2	312.9	-2.34	-6.46		
MD6	258.2	312.8	-2.10	-6.18		
MD6	258.2	312.8	-1.12	-5.66		
MD6	258.2	312.8	-1.97	-6.94		
MD6	258.1	312.5	-2.29	-5.87		
MD6	258.1	312.4	-2.40	-5.63		
MD6	258.0	312.0	-1.83	-5.98		
MD6	257.8	311.3	-0.47	-5.44	22.6	381
MD6	257.7	310.9	-1.41	-6.56		
MD6	257.7	310.9	-1.47	-6.29		
MD6	257.7	310.9	-0.69	-5.45		
MD6	257.7	310.9	-1.52	-5.72		
MD6	257.7	310.9	-1.95	-5.80		
MD6	257.7	310.8	-1.26	-5.58		
MD6	257.5	310.0	0.30	-5.61		
MD6	257.4	309.9	-0.97	-5.77	26.2	256
MD6	257.0	309.3	0.39	-6.15		
MD6	256.8	309.0	-0.05	-5.54	29.6	312
MD6	256.5	308.6	0.55	-5.22		
MD6	256.0	307.9	-0.53	-4.87	33.2	408
MD6	255.6	307.4	-0.01	-4.36	31.7	258
MD6	253.8	304.9	-4.29	-4.95	32.5	350
MD6	252.9	303.7	-2.04	-3.40		
MD6	252.0	302.5	-3.13	-4.36	36.0	687
MD6	250.1	299.9	2.61	-2.99		
MD6	249.1	298.9	3.39	-3.96		
MD6	242.0	291.5	1.98	-4.04		
MD6	240.0	289.4	2.65	-0.49		
MD6	234.5	283.6	0.24	-1.30		
MD6	231.2	280.2	2.81	-1.66		

Section	Stratigraphic Height (m)	Normalized Height Z* (m)	$\delta^{13}\text{C}$	$\delta^{18}\text{O}$	$\delta^{34}\text{S}$	$\text{SO}_4$ (ppm)
MD6	227.1	275.1	4.35	0.22		
MD6	222.5	269.4	1.47	-1.59		
MD6	215.0	260.0	2.05	-3.36		
MD6	211.9	257.6	5.09	-0.90		
MD6	205.7	252.7	-5.08	-4.74		
MD6	197.2	246.1	5.17	-1.10		
MD6	191.5	241.6	4.08	-1.57		
MD6	187.3	237.0	3.68	-0.44		
MD6	185.0	234.7	4.35	-1.51	30.0	1521
MD6	184.9	184.9	1.21	-3.54		
MD6	184.5	234.2	1.24	-4.12	29.4	877
MD6	184.2	233.9	0.43	-3.90	28.7	1027
MD6	184.0	233.7	1.46	-3.78	28.9	784
MD6	183.0	232.6	-1.46	-5.32	25.2	830
MD6	181.9	181.9	5.41	-1.70		
MD6	177.7	177.6	4.86	-3.25		
MD6	175.2	175.1	4.29	-2.24		
MD6	170.4	170.2	4.38	-3.08		
MD6	168.5	168.1	3.92	-2.56		
MD6	165.5	164.8	4.28	-3.57		
MD6	162.1	161.1	4.47	-2.45		
MD6	155.3	153.6	4.61	-3.03		
MD6	147.0	144.5	4.25	-2.52		
MD6	144.2	141.4	4.00	-3.19		
MD6	140.6	137.7	4.44	-2.54		
MD6	138.2	135.3	4.47	-3.16		
MD6	133.1	130.1	4.31	-3.02		
MD6	131.1	128.1	3.88	-4.07		
MD6	126.3	123.2	3.85	-3.77		
MD6	123.0	119.9	4.09	-3.97		
MD6	120.7	117.6	3.99	-5.02		
MD6	116.5	113.3	4.44	-2.39		
MD6	112.0	108.8	5.62	-1.51		
MD6	110.0	106.7	4.84	-2.38		
MD6	106.0	102.5	4.72	-2.66		
MD6	101.6	97.9	5.43	-3.07		
MD6	98.5	94.7	4.88	-2.69		
MD6	93.0	89.1	2.96	-7.01		
MD6	87.6	84.3	4.24	-6.87		
MD6	83.3	80.4	5.19	-7.06		
MD6	81.0	78.3	4.24	-6.89		
MD6	78.1	75.7	4.27	-7.06		
MD6	74.2	72.2	4.37	-7.08		
MD6	70.3	68.7	4.38	-7.34		
MD6	66.8	65.6	4.23	-6.75		
MD6	62.0	61.2	4.06	-6.91		
MD6	57.7	57.3	3.92	-6.28		
MD6	53.1	53.2	3.87	-7.00		
MD6	49.6	50.0	4.35	-6.51		
MD6	46.1	47.3	3.34	-6.72		

Section	Stratigraphic Height (m)	Normalized Height Z* (m)	$\delta^{13}\text{C}$	$\delta^{18}\text{O}$	$\delta^{34}\text{S}$	$\text{SO}_4$ (ppm)
MD6	42.2	44.3	4.16	-6.88		
MD6	38.3	41.2	4.10	-7.17		
MD6	33.5	37.5	4.05	-6.12		
MD6	29.0	34.0	3.83	-6.72		
MD6	25.5	31.3	2.93	-7.29		
MD6	22.0	28.6	4.20	-6.60		
MD6	20.0	27.0	4.44	-6.56		
MD6	17.0	24.5	4.25	-7.62		
MD6	15.7	22.8	4.43	-6.82		
MD6	14.2	20.8	4.57	-6.59		
MD6	12.4	18.5	4.35	-6.84		
MD6	9.1	14.2	4.21	-6.26		
MD6	7.1	11.6	4.38	-6.04		
MD6	7.1	11.6	4.49	-6.12		
MD6	5.1	9.0	4.25	-6.01		
MD6	2.7	5.9	4.14	-5.76		
MD6	2.7	5.9	4.27	-5.59		
MD6	1.0	2.5	3.68	-4.63		
MD6	0.5	1.3	3.49	-1.94		
MD6	0.3	0.8	3.32	-2.57		
MDE	293.4	320.0	-8.56	-6.56		
MDE	293.0	319.0	-6.16	-6.70		
MDE	292.5	317.8	-6.45	-5.38	29.3	493
MDE	292.5	317.8	-5.42	-6.51		
MDE	292.0	316.5	-4.75	-6.35		
MDE	291.5	315.3	-4.59	-5.50	29.8	493
MDE	291.5	315.3	-4.31	-6.18		
MDE	291.4	315.0	-3.40	-4.77	27.7	664
MDE	291.1	314.3	-1.92	-5.85		
MDE	290.2	312.3	0.09	-5.21		
MDE	290.0	311.8	-0.04	-5.16	29.9	445
MDE	289.7	311.1	0.66	-3.83		
MDE	289.4	310.5	0.05	-6.23		
MDE	289.3	310.2	0.15	-5.96		
MDE	289.3	310.1				
MDE	289.0	309.8	-0.83	-5.61	29.3	524
MDE	288.8	309.6	0.54	-6.32		
MDE	288.2	309.1	1.28	-5.08		
MDE	288.0	308.9	0.05	-5.21	33.6	535
MDE	287.5	308.4	1.04	-5.62		
MDE	287.1	308.1	1.64	-5.67		
MDE	287.0	308.0	-0.03	-4.78	31.3	720
MDE	286.9	307.9	0.64	-4.39		
MDE	286.2	307.2	0.27	-4.14		
MDE	286.0	307.0	1.22	-3.18	36.7	674
MDE	285.9	306.9	-0.68	-4.19		
MDE	285.2	306.3	1.28	-3.19		
MDE	285.2	306.3	1.54	-4.37		
MDE	285.0	306.1	1.28	-3.19	37.3	967
MDE	284.2	305.4	0.32	-5.47		

Section	Stratigraphic Height (m)	Normalized Height Z* (m)	$\delta^{13}\text{C}$	$\delta^{18}\text{O}$	$\delta^{34}\text{S}$	$\text{SO}_4$ (ppm)
MDE	284.0	305.2	-1.46	-4.29		
MDE	283.2	304.4	0.57	-2.95		
MDE	282.5	303.8	-4.03	-5.41	35.3	933
MDE	281.0	302.4	0.19	-3.60	23.6	293
MDE	281.5	302.9	-3.38	-5.50		
MDE	265.3	288.8	3.56	-1.72		
MDE	263.5	287.3	1.26	-2.63		
MDE	253.0	278.6	3.83	-1.15		
MDE	245.5	273.4	4.04	-2.00		
MDE	242.4	271.3	2.19	-0.67		
MDE	236.6	267.3	2.57	-1.75		
MDE	234.5	265.9	4.11	-1.21		
MDE	232.7	264.6	1.97	-1.41		
MDE	226.0	260.0	3.71	-2.78		
MDE	221.9	256.3	5.39	-2.20		
MDE	217.5	252.3	1.23	-4.69		
MDE	214.8	249.8	3.88	-0.33		
MDE	202.9	239.0	-0.05	-4.04		
MDE	200.1	236.3	5.22	-2.41		
MDE	197.4	233.7	5.96	-0.55		
MDE	193.4	229.9	-0.63	-0.21		
MDE	186.5	223.6	5.03	-1.26		
MDE	185.6	222.9	-1.33	-7.23		
MDE	183.0	220.8	5.57	-2.10		
MDE	174.2	213.8	5.37	-1.56		
MDE	168.1	208.7	1.53	-4.48		
MDE	166.6	207.4	4.45	-2.76		
MDE	164.0	205.1	3.64	-2.64		
MDE	160.4	201.8	3.26	-2.71		
MDE	158.1	199.8	2.91	-2.39		
MDE	156.3	198.2	4.27	-3.22		
MDE	153.4	195.6	3.33	-2.41		
MDE	150.2	192.7	4.50	-2.15		
MDE	147.3	190.1	3.58	-1.13		
MDE	144.0	187.2	4.19	-3.24		
MDE	141.0	184.0	4.67	-2.44		
MDE	136.3	176.5	4.79	-3.05		
MDE	132.0	169.7	2.97	-2.98		
MDE	129.5	167.0	4.16	-2.95		
MDE	126.3	163.6	3.70	-3.22		
MDE	123.1	160.2	4.32	-2.66		
MDE	120.4	157.4	4.65	-2.91		
MDE	118.6	155.5	3.37	-3.11		
MDE	114.0	150.6	3.35	-2.62		
MDE	110.7	147.1	4.31	-1.11		
MDE	107.0	143.2	3.41	-3.62		
MDE	104.0	140.0	3.38	-3.36		
MDE	101.6	138.1	3.08	-3.58		
MDE	99.3	136.4	3.23	-3.59		
MDE	96.0	133.8	3.81	-3.02		

Section	Stratigraphic Height (m)	Normalized Height Z* (m)	$\delta^{13}\text{C}$	$\delta^{18}\text{O}$	$\delta^{34}\text{S}$	$\text{SO}_4$ (ppm)
MDE	92.0	130.7	3.79	-4.32		
MDE	88.1	127.7	4.85	-4.16		
MDE	85.8	125.9	5.21	-2.41		
MDE	83.8	124.4	4.52	-2.86		
MDE	81.8	122.8	5.32	-2.26		
MDE	77.0	119.1	5.88	-2.63		
MDE	73.0	116.0	5.17	-6.13		
MDE	70.0	113.7	4.50	-5.99		
MDE	66.9	111.3	4.93	-6.07		
MDE	64.9	109.6	5.06	-7.63		
MDE	62.3	106.1	4.20	-4.59		
MDE	60.0	103.0	5.20	-6.37		
MDE	56.1	97.8	3.95	-5.16		
MDE	54.1	95.1	4.34	-6.84		
MDE	50.0	89.8	4.55	-7.15		
MDE	46.3	87.1	4.57	-6.89		
MDE	44.3	85.6	4.38	-6.70		
MDE	41.0	83.2	3.81	-4.57		
MDE	39.0	81.7	3.27	-1.81		
MDE	37.4	80.5	3.33	-2.74		
MDE	31.1	75.9	4.29	-7.08		
MDE	25.0	71.4	-6.40	-8.87		
MDE	23.0	69.9	4.40	-7.03		
MDE	20.1	66.9	4.06	-6.95		
MDE	19.2	65.9	5.70	-2.14		
MDE	18.2	64.9	4.61	-6.90		
MDE	16.0	62.6	4.53	-6.25		
MDE	14.0	60.5	3.90	-6.39		
MDE	9.0	55.2	4.16	-5.09		
MDE	5.0	51.0	3.70	-6.34		
MDE	2.0	48.3	3.18	-3.38		
MDE	1.0	47.5	4.18	-4.84		
MDE2	3.9	317.0	-3.94	-5.36		
MDE2	3.7	316.6	-4.21	-5.25		
MDE2	3.6	316.4	-2.93	-4.87		
MDE2	3.4	316.0	-2.66	-5.33		
MDE2	3.0	315.2	-2.22	-5.66		
MDE2	2.9	315.0	-1.97	-5.29		
MDE2	2.6	314.3	2.61	-2.09		
MDE2	2.5	314.1	-0.85	-5.00		
MDE2	2.0	313.0	0.91	-4.50		
MDE2	1.7	312.2	0.28	-4.79		
MDE2	1.5	311.8	0.68	-4.64		
MDE2	1.0	310.7	0.37	-6.58		
MDE2	0.4	309.7	0.10	-6.16		
MDE2	-0.1	309.3	1.27	-6.07		
NA1	22.3	320.0	-8.32	-6.40		
NA1	22.0	319.4	-5.89	-5.91		
NA1	21.2	317.8	-4.87	-5.67		
NA1	20.3	316.0	-3.99	-5.98		

Section	Stratigraphic Height (m)	Normalized Height Z* (m)	$\delta^{13}\text{C}$	$\delta^{18}\text{O}$	$\delta^{34}\text{S}$	$\text{SO}_4$ (ppm)
NA1	19.8	315.0	-3.37	-5.17		
NA1	19.0	313.5	-2.97	-5.58		
NA1	18.0	311.7	-1.95	-4.69		
NA1	17.3	310.4	-1.03	-6.94		
NA1	16.6	309.6	0.29	-5.13		
NA1	15.0	308.4	1.90	-4.76		
NA1	14.0	307.7	2.47	-4.89		
NA1	13.2	307.1	2.44	-4.72		
NA1	12.0	306.2	-5.26	-5.82		
NA1	10.8	305.3	2.13	-4.11		
NA1	10.3	304.9	3.07	-2.54		
NA1	9.0	304.0	2.64	-4.19		
NA1	7.8	303.1	4.97	-3.43		
NA1	7.0	302.5	5.16	-3.23		
NA1	6.0	301.7	-1.20	-5.55		
NA1	5.5	301.3	3.85	-5.42		
NA1	3.5	299.8	0.83	-5.67		
NA1	3.0	299.3	4.75	-8.54		
NA1	2.4	298.6	5.15	-8.36		
NA1	1.3	297.4	3.38	-6.42		
NA1	1.0	297.1	3.31	-4.13		
NA1	0.0	296.0	-4.50	-6.67		
PF1	28.3	300.4	1.40	-4.21		
PF1	27.6	299.3	1.16	-3.17		
PF1	27.1	298.2	1.49	-2.96		
PF1	26.6	297.1	1.03	-2.52		
PF1	26.2	296.2	1.42	-2.66		
PF1	26.0	295.8	1.85	-3.24		
PF1	24.0	291.3	0.83	-2.27		
PF1	22.0	286.9	1.76	-3.67		
PF1	20.2	282.9	0.78	-4.32		
PF1	19.6	281.6	1.98	-4.18		
PF1	18.8	279.9	2.12	-2.99		
PF1	17.5	278.3	2.25	-2.01		
PF1	16.6	277.3	2.45	-2.24		
PF1	15.6	276.1	1.19	-4.20		
PF1	14.2	274.4	2.70	-3.31		
PF1	12.6	272.5	2.03	-2.08		
PF1	10.5	270.0	1.69	-3.20		
PF1	10.0	269.4	1.62	-3.31		
PF1	7.5	266.4	2.13	-2.33		
PF1	6.8	265.6	2.65	-1.24		
PF1	5.7	264.3	2.98	-4.60		
PF1	4.5	262.9	2.41	-3.92		
PF1	3.5	261.7	2.44	-3.27		
PF1	2.3	260.2	2.50	-3.68		
PF1	1.7	259.3	2.21	-4.23		
PF1	0.5	257.2	2.25	-3.51		

Table C2  
 Chemostratigraphic data for the Oman Mountains

Section	Stratigraphic Height (m)	Normalized Height Z* (m)	$\delta^{13}\text{C}$	$\delta^{18}\text{O}$	$\delta^{34}\text{S}$	$\text{SO}_4$ (ppm)
AQ1	50.0	97.5	2.48	-11.53		
AQ1	14.7	11.6	2.41	-5.89		
AQ1	26.3	56.9	1.25	-10.04		
AQ1	67.5	112.7	2.55	-11.98		
AQ1	53.0	101.3	0.62	-4.56		
AQ1	37.1	78.2	1.33	-11.64		
AQ1	46.8	91.8	-0.11	-6.89		
AQ1	72.1	116.3	-1.98	-7.26		
AQ1	65.1	110.8	0.53	-7.05		
AQ1	9.9	1.9	3.35	-5.46		
AQ1	63.8	109.8	-0.33	-8.50		
AQ1	61.6	108.0	1.03	-11.66		
AQ1	51.4	100.0	0.06	-6.90		
AQ1	48.6	95.0	2.65	-9.92		
AQ1	40.5	82.1	3.81	-11.99		
AQ1	34.2	74.8	1.61	-10.64		
AQ1	20.6	34.1	0.09	-8.33		
AQ1	22.5	43.5	0.12	-12.74		
AQ1	62.6	108.8	1.32	-7.95		
AQ1	54.0	102.0	1.46	-4.27		
AQ1	39.7	81.2	2.59	-10.98		
AQ1	20.1	30.8	-1.85	-2.17		
AQ1	12.0	8.6	-0.75	-4.31		
AQ1	75.8	119.2	-0.31	-9.23		
AQ1	47.9	93.8	0.70	-10.85		
AQ1	47.3	92.7	1.56	-11.74		
AQ1	66.9	112.2	2.06	-10.45		
AQ1	13.8	10.6	1.45	-6.47		
AQ1	76.8	120.0	-0.92	-8.39		
AQ1	16.4	13.5	1.55	-6.98		
AQ1	46.2	90.7	2.75	-11.87		
AQ1	38.8	80.2	1.84	-11.91		
AQ1	32.3	72.7	3.52	-12.45		
AQ1	71.3	115.7	-0.36	-7.31		
AQ1	55.0	102.8	0.67	-4.10		
AQ1	44.1	87.0	1.66	-11.17		
AQ1	43.4	85.7	3.68	-12.26		
AQ1	17.5	14.8	5.77	-1.55		
AQ1	70.3	114.9	0.34	-10.88		
AQ1	64.8	110.6	1.68	-11.82		
AQ1	27.3	60.5	2.33	-12.27		
AQ1	41.1	82.8	3.86	-12.18		
AQ1	28.3	68.0	2.46	-12.35		
AQ1	69.8	114.5	2.17	-11.43		
AQ1	25.0	52.4	1.28	-12.22		
AQ1	35.4	76.2	3.39	-11.98		
AQ1	49.2	96.1	2.67	-11.25		
AQ1	68.2	113.2	1.93	-10.87		

Section	Stratigraphic Height (m)	Normalized Height Z* (m)	$\delta^{13}\text{C}$	$\delta^{18}\text{O}$	$\delta^{34}\text{S}$	$\text{SO}_4$ (ppm)
AQ1	36.1	77.0	3.01	-12.00		
AQ1	21.6	40.4	-0.26	-9.48		
AQ1	45.1	88.8	2.63	-11.73		
AQ1	30.4	70.5	3.53	-12.26		
AQ1	24.0	48.8	1.04	-12.59		
AQ1	23.3	46.4	0.85	-9.19		
AQ1	15.6	12.6	3.97	-6.32		
AQ1	33.5	74.0	1.65	-10.90		
WH1	180.8	112.4	-1.07	-9.00		
WH1	179.0	109.1	1.51	-12.55		
WH1	178.3	107.8	1.10	-11.69		
WH1	177.3	106.0	-0.04	-8.80		
WH1	176.4	104.4	2.15	-11.84		
WH1	175.3	102.4	2.07	-10.93		
WH1	174.0	100.0	2.35	-11.02		
WH1	172.8	99.4	1.90	-11.35		
WH1	170.3	98.3	2.68	-12.27		
WH1	169.9	98.1	2.59	-12.23		
WH1	168.0	97.2	1.92	-12.07		
WH1	167.5	96.9	2.39	-12.34		
WH1	167.0	96.7	1.81	-10.81		
WH1	165.9	96.2	0.95	-7.99		
WH1	164.4	95.5	1.42	-8.31		
WH1	163.4	95.0	0.82	-9.83		
WH1	162.3	94.5	0.39	-7.06		
WH1	161.3	94.0	1.86	-8.64		
WH1	161.0	93.9			25.0	255
WH1	160.5	93.7	2.42	-12.42	20.0	301
WH1	159.5	93.2	3.55	-10.33		
WH1	159.2	93.0	3.41	-11.26		
WH1	158.4	92.7	2.46	-12.06		
WH1	157.2	92.1	3.11	-10.00		
WH1	157.0	91.9			19.4	348
WH1	156.1	91.6	3.99	-9.21		
WH1	155.7	91.7			17.9	312
WH1	155.2	91.2	3.56	-9.41		
WH1	154.2	90.7	4.63	-11.44		
WH1	153.3	90.3	1.85	-9.05		
WH1	153.0	90.1	5.01	-8.84	21.0	304
WH1	152.0	89.7	5.34	-9.84	23.3	278
WH1	151.0	89.2	5.07	-9.56		
WH1	150.0	88.7	4.84	-9.29		
WH1	149.0	88.2	5.31	-9.60		
WH1	148.0	87.8	4.92	-9.03		
WH1	147.0	87.3	5.87	-8.47		
WH1	146.0	86.8	5.35	-9.23		
WH1	145.0	86.4	5.74	-9.32		
WH1	143.0	85.4	5.10	-7.86	27.5	222
WH1	142.0	84.9	5.75	-8.42		
WH1	141.8	84.8	5.77	-9.21	34.3	237

Section	Stratigraphic Height (m)	Normalized Height Z* (m)	$\delta^{13}\text{C}$	$\delta^{18}\text{O}$	$\delta^{34}\text{S}$	$\text{SO}_4$ (ppm)
WH1	139.0	83.3	5.28	-7.76		
WH1	138.0	82.7	5.07	-8.66		
WH1	137.9	82.7	5.84	-8.15		
WH1	136.0	81.6	5.65	-9.38		
WH1	135.0	81.1	5.85	-8.43		
WH1	134.0	80.5	5.87	-6.71		
WH1	133.0	80.0	5.39	-7.91	27.9	343
WH1	132.0	79.4	6.04	-7.49		
WH1	131.0	78.9	6.17	-9.01		
WH1	130.0	78.3	5.42	-5.29		
WH1	128.8	77.6	6.32	-8.11		
WH1	128.0	77.2	6.04	-6.33		
WH1	127.1	76.7	6.50	-7.55		
WH1	126.0	76.1	6.48	-8.43		
WH1	125.0	75.5	5.97	-8.72		
WH1	124.0	75.0	6.67	-6.86	21.4	247
WH1	123.0	74.4	6.60	-7.89		
WH1	119.0	72.2	7.07	-8.20		
WH1	118.0	71.7	6.92	-7.11		
WH1	117.0	71.1	6.41	-8.46		
WH1	116.0	70.6	7.01	-8.07		
WH1	115.0	70.0	7.26	-7.86	22.0	164
WH1	114.0	69.2	7.15	-8.59		
WH1	113.0	68.5	7.06	-7.43		
WH1	112.0	67.7	6.98	-7.21		
WH1	111.0	67.0	6.93	-7.83	28.4	159
WH1	109.9	66.1	6.85	-7.28		
WH1	108.0	64.7	6.74	-7.02		
WH1	107.9	64.6	7.22	-8.10		
WH1	107.0	63.9	6.90	-8.17		
WH1	106.0	63.2	6.69	-7.72		
WH1	105.0	62.4	7.09	-8.19	23.7	192
WH1	104.1	61.7	7.29	-7.88		
WH1	103.0	60.9	7.07	-7.87		
WH1	102.0	60.1	6.09	-8.20		
WH1	101.0	59.4	6.81	-8.92	19.3	169
WH1	101.0	59.4	6.81	-8.92	19.5	169
WH1	100.0	58.6	6.76	-8.40		
WH1	99.0	57.8	7.10	-8.63		
WH1	98.0	57.1	6.87	-7.22		
WH1	97.0	56.3	7.33	-7.72		
WH1	96.0	55.6	6.56	-8.52		
WH1	95.0	54.8	7.51	-8.35	22.6	213
WH1	94.0	54.1	7.15	-8.47		
WH1	93.0	53.3	7.10	-7.86		
WH1	92.0	52.5	7.46	-8.53		
WH1	90.0	51.0	7.33	-8.10	27.0	73
WH1	88.3	49.7	6.85	-7.86		
WH1	87.0	48.7	7.69	-7.25		
WH1	86.0	48.0	6.08	-9.69		

Section	Stratigraphic Height (m)	Normalized Height Z* (m)	$\delta^{13}\text{C}$	$\delta^{18}\text{O}$	$\delta^{34}\text{S}$	$\text{SO}_4$ (ppm)
WH1	85.0	47.2	7.36	-8.62		
WH1	84.0	46.5	7.48	-8.93		
WH1	83.0	45.7	7.39	-8.74	20.3	184
WH1	82.0	44.9	6.79	-8.60		
WH1	81.0	44.2	7.34	-8.83		
WH1	80.0	43.4	7.31	-8.73	20.9	258
WH1	79.0	42.7	7.43	-8.61		
WH1	78.0	41.9	7.44	-8.54		
WH1	77.0	41.1	7.23	-8.86		
WH1	74.0	39.1	6.84	-7.47		
WH1	73.0	38.6	6.55	-8.18	19.5	266
WH1	72.0	38.0	6.69	-8.27		
WH1	71.0	37.4	7.16	-8.64		
WH1	70.0	36.8	6.73	-8.98		
WH1	69.0	36.3	7.03	-8.58		
WH1	68.0	35.7	7.16	-7.95		
WH1	67.0	35.1	7.03	-8.64		
WH1	66.0	34.5	7.14	-8.03	18.2	241
WH1	65.0	34.0	7.66	-8.49		
WH1	64.0	33.4	7.28	-7.61		
WH1	63.0	32.8	7.27	-8.61		
WH1	62.0	32.2	7.31	-8.42		
WH1	60.6	31.4	7.26	-8.51		
WH1	60.0	31.1	7.11	-7.62		
WH1	59.0	30.5	7.06	-8.83		
WH1	58.0	29.9	6.57	-5.81	20.0	276
WH1	57.8	29.8	7.14	-8.52		
WH1	57.2	29.5	7.45	-8.26		
WH1	56.0	28.8	7.00	-8.52		
WH1	55.0	28.2	6.43	-8.78		
WH1	54.0	27.6	7.01	-7.71		
WH1	53.0	27.1	7.08	-9.26		
WH1	52.0	26.5	7.30	-8.62		
WH1	51.0	25.9	7.40	-9.19		
WH1	50.0	25.3	7.16	-8.72	20.3	293
WH1	49.0	24.8	7.17	-8.99		
WH1	48.0	24.2	7.22	-8.62		
WH1	47.0	23.6	6.95	-9.65		
WH1	46.0	23.0	6.95	-8.94		
WH1	45.0	22.5	6.61	-8.88	18.2	228
WH1	44.0	21.9	7.36	-8.42		
WH1	43.0	21.3	6.82	-9.43		
WH1	42.0	20.7	7.01	-9.90		
WH1	41.0	20.2	6.97	-9.83		
WH1	40.0	19.6	6.76	-9.99		
WH1	39.0	19.0	6.49	-9.91		
WH1	38.0	18.4	6.53	-10.73		
WH1	37.0	17.9	5.60	-10.57		
WH1	36.0	17.3	6.29	-9.54		
WH1	35.5	17.0	5.43	-10.85	25.3	234

Section	Stratigraphic Height (m)	Normalized Height Z* (m)	$\delta^{13}\text{C}$	$\delta^{18}\text{O}$	$\delta^{34}\text{S}$	$\text{SO}_4$ (ppm)
WH1	34.0	16.1	4.93	-11.00		
WH1	32.0	15.0	5.11	-11.69		
WH1	31.0	14.7	4.32	-12.29	17.6	199
WH1	29.7	14.4	5.40	-6.17		
WH1	28.3	14.0	4.03	-6.64		
WH1	27.4	13.7	5.49	-3.49		
WH1	26.5	13.5	6.24	-3.36		
WH1	25.2	13.1	4.58	-7.84		
WH1	24.0	12.8	5.72	-6.17		
WH1	23.4	12.6	6.35	-3.09		
WH1	23.0	12.5	6.44	-1.79		
WH1	21.9	12.2	4.12	-3.94	15.2	261
WH1	21.0	11.9	3.16	-6.88		
WH1	20.6	11.8	6.38	-3.11		
WH1	20.5	11.8	1.39	-5.42		
WH1	20.0	11.7	6.50	-3.40		
WH1	19.0	11.4	0.66	-4.46		
WH1	18.6	11.3	4.30	-1.91		
WH1	17.8	11.0	-1.73	-4.45		
WH1	16.3	10.6	2.09	-5.94	10.0	275
WH1	14.3	10.1	4.45	-5.10		
WH1	13.1	9.7	4.11	-5.65		
WH1	12.3	9.5	3.24	-5.77		
WH1	11.2	9.2	1.63	-7.74		
WH1	9.9	8.8	4.22	-6.74		
WH1	9.0	8.6	4.26	-6.80		
WH1	8.9	8.6	-3.25	-9.48		
WH1	8.9	8.6	-2.75	-9.64		
WH1	4.5	5.1	1.01	-12.08	9.9	353
WH1	4.5	5.1	-0.54	-6.19		
WH1	1.1	1.1	4.54	-6.93		
WH1	1.0	1.0	3.00	-7.85		
WH1	0.3	0.1	3.89	-7.15		
WH1	0.0	-0.2	4.31	-6.70	23.3	537
WM1	51.8	120.0	-13.49	-6.90		
WM1	50.8	118.0	-16.68	-4.08		
WM1	49.2	114.7	-16.28	-4.56		
WM1	42.3	100.6	-8.11	-2.68		
WM1	59	134.7	-22.57	-6.85		
WM1	8.3	24.6	3.04	-13.42		
WM1	50.8	118.0	-16.64	-3.98		
WM1	9.3	29.0	2.49	-12.00		
WM1	6.2	15.4	-6.18	-5.72		
WM1	6.6	17.2	0.61	-11.96		
WM1	12.2	41.3	1.45	-12.85		
WM1	10.1	32.5	2.97	-10.10		
WM1	36.6	91.9	-7.38	-9.77		
WM1	11.7	39.6	3.32	-11.22		
WM1	7.6	21.6	2.32	-2.19		
WM1	5.7	13.4	-8.88	-6.70		

Section	Stratigraphic Height (m)	Normalized Height Z* (m)	$\delta^{13}\text{C}$	$\delta^{18}\text{O}$	$\delta^{34}\text{S}$	$\text{SO}_4$ (ppm)
WM1	0.1	-1.1	-3.32	-3.61		
WM1	36.6	91.9	-7.31	-9.80		
WM1	59	134.7	-22.44	-6.91		
WM1	40.4	97.6	0.31	-3.74		
WM1	4.6	8.8	-6.14	-5.03		
WM1	3	5.1	-4.16	-7.56		
WM1	59.8	136.3	-23.40	-5.47		
WM1	51.8	120.0	-15.16	-5.10		
WM1	50.8	118.0	-16.66	-2.59		
WM1	49.2	114.7	-15.25	-3.17		
WM1	46	108.2	-7.31	-2.50		
WM1	44.4	104.9	-7.58	-2.56		
WM1	42.3	100.6	-7.91	-2.25		
WM1	41.7	99.6	-7.57	-2.95		
WM1	40.4	97.6	0.56	-3.14		
WM1	39.6	96.4	-6.99	-4.89		
WM1	38.5	94.8	-8.14	-4.18		
WM1	37.7	93.6	-8.14	-5.53		
WM1	36.6	91.9	-6.36	-8.12		
WM1	35.8	90.7	-1.42	-9.76		
WM1	34.8	89.2	-1.80	-8.58		
WM1	33.8	87.7	-4.11	-7.57		
WM1	32.2	85.3	-3.86	-9.23		
WM1	31.5	84.3	-2.78	-8.84		
WM1	30.9	83.5	2.03	-10.85		
WM1	30.4	82.8	2.24	-11.86		
WM1	29.5	81.5	1.32	-9.95		
WM1	29.1	81.0	1.17	-9.00		
WM1	28.2	79.7	1.61	-8.92		
WM1	27	78.1	-1.03	-8.92		
WM1	26.5	77.4	3.79	-10.39		
WM1	25	75.3	3.59	-8.97		
WM1	24	73.9	0.75	-8.31		
WM1	23.9	73.8	-1.54	-8.83		
WM1	23	72.5	3.17	-10.28		
WM1	21.3	70.1	3.81	-9.32		
WM1	20.6	68.1	3.67	-9.63		
WM1	19.4	64.3	5.38	-9.52		
WM1	18.8	62.3	5.30	-9.02		
WM1	16.2	54.0	2.57	-9.72		
WM1	15.7	52.4	5.06	-9.68		
WM1	15.7	52.4	3.05	-8.80		
WM1	14.8	49.6	2.55	-7.74		
WM1	14.6	48.9	3.15	-10.74		
WM1	13.8	46.4	2.97	-8.93		
WM1	13.8	46.4	3.21	-7.91		
WM1	12.6	42.6	5.22	-10.03		
WM1	12.2	41.3	1.39	-13.15		
WM1	11.7	39.6	3.28	-11.48		
WM1	10.1	32.5	2.99	-10.33		

Section	Stratigraphic Height (m)	Normalized Height Z* (m)	$\delta^{13}\text{C}$	$\delta^{18}\text{O}$	$\delta^{34}\text{S}$	$\text{SO}_4$ (ppm)
WM1	9.3	29.0	2.55	-11.77		
WM1	8.3	24.6	3.02	-13.83		
WM1	7.6	21.6	2.79	-13.08		
WM1	6.6	17.2	0.67	-11.79		
WM1	6.2	15.4	-6.41	-5.76		
WM1	5.7	13.4	-8.98	-6.81		
WM1	4.6	8.8				
WM1	0.1	-1.1	-3.45	-5.41		
WS1	42.0	31.2	6.20	-8.71		
WS1	104.2	81.1	5.24	-9.43		
WS1	55.0	42.5	6.50	-9.49	17.2	160
WS1	49.3	37.4	6.49	-10.12		
WS1	33.0	23.5	7.17	-10.59		
WS1	67.0	53.7	7.03	-9.02		
WS1	30.5	21.4	5.35	-10.82		
WS1	43.2	32.2	6.91	-10.27		
WS1	62.0	49.0	6.90	-9.55		
WS1	4.7	3.1	2.20	-8.51	24.7	163
WS1	60.5	47.6	6.55	-9.44		
WS1	23.1	15.1	5.22	-12.01		
WS1	63.9	50.8	7.00	-9.05		
WS1	0.4	0.3	7.68	-5.57	17.3	107
WS1	45.2	33.9	7.16	-9.69		
WS1	15.8	10.3	4.91	-4.65	15.2	234
WS1	27.3	18.7	5.70	-11.42		
WS1	59.4	46.6	6.06	-9.33	16.8	140
WS1	40.1	29.6	6.94	-8.99	18.1	122
WS1	64.3	51.2	7.16	-9.23		
WS1	48.3	36.6	5.98	-9.79		
WS1	35.6	25.8	8.33	-7.72		
WS1	32.4	23.0	4.83	-9.09		
WS1	31.4	22.2	6.77	-10.51		
WS1	5.5	3.6	1.45	-6.17		
WS1	35.2	25.4	6.96	-10.29		
WS1	110.7	84.8	5.08	-9.32		
WS1	171.9	129.8	-14.36	-12.76		
WS1	41.6	30.9	6.83	-9.37		
WS1	153.7	117.2	-3.02	-4.21		
WS1	103.3	80.6	5.18	-9.35		
WS1	26.0	17.6	5.82	-11.60		
WS1	108.6	83.6	5.14	-8.99		
WS1	44.1	33.0	7.33	-10.07		
WS1	106.3	82.3	5.39	-9.26		
WS1	105.2	81.7	5.42	-9.26		
WS1	25.0	16.7	5.82	-11.97		
WS1	187.2	139.4	-12.63	-14.69		
WS1	50.2	38.2	7.09	-9.89		
WS1	34.2	24.6	7.11	-9.69	21.2	141
WS1	68.6	55.2	6.64	-8.98		
WS1	111.5	85.2	4.78	-8.49	21.0	316

Section	Stratigraphic Height (m)	Normalized Height Z* (m)	$\delta^{13}\text{C}$	$\delta^{18}\text{O}$	$\delta^{34}\text{S}$	$\text{SO}_4$ (ppm)
WS1	54.5	42.0	6.95	-9.32		
WS1	156.1	119.7	-0.64	-6.66		
WS1	19.2	12.5	2.70	-12.22		
WS1	9.2	6.0	1.85	-4.38		
WS1	115.4	87.5	4.20	-10.37		
WS1	9.8	6.4	5.31	-6.63	22.8	324
WS1	37.7	27.5	6.75	-10.06		
WS1	119.1	89.7	3.63	-10.65		
WS1	28.3	19.5	6.32	-11.21		
WS1	107.3	82.9	5.25	-9.17		
WS1	39.0	28.7	6.65	-9.36		
WS1	201.0	148.1	-13.14	-14.76		
WS1	126.6	94.0	1.81	-8.56		
WS1	29.4	20.5	6.04	-11.02	22.5	197
WS1	53.1	40.7	6.96	-7.43		
WS1	175.7	132.2	-14.20	-13.69		
WS1	56.3	43.7	6.95	-9.28		
WS1	47.0	35.5	4.76	-6.92		
WS1	113.3	86.3	4.86	-9.88		
WS1	149.6	113.0	-3.09	-5.21	17.2	409
WS1	46.2	34.8	7.01	-9.48	21.1	172
WS1	112.9	86.0	4.51	-9.74		
WS1	7.0	4.6	2.15	-6.62		
WS1	52.3	40.0	6.93	-9.59	17.2	150
WS1	65.3	52.1	7.11	-9.02		
WS1	142.6	105.8	-1.16	-4.18		
WS1	66.6	53.3	6.99	-9.29		
WS1	144.9	108.2	-2.88	-4.83		
WS1	114.1	86.7	5.07	-9.82		
WS1	133.7	98.1	-0.81	-4.57		
WS1	58.3	45.6	6.69	-8.97		
WS1	61.6	48.7	5.92	-9.12		
WS1	167.3	126.9	-9.70	-6.96	26.0	415
WS1	169.2	128.1	-11.46	-8.13		
WS1	117.3	88.6	3.87	-10.44	23.3	108
WS1	200.3	147.7	-13.01	-14.98		
WS1	38.3	28.1	6.72	-10.00		
WS1	124.0	92.5	3.34	-9.48	23.6	186
WS1	24.2	16.0	5.29	-12.09	21.1	198
WS1	141.6	104.8	-1.34	-5.88	22.1	396
WS1	120.6	90.5	3.93	-7.27		
WS1	125.1	93.1	1.37	-12.64		
WS1	193.4	143.3	-12.20	-14.36	24.9	165
WS1	127.3	94.4	3.69	-4.86		
WS1	191.9	142.4	-12.97	-14.75		
WS1	51.0	38.9	7.08	-8.38		
WS1	194.9	144.3	-12.40	-14.22		
WS1	14.6	9.6	1.55	-8.99		
WS1	193.0	143.1	-12.49	-14.50		
WS1	121.1	90.8	3.28	-8.96	21.4	156

Section	Stratigraphic Height (m)	Normalized Height Z* (m)	$\delta^{13}\text{C}$	$\delta^{18}\text{O}$	$\delta^{34}\text{S}$	$\text{SO}_4$ (ppm)
WS1	166.3	126.2	-10.08	-8.98		
WS1	173.7	130.9	-14.73	-13.17		
WS1	203.9	149.9	-12.88	-15.18		
WS1	124.4	92.7	2.43	-12.81		
WS1	136.9	100.0	-1.71	-5.48		
WS1	196.5	145.3	-13.30	-14.75		
WS1	6.2	4.1	1.52	-7.77		
WS1	18.3	12.0	3.14	-12.49		
WS1	161.0	122.9	-2.12	-3.48		
WS1	178.2	133.7	-13.50	-13.61		
WS1	164.0	124.8	-10.23	-11.24		
WS1	185.9	138.6	-12.49	-13.59		
WS1	116.1	87.9	4.48	-10.31		
WS1	122.5	91.6	3.02	-11.43		
WS1	168.1	127.4	-11.24	-10.73		
WS1	184.6	137.8	-13.17	-14.21		
WS1	176.3	132.5	-12.70	-12.44	17.9	272
WS1	170.6	128.9	-11.96	-11.66		
WS1	195.8	144.8	-12.15	-14.14		
WS1	174.8	131.6	-10.62	-8.45		
WS1	188.0	139.9	-11.47	-12.39		
WS1	198.8	146.7	-12.37	-14.84		
WS1	183.6	137.1	-12.21	-13.23		
WS1	182.0	136.1	-11.38	-11.53		
WS1	197.8	146.1	-12.46	-14.25		
WS1	165.0	125.4	-9.37	-9.56		
WS1	181.1	135.6	-10.35	-11.89		
WS1	12.4	8.1	1.79	-11.99		
WS1	172.9	130.4	-10.51	-10.38		
WS1	11.4	7.5	7.14	-4.88		
WS1	189.1	140.6	-12.92	-14.63		
WS1	96.6	76.8	7.34	-7.01		
WS1	95.9	76.4	7.11	-7.57		
WS1	94.5	75.6	6.80	-6.93	18.7	190
WS1	94.4	75.6	7.24	-7.10		
WS1	93.9	75.3	7.59	-7.11		
WS1	92.3	74.4	7.56	-7.29		
WS1	91.7	74.1	7.66	-6.97		
WS1	90.6	73.4	7.41	-8.27		
WS1	89.5	72.8	7.52	-7.81		
WS1	88.1	72.0	7.64	-7.58		
WS1	86.5	71.1	7.79	-6.74		108
WS1	85.8	70.7	7.03	-7.38		
WS1	84.4	69.9	7.88	-6.69		
WS1	83.4	69.0	7.34	-7.27		
WS1	81.5	67.2	7.97	-7.32		
WS1	80.4	66.2	7.94	-7.52		
WS1	80.3	66.1	7.97	-7.65	21.1	209
WS1	79.8	65.6	7.49	-7.44		
WS1	78.6	64.5	7.78	-6.74		

Section	Stratigraphic Height (m)	Normalized Height Z* (m)	$\delta^{13}\text{C}$	$\delta^{18}\text{O}$	$\delta^{34}\text{S}$	$\text{SO}_4$ (ppm)
WS1	78.2	64.1	7.90	-7.11		
WS1	77.1	63.1	7.85	-7.39	20.0	92
WS1	76.2	62.3	7.68	-7.26		
WS1	75.1	61.2	7.19	-7.26		
WS1	74.3	60.5	7.78	-7.53		
WS1	73.5	59.8	7.42	-7.54		
WS1	71.3	57.7	7.41	-6.57		
WS1	69.6	56.1	6.92	-6.98		